GEOCHEMICAL INVESTIGATION OF CONTINENTAL WEATHEIRNG AND PALEO-OCEAN REDOX EVOLUTION

Cheng Cao

A dissertation submitted to the faculty at the University of North Carolina at Chapel Hill in partial fulfillment of the requirements for the degree of Doctor of Philosophy in the Department of Geological Sciences in the School of Art and Science.

Chapel Hill
2020

Approved by

Xiaoming Liu

Drew S. Coleman

Larry Benninger

Marc Alperin

Christopher T. Reinhard

ABSTRACT

Cheng Cao: Geochemical investigation of continental weathering and paleo-ocean redox evolution
(Under the direction of Xiaoming Liu)

Ancient marine carbonates are widely studied to extract geochemical information including elemental and isotopes signals to reconstruct primary seawater signalS therefore to understand the evolution of Earth's surface. Particularly, my PhD work focuses on exploring cerium anomaly and lithium isotopes in marine carbonates as tracers for oceanic redox condition and chemical weathering in the past. Chapter 1 develops a sequential leaching protocol for bulk carbonate to extract primary seawater rare-earth-element patterns. It demonstrates that the application of using marine carbonates as seawater geochemistry archives requires careful sample screening and appropriate sequential leaching. Chapter 2 uses Ce anomaly in marine carbonates to investigate the dissolved oxygen in the upper ocean during the Oceanic Anoxic Event 2 (OAE 2), which is the largest ocean deoxygenation event in the Cretaceous. In addition, I developed a thermodynamic model for Ce oxidation and quantitatively constrained the large part of the upper ocean may have lost up to 50% of dissolved oxygen in response to the OAE 2 compared to the fully recovered ocean post the event. Chapter 3 leverages the use of Li isotope in marine carbonate to trace not only the continental weathering but also changes in hydrothermal activities and reverse weathering. This case study reconstructs seawater Li isotopes from the early Permian to the early Triassic using bulk marine carbonates. A drop of 14‰ of seawater δ^7Li is observed in the Late Permian. Combined with the geologic-event timeline and

Li box model, it can be best explained by a paused reverse weathering and reduced continental chemical weathering rate.

To my mentor and friends, I couldn't have done this without you.
Thank you for all of your support along the way

ACKNOWLEDGMENTS

Five years ago, I was applying for Ph.D. positions in the U.S., and my undergraduate mentor, Fang Huang, introduced me to Xiaoming. Xiaoming has been a very supportive advisor professionally and a close friend personally and I count myself extremely lucky to have had her as a Ph.D. advisor. I was not exactly sure what to do for my Ph.D., and Xiaoming encouraged me to think independently and critically. The second year I was spending a lot of time on the leaching experiments, however, I keep getting confusing results and little progress was made. There was one month I did not talk to Xiaoming at all or anyone else in the group, but feeling stuck. Xiaoming reached out to me and said, you are not doing this alone, you should talk to people and seek for help, often discussions open your mind. I did more experiments and found out all the results from previous experiments were contaminated. In particular, I want to thank Wenshuai Li, who talks about the filtering process which inspired me to check if filter makes a difference to my results, and it did! I also thank Xiaoming for providing a such collaborative environment in the group. Everyone here is doing different interesting things rather than competing against one another. Xiaoming is patient, always energetic and students are her first priority. She taught almost everything I could hope to learn during my Ph.D., not just how to do science, but also how to pursue academic career, networking, and time management.

When Xiaoming and I came to UNC at 2015, we did not have a lab then. Now the PMS Lab has developed into a big family with a group of graduate colleagues-Wenshuai Li, Heather Hanna, Xikai Wang and undergraduate students as well as visiting scholars. I would like to extend my sincere thanks to them for those constructive feedbacks and discussions on my

research progress, and for the help in the lab. Special thanks to Clement Baitallie, who not only inspired me to develop the dissertation projects, but also coauthored in two of my manuscripts.

Over the last five years, I enjoyed my time very much in the Department of Geological Sciences. I'm extremely grateful to all the help and assistance from Ryan Mills. He distilled all the concentrated nitric and hydrochloric acids I needed for the research, taught me acid titration and helped me with Sr isotope analysis. Madelyn Percy helped me review multiple documents including manuscripts, proposals and applications. She also shows me how to analyze the XRD results. Josh Rosera taught me step by step to use the bomb. Connor Lawrence instructed me to powder rock samples. And Allen Glazner provided me access to the XRD instruments and demonstrated how to operate and prepare samples very patiently. Xiao Yang was my expert to ask a question about R programing and illustrator. Thanks should also go to Deborah Harris for making sure that I am on trach academically and watering my plants. I must also thank Deltra Tate for assistance in so many things, ordering, reimbursement, and writing all the supporting letters.

I would like to express my deepest appreciation to my committee. They have been very supportive and encouraging. Drew Coleman trained me to work in the clean lab, and provided me with access to all his lab facilities. Larry would send me papers relevant to my research, and he is always there whenever I have questions. I got a lot of Chemical Oceanography class that taught by Marc Alperin. The thermodynamic model of Ce oxidation would have gone nowhere without his help. He always asks me questions from a perspective of marine scientist and that has changed lots of my understanding of paleoceanography. Christopher Reinhard provides invaluable insights into the modeling work.

I'd like to recognize the assistance I received from Qiaohui Zhong who did a great number of strontium column work for me. Thanks also goes to Min Liu who wrote the python code for me to calculate the Li box model, and Ziliang Zhu who guided me to analyze those model results using R programing.

I met brilliant people at UNC, and some of them became close friends. I cannot leave UNC without mentioning how joyful they have made my life in the past five years. My time outside of work has been fulfilled with sports, cooking, and laughter. Special thanks to Yueting Luo, who has been an amazing roommate, and took care of me all the time. Once I cut my thumb, and she kept me away from the kitchen for a month and fed me well.

My success, the completion of my dissertation would not have been possible without the endless support and nurturing of my parents. They encouraged me to pursue my dreams and they are always on my side every time I make a decision.

My research was finacially supported by the UNC-Chapel Hill startup funds to X-ML, the GSA graduate student research grant, the Martin Fund fellowship and the NSF Career Award (EAR-1848153).

PREFACE

Parts of this work were done in collaboration with other talented scientists. Chapter 2 represents a publication for which I am the first author. Xiaoming Liu and Clement Bataille contributed to data interpretation and revising the manuscript. The paper was published previous to writing this thesis with the following citation:

> Cao, C., Liu, X.-M., Bataille, C. P., & Liu, C. (2020). What do Ce anomalies in marine carbonates really mean? A perspective from leaching experiments. *Chemical Geology*, *532*, 119413. https://doi.org/10.1016/j.chemgeo.2019.119413

Permission to include the article in its entirety in a PhD dissertation was retained from The Elsevier as explained at http://www.elsevier.com/wps/find/authorsview.authors/copyright#whatrights.

Chapter 3 represents work done in collaboration with Dr. Jeremy Owens and Dr. Hugh Jenkyns. I am the lead author on the paper, and Dr. Jeremy Owens and Hugh Jenkyns provided samples, and revised the manuscript together with Dr. Xiaoming Liu. The paper is under review in Paleoceanography and Paleoclimate now. Permission to include the article in its entirety in a PhD dissertation was retained from AGU publications as explained at https://agupubs.onlinelibrary.wiley.com/hub/journal/25724525/about/permissions.

Chapter 4 represents the work done in collaboration with Dr. Xiaoming Liu, Clement Bataille, Haijun Song, Huaichun Wu, Katherine Tierney, Matthew Saltzman, Christoph Korte and Zhaofeng Zhang. This work is currently in preparation for publication. Part of the data was obtained by Dr. Clement Bataille including the 2/3 of the Sr isotope data and ¼ of the Li isotope

data. The rest of coauthor contributed samples. I also received assistance from Qiaohui Zhong, who performed Sr chromatography and measurements for about 10 of my samples.

All copyrighted material included in this dissertation is used with permission from the relevant copyright holders.

TABLE OF CONTENTS

LIST OF TABLES

LIST OF FIGURES

LIST OF ABBREVIATIONS

Ce – Cerium

Ce/Ce* – Cerium anomaly

CO_2 – carbon dioxide

Eu/Eu* – Europium anomaly

Ho – Holmium

HREY – Heavy REY

MREY– Middle REY

ICP-MS – Inductively Coupled Plasma-Mass Spectrometer

IODP– International Ocean Discovery Program

KL – Key Largo limestone

kyr – thousand years

La/La* – lanthanum anomaly

Li – Lithium

LIP – large igneous provinces

LOWESS - locally weighted scatterplot smoothing

MC-ICP-MS – Multi-collector Inductively Coupled Plasma-Mass Spectrometer

NOAA – National Oceanic and Atmospheric Administration

OAEs – Oceanic Anoxic Events

OAE 2 – Oceanic Anoxic Event 2

ODP – Ocean Drilling Program

PAAS – Post Archean Australian Shale

PCE – Plenus Cold Event

PETM – Paleocene-Eocene Thermal Maximum

REY – rare earth elements and yttrium

SOM – sedimentary organic matter

Sr –strontium

TIMS – Thermal Ionization Mass Spectrometry

TOC– total organic carbon

USGS – United States Geological Survey

UCC – upper continental crust

UHMI – high matrix mode

WOA 13 – World Ocean Atlas 13

XRF X-ray fluorescence

XRD X-ray diffractometer

CHAPTER 1 - INTRODUCTION

Multiple Oceanic Anoxic Events (OAEs) existed in the Phanerozoic era despite of its widespread oxidized atmosphere (Jenkyns, 2010; Liu et al., 2016; Lyons et al., 2014). Often these OAEs coeval with climate perturbations and mass extinctions in the marine ecosystem. Due to global warming, the modern ocean is experiencing large-scale deoxygenation, with 2% dissolved oxygen loss over the last five decades and a recent model predicts 1-7% loss in oxygen by the year 2100 (Schmidtko et al., 2017). Past OAEs are analogues for current and future ocean deoxygenation, improving our understanding of the causes and consequences of such events, especially their relationships with climate change. Chemical weathering is another vital process that interacts with climate by regulating atmospheric CO_2 level. Particularly, silicate weathering is a major sink for atmospheric CO_2. Additionally, chemical weathering delivers cations and alkalinity to the ocean, sustaining long-term oceanography stability (Walker et al., 1981). To understand the relationships between the silicate weathering, climate and oceanic oxygen, my dissertation develops geochemical tracers including the Ce (cerium) anomaly and Li (lithium) isotopes in ancient marine carbonate rocks.

Ce anomaly in marine carbonate has been widely used to trace the oceanic redox conditions (Bellefroid et al., 2018; Ling et al., 2013; Liu et al., 1988; Tostevin et al., 2016; Wallace et al., 2017). Ce is one of the REY (rare earth elements and yttrium), which is a coherent group of elements in relation to the filling of the 4f electron shell across the REY series (Byrne and Li, 1995). Besides their similar physical and chemical properties, a number of deviations also occur to certain elements and Ce is one of the special elements due to its oxidation state.

REY has a predominant trivalent oxidation state, but Ce (III) could be oxidized to Ce (IV) in oxic condition. Ce (IV) is insoluble and it can be scavenged to the surface of Mn-Fe oxyhydroxides or organic particulates in the form of $Ce(OH)_4$, or CeO_2 (German and Elderfield, 1990; Moffett, 1994a, 1994b, 1990). Consequently, the remaining seawater will be depleted in dissolved Ce relative to other trivalent REY after the normalization to a standard such as Post Archean Australian Shale (PAAS) (Elderfield and Greaves, 1982) or the upper continental crust (UCC) (Rudnick and Gao, 2014). This is the so-called negative Ce anomaly. In anoxic conditions, the reduction of Ce (IV) releases Ce (III) back in the aqueous and displays no Ce anomaly or positive Ce anomaly. As a result of its distinct chemical behavior relative to other REY, Ce has been used as a redox proxy with oxic conditions usually showing a negative Ce anomaly (e.g. Modern Ocean) whereas anoxic and suboxic conditions correspond to no anomaly or slightly positive Ce anomaly. Much attention has been paid recently to the potential of using Ce anomaly in distinguishing between oxic and anoxic environments associated with anoxic events and mass extinction events (Lécuyer et al., 2004; Ling et al., 2013; Song et al., 2012; Wang et al., 1993).

REY (III) mono- and di-carbonate ion complexes are the dominant dissolved species in seawater, and REY incorporate into carbonate by substituting for Ca^{2+} (Byrne and Bingler, 1989; Wright et al., 1987; Zhong and Mucci, 1995). Moreover, Webb and Kamber (2000) demonstrated that REY are incorporated in high proportion and without biological fractionation in modern microbialites. Thus, primary deposited carbonates are assumed to preserve simultaneous shallow marine REY pattern. However, modern seawater REY characteristics are rarely found in ancient marine carbonate, likely due to the influence from local contaminative phases, including Fe-Mn oxyhydroxides and oxides, clays, organic matter, and siliciclastic

phases, during incorporation of mobilized REY into diagenetic carbonates (Banner et al., 1988; Palmer, 1985; Shields and Stille, 2001; Shields and Webb, 2004). Therefore, the potential of Ce as a redox proxy has been severely impeded by the lack of an effective digestion procedure to extract primary oceanic signals from ancient marine carbonates. In Chapter 2 of the dissertation, a sequential leaching protocol has been developed to avoid contaminations from non-carbonate phases. And this chapter is presented as an independent paper that has already been published in *Chemical Geology*.

Chapter 3 applies Ce anomaly in marine carbonates to study the redox condition in the upper ocean before, during and after Oceanic Anoxic Event 2 (OAE 2). The distinctive Ce anomaly patterns from seven study sites represent a complementary compilation to redox record of global ocean. The results suggest that deoxygenation in the global ocean in late Cretaceous results from super greenhouse climate and extreme anoxia is restricted in areas where ocean circulation further decreases oxygen supply. In addition, a thermo dynamic model of Ce oxidation is developed to quantitatively estimate the oxygen inventory in the upper ocean and calculated that more than 50% of oxygen may have been lost in the Atlantic and Indian Ocean during this event. Chapter 3 also describes my newly developed Ce oxidation model in detail.

Chapter 4 of my dissertation aims to develop Li isotopes in marine carbonate rocks to trace chemical weathering during the Permian-Triassic periods. Tracing past silicate weathering using marine rock record is rather challenging. Reconstructed seawater $^{87}Sr/^{86}Sr$ ratio - $(^{87}Sr/^{86}Sr)_{sw}$ is mainly used to study chemical weathering rate. However, this proxy cannot distinguish silicate weathering from carbonate weathering due to its similar high concentrations of Sr (strontium) in silicate and carbonate rocks (Bickle et al., 2005; Galy et al., 1999; Oliver et al., 2003; Palmer and Edmond, 1992). The advancement of MC-ICP-MS emerged new tracers of

chemical weathering such as Li isotopes (Huh et al., 1998; Pistiner and Henderson, 2003; Pogge von Strandmann et al., 2012, 2008, 2006).

Li is dominantly hosted in silicate rocks while its abundance is low in carbonate rocks. Two stable isotopes, ^{7}Li and ^{6}Li, have relative natural abundance of 92.41% and 7.59%, respectively (Penniston-Dorland et al., 2017). Large fractionation of Li isotopes takes place in seawater-basalt systems and river weathering regimes (Chan et al., 1992; Dellinger et al., 2015; Huh et al., 2001, 1998; Pistiner and Henderson, 2003; Pogge von Strandmann et al., 2010). The overall behavior of Li isotopes during weathering is well known. Primary mineral dissolution increases Li concentration in continental runoff with no significant isotope fractionation (Pistiner and Henderson, 2003). Secondary mineral formation takes Li from the fluid but preferentially incorporates ^{6}Li thus leaving the continental runoff with heavier $\delta^{7}Li$ (Chan et al., 1992; Kisakurek et al., 2005; Liu et al., 2013; Rudnick et al., 2004; Teng et al., 2004; Wimpenny et al., 2015, 2010). Therefore, the $\delta^{7}Li$ in river reflects weathering congruency, defined as the ratio of primary mineral dissolution to secondary mineral formation (Dellinger et al., 2017; Pogge von Strandmann and Henderson, 2015). And the $\delta^{7}Li$ together with Li flux reflect chemical weathering rate. Recently, a few studies used Li isotopes in marine carbonate materials to trace continent weathering in the past (Lechler et al., 2015; Pogge Von Strandmann et al., 2013; Sun et al., 2018; Wanner et al., 2014). However, the relationship between reconstructed seawater $\delta^{7}Li$ and continental weathering is not straightforward because seawater $\delta^{7}Li$ can be influenced significantly by other input and output sources such as hydrothermal and reserve weathering fluxes. In Chapter 4, I employed a case study to reconstruct the seawater $\delta^{7}Li$ based on bulk carbonate $\delta^{7}Li$ during the Permian to Early Triassic periods. Inferred seawater $\delta^{7}Li$ shows three major fluctuations and was used to develop steady state Li box models. The Li box models

suggest these fluctuations correspond to the changes in hydrothermal activity, reverse weathering and continental weathering, respectively.

Conclusions and outlook are presented in Chapter 5.

REFERENCES

Banner, J.L., G.N.Hanson, W.J.Meyers, 1988. Rare Earth Elements and Nd Isotopic Variations in Regionally Extensive Dolomites from the Burlington-Keokuk Formation (Mississippian) : Implications for REE Mobility during Carbonate Diagenesis. J. Sediment. Petrol. 58, 415–432.

Bellefroid, E.J., Hood, A.V.S., Hoffman, P.F., Thomas, M.D., Reinhard, C.T., Planavsky, N.J., 2018. Constraints on Paleoproterozoic atmospheric oxygen levels. Proc. Natl. Acad. Sci. 115, 8104–8109. https://doi.org/10.1073/pnas.1806216115

Bickle, M.J., Chapman, H.J., Bunbury, J., Harris, N.B.W., Fairchild, I.J., Ahmad, T., Pomiès, C., 2005. Relative contributions of silicate and carbonate rocks to riverine Sr fluxes in the headwaters of the Ganges. Geochim. Cosmochim. Acta 69, 2221–2240. https://doi.org/10.1016/j.gca.2004.11.019

Burton, K.W., Vigier, N., 2011. Lithium Isotopes as Tracers in Marine and Terrestrial Environments, in: Handbook of Environmental Isotope Geochemistry. Springer Berlin Heidelberg, Berlin, Heidelberg, pp. 41–59. https://doi.org/10.1007/978-3-642-10637-8_4

Byrne, R.H., Bingler, L.S., 1989. Comment on "Cerium: A chemical tracer for paleo-oceanic redox conditions" by Y.-G. Liu, M. R. U. Miah and R. A. Schmitt. Geochim. Cosmochim. Acta. https://doi.org/10.1016/0016-7037(89)90081-1

Byrne, R.H., Li, B., 1995. Comparative complexation behavior of the rare earths. Geochim. Cosmochim. Acta 59, 4575–4589. https://doi.org/10.1016/0016-7037(95)00303-7

Chan, L.H., Edmond, J.M., Thompson, G., Gillis, K., 1992. Lithium isotopic composition of submarine basalts: implications for the lithium cycle in the oceans. Earth Planet. Sci. Lett. 108, 151–160. https://doi.org/10.1016/0012-821X(92)90067-6

Dellinger, M., Gaillardet, J., Bouchez, J., Calmels, D., Louvat, P., Dosseto, A., Gorge, C., Alanoca, L., Maurice, L., 2015. Riverine Li isotope fractionation in the Amazon River basin controlled by the weathering regimes. Geochim. Cosmochim. Acta 164, 71–93. https://doi.org/10.1016/j.gca.2015.04.042

Elderfield, H., Greaves, M.J., 1982. The rare earth elements in seawater. Nature 296, 214–219. https://doi.org/10.1038/296214a0

Galy, A., France-Lanord, C., Derry, L.A., 1999. The strontium isotopic budget of Himalayan Rivers in Nepal and Bangladesh. Geochim. Cosmochim. Acta 63, 1905–1925. https://doi.org/10.1016/S0016-7037(99)00081-2

German, C.R., Elderfield, H., 1990. Application of the Ce anomaly as a paleoredox indicator: The ground rules. Paleoceanography 5, 823–833. https://doi.org/10.1029/PA005i005p00823

Huh, Y., Chan, L.H., Edmond, J.M., 2001. Lithium isotopes as a probe of weathering processes: Orinoco River. Earth Planet. Sci. Lett. 194, 189–199. https://doi.org/10.1016/S0012-821X(01)00523-4

Huh, Y., Chan, L.H., Zhang, L., Edmond, J.M., 1998. Lithium and its isotopes in major world rivers: implications for weathering and the oceanic budget. Geochim. Cosmochim. Acta 62, 2039–2051. https://doi.org/10.1016/S0016-7037(98)00126-4

Jenkyns, H.C., 2010. Geochemistry of oceanic anoxic events. Geochemistry, Geophys. Geosystems 11, 1–30. https://doi.org/10.1029/2009GC002788

Kisakurek, B., James, R.H., Harris, N.B.W., 2005. Li and δ7Li in Himalayan rivers: Proxies for silicate weathering? Earth Planet. Sci. Lett. 237, 387–401. https://doi.org/10.1016/j.epsl.2005.07.019

Lechler, M., Pogge von Strandmann, P.A.E., Jenkyns, H.C., Prosser, G., Parente, M., 2015. Lithium-isotope evidence for enhanced silicate weathering during OAE 1a (Early Aptian Selli event). Earth Planet. Sci. Lett. 432, 210–222. https://doi.org/10.1016/j.epsl.2015.09.052

Lécuyer, C., Reynard, B., Grandjean, P., 2004. Rare earth element evolution of Phanerozoic seawater recorded in biogenic apatites. Chem. Geol. 204, 63–102. https://doi.org/10.1016/j.chemgeo.2003.11.003

Lemarchand, E., Chabaux, F., Vigier, N., Millot, R., Pierret, M.C., 2010. Lithium isotope systematics in a forested granitic catchment (Strengbach, Vosges Mountains, France). Geochim. Cosmochim. Acta 74, 4612–4628. https://doi.org/10.1016/j.gca.2010.04.057

Ling, H.-F., Chen, X., Li, D., Wang, D., Shields-Zhou, G.A., 2013. Cerium anomaly variations in Ediacaran–earliest Cambrian carbonates from the Yangtze Gorges area, South China: Implications for oxygenation of coeval shallow seawater. Precambrian Res. 225, 110–127. https://doi.org/10.1016/j.precamres.2011.10.011

Liu, X.-M., Kah, L.C., Knoll, A.H., Cui, H., Kaufman, A.J., Shahar, A., Hazen, R.M., 2016. Tracing Earth's O2 evolution using Zn/Fe ratios in marine carbonates. Geochemical Perspect. Lett. 2, 24–34. https://doi.org/10.7185/geochemlet.1603

Liu, X.M., Rudnick, R.L., McDonough, W.F., Cummings, M.L., 2013. Influence of chemical weathering on the composition of the continental crust: Insights from Li and Nd isotopes in bauxite profiles developed on Columbia River Basalts. Geochim. Cosmochim. Acta 115, 73–91. https://doi.org/10.1016/j.gca.2013.03.043

Liu, Y., Miah, M.R.U., Schmitt, R.A., 1988. Cerium : A chemical tracer for paleo-oceanic redox conditions. Geochim. Cosmochim. Acta 52, 1361–1371.

Lyons, T.W., Reinhard, C.T., Planavsky, N.J., 2014. The rise of oxygen in Earth's early ocean

and atmosphere. Nature 506, 307–15. https://doi.org/10.1038/nature13068

Moffett, J.W., 1994a. A radiotracer study of cerium and manganese uptake onto suspended particles in Chesapeake Bay. Geochim. Cosmochim. Acta 58, 695–703. https://doi.org/10.1016/0016-7037(94)90499-5

Moffett, J.W., 1994b. The relationship between cerium and manganese oxidation in the marine environment. Limnol. Oceanogr. 39, 1309–1318. https://doi.org/10.4319/lo.1994.39.6.1309

Moffett, J.W., 1990. Microbially mediated cerium oxidation in sea water. Nature 345, 421–423. https://doi.org/10.1038/345421a0

Oliver, L., Harris, N., Bickle, M., Chapman, H., Dise, N., Horstwood, M., 2003. Silicate weathering rates decoupled from the 87Sr/86Sr ratio of the dissolved load during Himalayan erosion. Chem. Geol. 201, 119–139. https://doi.org/10.1016/S0009-2541(03)00236-5

Palmer, M.R., 1985. Rare earth elements in foraminifera tests. Earth Planet. Sci. Lett. 73, 285–298.

Palmer, M.R., Edmond, J.M., 1992. Controls over the strontium isotope composition of river water. Geochim. Cosmochim. Acta 56, 2099–2111. https://doi.org/10.1016/0016-7037(92)90332-D

Penniston-Dorland, S., Liu, X.-M., Rudnick, R.L., 2017. Lithium Isotope Geochemistry, in: Reviews in Mineralogy and Geochemistry. pp. 165–217. https://doi.org/10.2138/rmg.2017.82.6

Pistiner, Henderson, G.M., 2003. Lithium-isotope fractionation during continental weathering processes. Earth Planet. Sci. Lett. 214, 327–339. https://doi.org/10.1016/S0012-821X(03)00348-0

Pogge von Strandmann, P.A.E., Burton, K.W., James, R.H., van Calsteren, P., Gislason, S.R., 2010. Assessing the role of climate on uranium and lithium isotope behaviour in rivers draining a basaltic terrain. Chem. Geol. 270, 227–239. https://doi.org/10.1016/j.chemgeo.2009.12.002

Pogge von Strandmann, P.A.E., Burton, K.W., James, R.H., van Calsteren, P., Gíslason, S.R., Mokadem, F., 2006. Riverine behaviour of uranium and lithium isotopes in an actively glaciated basaltic terrain. Earth Planet. Sci. Lett. 251, 134–147. https://doi.org/10.1016/j.epsl.2006.09.001

Pogge von Strandmann, P.A.E., Burton, K.W., James, R.H., van Calsteren, P., Gislason, S.R., Sigfússon, B., 2008. The influence of weathering processes on riverine magnesium isotopes in a basaltic terrain. Earth Planet. Sci. Lett. 276, 187–197. https://doi.org/10.1016/j.epsl.2008.09.020

Pogge Von Strandmann, P.A.E., Jenkyns, H.C., Woodfine, R.G., 2013. Lithium isotope evidence for enhanced weathering during Oceanic Anoxic Event 2. Nat. Geosci. 6, 668–672. https://doi.org/10.1038/ngeo1875

Pogge von Strandmann, P.A.E., Opfergelt, S., Lai, Y.J., Sigfússon, B., Gislason, S.R., Burton, K.W., 2012. Lithium, magnesium and silicon isotope behaviour accompanying weathering in a basaltic soil and pore water profile in Iceland. Earth Planet. Sci. Lett. 339–340, 11–23. https://doi.org/10.1016/j.epsl.2012.05.035

Rudnick, R.L., Gao, S., 2014. Composition of the Continental Crust, 2nd ed, Treatise on Geochemistry: Second Edition. Elsevier Ltd. https://doi.org/10.1016/B978-0-08-095975-7.00301-6

Rudnick, R.L., Tomascak, P.B., Njo, H.B., Gardner, L.R., 2004. Extreme lithium isotopic fractionation during continental weathering revealed in saprolites from South Carolina. Chem. Geol. 212, 45–57. https://doi.org/10.1016/j.chemgeo.2004.08.008

Schmidtko, S., Stramma, L., Visbeck, M., 2017. Decline in global oceanic oxygen content during the past five decades. Nature 542, 335–339. https://doi.org/10.1038/nature21399

Shields, G., Stille, P., 2001. Diagenetic constraints on the use of cerium anomalies as palaeoseawater redox proxies: An isotopic and REE study of Cambrian phosphorites. Chem. Geol. 175, 29–48. https://doi.org/10.1016/S0009-2541(00)00362-4

Shields, G.A., Webb, G.E., 2004. Has the REE composition of seawater changed over geological time? Chem. Geol. 204, 103–107. https://doi.org/10.1016/j.chemgeo.2003.09.010

Song, Haijun, Wignall, P.B., Tong, J., Bond, D.P.G., Song, Huyue, Lai, X., Zhang, K., Wang, H., Chen, Y., 2012. Geochemical evidence from bio-apatite for multiple oceanic anoxic events during Permian-Triassic transition and the link with end-Permian extinction and recovery. Earth Planet. Sci. Lett. 353–354, 12–21. https://doi.org/10.1016/j.epsl.2012.07.005

Sun, H., Xiao, Y., Gao, Y., Zhang, G., Casey, J.F., Shen, Y., 2018. Rapid enhancement of chemical weathering recorded by extremely light seawater lithium isotopes at the Permian–Triassic boundary. Proc. Natl. Acad. Sci. 115, 3782–3787. https://doi.org/10.1073/pnas.1711862115

Teng, F.Z., McDonough, W.F., Rudnick, R.L., Dalpé, C., Tomascak, P.B., Chappell, B.W., Gao, S., 2004. Lithium isotopic composition and concentration of the upper continental crust. Geochim. Cosmochim. Acta 68, 4167–4178. https://doi.org/10.1016/j.gca.2004.03.031

Tostevin, R., Wood, R.A., Shields, G.A., Poulton, S.W., Guilbaud, R., Bowyer, F., Penny, A.M., He, T., Curtis, A., Hoffmann, K.H., Clarkson, M.O., 2016. Low-oxygen waters limited habitable space for early animals. Nat. Commun. 7, 12818. https://doi.org/10.1038/ncomms12818

Walker, J.C.G., Hays, P.B., Kasting, J.F., 1981. A negative feedback mechanism for the long-term stabilization of Earth's surface temperature. J. Geophys. Res. 86, 9776–9782. https://doi.org/10.1029/JC086iC10p09776

Wallace, M.W., Hood, A., Shuster, A., Greig, A., Planavsky, N.J., Reed, C.P., 2017. Oxygenation history of the Neoproterozoic to early Phanerozoic and the rise of land plants. Earth Planet. Sci. Lett. 466, 12–19. https://doi.org/10.1016/j.epsl.2017.02.046

Wang, K., Chatterton, B.D.E., Attrep Jr., M., Orth, C.J., 1993. Late Ordovician mass extinction in the Selwyn Basin, northwestern Canada: geochemical, sedimentological, and paleontological evidence. Can. J. Earth Sci. 30, 1870–1880. https://doi.org/10.1139/e93-165

Wanner, C., Sonnenthal, E.L., Liu, X.M., 2014. Seawater δ7Li: A direct proxy for global CO2 consumption by continental silicate weathering? Chem. Geol. 381, 154–167. https://doi.org/10.1016/j.chemgeo.2014.05.005

Webb, G.E., Kamber, B.S., 2000. Rare earth elements in Holocene reefal microbialites: a new shallow seawater proxy. Geochim. Cosmochim. Acta 64, 1557–1565. https://doi.org/10.1016/S0016-7037(99)00400-7

Wimpenny, J., Colla, C.A., Yu, P., Yin, Q.Z., Rustad, J.R., Casey, W.H., 2015. Lithium isotope fractionation during uptake by gibbsite. Geochim. Cosmochim. Acta 168, 133–150. https://doi.org/10.1016/j.gca.2015.07.011

Wimpenny, J., Gíslason, S.R., James, R.H., Gannoun, A., Pogge Von Strandmann, P.A.E., Burton, K.W., 2010. The behaviour of Li and Mg isotopes during primary phase dissolution and secondary mineral formation in basalt. Geochim. Cosmochim. Acta 74, 5259–5279. https://doi.org/10.1016/j.gca.2010.06.028

Wright, J., Schrader, H., Holser, W.T., 1987. Paleoredox variations in ancient oceans recorded by rare earth elements in fossil apatite. Geochim. Cosmochim. Acta 51, 631–644. https://doi.org/10.1016/0016-7037(87)90075-5

Zhong, S., Mucci, A., 1995. Partitioning of rare earth elements (REEs) between calcite and seawater solutions at 25°C and 1 atm, and high dissolved REE concentrations. Geochim. Cosmochim. Acta 59, 443–453. https://doi.org/10.1016/0016-7037(94)00381-U

CHAPTER 2 - WHAT DO CE ANOMALIES IN MARINE CARBONATES REALLY MEAN? A PERSPECTIVE FROM LEACHING EXPERIMENTS[1]

Introduction

1.1. The rare earth elements in seawater

Rare Earth Elements (REE) plus Yttrium in carbonates have been intensively used as redox paleoenvironmental proxies (Bellefroid et al., 2018; Grandjean-Lécuyer et al., 1993; Holser, 1997; Liu et al., 1988; Wallace et al., 2017; Wright et al., 1987). Yttrium is often included alongside REE because it has similar chemical behavior as Holmium (Ho). For convenience, REY is often used to represent rare earth elements and Yttrium and such term is used throughout this study. REY comprises a highly coherent group whose physical and chemical properties vary gradually along the series. However, the natural abundances of individual REY in the same reservoir can vary by orders of magnitude as a function of atomic number. The technique used to smooth out the natural odd-even effects is to normalize measured REY concentrations to a standard. In marine geochemistry, Post Archean Australian Shale (PAAS) (Pourmand et al., 2012; Taylor and Maclennan, 1981) is often used as the standard because the composition of the upper continental crust is closely approximated by the composition of shales, and additionally, weathering of continental crust provides the major input of REY into the ocean (Abbott et al., 2015; Goldstein and Jacobsen, 1988). Following the recent marine carbonate study by Liu et al, (2019), this study also adopts REY concentration in the upper continental crust (Rudnick and Gao, 2014) for normalization. The normalization makes subtle fractions (enrichments/depletions) of REY apparent.

The coherence of inter-element complexation behavior changes in relation to the filling of the 4f electron shell across the REY series (Byrne and Li, 1995). In seawater, REY are predominantly complexed with carbonate ions, and heavier REY (HREY) show stronger complexations (Byrne and Kim, 1990; Jong Hyeon Lee and Byrne, 1993; Lee and Byrne, 1992; Liu and Byrne, 1998). As a result, the typical normalized REY pattern in the modern open-ocean is enriched in HREY (Cantrell and Byrne, 1987; Byrne et al., 1991; Byrne and Li, 1995; Zhang and Nozaki, 1996; Barrat et al., 2000; Bau and Alexander, 2006). In addition to this enrichment trend, a number of deviations also occur to certain elements due to their special chemical properties. A positive La anomaly, for example, reflects a greater stability of La complexation originating from its empty 4f electron shell (Bolhar et al., 2004; Byrne and Kim, 1990; De Baar et al., 1991). Open-ocean REY is also characterized by large, super chondritic molar Y/Ho ratios in a range of 80-168 (Bau et al., 1996; Johannesson et al., 2006; Nozaki et al., 1997; Zhang et al., 1994). This observation has also been described as positive Y anomaly.

1.2. Ce anomaly and Eu anomaly

Besides the gradual filling of 4f electron shell, change of oxidation state also causes deviation from the coherent trend. REY has a predominant trivalent oxidation state, but Ce can be oxidized to the very insoluble Ce (IV) state on the surface of Mn oxides when oxygen is presented (Moffett, 1994, 1990). The preferential adsorption of Ce (IV) onto the Mn oxides and Fe hydroxides leaves the seawater depleted in Ce relative to other trivalent REY (German and Elderfield, 1990b). Another element deviation in the REY pattern due to redox change is Eu anomaly. Eu can exist in divalent state in strongly reducing environments. Variable but very small positive Eu anomalies were observed in seawater, while larger positive Eu anomalies were discovered where seawater mixes with hydrothermal fluids (Meyer et al., 2012).

Anomalies can be quantitatively calculated by comparing the normalized elemental concentration with its normalized neighboring REY. Traditional ways of calculating Ce anomaly include $Ce/Ce^* = [3Ce/(2La + Nd)]_{SN}$, where SN indicates shale-normalized (Elderfield and Greaves, 1982), and $Ce/Ce^* = [Ce/(0.5La + 0.5Pr)]_{SN}$ (Bau and Dulski, 1996). However, the anomalous behavior of La can artificially exaggerates the Ce anomaly. In this study, we use the equation proposed in Lawrence et al, (2006) to calculate Ce anomaly, Eu anomaly and La anomaly as well:

$$Ce/Ce^* = [Ce / (Pr \times (Pr / Nd))]_{SN}$$

$$Eu/Eu^* = [Eu / (Sm^2 \times Tb)^{1/3}]_{SN}$$

$$La/La^* = [La / (Pr \times (Pr / Nd))]_{SN}$$

This distinct chemical behavior of Ce has enabled it to serve as a marine redox tracer through geologic times. A negative Ce anomaly is ubiquitous in well-oxidized open ocean, while study of REE distribution in modern anoxic deep water (e.g. Cariaco Trench) illustrates the paucity of negative Ce anomaly (German et al., 1991; German and Elderfield, 1990b). On the other hand, the extent of negative Ce anomaly in the ocean also varies with water depth. For example, the Ce anomaly profile of North Pacific Ocean shows a sharp decrease in the surface ocean, and stabilizes at intermediate to the deep ocean (Zhang and Nozaki, 1998). In paleo-oceanography studies, Ce anomalies are used to distinguish between oxic and anoxic environments associated with oceanic anoxic events and mass extinction events (Bellefroid et al., 2018; Bodin et al., 2013; Lécuyer et al., 2004; Ling et al., 2013; Planavsky et al., 2010; Song et al., 2012; Wallace et al., 2017; Wang et al., 1993).

1.3. Extracting seawater REY from carbonate rocks

Using marine carbonate as a proxy to reconstruct REY pattern in seawater over geologic time is based on the assumption that no REY fractionation exists between the carbonate and the seawater where the carbonates were precipitated from (Byrne and Bingler, 1989; Voigt et al., 2017; Zhong and Mucci, 1995). REY that substitute into the calcite lattice remain stable during diagenesis, including burial dolomitization and even dissolution – re-precipitation in some meteoric environments (Banner et al., 1988; Bargar et al., 2009; Webb and Kamber, 2000). However, modern seawater REY characteristics are rarely found in ancient marine carbonate, likely due to the influence from local contaminative phases, including Fe-Mn oxyhydroxides and oxides, clays, organic matter, and siliciclastic phases, during incorporation of mobilized REY into diagenetic carbonates (Banner et al., 1988; Palmer, 1985; Shields and Stille, 2001; Shields and Webb, 2004). These contaminants often contain REY concentrations that are orders of magnitude greater than those in carbonate minerals. Moreover, no Ce, or even a positive Ce anomaly in the contaminates additionally increases the complexity of interpreting the Ce anomaly in ancient carbonates. Therefore, it is necessary to ensure the signal can be effectively extracted during the digestion process, as the dissolution of non-carbonate phases with high concentrations of REY can overwhelm the signal from the authigenic inventory. To extract primary oceanic REY signal out of marine sediments, various digestion methods were used in literature (Table 2.1). A few researchers applied one-step dissolution using concentrated acids including hydrofluoric acid (Bodin et al., 2015; Bolhar and Van Kranendonk, 2007; Frimmel, 2009; Khelen et al., 2017; Wang et al., 2015). After realizing the problem of introducing contaminations, weak acids were widely used in digestion processes (Allwood et al., 2010; Hohl et al., 2015; Ling et al., 2013; Nothdurft et al., 2004; Rongemaille et al., 2011). Recently, a few studies on developing sequential leaching protocols showed careful leaching method helps

reduce contamination and extracts REY only from primary crystalized calcite (Tostevin et al., 2016; Zhang et al., 2015).

Table 2.1 Literature review of carbonate digestion protocols.

Digestion Protocol	Data measured	Sample Type	References
	REY	Coral	Webb and Kamber, (2000)
50-120mg sample (water prewash) + 1N acetic acid	REY, trace elements	Carbonate	Nothdurft et al., (2004)
5% v/v acetic acid, 10 steps leaching, 24 h	REY, Sr isotopes	Carbonate	Rongemaille et al. (2011)
1g sample + 15% nitric acid	REY, trace elements	Bulk carbonate	Meyer et al. (2012)
1M acetic acid	REY, major and trace elements	Bulk carbonate	Ling et al. (2013)
250 mg sample + Concentrated Acid	Mn, REY	Bulk carbonate	Bodin et al., (2013)
Pre-clean: Water, physical clean, H_2O_2, HCl; Acid dissolve: 2% v/v nitric acid, 10 steps leaching	REE, U, Mo, Fe	Biogenic and abiogenic carbonate	Zaky et al., (2015)
2% v/v nitric acid, 10 steps and each step dissolves ~10% of total $CaCO_3$	REY	Bulk carbonate	Zhang et al., (2015)
Adjust total weight to include 25mg $CaCO_3$, prewash with DQ water, using 2% nitric acid to first dissolve 20% carbonate then dissolve 40% carbonate and collect leachate for analysis	REY, Fe species	Micro-drilled carbonate powder	Tostevin et al. (2016)

Most of the leaching sequence for carbonate digestion, however, is based on the Tessier extraction protocol which was originally developed for soil extraction (Tessier et al., 1979). Thus, there is a gap in testing the efficiency of applying this method to carbonate samples. In methods based on the Tessier extraction, ammonium acetate is applied on samples initially to remove exchangeable ions adsorbed on the surface and interlayers of Fe-Mn oxides, clay minerals and / or organic matter. Then acid digestion follows to release stably incorporated elements in carbonate phase. Both acetic acid and nitric acid are widely used in this step with concentration ranging from 0.4%v/v to 5%v/v (see Table 2.1). Alternatively, sodium acetate

buffer at pH = 5 is also recommended to dissolve carbonate phase (Tessier et al., 1979). However, most protocols were developed by testing ancient carbonate rocks, and the assessment of the efficiency of leaching method is based on natural sample. Here, we adopted known standards as endmembers to verify different leaching parameters. We carried out systematic leaching experiments to answer following questions. 1) Can ammonium acetate efficiently remove exchangeable ions? 2) What is the influence of each contaminative phase (Mn oxides, clay minerals, and siliciclastic materials) on the extracted REY signals during acid digestion? 3) What is the difference between using nitric acid and acetic acid during acid digestion? In the end, we provide a refined dissolution protocol for ancient marine calcite using ammonium acetate pre-leaching and acetic acid partial leaching. Moreover, we want to emphasize that this study focuses on calcite, and further testing will be needed to apply our methods to aragonite and dolomite.

Methods

2.1 Sample information

A Key Largo limestone (KL) that consists of 100% calcite, was collected in the Key Largo Bay, Florida. NOD-A-1 is a USGS certificated manganese nodule standard which was collected from the Atlantic ocean (Flanagan and Gottfried, 1980). The clay end member is represented by a Montmorillonite standard. As for siliciclastic material, another USGS certified standard SBC-1 (brush creek shale) is used. Mineralogical analysis of SBC-1 reveals major concentration of muscovite, quartz, kaolinite, and chlorite with minor amounts of calcite, siderite, anatase, rutile, and pyrite. Purchased USGS standards came in powder form and KL was collected as a carbonate rock. Weathered surfaces on KL were removed using a rock saw. The fresh material was then crushed using a Bico VD Chipmunk jaw crusher and Bico badger jaw

crusher, and powdered using Spex CertiPrep shatterbox and mixer mill. A semi-quantitative mineralogy of samples was determined by a Rigaku Miniflex II X-ray diffractometer.

All reagents used in this study were made from concentrated acid in ultrapure grade or by lab distillation. Concentrated acetic acid and nitric acid were diluted by Milli-Q water into reagents at different pH, as shown in Table 2.2. Deionized water (18.2 MΩ) was acquired using a Milli-Q system (Direct-Q® 3UV). Analytical grade 1M sodium acetate was made from concentrated acetic acid and concentrated sodium hydroxide buffered by acetic acid at pH=5. Ammonium acetate was made using concentrated ammonia hydroxide and acetic acid. All reagents were checked using an Agilent™ 7900 ICP-MS to make sure elemental concentrations were close to instrumental background and REY concentrations are all below detection limit.

Table 2.2 List of acids used in this study.

pH	Acetic acid	pH	Nitric acid
5	1M Sodium acetate buffer	1.3	0.05M
3	0.07M	1	0.1M
2.5	0.4M	0.7	0.2M
2	1.47M	0.52	0.3M

2.2 Analytical methods

All samples were prepared and analyzed at the University of North Carolina-Chapel Hill. For quantitative elemental concentrations, all samples were analyzed on an Agilent™ 7900 ICP-MS in UHMI (high matrix) mode and run against multi-elemental matrix-matched standards within an appropriate concentration range. Helium gas was also used as carrier gas to reduce interferences. Isobaric interferences were monitored using Ce oxide and the formation doubly charged ions was monitored using Ba^{2+}. Ba-oxide formation was significantly less than 2% of the total Ba in solution. Both ^{151}Eu and ^{153}Eu were regularly measured in samples, no bias was observed between $^{151}Eu/^{153}Eu$. Thus, no correction for BaO interference was required. 100ppb of

internal Berylium, Gemanium, Indium, Bismuth standards were used to correct for instrumental drift during every analytical session. Background intensities were monitored periodically by aspirating 2% v/v HNO_3 blank. We used a limestone standard, NIST-1d, as a carbonate standard during every batch run, giving a long-term relative standard deviation of <10% for most REY and major elements, with a larger standard deviation for some transitional metals and less concentrated REYs. Seven REYs have less than 10% accuracy error compared to Barca et al. (2011), and the rest eight of them have accuracy error of 10-20%. The accuracy error of other elements is less than 10% based on certificate values and GeoReM database (Jochum et al., 2005).

2.3 Ammonium acetate leaching

100 mg of NOD-A-1 and Montmorillonite powders were first digested using concentrated HF + aqua regia, then analyzed for elemental concentrations. KL is completely dissolved in weak acetic acid for whole rock analysis. Normalized REY signals are presented in Fig. 2.1 and raw concentration data are included in appendix 2.1. Although ammonium acetate in variable concentration has been widely adopted in carbonate digestion protocol, the actual role it plays in reducing contaminated REY signals is poorly constrained. Therefore, we conducted the following batch experiments. We weighed 50mg of NOD-A-1, montmorillonite, SBC-1 powders and transferred them to individual 15ml centrifuge tubes. Next, 10ml of 0.2M ammonium acetate was added to each centrifuge tube. Then, the sample and reagents were mixed well using a Votex mixer and placed in ultrasonic bath for 30 min. Tubes were taken out for mixing once every 15 mins during ultrasonic bath sessions, followed by centrifuging at 5000 rpm for 10 mins. Leachate was separated from the centrifuge tube by passing the fluid through Thermo Scientific™ Titan 3™ Cellulose Acetate Syringe Filters (pore size: 0.22μm), and residues were left in the tube and

rinsed with Milli-Q water before next step. For each standard, three leaching steps were taken. Leachates were dried down in Teflon beakers and loaded in 2% v/v nitric acid for ICP-MS analysis. One of the most innovative features of this study is that we introduced syringe filters to remove floating particles in all leachate during separation, and all leachate in this study were passed through syringe filters. Comparative experiments without filters were also conducted, and results are presented in Fig. 2.2. Moreover, using the same experimental procedure, molarity, pH and reaction time of ammonium acetate buffer was individually tested for NOD-A-1. The detailed experimental parameter is described in Fig. 2.2.

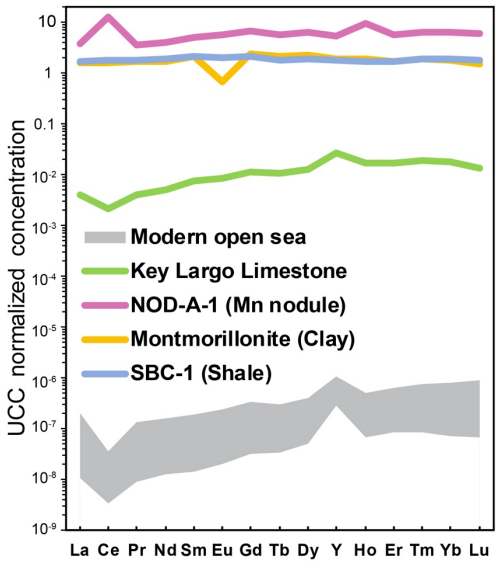

Figure 2.1 UCC-normalized REY patterns of modern seawater, Key Largo limestone, Mn nodule (NOD-A-1), Montmorillonite, and shale (SBC-1).

Data of modern seawater are from Alibo and Nozaki, (1999) and Zhang and Nozaki, (1996); SBC-1 data are from the USGS certificate; and Key Largo limestone, Montmorillonite and NOD-A-1 data are from our own whole rock analysis. Raw data are also included in appendix 2.1.

2.4 Acid Comparison

2.4.1 Single standard experiments

Two-step acid leaching was performed on NOD-A-1, SBC and montmorillonite. Eight sets of 50 mg of each standard were weighed and placed in eight 15 ml centrifuge tubes to be leached by reagents listed in Table 2.2 for two steps following protocol described in section 2.3.

2.4.2 Two-component mixing experiment

To monitor how each contaminative phase (Mn-Fe oxides, clay, or siliciclastic materials) alters the REY signal extracted from the carbonate phase, 200mg samples were produced by mixing the pure limestone endmember (80%) with one of the standards (NOD-A-1, montmorillonite or SBC-1) (20%). The leaching procedures described in the previous section were applied to these samples. Besides adding 10 ml reagents in each step, the volume of acid added is calculated to only dissolve less than 30% of the $CaCO_3$ in bulk samples based on the total moles of H+ in acid.

2.5 Multi-component mixing experiment

200 mg samples were produced by mixing KL and representative contaminative endmembers in different percentages (Table 2.3). Clay standards Ilite and kaolinite were used in addition to the SBC, NOD-A-1, and Montmorillonite standards discussed previously. Each sample was leached with 10 ml 1M ammonium acetate (pH=7) for two steps, and then 5ml 0.3M acetic acid for three steps. Each step lasted for 30 mins, and detailed leaching procedures are described in section 2.3.

Table 2.3 Summary of sample composition prepared for mixing experiments.

Total contamination	Montmorillonite	Ilite	Kaolinite	SBC	NOD-A-1	KL
5%	1%	1%	1%	1%	1%	95%
10%	2.5%	2.5%	2.5%	2.5%	0%	90%
13%	2.5%	2.5%	2.5%	2.5%	2.5%	87.5%
15%	5%	5%	5%	0%	0%	85%
20%	5%	5%	5%	5%	0%	80%
21%	5%	5%	5%	5%	1%	79%
25%	5%	5%	5%	5%	5%	75%
40%	10%	10%	10%	10%	0%	60%

Results

3.1 Ammonium acetate leaching

3.1.1 Use of filters

Leaching protocols in previous studies often involve separating leachate and residues after centrifugation, but none mentions filtering leachate during separation (Liu et al., 2013; Tostevin et al., 2016; Zaky et al., 2015; Zhang et al., 2015). In this study, we compared REY patterns in filtered leachate with those from non-filtered leachate when Mn nodules (NOD-A-1) are leached in ammonium acetate (Fig. 2.2a). The REY patterns from non-filtered leachate are consistent with bulk Mn nodules (NOD-A-1) (Fig. 2.1) and show a positive Ce anomaly in two leaching steps. In contrast, in leachate that is filtered, REY concentrations are ten times lower, and a negative Ce anomaly is present. We also ran plain 2% nitric acid and ICP-MS calibration standard through filter for one to five times, and filtered solutions show similar concentration / counts per second to solution before filtration. This indicate filtration does not influence the elemental concentration in any way. Differences we see in REY pattern in filtered and non-filtered solutions are resulted from removing the particulates by syringe filters.

3.1.2 Representative contaminative endmember comparison

Ammonium acetate leaching results of Mn nodule, Montmorillonite and Shale are plotted in Fig. 2.2b. REY in Mn nodule leachate exhibit seawater-like pattern (Fig. 2.1) – negative Ce anomaly, positive Y anomaly and HREY enrichment. REY patterns in Montmorillonite leachate resemble its bulk composition. Lastly, REY patterns for SBC-1 are not totally flat but enriched in MREY.

3.1.3 Influence of ammonium acetate concentration, pH and reaction time

The influence of ammonium acetate concentration, reaction time, and pH on REY patterns of Mn nodule is presented in Fig. 2.2c. Here we notice a continuous increase of REY concentration as the ammonium acetate concentration increases from 0.2M to 2M. In addition, doubling the reaction time from 0.5h to 1h has negligible influence on both REY concentrations and patterns. REY concentrations even decrease after 24h. As for the influence of pH, nearly no REY are leached when ammonium acetate is buffered at pH=8. However, this result is not plotted because the concentrations are below the detection limit. Decreasing the pH of ammonium acetate buffer from 7 to 5 notably improved total REY extracted from the Mn nodule. Although no difference is seen in terms of REY pattern at three pH levels.

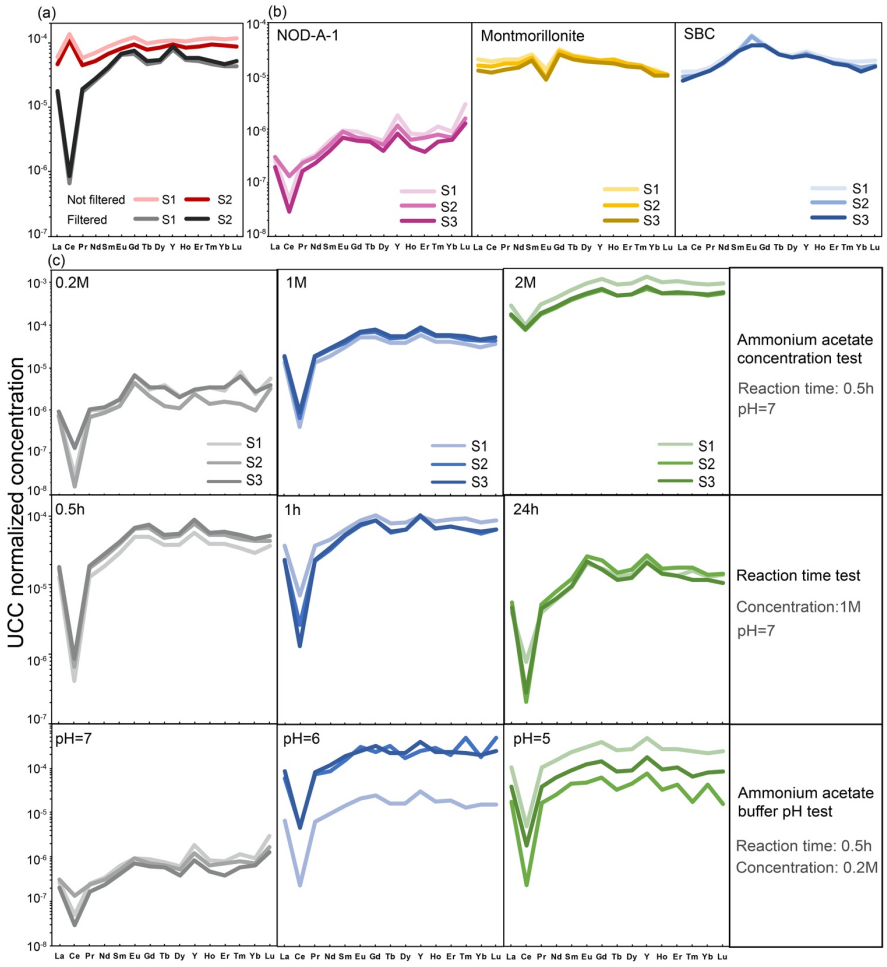

Figure 2.2 UCC normalized REY patterns in pre-cleaning leachates using ammonium acetae.

(a). REY patterns of NOD-A-1 leached in ammonium acetate. Filtered and non-filtered leachate are shown for comparison. (b). REY patterns for NOD-A-1, Montmorillonite, and SBC-1 in sequential leachate with 0.2M ammonium acetate. For each step, 10ml reagents are added and react for 0.5h. The y-axis scale is consistent between plots for ease of comparison. (c). REY patterns of NOD-A-1 in sequential leachate with ammonium acetate. The experimental setting for each test is described at the end of each row, and y-axis scale is consistent with plots in each row for the ease of comparison. Raw data can be found in appendix 2.2.

3.2 Acid comparison

3.2.1 Mn nodule (NOD-A-1)

Bulk Mn nodule is strongly enriched in REY compared to carbonate (Fig. 2.1). Besides an overall flat pattern, a positive Ce anomaly and slightly positive Y anomaly are observed. However, the REY patterns in leachate using acetic acid or nitric acid are different from that of the bulk Mn nodule (Fig. 2.3a, 2.3d). When using acetic acid, the REY signal extracted from the Mn nodule shows a seawater-like pattern with a negative Ce anomaly and a positive Y anomaly, while there is nearly no HREY enrichment. Total REY concentration increases with decreasing pH, and the REY concentration in 1M sodium acetate buffer is between acetic acid at pH=2 and pH=2.5 (Fig. 2.3a). Comparatively, the REY signal extracted from the Mn nodule using nitric acid has higher concentration and lacks the positive Y anomaly as well as HREY enrichment (Fig. 2.3d). As for Ce anomaly, there is negative Ce/Ce* in lower molarity (0.05M), no or slightly positive Ce/Ce* in 0.1M nitric leachate, and positive Ce/Ce* in leachate with nitric acid >0.1M.

3.2.2 Montmorillonite

The UCC-normalized REY signal in montmorillonite leachate (Fig. 2.3b, 2.3e) shows identical pattern as the bulk montmorillonite (Fig. 2.1) regardless of the leaching acid species: acetic or nitric acid. There is a slight enrichment in the MREY except for Eu which shows depletion. In acetic acid, the highest REY concentration appears in the leachate with a 1M sodium acetate buffer. When Mn oxides in leached with acetic acid at different pH, total REY concentration increases with decreasing pH (Fig. 2.3a). But this relationship is not observed during the leaching of montmorillonite. In nitric acid, the REY concentration increases with acid

molarity, and all leachate reacted with nitric acid has higher REY concentrations than those reacted with acetic acid.

3.2.3 Shale (SBC-1)

The bulk shale has a flat UCC normalized pattern (Fig. 2.1), but both acid leachate show an “M” shaped REY pattern which is different from the bulk signal (Fig 2.3c, 2.3f). In other words, REY signal in leachate are enriched in MREY.

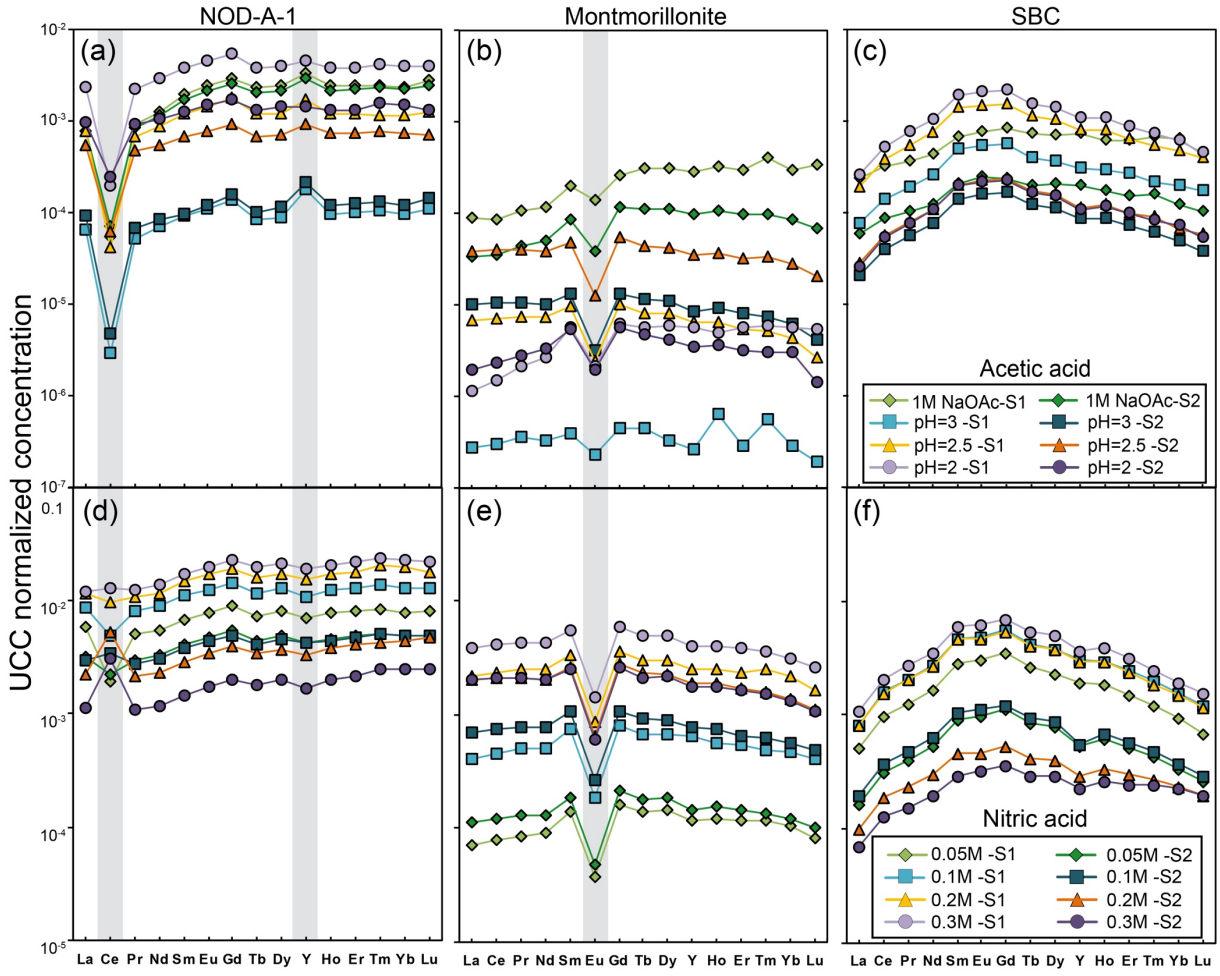

Figure 2.3 REY patterns for NOD-A-1, montmorillonite and SBC-1 in sequential leachate using acetic acid (upper panel) and nitric acid (lower panel).

Two leaching steps are shown in the same color scheme using lighter and darker colors to indicate step 1 and 2, respectively. The REY concentrations in leachate from each step are normalized to UCC. Raw data are included in appendix 2.3.

3.3 Two-component mixing experiments

Here we compare the REY patterns of the leachate from our artificial mixture with that of pure carbonate and pure non-carbonate phases (Fig. 2.4). Firstly, mixture composing of 20% Mn oxides and 80% pure carbonate are leached in acetic acid group including sodium acetate buffer and nitric acid group. As showed in Fig. 2.4a, REY concentrations in leachate are between the mixed samples and the pure carbonate, except for the two steps using acetic acid at pH=3. Moreover, the REY concentrations are higher as we decrease the pH of acetic acid, but 1M ammonium acetate produces higher REY concentrations than acetic acid at pH=2. Some REY concentrations in leachate of acetic acid at pH=3 show some zig-zag patterns because the REY concentrations are close to the detection limit of the ICP-MS and they have high uncertainty. The rest of REY show coherent seawater-like patterns. Comparing the mixed sample leachate to the pure limestone endmember, the negative Ce anomaly is exaggerated in all reagents. Meanwhile, a diminished positive Y anomaly is shown in acetic acid leachate at pH=2 and 1M sodium acetate buffer. As shown in Fig. 2.4b, only the second step using 0.1M nitric acid extracts a REY pattern that has a higher concentration than the pure limestone endmember. A few noteworthy characteristics in nitric acid leachate are the positive Y anomaly in all steps, and the exaggerated negative Ce anomaly.

Acid leaching results of mixing samples containing 20% of pure montmorillonite and 80% of pure carbonate are showed in Fig. 2.4b. There is a small but observable negative Eu anomaly (0.8-0.98) in leachate. The REY patterns in all leachate are consistent with the bulk pure limestone pattern except for one outlier, the second step of acetic acid at pH=3. This may be due to incomplete mixing between solids and reagents at this specific step. However, the results differ when using nitric acid. Fig. 2.4d displays two groups of REY patterns using limestone (KL) signal as a boundary. The first step of nitric acid always shows a REY pattern far below the

bulk limestone. Additionally, they also contain the HREY enrichment, a positive La anomaly, a positive Y anomaly, and a prominent positive Eu anomaly which is contrary to the leaching signal when only Montmorillonite is present. The second steps, excluding 0.1M nitric acid which displays an exceptionally low concentration, almost coincide with the bulk limestone. In addition to the slight positive La anomaly, the Eu anomalies here are moderately negative (0.5-0.7).

When shale is leached together with limestone using acetic acid, REY patterns resemble that of the limestone (Fig. 2.4c). In fact, the first step of acetic acid at pH=3 almost overlaps with the bulk limestone signal, and the rest of the REY curves are slightly above it. In addition to the HREY enrichment among all patterns, La depletions increase with increasing acetic acid concentration. And nitric acid leaching shows variable signals for acid of different molarity. First, the first steps display lower REY concentrations than that of bulk limestone, but the second steps show higher than or close to limestone REY concentrations. Second, rather than an expected elevated HREY concentrations like limestone, the MREY are enriched in all leachate. This “M” (MREY enriched) shape is also illustrated in Fig. 2.3f when only shale is leached with nitric acid without limestone.

Other major and trace elements in the leachate during the mixing experiment are also measured. Elemental ratios and key REY parameters also show differences between acetic acid and nitric acid leachate as well as among samples (Fig. 2.5). In leaching experiments with both acids, the Key Largo limestone mixed with the Mn nodule always has a much higher Mg/Ca ratio and larger range of values. In contrast, both montmorillonite and shale have Mg/Ca values closer to those of bulk limestone, and shale has the least effect on this ratio. The same trend is also observed in Sr/Ca ratios. In contrast, limestone mixed with the Mn nodule has Mn/Ca and Rb/Sr ratios almost identical to those of bulk limestone, whereas both values increase when shale

and calcite are mixed. As for the key REY characteristics in leaching experiments of both acids, nitric leaching produces higher La/La* and Y/Ho on average. Ce/Ce*, Eu/Eu* and Yb/Nd are more variable among different contaminative phases than between different acids. It is worth emphasizing that Mn nodule has a strong effect on the Ce anomaly in both acids.

Plots of elemental ratios against key REY parameters provide more evidence to identify contamination sources for REY signals (Fig. 2.6). For acetic acid leaching, Ce/Ce* increases along with increasing Al/Ca (Fig. 2.6a), except for Mn oxides, where La/La* shows negative trend with Al/Ca (Fig. 2.6b). Yb/Nd and Y/Ho also show similar trends with Mn/Ca, but Ce/Ce* has a more complicated trend that depends more on the contamination sources (Fig. 2.6d, e), as does the relationship between Ce/Ce* and Mg/Ca (Fig. 2.6g). These diverse trends in Ce/Ce* reveal some complexity in using Mn/Ca or Sr/Ca as a tool to evaluate Ce anomaly or to identify contaminants.

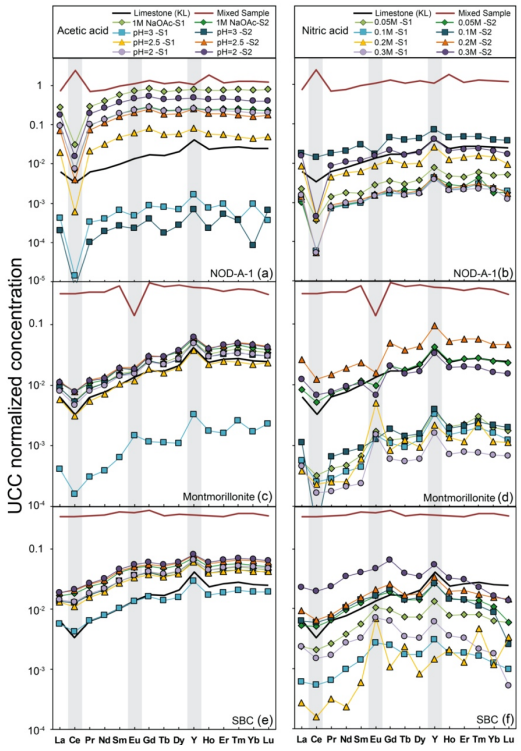

Figure 2.4 Normalized REY pattern in mixing experiments.

Figures in left column show results from acetic acid while those in the right column show results from nitric acid. (a) & (b): Key Largo limestone with 20% Mn nodule; (c) & (d): Key Largo limestone with 20% Montmorillonite; (e) & (f): Key Largo limestone with shale. In each batch experiment, the two steps are shown in same color as lighter and darker. Two reference lines are also plotted here, the black solid line named "KL" in both legends represents the bulk REY in Key Largo limestone, and the red solid line named "mixed sample" represents the bulk concentration of REY in the mixed sample consisting of pure limestone and one of the standards in 4:1. Ca concentration in leachate is used to estimate the weight of $CaCO_3$ dissolved in sample. The REY concentrations in leachate from each step are normalized to the weight of $CaCO_3$, and then normalized to UCC. The scale is consistent among plots in each row. Original data can be accessed in appendix 2.4.

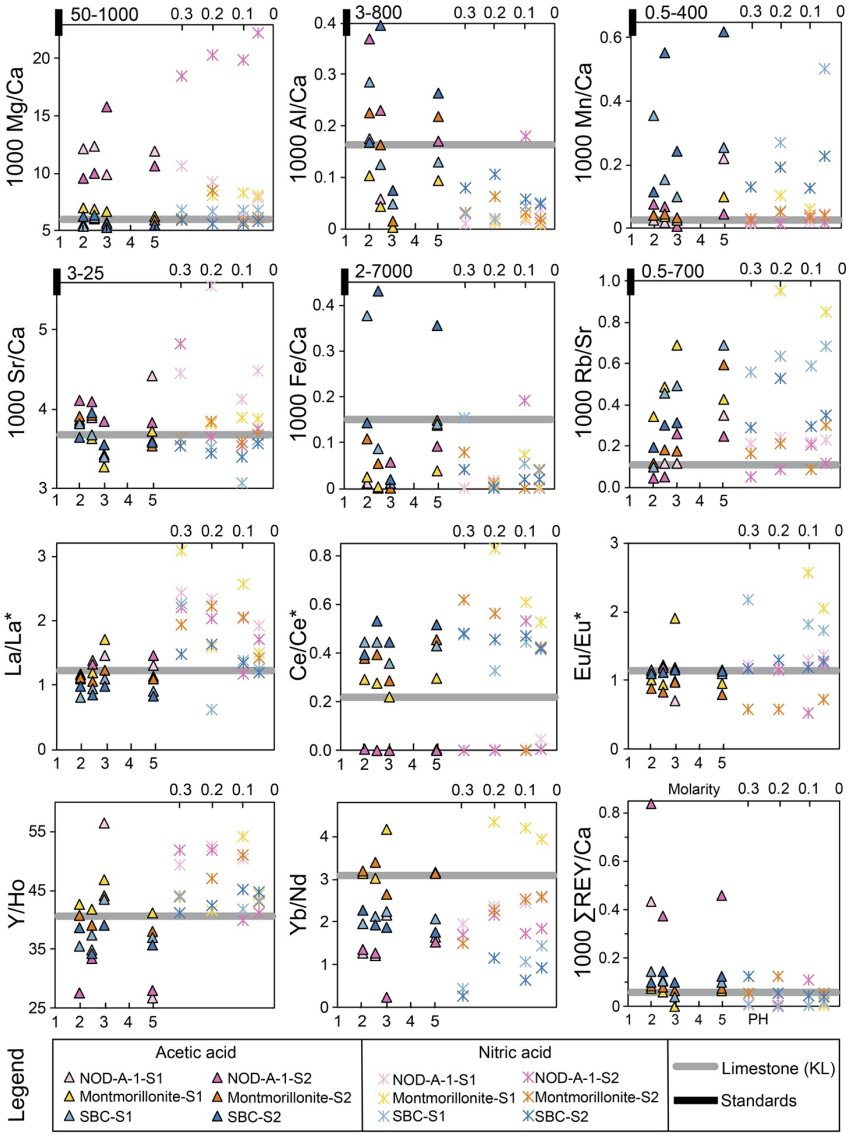

Figure 2.5 Cross plots of Mg/Ca, Al/Ca, Mn/Ca, Sr/Ca, Fe/Ca, Rb/Sr and REY parameters in mixing experiments.

Primary axis shows pH of acetic acid, and secondary axis shows molarity of nitric acid. Data are included in appendix 2.5 and appendix 2.6.

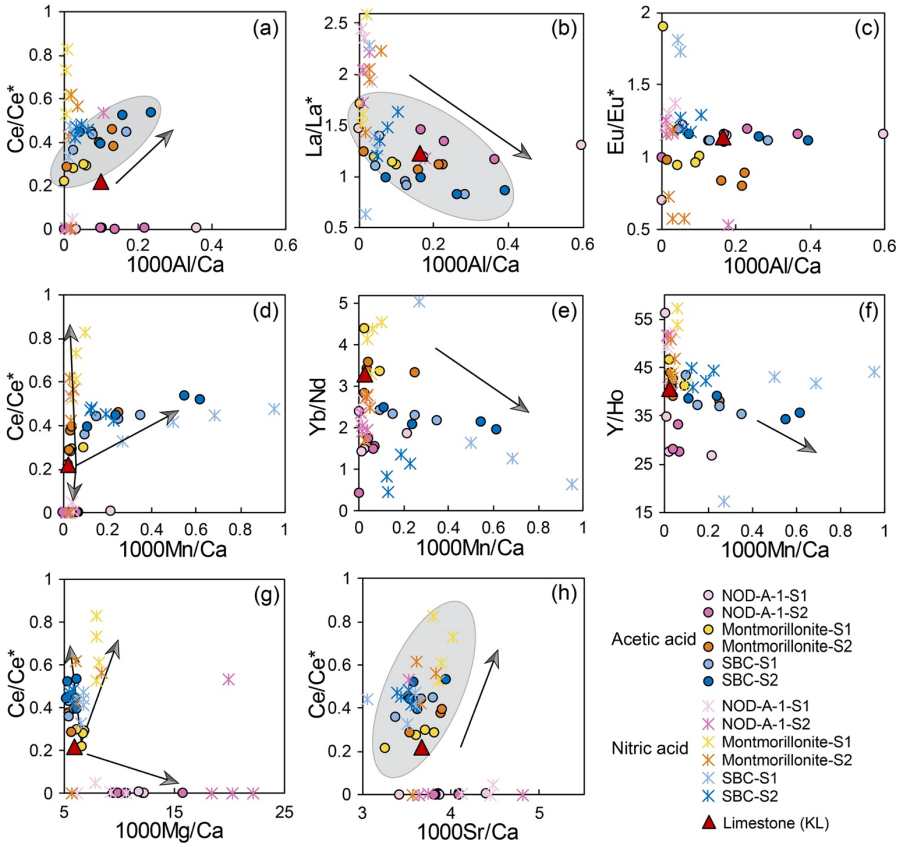

Figure 2.6 Cross plots of key REY parameters (Y/Ho, Yb/Nd, Ce/Ce*, Eu/Eu*, La/La*) versus Mg/Ca, Mn/Ca, Al/Ca, Sr/Ca in mixing experiments.

The gray fields and arrows help guiding the relationship between key REY parameters and elemental ratios. Gray field in (a) includes data from acetic acid leaching of montmorillonite and SBC, showing positive relationship between Ce anomaly and Al/Ca ratio. Gray field in (b) includes all acetic acid leaching data, showing a negative relationship between La anomaly and Al/Ca ratio. Gray filed in (h) includes data from both acid leaching of montmorillonite and SBC, showing positive relationship between Ce anomaly and Sr/Ca ratio. Arrows in (d), (g) indicate different relationship between Ce anomaly and Mn/Ca or Mg/Ca ratio depending on contaminant source.

3.4 Multi-component mixing experiment

Based on the results of ammonium acetate leaching and acid comparison, samples are pre-leached by 1M ammonium acetate (pH=7), and acid leached by 0.3M acetic acid. REY concentrations are also normalized to both Ca concentrations and UCC. Absolute concentrations are presented in appendix 2.7. As shown in Fig. 2.7, REY signals in A1 and A2 are not smooth due to mixing of signals from different contaminative endmembers as well as analytical errors when REY concentrations are close to the detection limit of the ICP-MS. In acid leaching steps, REY signals are smooth and coherent. We notice that REY concentrations increase over three acid leaching steps (Fig. 2.8). Meanwhile, within each step, REY concentrations also increase with higher proportions of non-carbonate phases in mixed samples (Fig. 2.8). Moreover, samples with the Mn nodule (At 5%, 13%，21%，25% contamination level) always show more depleted Ce compared to the bulk limestone (Fig 2.8). But this effect is barely noticeable when the Mn nodule only comprises 1% of the total sample, for example, mixed sample with 5% total contamination and 21% total contamination have similar Ce anomaly value with bulk limestone in S1 and S2. REY concentrations in samples without the Mn nodule are slightly elevated from the bulk limestone but reproduced all key features until total contaminative phases increased to 40%. The sample with 40% contaminative phases presents REY signal with depleted La and enriched MREY. Ce anomaly is not altered in S1, while it is slightly altered in S2, and is more negative in S3 (Fig. 2.7, 2.8). La depletion and MREY depletion also appear in all samples in S3 (Fig. 2.8). The presence of illite and kaolinite does not contaminate REY signal in leachate even though they have different bulk REY patterns (Appendix 2.1).

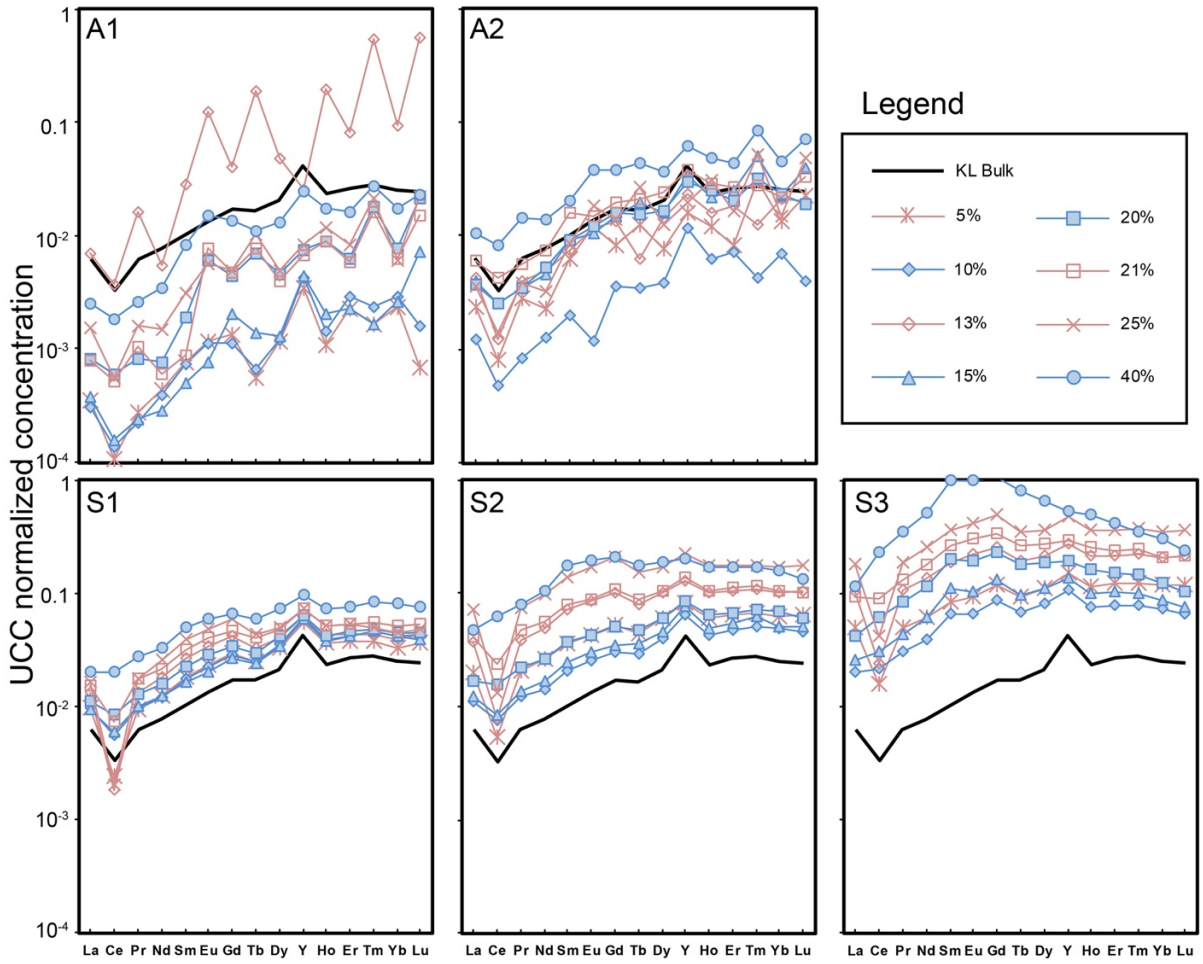

Figure 2.7 Calcite- and UCC-normalized REY patterns in each step of mixing experiments following our recommended leaching procedure.

For each total contamination level, percentage of each endmember is also listed below each level and also in Table 2.3. Samples containing the Mn nodule are represented by open red symbols, and samples without the Mn nodule are shown by closed blue symbols. The solid black line represents bulk REY in the Key Largo limestone. The scale is consistent among plots in each row and column. A1-A2: 10ml 1M ammonium acetate; S1-S3: 5ml 0.3M acetic acid. REY concentrations before normalization are presented in appendix 2.7.

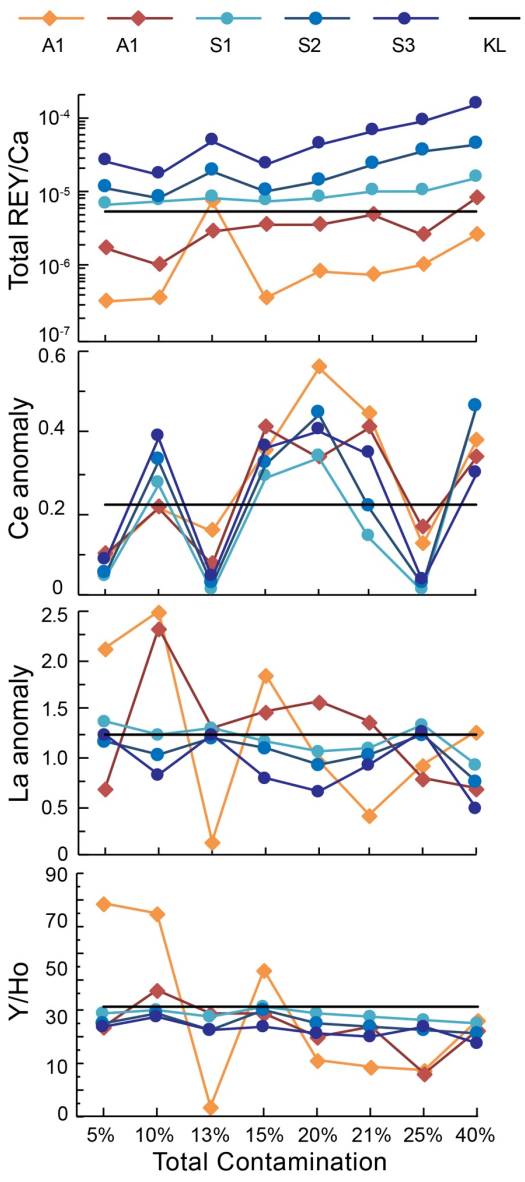

Figure 2.8 Key REY parameters in each step of multi-component mixing experiment following the recommended leaching procedure (described in Fig. 2.7).

Mixing details are presented in Table 2.3.

Discussion

4.1 Mechanism of adsorbed REY removal via ammonium acetate

The adsorbed rare earth elements can be easily exchanged when encountering cations, such as Na^+, NH_4^+, and Mg^{2+} (Bruque et al., 1980; Coppin et al., 2002; Moldoveanu and Papangelakis, 2013, 2012; Yang and Zhang, 2015). The difference in the capability of the REY desorption is caused by cation hydration energies as well as the complexation ability of anions with REY (Bentouhami et al., 2004; Miller et al., 1982; Moldoveanu and Papangelakis, 2012; Teppen and Miller, 2006; Wood, 1990). When extracting REY adsorbed on clay minerals, it was established that the leaching efficiency followed the order $Cs^+ > NH_4^+ > Na^+ > Li^+$ in both sulfate and chloride systems (Moldoveanu and Papangelakis, 2012). Therefore, ammonium acetate is selected in this study to leach exchangeable REY. This reagent is also widely used in leaching protocols for carbonates (Liu et al., 2013; Pogge von Strandmann et al., 2013; Tessier et al., 1979). However, in mixing experiment (Fig. 2.7), even after pre-leaching with two steps of ammonium acetate, Ce is still more depleted in the leachate compared to the pure carbonate. In this case, considering the significant influence of Mn nodule on the Ce anomaly in carbonates, a more efficient ion exchanging reagent should be investigated in future.

Result of ammonium acetate reaction time hints that desorption process occurs quickly, probably within 0.5h, and prolonged leaching (24h) does not improve extraction (Fig. 2.2c). Tian et al. (2010) studied the leaching of rare earth elements from weathered ores and reported that the process approaches equilibrium after 8 mins. Extraction kinetics for REY on clay minerals were also found to be within 5 mins (Moldoveanu and Papangelakis, 2013, 2012), while Aja (1998) observed that Nd adsorption onto kaolinite equilibrates after 15-minute reaction time. Additionally, Bruque et al. (1980) found that agitation leaching in excess of 1 h led to a decrease in lanthanide aqueous concentration due to hydrolysis. And this agrees with our results that

reacting for 24h shows the lowest REY concentration. It was suggested that a 30-minute leaching time is sufficient to reach maximum extraction (Moldoveanu and Papangelakis, 2013) and our results support this conclusion.

4.2 Acid comparison

4.2.1 Mn nodules

In acetic acid leaching of Mn nodules only, REY pattern resembles carbonate REY pattern, but the negative Ce anomaly is exaggerated (Fig. 2.3a). NOD-A-1 is collected from the Atlantic Ocean, so it is possible this standard contains small amount of carbonate. The carbonate-like REY pattern could be partially caused by input from carbonate mineral, but the signal should be mainly contributed by Mn nodule because the pattern is consistent among three steps. Exaggerated negative Ce anomaly suggests acetic acid does not dissolve oxidized Ce. Otherwise the leachate should have positive Ce anomaly because the bulk Mn nodule is enriched in Ce due to preferential scavenging of oxidized Ce.

Acetic acid leaching of limestone and Mn nodule mixture shows a mixed signal from both the pure limestone endmember and the Mn nodule endmember because the negative Ce anomaly is still exaggerated here compared to pure limestone endmember. A simple assumption could be made here that the majority of Ce in Mn nodule is oxidized, and is left behind during acid leaching. Meanwhile, the trivalent REY desorb in acid leaching, and this strongly Ce-depleted signal is mixed with the REY signal from dissolved carbonate mineral. On the other hand, Mn nodule could contribute a positive Ce anomaly to the carbonate signal either because 1) the solutions are not filtered or 2) too much acid is added so that any leftover acid consumes all the $CaCO_3$ and extracts REY from the Mn nodule. Overall, Ce anomaly is higher in nitric acid leaching.

Nitric acid leaching of Mn nodules only shows positive Ce/Ce* in leachate when the molarity of the acid is higher than 0.1M (Fig. 2.3d). This indicates nitric acid of 0.1M or higher has the capability to desorb oxidized Ce on the surface of Mn oxides, and using nitric acid has the risk of introducing false positive Ce anomalies into the extracted signal. When Mn nodule and limestone mixture is leached using acetic acid, positive Ce anomaly is absent in nitric leaching. It hints that nitric acid preferentially reacts with calcium carbonate when it is present together with Mn nodules. Also, oxidized Ce will not react with nitric acid if the amount of acid does not dissolve most of the $CaCO_3$.

Our results suggest a different perspective from those proposed by Zhang et al. (2015) and Tostevin et al. (2016), who suggested using nitric acid for sequential leaching of REY in carbonates, 5% and 2%, respectively. Co-existing Mn nodules in carbonates can alter Ce anomalies in two ways. First, unfiltered leachate can produce a positive Ce anomaly using the traditional method – pipetting leachate from residues. Second, as revealed in Fig. 2.4a, 2.4d, the super-depleted Ce from Mn oxide may overprint the original Ce anomaly signals recorded in primary carbonates. Moreover, many previous studies try to screen data for Mn oxide contamination using Mn/Ca or Mn/Sr ratios. Yet, in the mixing experiment of limestone with Mn nodules, both ratios are similar in acid leachate of mixed samples and in pure limestone (Fig. 2.6d and appendix 2.6). Assuming the majority of REY in Mn oxide was bonded by surface complexation, REY desorption does not require Mn dissolution, thus Ce anomaly does not necessarily correlate with Mn/Ca ratio.

In terms of natural samples, they usually contain much less Mn oxides. However, the existence of Mn oxides in ancient carbonate rocks is difficult to detect using XRD (X-ray Diffraction) analysis. Mn oxides litter the sediment surface in the deep sea. They also form under

the sediment water interface at the oxic/post-oxic boundary (Boyle, 1983; De Baar et al., 1988). Down core sediments have much higher Mn/Ca ratios than core top sediments. The amount of Mn observed in these samples cannot be simply attributed to surface adsorption of Mn, so it is likely that the extra Mn exist in calcite as a surface phase (Boyle, 1983). Therefore, micro drilling cannot preclude Mn/Fe oxides. Foraminifera generally acquire a diagenetic Fe-Mn oxide/hydroxide coating when buried in sediments. There are evidences that the REY contents of the coatings have been diagenetically modified (Burton and Vance, 2000; Palmer, 1985; Palmer and Elderfield, 1986). A recent reducing cleaning test showed the majority of the REY are associated with a ferromanganese-rich coating that forms on the surface of foraminifera (Palmer, 1985). The intergrow of this coating is at ~0.1% level, however, higher degrees of overgrowth may alter foraminifera trace element values. In contrast, the concentration of REY in the calcite lattice is very low. But this artifact can be avoided by avoiding bulk samples with high Mn/Ca. Other attempts that can be made to avoid contamination from Mn/Fe oxides include SEM elemental mapping of carbonate samples to distinguish Mn-rich zones (Tachikawa et al., 2013). Or as mentioned earlier, more efficient REY extracting reagents should be explored for high Mn samples.

4.2.2 Montmorillonite

Clay minerals contain layers of shared octahedral aluminum and tetrahedral silicon sheets. Often, cation substitution of the interlayer space leads to a charge imbalance, thus increases the ability of clay to attract cations to its negative charged sites. Most of the surface-adsorbed lanthanides occur as simple “clay-REE” species or as hydrolyzed “clay-O-REE^{2+}” species, therefore these lanthanides are exchangeable (Klika et al., 2016; Moldoveanu and Papangelakis, 2013, 2012). When comparing between nitric acid and acetic acid, we selected

montmorillonite to represent contamination from clay. To have a comprehensive understanding of the contamination from clay minerals, Ilite and Kaolinite (USGS clay standards) are also added as contaminative phases in mixing experiments following recommended procedure (Fig. 2.7). They have slightly different REY concentrations and patterns compared to montmorillonite, especially in terms of Eu anomaly. Ilite has no Eu anomaly (0.98) and kaolinite has a positive Eu anomaly (1.83) (raw REY concentrations are included in appendix 2.1). Nevertheless, Fig. 2.4 and Fig. 2.7 clearly show all three kinds of clay contaminations are excluded through acetic acid leaching. In contrast, Eu anomaly is influenced by in nitric acid leaching of limestone and montmorillonite mixture. Considering the marked Eu depletion in nitric leachate of pure montmorillonite (Fig. 2.3e), slight negative Eu anomaly in mixing experiment (Fig. 2.4d) likely reflects contamination from the REY in clay, although this contamination is minor since the REY signal in leachate resembles all the other characteristics of REY in bulk limestone. Thus, positive Eu anomaly in dissolved carbonates may not indicate hydrothermal activities (Van Kranendonk et al., 2003) but contamination from clay minerals using nitric acid.

4.2.3 Shale (SBC-1)

In terms of shale contamination, acetic acid eliminates REY contaminations in mixing experiment test. The “M” shaped REY pattern in nitric acid leaching (Fig. 2.4f) suggests interfering signal from shale is significant to reshape limestone REY signal. Besides Mn/Fe oxides, clay minerals, and siliciclastic materials, organic matter can also contaminate REY in carbonates. REY concentrations in sedimentary organic matter (SOM) extracted using a mixed hydrogen peroxide and nitric acid solution are two orders of magnitude higher than those in pure carbonate phase (Hu et al., 2014). Most SOM exhibits remarkably similar shale-normalized REY patterns, characterized by a MREY enrichment (Freslon et al., 2014). The SBC-1 certificate

shows that this shale standard contains 1.23% of organic carbon. Therefore, the observed MREY enrichment in nitric acid leachate is also likely due to a mixed signal from organic matter other than siliciclastic phases in shale (Fig. 2.4f). Nevertheless, the detailed effect of organic matter on contaminating the REY signal in carbonates is not investigated in this study.

To summarize, the combined evidences from mixing experiments involving the shale and montmorillonite suggest it is very difficult to recover the REY in limestone through nitric acid leaching. But acetic acid barely introduces noticeable REY contamination from clay or shale. However, at 20% contamination level, it is still difficult to avoid the effects from the Mn nodule by simple acetic acid leaching.

4.3. Recommended leaching protocol

The multi-component mixing experiment demonstrated that 0.3M acetic acid leaching successfully extracts REY signals from carbonate phase when total contaminations were less than 25%, and only the second or first two leaching steps should be collected for analysis. Thus, we recommend a step-by-step partial leaching protocol to extract REY signals from ancient carbonate samples that are mainly composed of calcite (Fig. 2.9). A few key points are listed below.

1. Semi-quantitative mineralogical determination is recommended to preselect bulk carbonate samples with at least 75% $CaCO_3$ using XRF and XRD.

2. At each step, powders and reagents should be mixed well using a vortex mixer and stay in ultrasonic water bath for 30 mins. During this time, an extra pump of vortex mixing is recommended to improve reaction efficiency.

3. Between ammonium acetate leaching and acetic acid leaching step, residue should be rinsed twice with DI water (18.2 MΩ) to eliminate carry-over effect on REY signals. Elemental

analysis of the second rinse shows REY concentrations close to detection limit, indicating two rinses are sufficient to eliminate the influence of remaining REY in the residue.

4. Then 5ml 0.3M acetic acid can be added to the residue. During this stage the cap needs to be removed every time after mixing in order to release CO_2 gas. After centrifuging, a metal-free filter with pore size of 0.22μm should be used to separate leachate from residue. For samples containing less than 85% $CaCO_3$, only the first step leachate should be collected for the REY analysis. If samples contain more than 85% $CaCO_3$, another acid leaching step can be applied to collect additional samples.

Using this protocol, authigenic REY signals in calcite can be extracted. This protocol could also be applicable to dolomite and aragonite because it is mainly used to remove contaminations from non-carbonate phases. However, when adapting this protocol to marine carbonates that are diagenetically altered, attention needs to be paid on fractionations between the first two acid leaching steps. For example, for acient carbonates contain dolomite and calcite, one may need to adjust the volumn of acid to each step because dolomite reacts with acid more slowly than calcite (Chou et al., 1989; Tostevin et al., 2016; Zhang et al., 2015). The performance of dolomite and calcite mixture during this protocol will need further invesitigation. Idealy, we can calculate the volume of acid to add in the first and second steps in order to dissolve calcite first, and then dolomite.

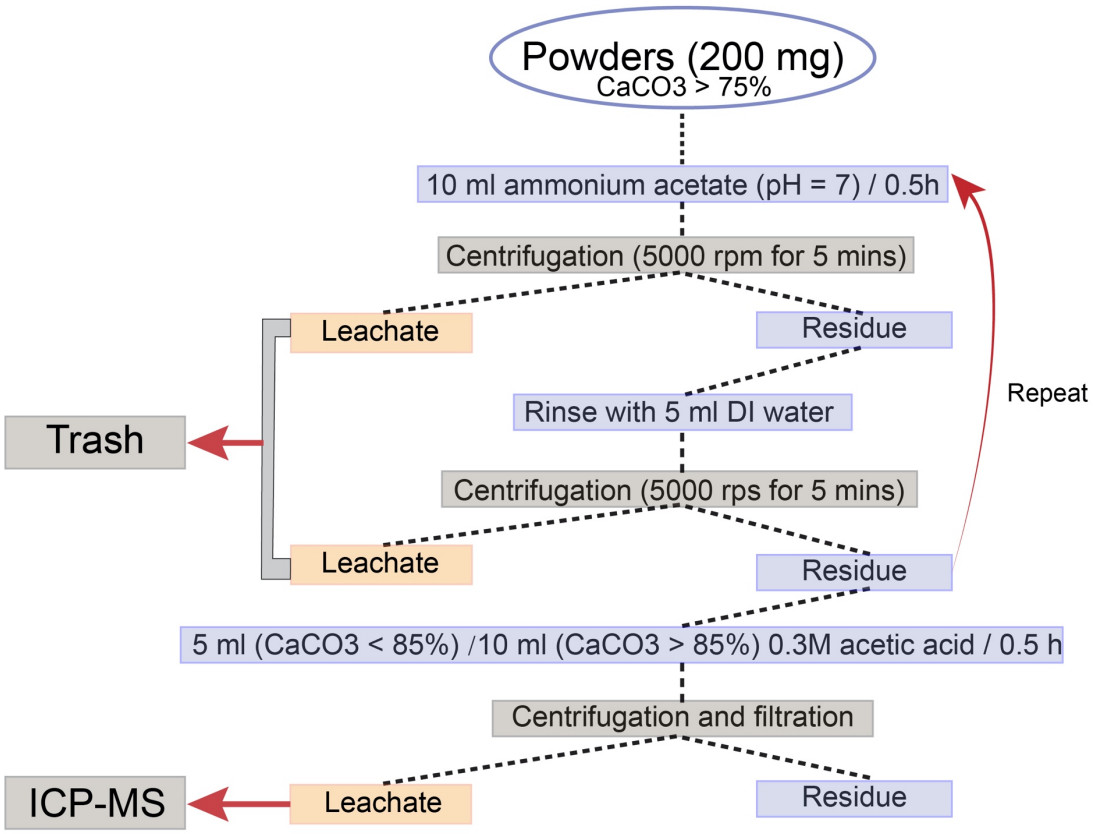

Figure 2.9 A recommended protocol for calcite digestion.

4.4. Application for tracing paleo-redox conditions

Many have tried to use ancient marine carbonates to reconstruct paleo-redox associated with oceanic anoxic events and mass extinction events (Bellefroid et al., 2018; Bodin et al., 2013; Lécuyer et al., 2004; Ling et al., 2013; Planavsky et al., 2010; Song et al., 2012; Wallace et al., 2017; Wang et al., 1993). However, less attention has been paid on sample dissolution methods even though variability of REY patterns as a result of the leaching procedure can be as large as the natural variability of REY patterns in seawater. Therefore, identifying an appropriate leaching protocol to extract REY from ancient marine carbonates remains a real challenge. Most interpretations of marine carbonate Ce/Ce* assume that a negative Ce anomaly represents an

oxic or suboxic depositional environment, and a positive Ce anomaly represents anoxic depositional environment. This study provides a different perspective: through mixing experiments we demonstrated that Ce anomalies in carbonates may come from non-carbonate phases during dissolution processes. Leaching using weak acetic acid reduces contamination from clay minerals and shale, while preserving all key REY parameters. Conversely, weak nitric acid leads to higher Ce/Ce* on average, especially when clay minerals are present (Fig. 2.5). Moreover, we eliminate the false positive Ce anomaly from Mn oxide contamination by filtering the leachate, which is not mentioned in earlier dissolution studies. However, this study does not provide a solution to reduce the exaggerated Ce depletion caused by Mn oxides. Thus, further investigation is required to improve this protocol for samples containing high Mn oxides to avoid erroneous interpretation of REY signals. Our results also suggest Mn oxide contamination on Ce anomaly in ancient marine carbonates can be either way. This could be crucial when working with ancient marine carbonates although Mn oxide concentrations rarely exceed 2.5% in natural samples (Albut et al., 2018; Kurzweil et al., 2016). Therefore, when using positive Ce anomaly to trace anoxic events, we should avoid artificially increased Ce anomaly likely introduced by clay minerals, and unfiltered samples. While using negative Ce anomaly to indicate oxic environment during periods of oxygen rise, we should avoid artificially low Ce anomaly values, for example, from Fe-Mn oxide/hydroxide coatings after filtering samples.

Conclusion

We demonstrate that variability of REY patterns as a result of the leaching procedure can be as large as the natural variability of REY patterns in seawater. To extract REY signal from carbonate, this study advances the leaching procedure for carbonate dissolution in three ways. First, we discovered non-filtered leachate carries contaminative REY signals, particularly that unremoved Mn oxides can cause a positive Ce anomaly. Therefore, we recommend using syringe

filters to separate leachate from leaching residue. Second, we investigated pre-leaching using ammonium acetate with different reagent concentration, reaction time with sample, and pH. We suggest that using 1M ammonium acetate, 0.5 h reaction time and neutral pH or pH slightly lower than 7 achieve the highest extraction efficiency. Although two pre-leaching steps are still not enough to completely remove all influence from >2.5% Mn oxide, exaggerated Ce depletion is not observed when Mn oxides are less than 2.5%. At last, our acid comparison experiments demonstrate that contaminations from clay and siliciclastic minerals are largely reduced with acetic acid leaching. Additionally, nitric acid leaching often leads to Eu anomalies when clay minerals are present and "MREY" enrichment when shale is present. Care should be taken in sample selection and preparation to minimize the amount of Mn oxide. Overall, our refined leaching protocol provides a robust method to extract authigenic REY signal from marine carbonates and can be widely applicable to trace metal work in paleo-ocean communities.

REFERENCES

Abbott, A.N., Haley, B.A., McManus, J., Reimers, C.E., 2015. The sedimentary flux of dissolved rare earth elements to the ocean. Geochim. Cosmochim. Acta 154, 186–200. https://doi.org/10.1016/j.gca.2015.01.010

Aja, S.U., 1998. The sorption of the rare earth element, Nd, onto kaolinite at 25 °C. Clay clay Miner. Miner. 46, 103–109. https://doi.org/10.1346/CCMN.1998.0460112

Albut, G., Babechuk, M.G., Kleinhanns, I.C., Benger, M., Beukes, N.J., Steinhilber, B., Smith, A.J.B., Kruger, S.J., Schoenberg, R., 2018. Modern rather than Mesoarchaean oxidative weathering responsible for the heavy stable Cr isotopic signatures of the 2.95 Ga old Ijzermijn iron formation (South Africa). Geochim. Cosmochim. Acta 228, 157–189. https://doi.org/10.1016/j.gca.2018.02.034

Allwood, A.C., Kamber, B.S., Walter, M.R., Burch, I.W., Kanik, I., 2010. Trace elements record depositional history of an Early Archean stromatolitic carbonate platform. Chem. Geol. 270, 148–163. https://doi.org/10.1016/j.chemgeo.2009.11.013

Banner, J.L., G.N.Hanson, W.J.Meyers, 1988. Rare Earth Elements and Nd Isotopic Variations in Regionally Extensive Dolomites from the Burlington-Keokuk Formation (Mississippian) : Implications for REE Mobility during Carbonate Diagenesis. J. Sediment. Petrol. 58, 415–432.

Barca, D., Belfiore, C.M., Crisci, G.M., La Russa, M.F., Pezzino, A., Ruffolo, S.A., 2011. A new methodological approach for the chemical characterization of black crusts on building stones: a case study from the Catania city centre (Sicily, Italy). J. Anal. At. Spectrom. 26, 1000. https://doi.org/10.1039/c0ja00226g

Bargar, J.R., Fuller, C.C., Marcus, M.A., Brearley, A.J., Perez De la Rosa, M., Webb, S.M., Caldwell, W.A., 2009. Structural characterization of terrestrial microbial Mn oxides from Pinal Creek, AZ. Geochim. Cosmochim. Acta 73, 889–910. https://doi.org/10.1016/J.GCA.2008.10.036

Barrat, J.A., Boulègue, J., Tiercelin, J.J., Lesourd, M., 2000. Strontium isotopes and rare-earth element geochemistry of hydrothermal carbonate deposits from Lake Tanganyika, east Africa. Geochim. Cosmochim. Acta 64, 287–298. https://doi.org/10.1016/S0016-7037(99)00294-X

Bau, M., Alexander, B., 2006. Preservation of primary REE patterns without Ce anomaly during dolomitization of Mid-Paleoproterozoic limestone and the potential re-establishment of marine anoxia immediately after the “Great Oxidation Event.” South African J. Geol. 109, 81–86. https://doi.org/10.2113/gssajg.109.1-2.81

Bau, M., Dulski, P., 1996. Premmbrinn Resenrth Distribution of yttrium and rare-earth elements in the Penge and Kuruman iron-formations, Transvaal Supergroup, South Africa.

Precambrian Res. 79, 37–55. https://doi.org/10.1016/0301-9268(95)00087-9

Bau, M., Koschinsky, A., Dulski, P., Hein, J.R., 1996. Comparison of the partitioning behaviours of yttrium, rare earth elements, and titanium between hydrogenetic marine ferromanganese crusts and seawater. Geochim. Cosmochim. Acta 60, 1709–1725. https://doi.org/10.1016/0016-7037(96)00063-4

Bellefroid, E.J., Hood, A.V.S., Hoffman, P.F., Thomas, M.D., Reinhard, C.T., Planavsky, N.J., 2018. Constraints on Paleoproterozoic atmospheric oxygen levels. Proc. Natl. Acad. Sci. 115, 8104–8109. https://doi.org/10.1073/pnas.1806216115

Bentouhami, E., Bouet, G.M., Meullemeestre, J., Vierling, F., Khan, M.A., 2004. Physicochemical study of the hydrolysis of Rare-Earth elements (III) and thorium (IV). Comptes Rendus Chim. 7, 537–545. https://doi.org/10.1016/j.crci.2004.01.008

Bodin, S., Godet, A., Westermann, S., Föllmi, K.B., 2013. Secular change in northwestern Tethyan water-mass oxygenation during the late Hauterivian–early Aptian. Earth Planet. Sci. Lett. 374, 121–131. https://doi.org/10.1016/j.epsl.2013.05.030

Bodin, S., Meissner, P., Janssen, N.M.M., Steuber, T., Mutterlose, J., 2015. Large igneous provinces and organic carbon burial: Controls on global temperature and continental weathering during the Early Cretaceous. Glob. Planet. Change 133, 238–258. https://doi.org/10.1016/j.gloplacha.2015.09.001

Bolhar, R., Kamber, B.S., Moorbath, S., Fedo, C.M., Whitehouse, M.J., 2004. Characterisation of early Archaean chemical sediments by trace element signatures. Earth Planet. Sci. Lett. 222, 43–60. https://doi.org/10.1016/j.epsl.2004.02.016

Bolhar, R., Van Kranendonk, M.J., 2007. A non-marine depositional setting for the northern Fortescue Group, Pilbara Craton, inferred from trace element geochemistry of stromatolitic carbonates. Precambrian Res. 155, 229–250. https://doi.org/10.1016/j.precamres.2007.02.002

Boyle, E.A., 1983. Manganese carbonate overgrowths on foraminifera tests. Geochim. Cosmochim. Acta 47, 1815–1819. https://doi.org/10.1016/0016-7037(83)90029-7

Bruque, S., Mozas, T., Rodriguez, A., 1980. Factors influencing retention of Lanthanide ions by montmorillonite. Clay Miner. 413–420.

Burton, K.W., Vance, D., 2000. Glacial-interglacial variations in the neodymium isotope composition of seawater in the Bay of Bengal recorded by planktonic foraminifera. Earth Planet. Sci. Lett. 176, 425–441. https://doi.org/10.1016/S0012-821X(00)00011-X

Byrne, R.H., Bingler, L.S., 1989. Comment on “Cerium: A chemical tracer for paleo-oceanic redox conditions” by Y.-G. Liu, M. R. U. Miah and R. A. Schmitt. Geochim. Cosmochim. Acta. https://doi.org/10.1016/0016-7037(89)90081-1

Byrne, R.H., Kim, K.-H., 1990. Rare earth element scavenging in seawater. Geochim. Cosmochim. Acta 54, 2645–2656. https://doi.org/10.1016/0016-7037(90)90002-3

Byrne, R.H., Lee, J.H., Bingler, L.S., 1991. Rare earth element complexation by PO43 - ions in aqueous solution. Geochim. Cosmochim. Acta 55, 2729–2735.

Byrne, R.H., Li, B., 1995. Comparative complexation behavior of the rare earths. Geochim. Cosmochim. Acta 59, 4575–4589. https://doi.org/10.1016/0016-7037(95)00303-7

Cantrell, K.J., Byrne, R.H., 1987. Rare earth element complexation by carbonate and oxalate ions. Geochim. Cosmochim. Acta 51, 597–605. https://doi.org/10.1016/0016-7037(87)90072-X

Chou, L., Garrels, R.M., Wollast, R., 1989. Comparative study of the kinetics and mechanisms of dissolution of carbonate minerals. Chem. Geol. 78, 269–282. https://doi.org/10.1016/0009-2541(89)90063-6

Coppin, F., Berger, G., Bauer, A., Castet, S., Loubet, M., 2002. Sorption of lanthanides on smectite and kaolinite. Chem. Geol. 182, 57–68. https://doi.org/10.1016/S0009-2541(01)00283-2

De Baar, H.J.W., German, C.R., Elderfield, H., van Gaans, P., 1988. Rare earth element distributions in anoxic waters of the Cariaco Trench. Geochim. Cosmochim. Acta 52, 1203–1219. https://doi.org/10.1016/0016-7037(88)90275-X

De Baar, H.J.W., Schijf, J., Byrne, R.H., 1991. Solution Chemistry of the Rare Earth Elements in Seawater. Eur. J. Solid State Inorg. Chem. 28, 357–373.

Elderfield, H., Greaves, M.J., 1982. The rare earth elements in seawater. Nature 296, 214–219. https://doi.org/10.1038/296214a0

Flanagan, F.J., Gottfried, D., 1980. USGS rock standards, III: Manganese-nodule reference samples USGS-Nod-A-1 and USGS-Nod-P-1, U.S. Geological Survey Professional Paper.

Freslon, N., Bayon, G., Toucanne, S., Bermell, S., Bollinger, C., Chéron, S., Etoubleau, J., Germain, Y., Khripounoff, A., Ponzevera, E., Rouget, M.L., 2014. Rare earth elements and neodymium isotopes in sedimentary organic matter. Geochim. Cosmochim. Acta 140, 177–198. https://doi.org/10.1016/j.gca.2014.05.016

Frimmel, H.E., 2009. Trace element distribution in Neoproterozoic carbonates as palaeoenvironmental indicator. Chem. Geol. 258, 338–353. https://doi.org/10.1016/j.chemgeo.2008.10.033

German, C., Holliday, B.P., Elderfield, H., 1991. Redox cycling of rare earth elements in the suboxic zone of the Black Sea. Geochim. Cosmochim. Acta 55, 3553–3558. https://doi.org/10.1016/0016-7037(91)90055-A

German, C.R., Elderfield, H., 1990a. Rare earth elements in the NW Indian Ocean. Geochim. Cosmochim. Acta 54, 1929–1940. https://doi.org/10.1016/0016-7037(90)90262-J

German, C.R., Elderfield, H., 1990b. Application of the Ce anomaly as a paleoredox indicator: The ground rules. Paleoceanography 5, 823–833. https://doi.org/10.1029/PA005i005p00823

Goldstein, S.J., Jacobsen, S.B., 1988. Rare earth elements in river waters. Earth Planet. Sci. Lett. 89, 35–47. https://doi.org/10.1016/0012-821X(88)90031-3

Grandjean-Lécuyer, P., Feist, R., Albarede, F., 1993. Rare earth elements in old biogenic apatites. Geochim. Cosmochim. Acta 57, 2507–2514. https://doi.org/10.1016/0016-7037(93)90413-Q

Hohl, S. V., Becker, H., Herzlieb, S., Guo, Q., 2015. Multiproxy constraints on alteration and primary compositions of Ediacaran deep-water carbonate rocks, Yangtze Platform, South China. Geochim. Cosmochim. Acta 163, 262–278. https://doi.org/10.1016/j.gca.2015.04.037

Holser, W.T., 1997. Evaluation of the application of rare-earth elements to paleoceanography. Palaeogeogr. Palaeoclimatol. Palaeoecol. 132, 309–323. https://doi.org/10.1016/S0031-0182(97)00069-2

Hu, Y., Feng, D., Peckmann, J., Roberts, H.H., Chen, D., 2014. New insights into cerium anomalies and mechanisms of trace metal enrichment in authigenic carbonate from hydrocarbon seeps. Chem. Geol. 381, 55–66. https://doi.org/10.1016/J.CHEMGEO.2014.05.014

Jochum, K.P., Nohl, U., Herwig, K., Lammel, E., Stoll, B., Hofmann, A.W., 2005. GeoReM: A New Geochemical Database for Reference Materials and Isotopic Standards. Geostand. Geoanalytical Res. 29, 333–338. https://doi.org/10.1111/j.1751-908X.2005.tb00904.x

Johannesson, K.H., Hawkins, D.L., Cortés, A., 2006. Do Archean chemical sediments record ancient seawater rare earth element patterns? Geochim. Cosmochim. Acta 70, 871–890. https://doi.org/10.1016/j.gca.2005.10.013

Jong Hyeon Lee, Byrne, R.H., 1993. Complexation of trivalent rare earth elements (Ce, Eu, Gd, Tb, Yb) by carbonate ions. Geochim. Cosmochim. Acta 57, 295–302. https://doi.org/10.1016/0016-7037(93)90432-V

Khelen, A.C., Manikyamba, C., Ganguly, S., Singh, T.D., Subramanyam, K.S.V., Ahmad, S.M., Reddy, M.R., 2017. Geochemical and stable isotope signatures of Proterozoic stromatolitic carbonates from the Vempalle and Tadpatri Formations, Cuddapah Supergroup, India: Implications on paleoenvironment and depositional conditions. Precambrian Res. 298, 365–384. https://doi.org/10.1016/j.precamres.2017.05.021

Klika, Z., Seidlerová, J., Valášková, M., Kliková, C., Kolomazník, I., 2016. Uptake of Ce(III)

and Ce(IV) on montmorillonite. Appl. Clay Sci. 132–133, 41–49. https://doi.org/10.1016/J.CLAY.2016.05.012

Kurzweil, F., Wille, M., Gantert, N., Beukes, N.J., Schoenberg, R., 2016. Manganese oxide shuttling in pre-GOE oceans – evidence from molybdenum and iron isotopes. Earth Planet. Sci. Lett. 452, 69–78. https://doi.org/10.1016/j.epsl.2016.07.013

Lawrence, M.G., Greig, A., Collerson, K.D., Kamber, B.S., 2006. Rare earth element and yttrium variability in South East Queensland waterways. Aquat. Geochemistry 12, 39–72. https://doi.org/10.1007/s10498-005-4471-8

Lécuyer, C., Reynard, B., Grandjean, P., 2004. Rare earth element evolution of Phanerozoic seawater recorded in biogenic apatites. Chem. Geol. 204, 63–102. https://doi.org/10.1016/j.chemgeo.2003.11.003

Lee, J.H., Byrne, R.H., 1992. Examination of comparative rare earth element complexation behavior using linear free-energy relationships. Geochim. Cosmochim. Acta 56, 1127–1137. https://doi.org/10.1016/0016-7037(92)90050-S

Ling, H.-F., Chen, X., Li, D., Wang, D., Shields-Zhou, G.A., 2013. Cerium anomaly variations in Ediacaran–earliest Cambrian carbonates from the Yangtze Gorges area, South China: Implications for oxygenation of coeval shallow seawater. Precambrian Res. 225, 110–127. https://doi.org/10.1016/j.precamres.2011.10.011

Liu, C., Wang, Z., Raub, T.D., 2013. Geochemical constraints on the origin of Marinoan cap dolostones from Nuccaleena Formation, South Australia. Chem. Geol. 351, 95–104. https://doi.org/10.1016/j.chemgeo.2013.05.012

Liu, X., Byrne, R.H., 1998. Comprehensive investigation of yttrium and rare earth element complexation by carbonate ions Using ICP-mass spectrometry. J. Solution Chem. 27, 803–815. https://doi.org/10.1023/a:1022677119835

Liu, X.M., Hardisty, D.S., Lyons, T.W., Swart, P.K., 2019. Evaluating the fidelity of the cerium paleoredox tracer during variable carbonate diagenesis on the Great Bahamas Bank. Geochim. Cosmochim. Acta 248, 25–42. https://doi.org/10.1016/j.gca.2018.12.028

Liu, Y., Miah, M.R.U., Schmitt, R.A., 1988. Cerium : A chemical tracer for paleo-oceanic redox conditions. Geochim. Cosmochim. Acta 52, 1361–1371.

Meyer, E.E., Quicksall, A.N., Landis, J.D., Link, P.K., Bostick, B.C., 2012. Trace and rare earth elemental investigation of a Sturtian cap carbonate, Pocatello, Idaho: Evidence for ocean redox conditions before and during carbonate deposition. Precambrian Res. 192, 89–106. https://doi.org/10.1016/j.precamres.2011.09.015

Miller, S.E., Heath, G.R., Gonzalez, R.D., 1982. Effect of temperature on the sorption of Yb by montmorillonite. Clays Clay Miner. 30, 111–122.

https://doi.org/10.1346/CCMN.1983.0310103

Moffett, J.W., 1994. The relationship between cerium and manganese oxidation in the marine environment. Limnol. Oceanogr. 39, 1309–1318. https://doi.org/10.4319/lo.1994.39.6.1309

Moffett, J.W., 1990. Microbially mediated cerium oxidation in sea water. Nature 345, 421–423. https://doi.org/10.1038/345421a0

Moldoveanu, G.A., Papangelakis, V.G., 2013. Recovery of rare earth elements adsorbed on clay minerals: II. Leaching with ammonium sulfate. Hydrometallurgy 131–132, 158–166. https://doi.org/10.1016/j.hydromet.2012.10.011

Moldoveanu, G.A., Papangelakis, V.G., 2012. Recovery of rare earth elements adsorbed on clay minerals: I. Desorption mechanism. Hydrometallurgy 117–118, 71–78. https://doi.org/10.1016/j.hydromet.2012.02.007

Nothdurft, L.D., Webb, G.E., Kamber, B.S., 2004. Rare earth element geochemistry of Late Devonian reefal carbonates, Canning Basin, Western Australia: Confirmation of a seawater REE proxy in ancient limestones. Geochim. Cosmochim. Acta 68, 263–283. https://doi.org/10.1016/S0016-7037(03)00422-8

Nozaki, Y., Zhang, J., Amakawa, H., 1997. The fractionation between Y and Ho in the marine environment. Earth Planet. Sci. Lett. 148, 329–340. https://doi.org/10.1016/S0012-821X(97)00034-4

Palmer, M.R., 1985. Rare earth elements in foraminifera tests. Earth Planet. Sci. Lett. 73, 285–298.

Palmer, M.R., Elderfield, H., 1986. Rare earth elements and neodymium isotopes in ferromanganese oxide coatings of Cenozoic foraminifera from the Atlantic Ocean. Geochim. Cosmochim. Acta 50, 409–417. https://doi.org/10.1016/0016-7037(86)90194-8

Planavsky, N., Bekker, A., Rouxel, O.J., Kamber, B., Hofmann, A., Knudsen, A., Lyons, T.W., 2010. Rare Earth Element and yttrium compositions of Archean and Paleoproterozoic Fe formations revisited: New perspectives on the significance and mechanisms of deposition. Geochim. Cosmochim. Acta 74, 6387–6405. https://doi.org/10.1016/J.GCA.2010.07.021

Pogge von Strandmann, P.A.E., Jenkyns, H.C., Woodfine, R.G., 2013. Lithium isotope evidence for enhanced weathering during Oceanic Anoxic Event 2. Nat. Geosci. 6, 668–672. https://doi.org/10.1038/ngeo1875

Pourmand, A., Dauphas, N., Ireland, T.J., 2012. A novel extraction chromatography and MC-ICP-MS technique for rapid analysis of REE, Sc and Y: Revising CI-chondrite and Post-Archean Australian Shale (PAAS) abundances. Chem. Geol. 291, 38–54. https://doi.org/10.1016/j.chemgeo.2011.08.011

Rongemaille, E., Bayon, G., Pierre, C., Bollinger, C., Chu, N.C., Fouquet, Y., Riboulot, V., Voisset, M., 2011. Rare earth elements in cold seep carbonates from the Niger delta. Chem. Geol. 286, 196–206. https://doi.org/10.1016/j.chemgeo.2011.05.001

Rudnick, R.L., Gao, S., 2014. Composition of the Continental Crust, 2nd ed, Treatise on Geochemistry: Second Edition. Elsevier Ltd. https://doi.org/10.1016/B978-0-08-095975-7.00301-6

Shields, G., Stille, P., 2001. Diagenetic constraints on the use of cerium anomalies as palaeoseawater redox proxies: An isotopic and REE study of Cambrian phosphorites. Chem. Geol. 175, 29–48. https://doi.org/10.1016/S0009-2541(00)00362-4

Shields, G.A., Webb, G.E., 2004. Has the REE composition of seawater changed over geological time? Chem. Geol. 204, 103–107. https://doi.org/10.1016/j.chemgeo.2003.09.010

Song, Haijun, Wignall, P.B., Tong, J., Bond, D.P.G., Song, Huyue, Lai, X., Zhang, K., Wang, H., Chen, Y., 2012. Geochemical evidence from bio-apatite for multiple oceanic anoxic events during Permian-Triassic transition and the link with end-Permian extinction and recovery. Earth Planet. Sci. Lett. 353–354, 12–21. https://doi.org/10.1016/j.epsl.2012.07.005

Tachikawa, K., Toyofuku, T., Basile-Doelsch, I., Delhaye, T., 2013. Microscale neodymium distribution in sedimentary planktonic foraminiferal tests and associated mineral phases. Geochim. Cosmochim. Acta 100, 11–23. https://doi.org/10.1016/j.gca.2012.10.010

Taylor, S.R., Maclennan, S.M., 1981. The composition and evolution of the continental crust: rare earth element evidence from sedimentary rocks. Philos. Trans. R. Soc. London. Ser. A, Math. Phys. Sci. 381–399.

Teppen, B.J., Miller, D.M., 2006. Hydration Energy Determines Isovalent Cation Exchange Selectivity by Clay Minerals. Soil Sci. Soc. Am. J. 70, 31. https://doi.org/10.2136/sssaj2004.0212

Tessier, A., Campbell, P.G.C., Bisson, M., 1979. Sequential Extraction Procedure for the Speciation of Particulate Trace Metals. Anal. Chem. 51, 844–851. https://doi.org/10.1021/ac50043a017

Tian, J., Chi, R., Yin, J., 2010. Leaching process of rare earths from weathered crust elution-deposited rare earth ore. Trans. Nonferrous Met. Soc. China 20, 892–896. https://doi.org/10.1016/S1003-6326(09)60232-6

Tostevin, R., Shields, G.A., Tarbuck, G.M., He, T., Clarkson, M.O., Wood, R.A., 2016. Effective use of cerium anomalies as a redox proxy in carbonate-dominated marine settings. Chem. Geol. 438, 146–162. https://doi.org/10.1016/j.chemgeo.2016.06.027

Van Kranendonk, M.J., Webb, G.E., Kamber, B.S., 2003. Geological and trace element evidence

for a marine sedimentary environment of deposition and biogenicity of 3.45 Ga stromatolitic carbonates in the Pilbara Craton, and support for a reducing Archaean ocean. Geobiology 1, 91–108. https://doi.org/10.1046/j.1472-4669.2003.00014.x

Voigt, M., Mavromatis, V., Oelkers, E.H., 2017. The experimental determination of REE partition coefficients in the water-calcite system. Chem. Geol. 462, 30–43. https://doi.org/10.1016/j.chemgeo.2017.04.024

Wallace, M.W., Hood, A., Shuster, A., Greig, A., Planavsky, N.J., Reed, C.P., 2017. Oxygenation history of the Neoproterozoic to early Phanerozoic and the rise of land plants. Earth Planet. Sci. Lett. 466, 12–19. https://doi.org/10.1016/j.epsl.2017.02.046

Wang, K., Chatterton, B.D.E., Attrep Jr., M., Orth, C.J., 1993. Late Ordovician mass extinction in the Selwyn Basin, northwestern Canada: geochemical, sedimentological, and paleontological evidence. Can. J. Earth Sci. 30, 1870–1880. https://doi.org/10.1139/e93-165

Wang, S., Magalhães, V.H., Pinheiro, L.M., Liu, J., Yan, W., 2015. Tracing the composition, fluid source and formation conditions of the methane-derived authigenic carbonates in the Gulf of Cadiz with rare earth elements and stable isotopes. Mar. Pet. Geol. 68, 192–205. https://doi.org/10.1016/j.marpetgeo.2015.08.022

Webb, G.E., Kamber, B.S., 2000. Rare earth elements in Holocene reefal microbialites: A new shallow seawater proxy. Geochim. Cosmochim. Acta 64, 1557–1565. https://doi.org/10.1016/S0016-7037(99)00400-7

Wood, S.A., 1990. The aqueous geochemistry of the rare-earth elements and yttrium. 1. Review of available low-temperature data for inorganic complexes and the inorganic REE speciation of natural waters. Chem. Geol. 82, 159–186. https://doi.org/10.1016/0009-2541(90)90080-Q

Wright, J., Schrader, H., Holser, W.T., 1987. Paleoredox variations in ancient oceans recorded by rare earth elements in fossil apatite. Geochim. Cosmochim. Acta 51, 631–644. https://doi.org/10.1016/0016-7037(87)90075-5

Yang, X., Zhang, J., 2015. Recovery of rare earth from ion-adsorption rare earth ores with a compound lixiviant. Sep. Purif. Technol. 142, 203–208. https://doi.org/10.1016/j.seppur.2014.11.050

Zaky, A.H., Brand, U., Azmy, K., 2015. A new sample processing protocol for procuring seawater REE signatures in biogenic and abiogenic carbonates. Chem. Geol. 416, 36–50. https://doi.org/10.1016/j.chemgeo.2015.10.015

Zhang, J., Amakawa, H., Nozaki, Y., 1994. The comparative behaviors of yttrium and lanthanides in the seawater of the North Pacific. Geophys. Res. Lett. 21, 2677–2680. https://doi.org/10.1029/94GL02404

Zhang, J., Nozaki, Y., 1998. Behavior of rare earth elements in seawater at the ocean margin: a study along the slopes of the Sagami and Nankai troughs near Japan. Geochim. Cosmochim. Acta 62, 1307–1317. https://doi.org/10.1016/S0016-7037(98)00073-8

Zhang, J., Nozaki, Y., 1996. Rare earth elements and yttrium in seawater: ICP-MS determinations in the East Caroline, Coral Sea, and South Fiji basins of the western South Pacific Ocean. Geochim. Cosmochim. Acta 60, 4631–4644. https://doi.org/10.1016/S0016-7037(96)00276-1

Zhang, K., Zhu, X.K., Yan, B., 2015. A refined dissolution method for rare earth element studies of bulk carbonate rocks. Chem. Geol. 412, 82–91. https://doi.org/10.1016/j.chemgeo.2015.07.027

Zhong, S., Mucci, A., 1995. Partitioning of rare earth elements (REEs) between calcite and seawater solutions at 25°C and 1 atm, and high dissolved REE concentrations. Geochim. Cosmochim. Acta 59, 443–453. https://doi.org/10.1016/0016-7037(94)00381-U

CHAPTER 3 - LATE CRETACEOUS CERIUM ANOMALIES AND GLOBALLY DINSTINCTIVE REDOX RESPONSES BEFORE, DURING AND AFTER OCEANIC ANOXIC EVENT 2

Introduction

The oxygen content in the modern ocean has been declining substantially (2%) during the past four decades, and oceanic models project further deoxygenation up to 7% by the end of the century (Schmidtko et al., 2017). The global ocean has gone through multiple deoxygenation events over Earth's history. The widespread development of Cretaceous organic-rich sediments during specific time intervals has been attributed to several so-called oceanic anoxic events (OAEs) during which marine waters were depleted in oxygen at a regional to global scale. At the Cenomanian–Turonian boundary (~94 Ma), a large positive carbon-isotope excursion marks and conventionally can be used to define the most significant such event in the Cretaceous, namely OAE 2 (Arthur et al., 1990; Jenkyns, 2010, 1980; Schlanger et al., 1987; Schlanger and Jenkyns, 1976; Scholle and Arthur, 1980). It has been hypothesized that this event was triggered by massive basalt–seawater interaction (i.e. processes such as volcanism, hydrothermal activity, submarine weathering of mafic igneous rock) related to the formation of one or more Large Igneous Provinces (LIPs) including oceanic plateaus, which caused a cascade of environmental changes ultimately leading to increased global accumulation of organic matter. Evidence for this phenomenon derives from strontium-, osmium- and neodymium profiles (Du Vivier et al., 2015, 2014; Jones and Jenkyns, 2001; Kerr, 1998; Sinton and Duncan, 1997; Turgeon and Brumsack, 2006; Zheng et al., 2013). A warmer climate and long-term sea-level rise accelerated multiple environmental perturbations such as continental and submarine weathering, which provided

nutrients for surface-ocean planktonic photosynthesis (e.g. Schlanger et al., 1981; Larson, 1991; Sinton and Duncan, 1997; Bach and Irber, 1998; Kerr, 1998; Adams et al., 2010; Barclay et al., 2010; Blättler et al., 2011; Pogge Von Strandmann et al., 2013; Jenkyns et al., 2017).

Multiple studies of this event have been undertaken to investigate the timing and extent of oceanic anoxia, at regional and global scales, in both deep water and the upper levels of the ocean. Organic-rich black shales that are the hallmark of the event are widely distributed, with a strong bias to the northern hemisphere with most localities in the North Atlantic Ocean and its surrounding epicontinental seas and the continental margins of the Alpine-Mediterranean Tethys, with sparse occurrences known from the paleo-equatorial Pacific and Indian Oceans (Owens et al., 2018; Pancost et al., 2004; Schlanger et al., 1987; Trabucho Alexandre et al., 2010). In part, this distribution has been hypothesized to be a result of local watermass stratification leading to euxinia, aided by increased fluvial input to the oceans as well as enhanced upwelling in peri-equatorial regions (Sinninghe Damsté and Köster, 1998; van Bentum et al., 2009; Jenkyns, 2010). One proposed model to drive enhanced organic-carbon burial is through increased preservation and to achieve anoxia in the deeper waters requires the replenishment of O_2-rich surface waters to be slower than its loss during organic-matter decomposition. During OAE 2, a smaller temperature gradient would likely have reduced global ocean circulation by reducing deep-water formation (Blumenberg and Wiese, 2012; Thierstein and Berger, 1978). Sinking saline water derived from tropical shelf seas is another possibility and could also have led to a shortage of oxygen supply to the deep ocean (Brass et al., 1982). Nevertheless, this hypothesis lacks clear geochemical evidence, though it is supported by some modeling studies (Slingerland et al., 1996; Trabucho Alexandre et al., 2010).

The extent of anoxia in near-surface waters during OAE 2 varied spatially, as indicated by iodine:calcium ratios (I/Ca) in carbonates (Owens et al., 2016a; Zhou et al., 2015). Additionally, proxy data, including trace-element abundance in carbonate-rich sections, indicate that magnitudes of oxygen depletion in the water column were subject to significant fluctuations during OAE 2 itself with episodes of reoxygenation such as the so-called Plenus Cold Event (Hetzel et al., 2009; Owens et al., 2012; Owens et al., 2013; Goldberg et al., 2016; Jenkyns et al., 2017; Owens et al., 2017; Jenkyns, 2018; O'Connor et al., 2020). Significantly, evidence from Tl isotopes reveals that global deoxygenation predated the OAE or onset of enhanced organic-matter burial as defined by the carbon-isotope excursion (Ostrander et al., 2017). Another study of the Tarfaya upwelling system in the proto-North Atlantic concluded that the transition of oxic to euxinic conditions happened prior to OAE 2 with a time lag of ~400kyr, based on nitrogen isotopes, and 115kyr based on vanadium and molybdenum concentrations (Scholz et al., 2019).

To understand the extent that oceanographic changes may have influenced oxygen in the global upper ocean in terms of regional differences, this study compares redox responses between restricted basins and the open ocean using the Ce anomaly in marine carbonates. Rare-earth elements and yttrium (REY) constitute a well-characterized proxy in modern environments and are a promising tool for paleo-redox studies (e.g. Bodin et al., 2013; Tostevin et al., 2016). Under fully oxic conditions, Ce is progressively oxidized from soluble Ce(III) to insoluble Ce(IV), typically accumulating on the surface of ferromanganese oxyhydroxides on the seafloor. Consequently, the residual seawater becomes relatively depleted in Ce compared to other rare-earth elements (German and Elderfield, 1990). The reverse process, namely the reduction of Ce(IV) to Ce(III), which occurs in both anoxic ($O_2 = 0$) and suboxic ($O_2 < 5\mu mol/kg$) environments (Rue et al., 1997), increases the cerium content of seawater. The relative

enrichment or depletion of Ce relative to its neighbors in the periodic table is usually defined as a Ce anomaly, expressed as Ce/Ce* = Ce / (Pr *(Pr / Nd)) (Lawrence et al., 2006). Therefore, herewith all concentrations are normalized to UCC (Upper Continental Crust) following the approach of Liu et al. (2019).

The Ce anomaly in bulk marine carbonates should primarily reflect average redox conditions in near-surface waters below the air-sea exchange zone including the depth of the oxycline, which for this study will be considered as upper water column or upper ocean. In any geochemical study of ancient carbonate sediments, a negative Ce anomaly (Ce/Ce* <1) indicates that the environment was oxic and a positive to absent Ce anomaly (Ce/Ce* ≥1) indicates a suboxic or anoxic local condition. Importantly, Ce anomalies determined in marine carbonates have been demonstrated to provide a relatively robust Ce/Ce* record of primary seawater values even after recrystallization or dolomitization (Byrne and Bingler, 1989; Liu et al., 2019; Webb and Kamber, 2000; Wright et al., 1987; Zhong and Mucci, 1995). The relatively short residence time of Ce in seawater (< 500 yr) also makes it a sensitive tracer for local water-column redox conditions over geologically short intervals: OAE 2 is thought to have lasted for 500 to 900 kyr (Eldrett et al., 2015; Gangl et al., 2019; Li et al., 2017; Sageman et al., 2006; Voigt et al., 2004). Additionally, Ce occurs high on the redox ladder compared to other elements such as Mn and I (Lu et al., 2010). Thus, Ce can be one of the first geochemical species to record early deoxygenation or re-oxygenation. Herein, well-preserved carbonates from seven Cenomanian–Turonian sections worldwide are investigated for Ce anomalies.

Materials and Methods

2.1 Study sites

Samples derive from three land sections and four Ocean Drilling Program (ODP/IODP) holes (Fig. 3.1, Appendix 3.2). All three outcrop sections are from the northern hemisphere. Eastbourne (southern England), Clot Chevalier (south-east France) and Raia del Pedale (southern Italy) are situated in Europe. The Eastbourne coastal section exposes ~27 meters of light-colored pelagic epicontinental Chalk facies, of latest Cenomanian–earliest Turonian age, which was situated in the central part of the Anglo-Paris Basin at an estimated paleodepth of a few hundred meters (Hancock, 1975). Poorly lithified foraminiferal-nannofossil carbonates from this section have very low values of total organic carbon (TOC) and were not subject to appreciable diagenetic sulfate reduction in pore waters (Gale et al., 2005; Keller et al., 2001; Paul et al., 1999; Tsikos et al., 2004), which should have minimized alteration of the primary Ce anomaly. The Clot Chevalier locality is from the Vocontian Trough, a relatively deep subtropical basin on the northern margin of the Tethys. The section is ~35m thick and comprises alternating dark gray foraminiferal-nannofossil marlstones and light gray more indurated limestones of latest Cenomanian–earliest Turonian age. Micropalaeontological, lithostratigraphic and sedimentological analyses of nearby sections within the Vocontian Trough indicate deposition in a hemipelagic domain and a paleodepth of a few hundred meters deepening to the north-east (Falzoni et al., 2016b; Gale et al., 2019). Raia del Pedale (Italy), is an organic-lean, platform carbonate dominantly comprising gray calcareous mudstone containing benthic foraminifera and thick-shelled fossils such as rudists. Thin centimeter-scale black laminated carbonates occur at some levels. This ‘shallow-water’ section was likely deposited in water depths of only a few meters or tens of meters (Parente et al., 2008; Frijia et al., 2019).

The four ODP/IODP holes are situated in the southern Indian Ocean. ODP Sites 763, 765, 766 form a depth transect on the western margin of Australia. Hole 763B (Exmouth Plateau; 45°S paleolatitude at 90 Ma) was likely deposited in intermediate depths during the Cretaceous (Haq et al., 1992). Hole 763B recovered upper Albian to lower Campanian nannofossil chalks with clay classified as calcareous claystones to claystones (Haq et al., 1991). ODP Holes 766A and 765C are situated on the Exmouth Plateau and Argo Abyssal Plain, respectively, and they are relatively deep-water sites (Gradstein, 1992). Cenomanian–Maastrichtian sediments from Hole 766A largely comprise zeolitic nannofossil oozes and clays locally pink to pale brown to gray and lighter colored graded foraminiferal-rich levels. Coeval sediments from Hole 765C are broadly similar to those in Hole 766A for the Cenomanian–Turonian interval (Ludden and Gradstein, 1990). ODP Hole 1138A, which sampled an organic-rich shale of Cenomanian–Turonian boundary age, is located on the Central Kerguelen Plateau and has been suggested to have been deposited in shallow to intermediate water depths as the seafloor underwent thermal subsidence between ~94 Ma and 86 Ma (Dickson et al., 2017; Frey et al., 2000). Sediments at this site are composed of calcareous sandstone and claystone in the Cenomanian and interbedded chalk, nannofossil claystone, and foraminifera-bearing nannofossil chalk in the Turonian–upper Maastrichtian (Dickson et al., 2017).

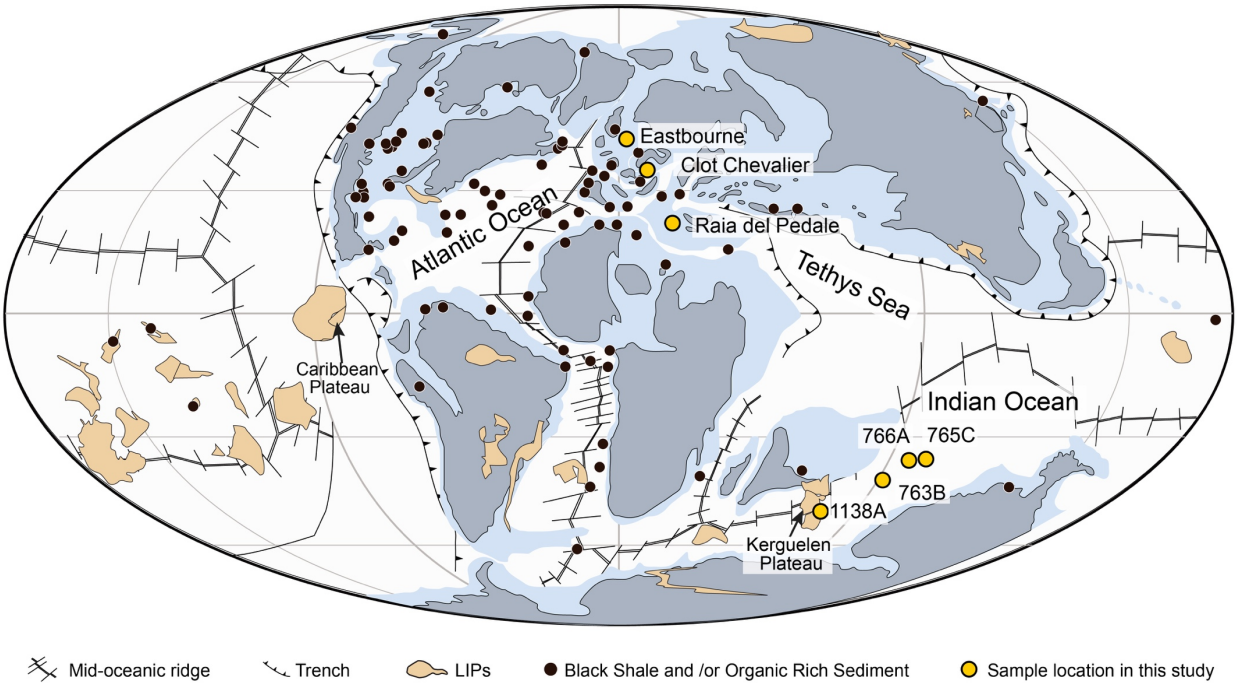

Figure 3.1 Sample locations in the mid-Cretaceous (ca. 90 Ma).

Black circles represent the location of the OAE-related organic-rich sediments (black shales) and yellow circles show the sampling locations of marine carbonate units. All locations are based on published literature (Arthur et al., 1987; Owens et al., 2018; Schlanger et al., 1987; Takashima et al., 2009, 2006; Trabucho Alexandre et al., 2010). The distribution of continental masses is based on Scotese (2004) and modified from Trabucho Alexandre et al. (2010). Landmasses and epicontinental seas are marked in gray and light blue. Sample locations for this study are marked in yellow circles (Murphy and Thomas, 2012; Thomas and Tilghman, 2014).

2.2 Sample preparation and Measurements

The methods used in this study were updated from (Cao et al., 2020). As demonstrated in the Fig. 3.2, for each selected sample about 200mg of powder was weighed into a 15ml centrifuge tube to which was added 10 ml of ammonium acetate buffer (1M, pH =7). Powders and reagents were subsequently mixed using a vortex mixer and remained in an ultrasonic water

bath for 30 mins, and an extra episode of vortex mixing was performed after 15 mins. Sample tubes were then cleaned on the outside and centrifuged for 10 mins at 3500 rpm. After that, the leachate was separated from the residue and discarded. This step was repeated twice more with an addition of 10 ml ammonium carbonate (1M, pH =7). Adding ammonium carbonate has been shown to remove contaminative REY more efficiently than ammonium acetate (unpublished data). Subsequently, the residue was rinsed twice with DI water (18.2 MΩ) before adding 5 ml 0.3M acetic acid. Procedures for this stage were mostly the same as for ammonium acetate leaching although the cap on the tubes needed to be removed every time after mixing in order for CO_2 gas to escape The leachate from this step was separated into a 5 ml beaker through a Thermo Scientific™ Titan 3™ Cellulose Acetate syringe filter (pore size: 0.22μm), and the residue was rinsed with DI water and the same acetic acid leaching step was repeated one more time. Sample leachates were evaporated to dryness and dissolved in 2% nitric acid for determination of elemental concentration. Measurements were made using an Agilent™ 7900 Quardrople ICP-MS (Inductively Coupled Plasma-Mass Spectrometer) under UHMI mode at UNC-Chapel Hill. 1ppm of internal Beryllium, Germanium, Indium, Rhodium, Bismuth standards were used to correct for instrumental drift during every analytical session. Background intensities were monitored periodically by aspirating 2% HNO_3 blanks. Precision and accuracy were assessed by repeat analysis of NIST SRM-1d, which gave a long-term relative standard deviation of <10% for most REY and major elements, with a slightly larger standard deviation for the transitional metal and less concentrated REY.

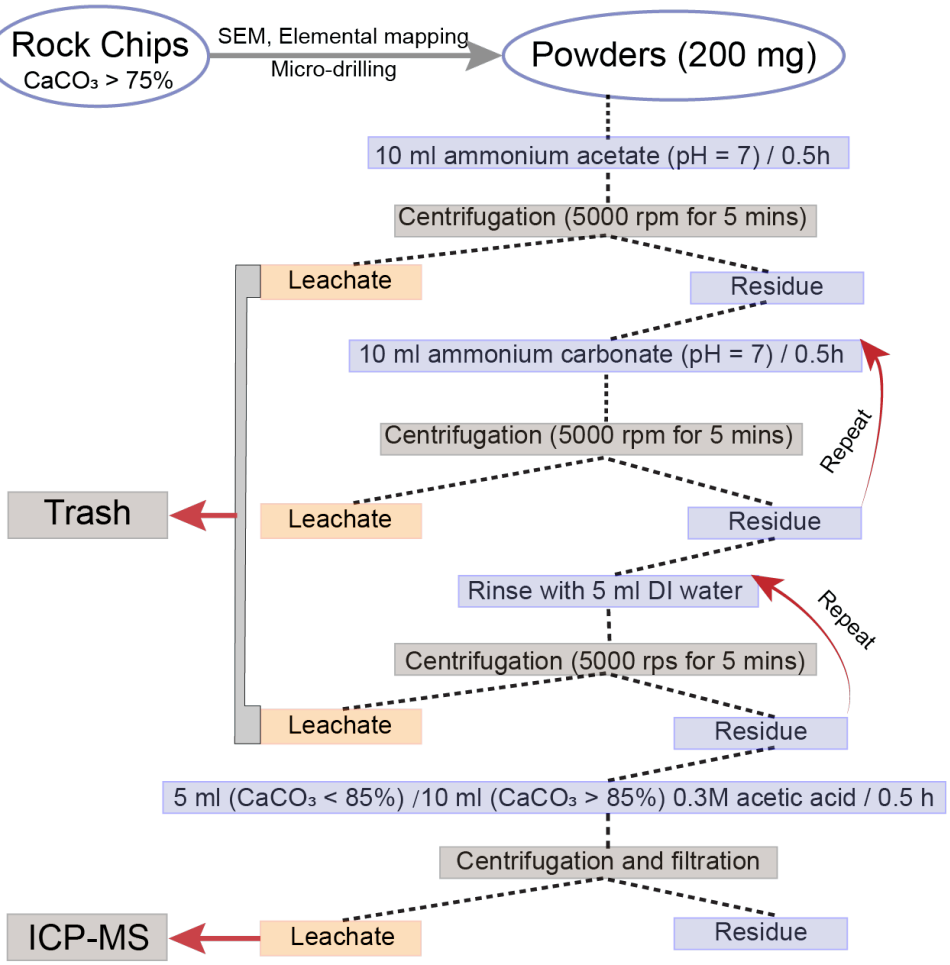

Figure 3.2 Detailed step-by-step protocol for sequential leaching.

2.3 Normalization

The Ce anomaly represents Ce abundances compared with those of its neighbors in the Periodic Table. For example, $Ce/Ce^* = [3Ce/(2La + Nd)]_{SN}$, where SN indicates shale-normalized (Elderfield and Greaves, 1982), or $Ce/Ce^* = [Ce/(0.5La + 0.5Pr)]_{SN}$ (Bau and Dulski, 1996). However, the anomalous behavior of La can artificially exaggerates the Ce anomaly, especially in Precambrian sediments. Therefore, in this study we have calculated Ce/Ce* using Upper continental Crust (UCC) - normalized Ce, Nd and Pr concentrations (eq. 1) to avoid potential problems with La anomalies (eq. 2) (Liu et al., 2019).

$Ce/Ce^* = Ce^*Nd / Pr^2$ (eq.1)

$La/La^* = [La / (Pr \times (Pr / Nd))]$ (eq.2)

$Nd/Nd^* = Nd^{\wedge 2}/(Pr^*Sm)$ (eq.3)

Results

3.1 Ce anomaly trends

The Ce/Ce* profiles in all seven study localities are plotted according to their chemostratigraphy in Fig. 3.3. Over the time intervals examined, the Ce/Ce* values vary from 0.5 to 0.8 in Eastbourne (n = 23), 0.5 to 1.1 in Clot Chevalier (n = 12), 1.0 to 1.7 in Raia del Pedale (n = 12). The Eastbourne profile shows that a two-stage increase with a negative excursion corresponding to the Plenus Cold Event that occurred during the early phase of OAE 2 (Fig. 3.3a). The Plenus Cold Event was initially proposed for the European Chalk Sea based on southward invasion of boreal faunas (Gale and Christensen, 1996; Keller et al., 2004; Forster et al., 2007; O'Connor et al., 2020). As for Clot Chevalier, Ce/Ce* shows a rapid positive shift before OAE 2, followed by a slow recovery that lasted through the entire event. At Raia del Pedale, the Ce/Ce* value is larger than 1 at the peak of the positive shift and all Ce/Ce* values are greater than 0.8.

The OAE 2 interval is less well constrained by carbon-isotope profiles in the southern hemisphere (Fig. 3.3b). In this study, we provide long-term Ce-anomaly data for the Late Cretaceous Southern Ocean at a coarser resolution. At Hole 763B, Ce/Ce* values shifted from 0.3 to 1.3 (n=39) starting at around late Albian–early Cenomanian boundary time. A continuous decrease in Ce/Ce* is observed over the upper Cenomanian to middle Turonian interval, followed by values that have small variability over the upper Turonian to lower Campanian interval. Ce/Ce* values at Hole 765C (n =16) generally decrease over the Turonian interval with a few higher values (0.8) in the upper Cenomanian. The Turonian is marked by lower Ce/Ce*

(0.3). At Hole 766A, Ce/Ce* values (n = 32) gradually increase in the upper Cenomanian and peak close to the boundary with the Turonian. Ce/Ce* values in higher stratigraphic levels, extending into the Campanian, are lower than 0.5. The Ce/Ce* record from Hole 1138A (n = 21) is similar to that of Hole 765C, decreasing from the upper Cenomanian to the lower Turonian then maintaining values around 0.3 for the higher parts of the Cretaceous, extending into the Maastrichtian.

In summary, Ce/Ce* values predominantly decreased starting from the late Cenomanian at European sites, a trend that continued into the OAE 2 interval. At ODP/IODP holes in the southern Indian Ocean, Ce/Ce* values in the late Turonian and subsequently were consistently between 0.3 and 0.5.

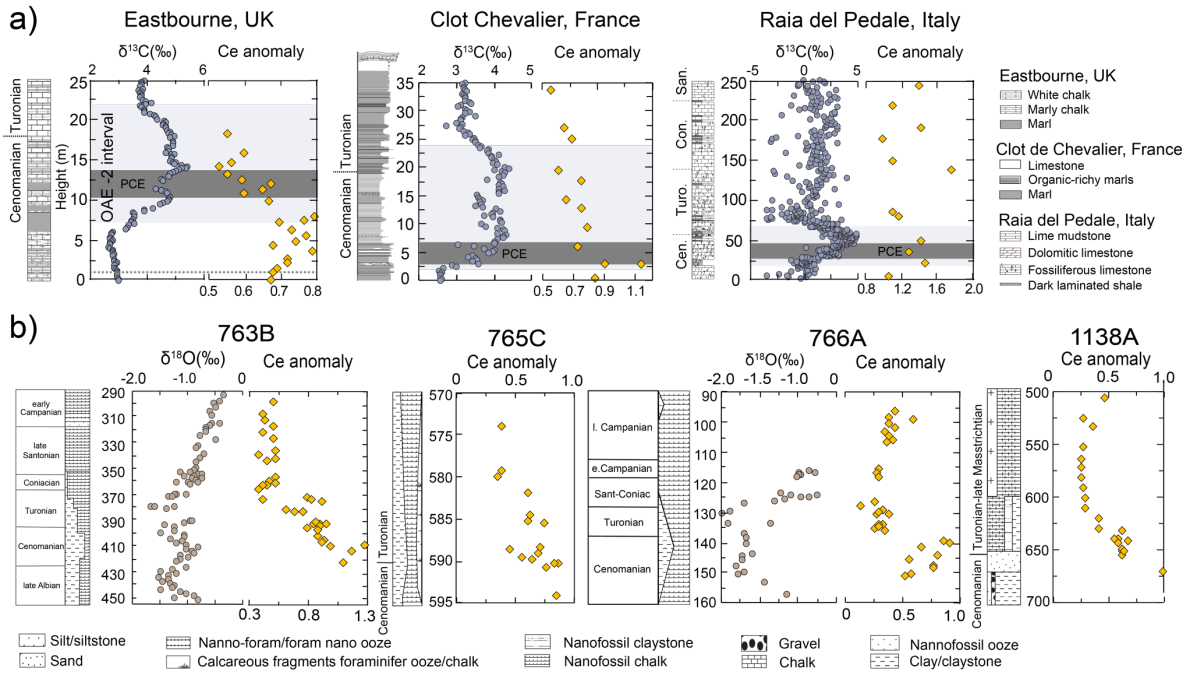

Figure 3.3 Detailed chemostratigraphic plots for OAE 2.

Panel a). documenting carbon- isotope and Ce/Ce* values at Eastbourne, UK; Clot Chevalier, France; Raia del Pedale, Italy; panel b). shows oxygen isotopes and Ce/Ce* values in samples from ODP/IODP Holes 763B, 765C, 766C and 1138A. OAE 2 is marked by the area in light gray, as delineated by the positive δ13C excursion (Gale et al., 2019; Keller et al., 2001; Owens et al., 2013; Tsikos et al., 2004). Light gray bar represents the OAE while the dark gray band marks the Plenus Cold Event (PCE). Gray dashed line (only at Eastbourne) represents the onset of the Ce/Ce* value shift. Lithostratigraphy for the ODP holes and Cenomanian–Turonian boundary are compiled from ODP/IODP publications: 763B (Haq et al., 1991); 765C (Ludden and Gradstein, 1990b); 766A (Ludden and Gradstein, 1990a) and 1138A (Coffin et al., 2000; Dickson et al., 2017). Oxygen isotopes from ODP Holes 763B and 766A are from Clarke and Jenkyns (1999).

3.2 Modeling oceanic dissolved oxygen using the Ce anomaly

Using thermodynamic calculations, we developed Ce oxidation models to quantitatively estimate the dissolved oxygen loss in the upper water column in response to OAE 2 in European sites and over the period of long-term warming in the southern hemisphere. Model details are described in SI information. In brief, we summarized all dissolved Ce speciations in seawater under the normal range of pe-pH conditions (Table A3.1). We also considered the major complexation reactions of Ce^{3+} with PO_4^{3-}, CO_3^{2-}, and OH^- (Table A3.2). Within the modern seawater pH range, the carbonate complex ($Ce(CO_3)^+$ or $Ce(CO_3)_2^-$) becomes the dominant species of dissolved Ce (Cantrell and Byrne, 1987; Nakada et al., 2017). Byrne et al. (1991) also suggested that trivalent Ce is tightly complexed with PO_4^{3-}. Based on each complexation, we assumed that oceanic dissolved oxygen is the only electron acceptor to oxidize trivalent Ce and have calculated stability constants for eleven possible oxidation models (Model #1-#11, SI information). All oxidation modes can be summarized as follows: $\log(\gamma_i C_{Ce}) = K - \frac{1}{4}\log(pO_2) + \partial_i \log\{\mathcal{X}_i\} - \beta_i pH,$ where C_{Ce} represents total dissolved Ce, and γ_i represents the relative activity coefficient for trivalent Ce species including $CePO_4^0$, $CeCO_3^+$, and $Ce(CO_3)_2^-$. $(\partial_i, \mathcal{X}_i)$ are expressed as $(1, PO_4^{3-})$, $(1, HCO_3^-)$, or $(2, CO_3^{2-})$. β_i ranges from 1 to 3, based on each complexation reaction.

Because this model is derived from thermodynamic principles, it represents equilibria in a closed system. To apply this model to a natural system, we further calibrated this model using two profiles. We used the South China Sea to calibrate for an open-ocean setting (Alibo and Nozaki, 2000), and the Black Sea (German et al., 1991) to calibrate for an anoxic–euxinic basin. Although the Carioco Basin might have been more ideal for the calibration, it lacks a good depth profile that contains all the parameters of the model such as phosphate, alkalinity, oxygen, pH

and rare-earth-element concentration. Despite the fact that the Black Sea is oceanograhically and geographically different from most reconstructed OAE settings, the main purpose is to calibrate the sensitivity of the model in an anoxic environment. In the open-ocean setting, the best model-predicted dissolved Ce compared to the measured value is $\log\{CePO_4^0\} = 17.9 + \log\{PO_4^{3-}\} - 0.25log(pO_2) - 3pH$ (Model #3) and $\log\{Ce(CO_3)_2^-\} = 18.13 + 2\log\{CO_3^{2-}\} - 3pH - 0.25log(pO_2)$ (Model #11). In the anoxic-basin setting, Model #3 also predicts the dissolved Ce closest to the measured value. Hence, we use Model #3 which gives the following relationship between the Ce anomaly and dissolved oxygen / phosphate / pH: $\frac{Ce}{Ce^*} \sim C_{Ce} \sim \frac{1}{\{pO_2\}^{\frac{1}{4}}}$; $\frac{Ce}{Ce^*} \sim C_{Ce} \sim \mathcal{X}_i^{\partial_i}$; $\frac{Ce}{Ce^*} \sim C_{Ce} \sim \{H^+\}^{\beta_i}$. Using these relationships, we assume the changes in seawater Ce anomaly is recorded by the carbonate Ce anomaly, and then we use changes in carbonate Ce/Ce* values to quantify changes in dissolved oxygen, pH and phosphate content in the ocean during the Late Cretaceous including OAE 2. The results are plotted in Fig. 3.4 together with $\delta^{13}C$, $\delta^{18}O$ and Ce/Ce* values. Due to different redox responses, baseline values of Ce/Ce* representing oxidation states are set at 0.5 for Eastbourne, Clot Chevalier and ODP/IODP holes, and 1.0 for Raia del Pedale based on the Ce anomaly post-OAE 2. For the southern hemisphere, we only plotted results from ODP hole763B as broadly representative of the open ocean since all four ODP/IODP holes show similar redox patterns but may not represent all distal deep-water localities. Based on changes in Ce/Ce*, the model calculated 50%–80% of dissolved oxygen loss in the upper water column during the Late Cenomanian in Eastbourne, Clot Chevalier, Raia del Pedale and Hole 763B.

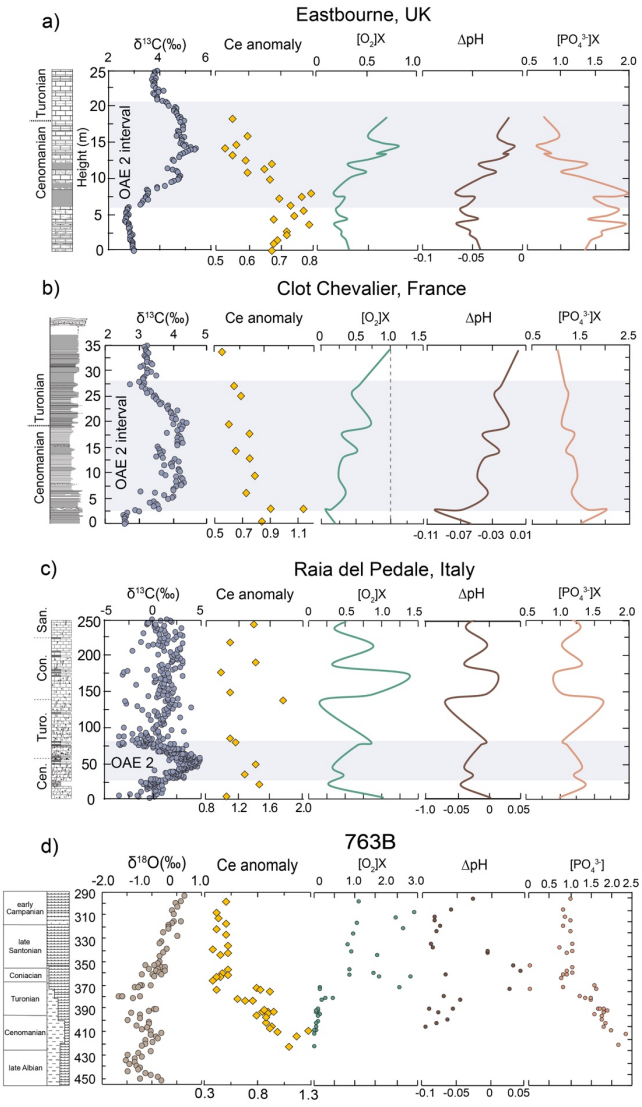

Figure 3.4 Modeling changes of oceanic dissolved oxygen, pH and phosphate concentrations.

Dissolved oxygen change (O_2 /post-OAE 2) is expressed as a ratio of dissolved oxygen compared to post-OAE 2; pH change (ΔpH) is expressed as $pH_t - pH_{post\text{-}OAE\ 2}$. Phosphate concentration change is also expressed in a ratio of phosphate compared to post-OAE 2 values. In the case of the ODP/IODP holes, post-OAE 2 refers to late Turonian time. Details of modeling parameters are shown in Appendix 3.3.

Discussion

We first discuss the fidelity of the Ce-anomaly data in the context of contamination from other phases and diagenetic alteration. We then examine the spatial heterogeneities in the redox responses by comparing the Ce anomalies determined in this study to other redox proxies. Subsequently, we discuss the controlling factors behind OAE 2 and the timing of deoxygenation. Finally, we discuss the modeling results and their global implication for modern ocean deoxygenation.

4.1. Fidelity of the Ce-anomaly data

We applied an updated leaching protocol to the samples to reduce contamination (Cao et al., 2020). The step involving ammonium acetate mainly extracts cations of low oxidation state, for example, Li, K, Mg, Sr. Ammonium carbonate has proven more effective in extracting elements of high oxidation state including rare-earth elements (unpublished data). 0.3M acetic acid was tested to prevent contaminative signals from Mn/Fe oxyhydroxides, clay minerals, and silicate phases (Cao et al., 2020). The Ce anomaly can potentially be influenced by post-depositional alteration. To investigate this possible problem and evaluate the fidelity of Ce-anomaly data, we also determined other element ratios, including Mg/Ca, Al/Ca, Mn/Ca, Sr/Ca, Fe/Ca, Rb/Sr, Mn/Sr as well as total rare-earth element + Yttrium (REY) concentrations and Nd anomaly (Fig. 3.5). We screened our Ce-anomaly data using a threshold for Mn/Sr (<3.0), and Rb/Sr (<1) (following Kaufman et al., 1993). Altered carbonate commonly have elevated Mn/Sr (Liu et al., 2013) ; and high Rb/Sr ratios might result from dolomitization or from interaction through diffusive exchange or dissolution-reprecipitation, or from reaction with clay minerals. Although the Ce anomaly has a range of 0–1.5, elemental ratios show minimal variability among sections, except for a few larger values found in samples from Holes 1138A and 765C, probably

due to minor leaching influences from volcanic glass, sand particles or clay minerals because such materials also show high Mn/Sr and Rb/Sr ratios. We found no correlation between the Ce anomaly and Mg/Ca, Sr/Ca, Fe/Ca, Rb/Sr, Mn/Sr, Total REY/Ca, and Nd/Nd* in any of the samples. Minor correlation between Ce anomaly and Al/Ca, Mn/Ca was found in samples from Hole ODP 1138A and 765C, probably also due to partial leaching of clay minerals and sand particles during chemical preparation.

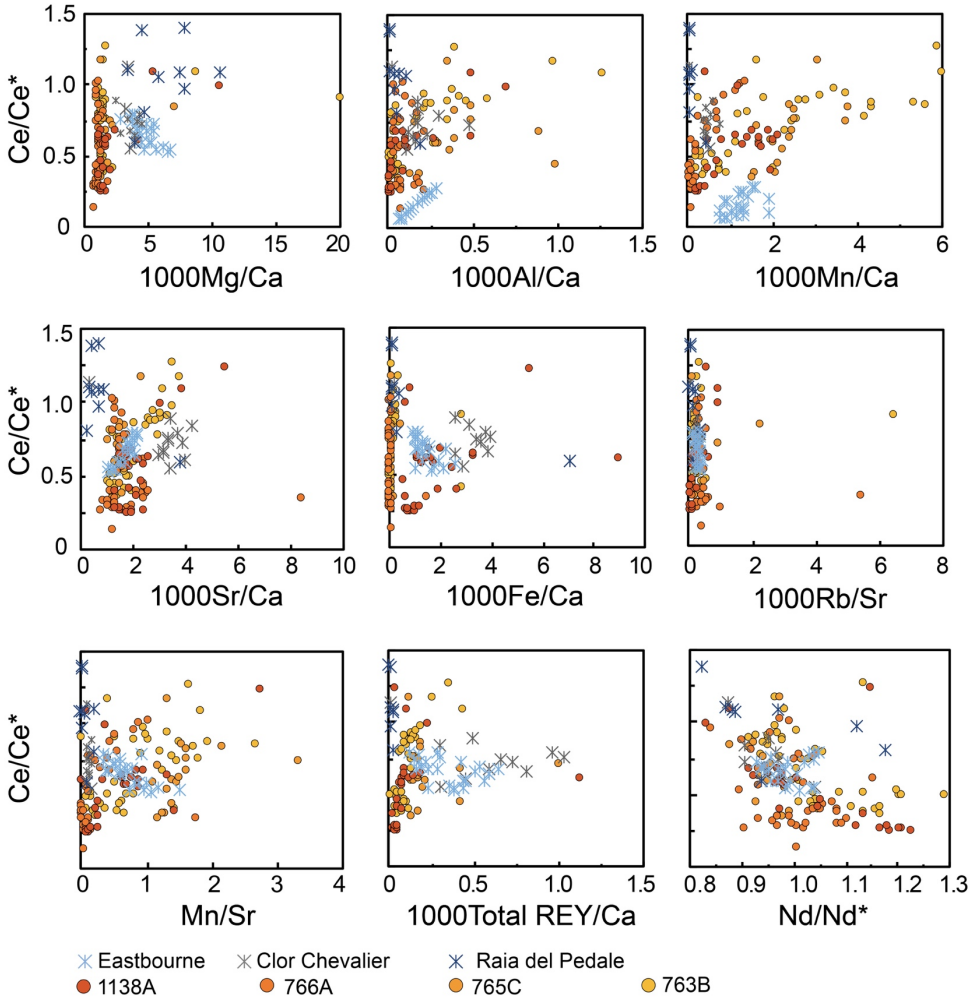

Figure 3.5 A comparison of REY with major- and trace-element alteration proxies for sequentially leached samples.

4.2. Geographically distinctive redox responses

A compilation of Ce/Ce* values in the modern ocean indicates that 90% of oxic seawater samples have Ce/Ce* values ranging from 0 to 0.5, with most values lower than 0.4. Higher values of the Ce anomaly are linked to low dissolved oxygen contents (Fig. A3.1.1). The increases in Ce/Ce* observed at the base of the Eastbourne and Clot Chevalier sections, therefore, suggest oxygen depletion in the upper ocean before and in the early phase of OAE 2. In the upper portion of these two sections, Ce/Ce* values are lower (0.5–0.6), suggesting that the upper water column at these sites became more oxygenated towards the end of OAE 2. At Eastbourne, the two positive Ce/Ce* excursions indicate two episodes of deoxygenation (or a phase of oxygenation within an overall episode of deoxygenation), which is consistent with the two-phase negative shifts in iodine/calcium ratios (Zhou et al., 2015) (Fig. 3.6). The intervening excursion to lower Ce/Ce* and higher I/Ca likely records a transient local watermass that was relatively more oxygenated, which may be related to the Plenus Cold Event (Jenkyns et al., 2017; O'Connor et al., 2020; Owens et al., 2013). Ce/Ce* ranging from 0.5 to 0.8 suggests that this location probably maintained suboxic to oxic conditions in the upper ocean during the entire OAE 2 interval. At Clot Chevalier, the positive shift of the Ce anomaly also started before the OAE 2 interval. The peak value (1.1) is present at the onset of the OAE level and subsequently, in higher stratigraphy, values of the Ce anomaly gradually decrease to 0.5. This trend indicates that, in this part of the Vocontian Trough, conditions were briefly anoxic before reoxygenation during the rest of OAE 2, an interpretation consistent with the relatively degraded nature of the organic matter in the section (Gale et al., 2019).

By contrast, Raia del Pedale has a Ce/Ce* range of 0.8–1.2, suggesting shallow anoxic watermasses with extreme anoxia at the peak of OAE 2. A positive excursion of the Ce anomaly is observed corresponding to OAE 2; however, this trend is not recorded in the I/Ca ratio. I/Ca

values are consistently low at ~1 umol/mol, indicating that the local near-surface waters were relatively oxygen-depleted (Zhou et al., 2015). Immediately above the falling limb of the $\delta^{13}C$ excursion (post-OAE 2) at Raia del Pedale, I/Ca values average 1.2 μmol/mol, which is lower than those found at Eastbourne at the same stratigraphic level (Lu et al., 2010). These data are consistent with our observed Ce/Ce*, which has overall higher values at Raia del Pedale, pointing to a more reducing environment than Eastbourne. This result is interesting because this section was likely deposited in a shallower water setting compare to Eastbourne. Reversal of the Ce/Ce* in Turonian and higher strata at Raia del Pedale suggests the presence of a more oxygenated water mass post-OAE 2 at this site. A subsequent Ce/Ce* positive shift across the Coniacian–Santonian boundary is plausibly related to OAE 3 (Fig. 3.3), the last oceanic anoxic event of the Cretaceous (Jenkyns, 2010; Locklair et al., 2011; März et al., 2008; Wagreich, 2012).

Both average and maximum Ce/Ce* values for the three European sites gradually increase towards lower latitudes (Fig. 3.7). However, such a spatial heterogeneity is not shown in any of the four ODP/IODP holes in the Southern Indian Ocean. Instead, they consistently have high Ce/Ce* values of ~0.8 in the upper Cenomanian, and low Ce/Ce* values of ~0.4 postdating the Cenomanian–Turonian boundary. $\delta^{18}O$ values from ODP Holes 763 and 766 indicate that a general warming trend continued throughout the Albian and Cenomanian into the early Turonian (Clarke and Jenkyns, 1999; Falzoni et al., 2016a): a pattern of climatic evolution that is global (Friedrich et al., 2012; O'Brien et al., 2017; Robinson et al., 2019). This Late Cretaceous warming is reflected in higher Ce/Ce*; subsequent cooling, albeit occurring at a slower rate, continued through the late Campanian and Maastrichtian and is marked by relatively low Ce/Ce* values. All Ce/Ce* values at the ODP/IODP holes in the southern Indian Ocean are lower than

1.0. Consequently, deoxygenation of the upper ocean apparently operated on more than regional scale because all the study sites show an increase of the Ce anomaly during the Late Cretaceous. However, only Clot Chevalier, Raia del Pedale and Hole 763B contain anoxia-indicative Ce anomaly values, thereby suggesting that intense oxygen depletion was probably restricted to relatively small areas.

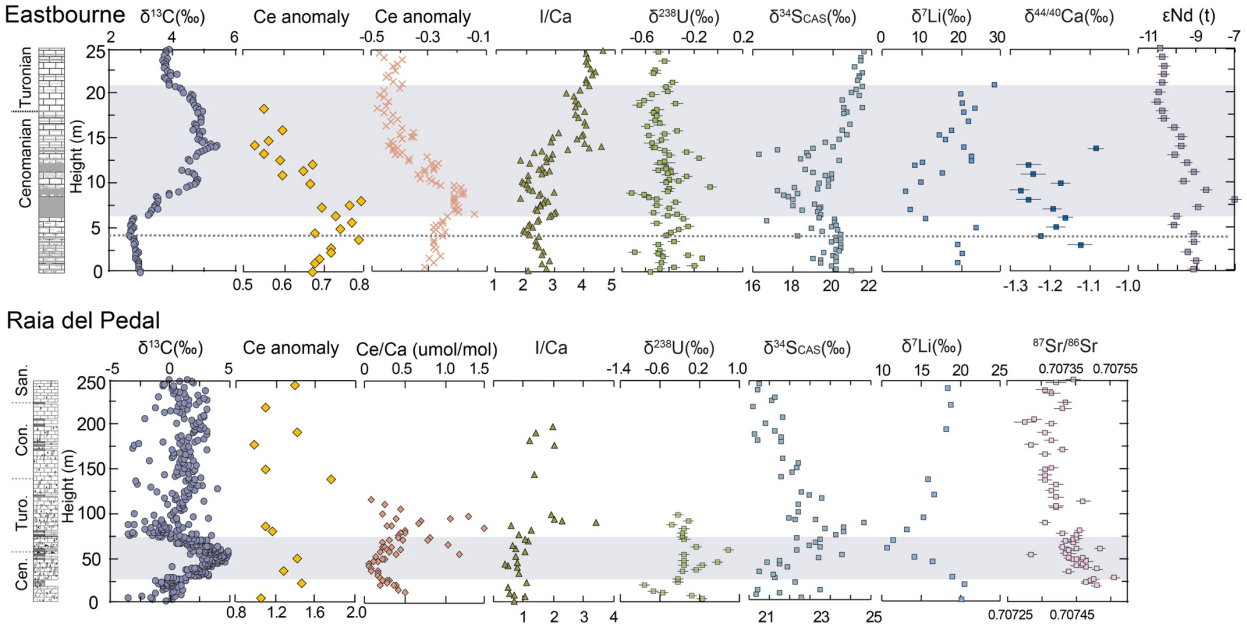

Figure 3.6 Geochemical data compilation for Eastbourne and Raia del Pedale.

The Ce-anomaly data in pink crosses (Ce/Ce*= log(3Ce/(2La+Nd)) and I/Ca ratios indicate local, and $\delta^{238}U$ and $\delta^{34}S_{CAS}$ values indicate global redox changes over the studied interval (Clarkson et al., 2018; Lu et al., 2010; Owens et al., 2013; Zhou et al., 2015). $\delta^{7}Li$, $\delta^{44/40}Ca$ and $^{87}Sr/^{86}Sr$ record weathering/alteration of oceanic and continental crust (Du Vivier et al., 2015; Pogge von Strandmann et al., 2013), while Nd isotopes are used to constrain oceanic circulation and hydrothermal activity (Zheng et al., 2013). The gray area marks the OAE 2 interval as defined by the $\delta^{13}C$ profile. The dashed line in the Eastbourne graph marks the initiation of deoxygenation at this locality according to redox proxy data; this point in time, as represented by this line, manifestly preceded OAE 2, as conventionally fixed by the initial rise in carbon-isotope values

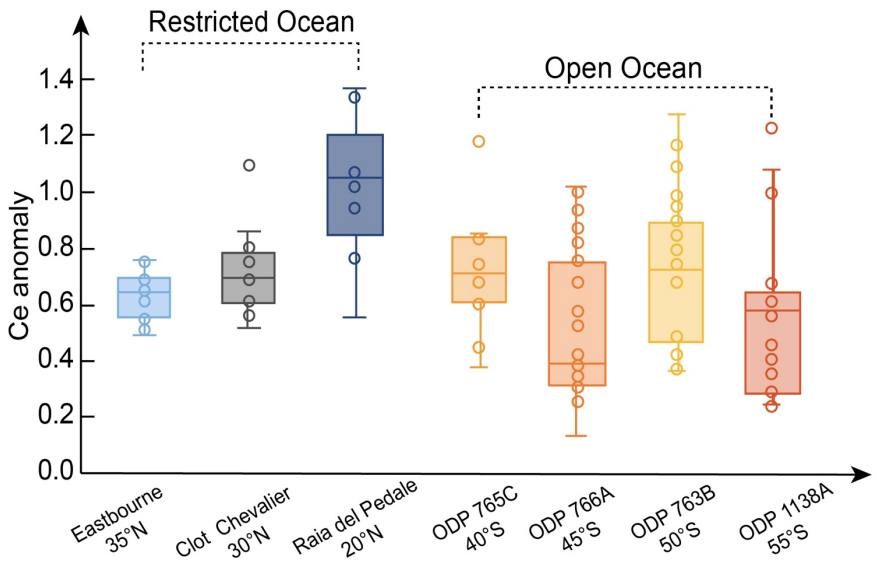

Figure 3.7 Box and whisker plots of Ce/Ce* values in each site.

Estimated paleolatitudes for each section and ODP holes are based on Haq et al. (1992); Martin et al. (2010); Robinson et al. (2010); Owens et al. (2013); Gale et al. (2019).

4.3 Implications for modern oceanic deoxygenation

Ce-anomaly records in marine carbonates of the OAE 2 interval provide more evidence for the heterogenous redox responses in the upper ocean alongside the I/Ca proxy. Additionally, the ODP/IODP profiles are essential to the global redox compilation because the Indian Ocean is much less studied compared to the Atlantic Ocean. Most significantly, the Ce oxidation model developed in this study is the first attempt to quantify oxygen loss in the upper ocean using thermodynamic calculations. Based on our modeling results, the global ocean would have lost on average 50% of the dissolved oxygen during the late Cenomanian proceeding OAE 2. Importantly, the modern ocean is losing oxygen at the rate of 2% per 40yrs, and this work suggests that losing 50% dissolved oxygen over 500 kyr is possible, and such rates are applicable to the past.

Redox chemostratigraphic records of the European sites indicate that peak deoxygenation characterized the early stages of OAE 2. Other factors such as ocean acidification (pH decrease of 0.1) or elevated phosphate concentrations (up to 2 times) could also have caused the enlarged Ce anomaly, based on model calculations. The pH would have decreased by up to 0.1 (calculated using $\frac{Ce}{Ce^*} \sim C_{Ce} \sim \{H^+\}$. Using $\frac{Ce}{Ce^*} \sim C_{Ce} \sim PO_4^{3-}$, phosphate could have increased by 50%–100% to accommodate the observed Ce/Ce* changes. Monteiro et al., (2012) also suggested the oceanic phosphate concentration would have doubled during the event. During sea-level rise, coastal erosion may have increased the supply of phosphorus to the ocean by up to 20% (Bjerrum et al., 2006). In addition, in suboxic and anoxic conditions, accumulation rates of phosphorus are low: evidence from P-depleted sediments and high organic C/total P indicates that this major nutrient was efficiently regenerated from the sediment (cf. Nederbragt et al., 2004; Mort et al., 2008; Kraal et al., 2010). The increased P availability may have helped to sustain high productivity during OAE 2.

At this stage, we cannot distinguish between these effects, and more work to constrain these changes quantitatively is required to address these limitations for the utilization of Ce/Ce* to track levels of dissolved oxygen. Nonetheless, our Ce oxidation model provides the first quantitative estimate of oxygen loss in the upper ocean before, during and after OAE 2 based on globally extensive Ce/Ce* records. However, relatively high Ce anomalies (>0.5) in the modern ocean are usually associated with low-oxygen watermasses or the surface ocean in the tropics (see SI information for a detailed discussion). Given that increases in the Ce anomaly in the late Cenomanian are consistently recorded in all study sites, the geochemical patterns in this interval should primarily reflect deoxygenation in the upper ocean.

4.4. Deoxygenation mechanism

It is evident that deoxygenation in the ocean interior results from an imbalance of oxygen supply and consumption (Keeling et al., 2010; Levin, 2018; Oschlies et al., 2018). Air–sea gas exchange keeps surface waters continuously approaching oxygen saturation. Currently, warming is considered the main driver for surface-water oxygen decline because oxygen solubility decreases with increasing ocean temperature. For example, seawater warming from 10°C to 30°C leads to a 30% loss in oxygen solubility (Kester, 1975). OAE 2 is assumed to represent a hyperthermal within the overall context of a CO_2-inspired greenhouse climate with relatively elevated sea-surface temperatures, in excess of 35°C, at low latitudes (Adams et al., 2010; Barclay et al., 2010; Forster et al., 2007; Friedrich et al., 2012, 2006; Huber et al., 2002; O'Brien et al., 2017; Robinson et al., 2019). However, ocean warming alone cannot completely explain the different regional patterns. Furthermore, the decline in oxygen solubility cannot account for >50% of dissolved oxygen loss as suggested by our modeling results. The distribution of oxygen in the upper water column is affected by the downwelling of oxygen-rich surface water, and upwelling of oxygen-poor waters. Sluggish ocean circulation, or overturning associated with tropical deep-water formation, could have substantially reduced the supply of oxygen in the ocean below the surface saturation zone. For example, Brass et al. (1982) introduced the WSBW (warm saline bottom water) hypothesis, in which increased evaporation in the tropical shelf areas produced very warm dense brines that sank to form deep water instead of the cold and relatively salty water currently downwelling at high latitudes. Trabucho Alexandre et al. (2010) supported this hypothesis and further suggested an estuarine circulation between the North Atlantic and Pacific Oceans during the mid-Cretaceous. Such Pacific-derived nutrient-rich deep water would have been depleted in dissolved oxygen due to its decreased solubility in warm water and, where locally upwelled in the Atlantic and surrounding areas, favored high

productivity and the deposition of organic-rich sediments, particularly during OAEs. Such a mechanism may have been responsible for significant anoxia, even in waters of modest depth such as at Raia del Pedale during OAE 2. Significantly, evidence for intermittent low-oxygen conditions in this section around Cenomanian–Turonian boundary time is found in the local development of black microbially laminated carbonates with total organic carbon (TOC) contents up to 1% (Frijia et al., 2019). By contrast, Eastbourne was not greatly affected by an anoxic upper water column at this time due to its higher latitude, different oceanographic setting and ocean circulation, at times bringing Arctic waters to the region. This paleoceanographic model is supported by a positive εNd excursion at this site, which was likely due to the transport of radiogenic Nd from a volcanic source, most likely the High Arctic LIP via boreal seawater, or Caribbean LIP via other routes (Fig. 3.8) (Zheng et al., 2013). Because Eastbourne has relatively low Ce/Ce* values over the OAE 2 interval, it is unlikely that this area received waters from the Pacific at this time because they would have been more depleted in oxygen.

The overall εNd pattern of oceanographic responses in the four IODP/ODP holes in the southern Indian Ocean indicates that the seafloor was actively ventilated during much of Late Cretaceous time (Fig. 3.8). Thus, the accumulation and burial of anomalously high amounts of organic carbon in seafloor sediments in this area during OAE 2 has been attributed to enhanced surface-water productivity and high carbon flux to the seafloor, instead of diminished bottom-water ventilation (Thomas and Tilghman, 2014).

Lastly, high consumption of oxygen via biotic respiration in the upper ocean could have further increased net oxygen loss. By contrast, the increased burial of organic carbon during most of the OAE 2 interval (Plenus Cold Event excepted) would have released oxygen into the ocean–atmosphere system, potentially ventilating a range of environments, all other factors being equal

(e.g. Holland, 1984). The dominantly negative trend of Ce/Ce*, as exemplified by OAE 2, can be explained by this process. However, the increase of Ce/Ce* in the early stages of the positive $\delta^{13}C$ excursion (early OAE 2) suggests that, even when oxygen was supplied by organic-carbon burial, respiration rates in the water column were still relatively high, causing the water column to become depleted in oxygen. Elevated oxygen consumption could have had many other causes, including CO_2 effects on organisms, ecosystems, and the quality of sinking particles, as well as changes in nutrient supply from the ocean interior or land. The relatively light δ^7Li signatures found in several OAE 2 sections suggest an increase in silicate weathering rate and weathering intensity in both subaerial and marine realms, and such processes would have stimulated nutrient supply and consequent planktonic productivity (Pogge von Strandmamm et al., 2013).

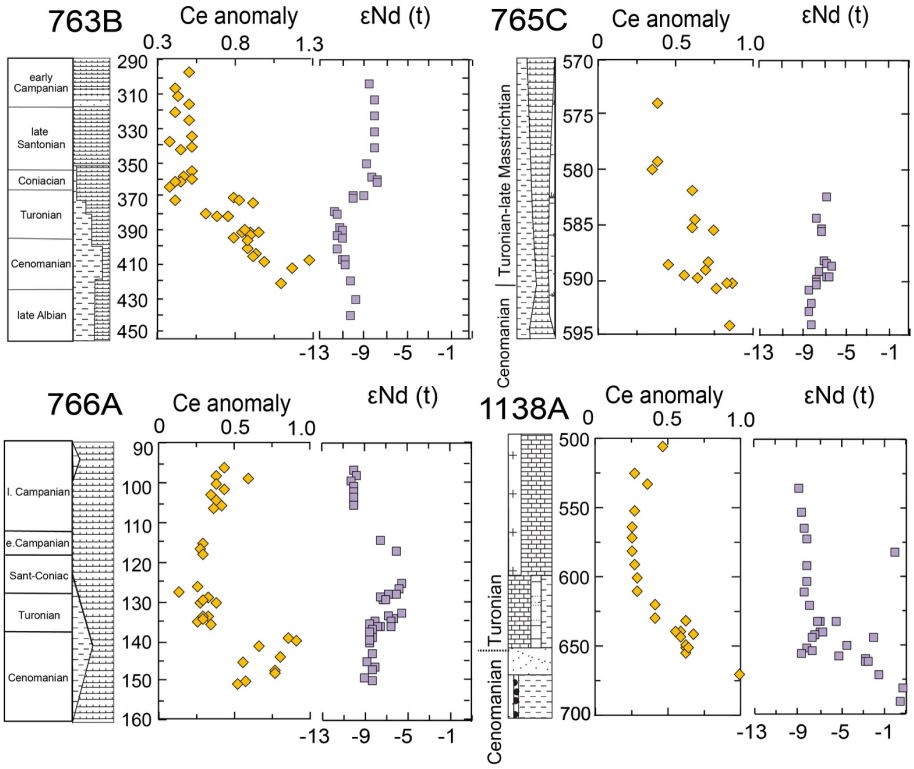

Figure 3.8 Geochemical data compilation for ODP sites in the southern Indian Ocean. Nd isotopes are replotted against sediment depth, and depths for each sample are compiled from Martin et al. (2010) and Thomas and Tilghman (2014), as well as calculated using ODP core summary database.

4.5 Deoxygenation timing

The Cenomanian–Turonian $\delta^{13}C$ curve acts as both a stratigraphic marker and as a monitor of global marine organic-carbon burial with its first (stratigraphically lowest) positive shift conventionally taken as defining the onset of OAE 2 (e.g. Jenkyns et al., 2017). Importantly, the Ce/Ce* positive excursion took place prior to the OAE for European sites indicating that, at least locally, deoxygenation occurred before significant enhanced global carbon burial. This phenomenon is equally suggested by drawdown of vanadium in an equatorial Atlantic ODP site (Demerara Rise) that initiated ~75kyr prior to the onset of OAE 2, which itself

coincided with a drop in molybdenum content: phenomena that illustrate the differential expansion of anoxia and euxina in the water colum (Owens et al., 2016b). Similarly, Ostrander et al. (2017), based on Tl-isotope records from the same ODP site, have calculated that deoxygenation at the sediment–water interface expanded ~43 kyr before the globally recognized carbon-cycle perturbation of OAE 2. In addition, nitrogen isotopes suggest that the transition from oxia to anoxia took place locally (Tarfaya, Morocco) even earlier in an area of persistent upwelling (Scholz et al., 2019). Hence, the redox conditions that characterized OAE 2 began to develop well before its onset, as conventionally described by the initial rise in carbon-isotope values. Significantly, most of the upper ocean remained oxic to suboxic during OAE 2.

Conclusion

With appropriate dissolution methods, the Ce anomaly in ancient marine carbonate rocks is a sensitive paleo-redox tracer not only for local basins but also on a global scale if compiling such records from multiple representative areas. The results of this study show that deoxygenation occurred in the upper ocean of the European area and Indian Ocean during the Cenomanian and early Turonian stages of the Late Cretaceous. However, extreme anoxia was restricted to ocean basins where high oxygen demand was met with low oxygen supply from diffusion and ocean circulation, locally even in relatively shallow-water areas. The Ce-anomaly records from northern and southern Europe and the proto-Indian Ocean reveal redox conditions in the upper ocean during OAE 2 that were geographically distinctive and dynamic. The timing of deoxygenation in the upper ocean was not uniform and predated the positive movement in the carbon-isotope signature used to define the onset of OAE 2 at Eastbourne, a phenomenon already indicated by some trace-element data and thallium isotopes at a global scale. A progressive increase in the average Ce anomaly in three European sites situated at progressively lower latitudes in the Northern Hemisphere is consistent with an overturning in the North Atlantic

Ocean and surrounding seas during OAE 2. Local redox variations, particularly if manifested as extreme anoxia, were likely influenced by different factors including continental weathering and nutrient supply, upwelling, planktonic productivity, ocean circulation, watermass stratification, and thermocline depth. The overall decreasing Ce/Ce* after the onset of OAE 2 in late Cenomanian and subsequent stages indicates reoxygenation in the upper ocean, possibly driven by global organic-matter burial, causing oxygen release to the ocean–atmosphere system. Significantly lower Ce/Ce* values through the late Turonian into the Maastrichtian suggest that the upper ocean recovered to a fully oxidized state, probably due to long-term cooling. Our Ce oxidation model suggests a greater than 50% loss in oceanic oxygen in the run-up to the Cenomanian-Turonian Boundary interval in multiple sites followed by local recovery to better-ventilated conditions. Complemantary Ce-anomaly records from areas such as the Pacific Ocean would allow us to obtain a comprehensive understanding of the redox response to the OAE 2 in the upper ocean at global scale.

REFERENCES

Adams, D.D., Hurtgen, M.T., Sageman, B.B., 2010. Volcanic triggering of a biogeochemical cascade during Oceanic Anoxic Event 2. Nat. Geosci. 3, 201–204. https://doi.org/10.1038/ngeo743

Alibo, D.S., Nozaki, Y., 2000. Dissolved rare earth elements in the South China Sea: Geochemical characterization of the water masses. J. Geophys. Res. Ocean. 105, 28771–28783. https://doi.org/10.1029/1999JC000283

Arthur, M.A., Brumsack, H.J., Jenkyns, H.C., Schlanger, S.O., 1990. Stratigraphy, geochemistry, and paleoceanography of organic carbon- rich Cretaceous sequences, in: Ginsburg, R.N., Beaudoin, B. (Eds.), Cretaceous Resources, Events and Rhythms. Kluwer; NATO ASI Series C, 304, pp. 75–119. https://doi.org/10.1007/978-94-015-6861-6_6

Bach, W., Irber, W., 1998. Rare earth element mobility in the oceanic lower sheeted dyke complex: evidence from geochemical data and leaching experiments. Chem. Geol. 151, 309–326. https://doi.org/10.1016/S0009-2541(98)00087-4

Banner, J.L., G.N.Hanson, W.J.Meyers, 1988. Rare Earth Elements and Nd Isotopic Variations in Regionally Extensive Dolomites from the Burlington-Keokuk Formation (Mississippian) : Implications for REE Mobility during Carbonate Diagenesis. J. Sediment. Petrol. 58, 415–432.

Barclay, R.S., McElwain, J.C., Sageman, B.B., 2010. Carbon sequestration activated by a volcanic CO2 pulse during Ocean Anoxic Event 2. Nat. Geosci. 3, 205–208. https://doi.org/10.1038/ngeo757

Bargar, J.R., Fuller, C.C., Marcus, M.A., Brearley, A.J., Perez De la Rosa, M., Webb, S.M., Caldwell, W.A., 2009. Structural characterization of terrestrial microbial Mn oxides from Pinal Creek, AZ. Geochim. Cosmochim. Acta 73, 889–910. https://doi.org/10.1016/J.GCA.2008.10.036

Bau, M., Dulski, P., 1996. Premmbrinn Resenrth Distribution of yttrium and rare-earth elements in the Penge and Kuruman iron-formations, Transvaal Supergroup, South Africa. Precambrian Res. 79, 37–55. https://doi.org/10.1016/0301-9268(95)00087-9

Bjerrum, C.J., Bendtsen, J., Legarth, J.J.F., 2006. Modeling organic carbon burial during sea level rise with reference to the Cretaceous. Geochemistry, Geophys. Geosystems 7, 1–24. https://doi.org/10.1029/2005GC001032

Blättler, C.L., Jenkyns, H.C., Reynard, L.M., Henderson, G.M., 2011. Significant increases in global weathering during Oceanic Anoxic Events 1a and 2 indicated by calcium isotopes. Earth Planet. Sci. Lett. 309, 77–88. https://doi.org/10.1016/j.epsl.2011.06.029

Blumenberg, M., Wiese, F., 2012. Imbalanced nutrients as triggers for black shale formation in a

shallow shelf setting during the OAE 2 (Wunstorf, Germany). Biogeosciences 9, 4139–4153. https://doi.org/10.5194/bg-9-4139-2012

Bodin, S., Godet, A., Westermann, S., Föllmi, K.B., 2013. Secular change in northwestern Tethyan water-mass oxygenation during the late Hauterivian–early Aptian. Earth Planet. Sci. Lett. 374, 121–131. https://doi.org/10.1016/j.epsl.2013.05.030

Brass, G., Southam, J., Peterson, W.H., 1982. Warm saline bottom water in the ancient ocean. Nature 296, 620–623. https://doi.org/10.1038/296620a0

Byrne, R.H., Bingler, L.S., 1989. Comment on "Cerium: A chemical tracer for paleo-oceanic redox conditions" by Y.-G. Liu, M. R. U. Miah and R. A. Schmitt. Geochim. Cosmochim. Acta. https://doi.org/10.1016/0016-7037(89)90081-1

Byrne, R.H., Lee, J.H., Bingler, L.S., 1991. Rare earth element complexation by PO43 - ions in aqueous solution. Geochim. Cosmochim. Acta 55, 2729–2735.

Cantrell, K.J., Byrne, R.H., 1987. Rare earth element complexation by carbonate and oxalate ions. Geochim. Cosmochim. Acta 51, 597–605. https://doi.org/10.1016/0016-7037(87)90072-X

Cao, C., Liu, X.-M., Bataille, C.P., Liu, C., 2020. What do Ce anomalies in marine carbonates really mean? A perspective from leaching experiments. Chem. Geol. 532, 119413. https://doi.org/10.1016/j.chemgeo.2019.119413

Clarke, L.J., Jenkyns, H.C., 1999. New oxygen isotope evidence for long-term Cretaceous climatic change in the Southern Hemisphere. Geology 27, 699–702. https://doi.org/10.1130/0091-7613(1999)027<0699:NOIEFL>2.3.CO;2

Damsté, J.S.S., Köster, J., 1998. A euxinic southern North Atlantic Ocean during the Cenomanian/Turonian oceanic anoxic event. Earth Planet. Sci. Lett. 158, 165–173.

Dickson, A.J., Saker-Clark, M., Jenkyns, H.C., Bottini, C., Erba, E., Russo, F., Gorbanenko, O., Naafs, B.D.A., Pancost, R.D., Robinson, S.A., van den Boorn, S.H.J.., Idiz, E., 2017. A Southern Hemisphere record of global trace-metal drawdown and orbital modulation of organic-matter burial across the Cenomanian–Turonian boundary (Ocean Drilling Program Site 1138, Kerguelen Plateau). Sedimentology 64, 186–203. https://doi.org/10.1111/sed.12303

Du Vivier, A.D.C., Jacobson, A.D., Lehn, G.O., Selby, D., Hurtgen, M.T., Sageman, B.B., 2015. Ca isotope stratigraphy across the Cenomanian-Turonian OAE 2: Links between volcanism, seawater geochemistry, and the carbonate fractionation factor. Earth Planet. Sci. Lett. 416, 121–131. https://doi.org/10.1016/j.epsl.2015.02.001

Du Vivier, A.D.C., Selby, D., Sageman, B.B., Jarvis, I., Gröcke, D.R., Voigt, S., 2014. Marine 187Os/188Os isotope stratigraphy reveals the interaction of volcanism and ocean circulation

during Oceanic Anoxic Event 2. Earth Planet. Sci. Lett. 389, 23–33.

Elderfield, H., Greaves, M.J., 1982. The rare earth elements in seawater. Nature 296, 214–219. https://doi.org/10.1038/296214a0

Eldrett, J.S., Ma, C., Bergman, S.C., Lutz, B., Gregory, F.J., Dodsworth, P., Phipps, M., Hardas, P., Minisini, D., Ozkan, A., Ramezani, J., Bowring, S.A., Kamo, S.L., Ferguson, K., Macaulay, C., Kelly, A.E., 2015. An astronomically calibrated stratigraphy of the Cenomanian, Turonian and earliest Coniacian from the Cretaceous Western Interior Seaway, USA: Implications for global chronostratigraphy. Cretac. Res. 56, 316–344. https://doi.org/10.1016/j.cretres.2015.04.010

Falzoni, F., Petrizzo, M.R., Clarke, L.J., MacLeod, K.G., Jenkyns, H.C., 2016a. Long-term Late Cretaceous oxygen-and carbon isotope trends and planktonic foraminiferal turnover: A new record from the southern midlatitudes. Bull. Geol. Soc. Am. 128, 1725–1735. https://doi.org/10.1130/B31399.1

Falzoni, F., Petrizzo, M.R., Jenkyns, H.C., Gale, A.S., Tsikos, H., 2016b. Planktonic foraminiferal biostratigraphy and assemblage composition across the Cenomanian-Turonian boundary interval at Clot Chevalier (Vocontian Basin, SE France). Cretac. Res. 59, 69–97. https://doi.org/10.1016/j.cretres.2015.10.028

Forster, A., Schouten, S., Moriya, K., Wilson, P.A., Damsté, J.S.S., 2007. Tropical warming and intermittent cooling during the Cenomanian/Turonian oceanic anoxic event 2: Sea surface temperature records from the equatorial Atlantic. Paleoceanography 22, 1–14. https://doi.org/10.1029/2006PA001349

Frey, F.A., Coffin, M.F., Wallace, P.J., Weis, D., Zhao, X., Wise, S.W., Wähnert, V., Teagle, D.A.H., Saccocia, P.J., Reusch, D.N., Pringle, M.S., Nicolaysen, K.E., Neal, C.R., Müller, R.D., Moore, C.L., Mahoney, J.J., Keszthelyi, L., Inokuchi, H., Duncan, R.A., Delius, H., Damuth, J.E., Damasceno, D., Coxall, H.K., Borre, M.K., Boehm, F., Barling, J., Arndt, N.T., Antretter, M., 2000. Origin and evolution of a submarine large igneous province: The Kerguelen Plateau and Broken Ridge, southern Indian Ocean. Earth Planet. Sci. Lett. 176, 73–89. https://doi.org/10.1016/S0012-821X(99)00315-5

Friedrich, O., Erbacher, J., Mutterlose, J., 2006. Paleoenvironmental changes across the Cenomanian/Turonian Boundary Event (Oceanic Anoxic Event 2) as indicated by benthic foraminifera from the Demerara Rise (ODP Leg 207). Rev. Micropaleontol. 49, 121–139. https://doi.org/10.1016/j.revmic.2006.04.003

Friedrich, O., Norris, R.D., Erbacher, J., 2012. Evolution of middle to late Cretaceous oceans-A 55 m.y. Record of Earth's temperature and carbon cycle. Geology 40, 107–110. https://doi.org/10.1130/G32701.1

Frijia, G., Forkner, R., Minisini, D., Pacton, M., Struck, U., Mutti, M., 2019. Cyanobacteria Proliferation in the Cenomanian-Turonian Boundary Interval of the Apennine Carbonate

Platform: Immediate Response to the Environmental Perturbations Associated With OAE-2? Geochemistry, Geophys. Geosystems 20, 2698–2716. https://doi.org/10.1029/2019GC008306

Gale, A.S., Christensen, W.K., 1996. Occurrence of the belemnite Actinocamax plenus in the Cenomanian of SE France and its significance. Bull. Geol. Soc. Denmark 43, 68–77.

Gale, A.S., Jenkyns, H.C., Tsikos, H., van Breugel, Y., Sinninghe Damsté, J.S., Bottini, C., Erba, E., Russo, F., Falzoni, F., Petrizzo, M.R., Dickson, A.J., Wray, D.S., 2019. High-resolution bio- and chemostratigraphy of an expanded record of Oceanic Anoxic Event 2 (Late Cenomanian–Early Turonian) at Clot Chevalier, near Barrême, SE France (Vocontian Basin). Newsletters Stratigr. 52, 97–129. https://doi.org/10.1127/nos/2018/0445

Gale, A.S., Kennedy, W.J., Voigt, S., Walaszczyk, I., 2005. Stratigraphy of the Upper Cenomanian-Lower Turonian Chalk succession at Eastbourne, Sussex, UK: Ammonites, inoceramid bivalves and stable carbon isotopes. Cretac. Res. 26, 460–487. https://doi.org/10.1016/j.cretres.2005.01.006

Gangl, S.K., Moy, C.M., Stirling, C.H., Jenkyns, H.C., Crampton, J.S., Clarkson, M.O., Ohneiser, C., Porcelli, D., 2019. High-resolution records of Oceanic Anoxic Event 2: Insights into the timing, duration and extent of environmental perturbations from the palaeo-South Pacific Ocean. Earth Planet. Sci. Lett. 518, 172–182. https://doi.org/10.1016/j.epsl.2019.04.028

German, C., Holliday, B.P., Elderfield, H., 1991. Redox cycling of rare earth elements in the suboxic zone of the Black Sea. Geochim. Cosmochim. Acta 55, 3553–3558. https://doi.org/10.1016/0016-7037(91)90055-A

German, C.R., Elderfield, H., 1990. Application of the Ce anomaly as a paleoredox indicator: The ground rules. Paleoceanography 5, 823–833. https://doi.org/10.1029/PA005i005p00823

Goldberg, T., Poulton, S.W., Wagner, T., Kolonic, S.F., Rehkämper, M., 2016. Molybdenum drawdown during Cretaceous Oceanic Anoxic Event 2. Earth Planet. Sci. Lett. 440. https://doi.org/10.1016/j.epsl.2016.02.006

Gradstein, F.M., 1992. 43 . Legs 122 and 123 , Northwestern Australian Margin — a Stratigraphic and. Proc. Ocean Drill. Program, Sci. Results 123 123, 801–816. https://doi.org/10.2973/odp.proc.sr.123.110.1992

Hancock, J.M., 1975. The petrology of the Chalk. Proc. Geol. Assoc. 86, 499–535. https://doi.org/10.1016/S0016-7878(75)80061-7

Haq, B.U., Boyd, R.L., Exon, N.F., von Rad, U., 1992. Evolution of the Central Exmouth Plateau: A Post-Drilling Perspective, in: Proceedings of the Ocean Drilling Program, 122 Scientific Results. Ocean Drilling Program, pp. 801–816. https://doi.org/10.2973/odp.proc.sr.122.182.1992

Haq, B.U., von Rad, U., O'Connell, S., 1991. Shipboard Scientific Party,1990. Site 763., in: Proc. ODP, Init, Repts., 122. College Station, TX (Ocean Drilling Program), pp. 289–352. https://doi.org/10.2973/odp.proc.ir.122.109.1990

Hetzel, A., Böttcher, M.E., Wortmann, U.G., Brumsack, H.-J., 2009. Paleo-redox conditions during OAE 2 reflected in Demerara Rise sediment geochemistry (ODP Leg 207). Palaeogeogr. Palaeoclimatol. Palaeoecol. 273, 302–328.

Huber, B.T., Norris, R.D., MacLeod, K.G., 2002. Deep-sea paleotemperature record of extreme warmth during the Cretaceous. Geology 30, 123–126. https://doi.org/10.1130/0091-7613(2002)030<0123:DSPROE>2.0.CO;2

Jenkyns, H.C., 2018. Transient cooling episodes during Cretaceous Oceanic Anoxic Events with special reference to OAE 1a (Early Aptian). Philos. Trans. R. Soc. A Math. Phys. Eng. Sci. https://doi.org/10.1098/rsta.2017.0073

Jenkyns, H.C., 2010. Geochemistry of oceanic anoxic events. Geochemistry, Geophys. Geosystems 11, 1–30. https://doi.org/10.1029/2009GC002788

Jenkyns, H.C., 1980. Cretaceous anoxic events: from continents to oceans. J. Geol. Soc. London. 137, 171–188. https://doi.org/10.1144/gsjgs.137.2.0171

Jenkyns, H.C., Dickson, A.J., Ruhl, M., van den Boorn, S.H.J.M., 2017. Basalt-seawater interaction, the Plenus Cold Event, enhanced weathering and geochemical change: deconstructing Oceanic Anoxic Event 2 (Cenomanian-Turonian, Late Cretaceous). Sedimentology 64, 16–43. https://doi.org/10.1111/sed.12305

Jones, C.E., Jenkyns, H.C., 2001. Seawater strontium isotopes, oceanic anoxic events, and seafloor hydrothermal activity in the Jurassic and Cretaceous. Am. J. Sci. 301, 112–149. https://doi.org/10.2475/ajs.301.2.112

Kaufman, A.J., Jacobsen, S.B., Knoll, A.H., 1993. The Vendian record of Sr and C isotopic variations in seawater: Implications for tectonics and paleoclimate. Earth Planet. Sci. Lett. 120, 409–430. https://doi.org/10.1016/0012-821X(93)90254-7

Keeling, R.F., Körtzinger, A., Gruber, N., 2010. Ocean Deoxygenation in a Warming World. Ann. Rev. Mar. Sci. 2, 199–229. https://doi.org/10.1146/annurev.marine.010908.163855

Keller, G., Berner, Z., Adatte, T., Stueben, D., 2004. Cenomanian-Turonian and δ13C, and δ18O, sea level and salinity variations at Pueblo, Colorado. Palaeogeogr. Palaeoclimatol. Palaeoecol. 211, 19–43. https://doi.org/10.1016/j.palaeo.2004.04.003

Keller, G., Han, Q., Adatte, T., Burns, S.J., 2001. Palaeoenvironment of the Cenomanian–Turonian transition at Eastbourne, England. Cretac. Res. 22, 391–422. https://doi.org/10.1006/cres.2001.0264

Kerr, A.C., 1998. Oceanic plateau formation: a cause of mass extinction and black shale deposition around the Cenomanian-Turonian boundary? J. Geol. Soc. London. 155, 619–626. https://doi.org/10.1144/gsjgs.155.4.0619

Kester, D.R., 1975. Dissolves gases other than CO2, in: Chemical Oceanography. Nature Publishing Group, pp. 497–556. https://doi.org/10.1038/srep17097

Kraal, P., Slomp, C.P., Forster, A., Kuypers, M.M.M., 2010. Phosphorus cycling from the margin to abyssal depths in the proto-Atlantic during oceanic anoxic event 2. Palaeogeogr. Palaeoclimatol. Palaeoecol. 295, 42–54. https://doi.org/10.1016/j.palaeo.2010.05.014

Larson, R.L., 1991. Latest pulse of Earth: evidence for a mid-Cretaceous superplume. Geology. https://doi.org/10.1130/0091-7613(1991)019<0547:LPOEEF>2.3.CO;2

Lawrence, M.G., Greig, A., Collerson, K.D., Kamber, B.S., 2006. Rare earth element and yttrium variability in South East Queensland waterways. Aquat. Geochemistry 12, 39–72. https://doi.org/10.1007/s10498-005-4471-8

Levin, L.A., 2018. Manifestation, Drivers, and Emergence of Open Ocean Deoxygenation. Ann. Rev. Mar. Sci. 10, 229–260. https://doi.org/10.1146/annurev-marine-121916-063359

Li, Y.X., Montañez, I.P., Liu, Z., Ma, L., 2017. Astronomical constraints on global carbon-cycle perturbation during Oceanic Anoxic Event 2 (OAE2). Earth Planet. Sci. Lett. 462, 35–46. https://doi.org/10.1016/j.epsl.2017.01.007

Liu, X.M., Hardisty, D.S., Lyons, T.W., Swart, P.K., 2019. Evaluating the fidelity of the cerium paleoredox tracer during variable carbonate diagenesis on the Great Bahamas Bank. Geochim. Cosmochim. Acta 248, 25–42. https://doi.org/10.1016/j.gca.2018.12.028

Locklair, R., Sageman, B., Lerman, A., 2011. Marine carbon burial flux and the carbon isotope record of Late Cretaceous (Coniacian-Santonian) Oceanic Anoxic Event III. Sediment. Geol. 235, 38–49. https://doi.org/10.1016/j.sedgeo.2010.06.026

Lu, Z., Jenkyns, H.C., Rickaby, R.E.M., 2010. Iodine to calcium ratios in marine carbonate as a paleo-redox proxy during oceanic anoxic events. Geology 38, 1107–1110. https://doi.org/10.1130/G31145.1

Ludden, J.N., Gradstein, F.M., 1990. Shipboard Scientific Party, 1990. Site 766, in: Proc. ODP, Init. Repts. College Station, TX (Ocean Drilling Program, pp. 269–352.

März, C., Poulton, S.W., Beckmann, B., Küster, K., Wagner, T., Kasten, S., 2008. Redox sensitivity of P cycling during marine black shale formation: Dynamics of sulfidic and anoxic, non-sulfidic bottom waters. Geochim. Cosmochim. Acta 72, 3703–3717. https://doi.org/10.1016/j.gca.2008.04.025

Monteiro, F.M., Pancost, R.D., Ridgwell, A., Donnadieu, Y., 2012. Nutrients as the dominant

control on the spread of anoxia and euxinia across the Cenomanian-Turonian oceanic anoxic event (OAE2): Model-data comparison. Paleoceanography 27, 1–17. https://doi.org/10.1029/2012PA002351

Nakada, R., Tanaka, M., Tanimizu, M., Takahashi, Y., 2017. Aqueous speciation is likely to control the stable isotopic fractionation of cerium at varying pH. Geochim. Cosmochim. Acta 218, 273–290. https://doi.org/10.1016/j.gca.2017.09.019

Nederbragt, A.J., Thurow, J., Vonhof, H., Brumsack, H.J., 2004. Modelling oceanic carbon and phosphorus fluxes: Implications for the cause of the late Cenomanian Oceanic Anoxic Event (OAE2). J. Geol. Soc. London. 161, 721–728. https://doi.org/10.1144/0016-764903-075

O'Brien, C.L., Robinson, S.A., Pancost, R.D., Sinninghe Damsté, J.S., Schouten, S., Lunt, D.J., Alsenz, H., Bornemann, A., Bottini, C., Brassell, S.C., Farnsworth, A., Forster, A., Huber, B.T., Inglis, G.N., Jenkyns, H.C., Linnert, C., Littler, K., Markwick, P., McAnena, A., Mutterlose, J., Naafs, B.D.A., Püttmann, W., Sluijs, A., van Helmond, N.A.G.M., Vellekoop, J., Wagner, T., Wrobel, N.E., 2017. Cretaceous sea-surface temperature evolution: Constraints from TEX86 and planktonic foraminiferal oxygen isotopes. Earth-Science Rev. https://doi.org/10.1016/j.earscirev.2017.07.012

O'Connor, L.K., Jenkyns, H.C., Robinson, S.A., Remmelzwaal, S.R.C., Batenburg, S.J., Parkinson, I.J., Gale, A.S., 2020. A re-evaluation of the Plenus Cold Event, and the links between CO 2 , temperature, and seawater chemistry during OAE 2. Paleoceanogr. Paleoclimatology. https://doi.org/10.1029/2019PA003631

Oschlies, A., Brandt, P., Stramma, L., Schmidtko, S., 2018. Drivers and mechanisms of ocean deoxygenation. Nat. Geosci. https://doi.org/10.1038/s41561-018-0152-2

Ostrander, C.M., Owens, J.D., Nielsen, S.G., 2017. Constraining the rate of oceanic deoxygenation leading up to a Cretaceous Oceanic Anoxic Event (OAE-2: ~94 Ma). Sci. Adv. 3, e1701020. https://doi.org/10.1126/sciadv.1701020

Owens, J.D., Gill, B.C., Jenkyns, H.C., Bates, S.M., Severmann, S., Kuypers, M.M.M., Woodfine, R.G., Lyons, T.W., 2013. Sulfur isotopes track the global extent and dynamics of euxinia during Cretaceous Oceanic Anoxic Event 2. Proc. Natl. Acad. Sci. U. S. A. 110, 18407–12. https://doi.org/10.1073/pnas.1305304110

Owens, J.D., Lyons, T.W., Hardisty, D.S., Lowery, C.M., Lu, Z., Lee, B., Jenkyns, H.C., 2017. Patterns of local and global redox variability during the Cenomanian-Turonian Boundary Event (Oceanic Anoxic Event 2) recorded in carbonates and shales from central Italy. Sedimentology 64, 168–185. https://doi.org/10.1111/sed.12352

Owens, J.D., Lyons, T.W., Hardisty, D.S., Lowery, C.M., Lu, Z., Lee, B., Jenkyns, H.C., 2016a. Patterns of local and global redox variability during the Cenomanian-Turonian Boundary Event (Oceanic Anoxic Event 2) recorded in carbonates and shales from central Italy.

Sedimentology 64, 168–185. https://doi.org/10.1111/sed.12352

Owens, J.D., Lyons, T.W., Li, X., MacLeod, K.G., Gordon, G., Kuypers, M.M.M., Anbar, A., Kuhnt, W., Severmann, S., 2012. Iron isotope and trace metal records of iron cycling in the proto-North Atlantic during the Cenomanian-Turonian oceanic anoxic event (OAE-2). Paleoceanography 27, 1–13. https://doi.org/10.1029/2012PA002328

Owens, J.D., Lyons, T.W., Lowery, C.M., 2018. Quantifying the missing sink for global organic carbon burial during a Cretaceous oceanic anoxic event. Earth Planet. Sci. Lett. 499, 83–94. https://doi.org/10.1016/j.epsl.2018.07.021

Owens, J.D., Reinhard, C.T., Rohrssen, M., Love, G.D., Lyons, T.W., 2016b. Empirical links between trace metal cycling and marine microbial ecology during a large perturbation to Earth's carbon cycle. Earth Planet. Sci. Lett. 449, 407–417. https://doi.org/10.1016/j.epsl.2016.05.046

Pancost, R.D., Crawford, N., Magness, S., Turner, A., Jenkyns, H.C., Maxwell, J.R., 2004. Further evidence for the development of photic-zone euxinic conditions during Mesozoic oceanic anoxic events. J. Geol. Soc. London. 161, 353–364.

Parente, M., Frijia, G., Di Lucia, M., Jenkyns, H.C., Woodfine, R.G., Baroncini, F., 2008. Stepwise extinction of larger foraminifers at the Cenomanian-Turonian boundary: A shallow-water perspective on nutrient fluctuations during oceanic anoxic event 2 (Bonarelli event). Geology 36, 715–718. https://doi.org/10.1130/G24893A.1

Paul, C.R.C., Lamolda, M.A., Mitchell, S.F., Vaziri, M.R., Gorostidi, A., Marshall, J.D., 1999. The Cenomanian-Turonian boundary at Eastbourne (Sussex, UK): A proposed european reference section. Palaeogeogr. Palaeoclimatol. Palaeoecol. 150, 83–121. https://doi.org/10.1016/S0031-0182(99)00009-7

Pogge Von Strandmann, P.A.E., Jenkyns, H.C., Woodfine, R.G., 2013. Lithium isotope evidence for enhanced weathering during Oceanic Anoxic Event 2. Nat. Geosci. 6, 668–672. https://doi.org/10.1038/ngeo1875

Robinson, S.A., Dickson, A.J., Pain, A., Jenkyns, H.C., Brien, C.L.O., Lunt, D.J., 2019. Southern Hemisphere sea-surface temperatures during the Cenomanian – Turonian : Implications for the termination of Oceanic Anoxic Event 2. Geology 47, 1–4. https://doi.org/10.1130/G45842.1/4607014/g45842.pdf

Rue, E.L., Smith, G.J., Cutter, G.A., Bruland, K.W., 1997. The response of trace element redox couples to suboxic conditions in the water column. Deep. Res. Part I Oceanogr. Res. Pap. 44, 113–134. https://doi.org/10.1016/S0967-0637(96)00088-X

Sageman, B.B., Meyers, S.R., Arthur, M.A., 2006. Orbital time scale and new C-isotope record for Cenomanian-Turonian boundary stratotype. Geology 34, 125. https://doi.org/10.1130/G22074.1

Schlanger, S.O., Arthur, M.A., Jenkyns, H.C., Scholle, P.A., 1987. The Cenomanian-Turonian Oceanic Anoxic Event, I. Stratigraphy and distribution of organic carbon-rich beds and the marine 13C excursion. Geol. Soc. London, Spec. Publ. 26, 371–399.

Schlanger, S.O., Jenkyns, H.C., 1976. Cretaceous Oceanic Anoxic Events: Causes and Concequences. Geol. En Minbouw 55, 179–184.

Schlanger, S.O., Jenkyns, H.C., Premoli-Silva, I., 1981. Volcanism and vertical tectonics in the Pacific Basin related to global Cretaceous transgressions. Earth Planet. Sci. Lett. 52, 435–449. https://doi.org/10.1016/0012-821X(81)90196-5

Schmidtko, S., Stramma, L., Visbeck, M., 2017. Decline in global oceanic oxygen content during the past five decades. Nature 542, 335–339. https://doi.org/10.1038/nature21399

Scholle, P.A., Arthur, M.A., 1980. Carbon isotope fluctuations in Cretaceous pelagic limestones: potential stratigraphic and petroleum exploration tool. Am. Assoc. Pet. Geol. Bull. 64, 67–87. https://doi.org/10.1306/2f91892d-16ce-11d7-8645000102c1865d

Scholz, F., Beil, S., Flögel, S., Lehmann, M.F., Holbourn, A., Wallmann, K., Kuhnt, W., 2019. Oxygen minimum zone-type biogeochemical cycling in the Cenomanian-Turonian Proto-North Atlantic across Oceanic Anoxic Event 2. Earth Planet. Sci. Lett. 517, 50–60. https://doi.org/10.1016/j.epsl.2019.04.008

Sinton, C.W., Duncan, R.A., 1997. Potential links between ocean plateau volcanism and global ocean anoxia at the Cenomanian-Turonian boundary. Econ. Geol. 92, 836–842.

Slingerland, R., Kump, L.R., Arthur, M.A., Fawcett, P.J., Sageman, B.B., Barron, E.J., 1996. Estuarine circulation in the Turonian Western Interior seaway of North America : Discussion and reply. Gelogical Soc. Am. Bull. 129, 941–952. https://doi.org/10.1130/0016-7606(1996)108<0941:ECITTW>2.3.CO;2

Thierstein, H.R., Berger, W.H., 1978. Injection events in ocean history. Nature 276, 461–466. https://doi.org/10.1038/276461a0

Tostevin, R., Shields, G.A., Tarbuck, G.M., He, T., Clarkson, M.O., Wood, R.A., 2016. Effective use of cerium anomalies as a redox proxy in carbonate-dominated marine settings. Chem. Geol. 438, 146–162. https://doi.org/10.1016/j.chemgeo.2016.06.027

Trabucho Alexandre, J., Tuenter, E., Henstra, G.A., Van Der Zwan, K.J., Van De Wal, R.S.W., Dijkstra, H.A., De Boer, P.L., 2010. The mid-Cretaceous North Atlantic nutrient trap: Black shales and OAEs. Paleoceanography 25, 1–14. https://doi.org/10.1029/2010PA001925

Tsikos, H., Jenkyns, H.C., Walsworth-Bell, B., Petrizzo, M.R., Forster, A., Kolonic, S., Erba, E., Silva, I.P., Baas, M., Wagner, T., Sinninghe, J.S., 2004. Carbon-isotope stratigraphy recorded by the Cenomanian-Turonian Oceanic Anoxic Event: correlation and implications based on three key localities. J. Geol. Soc. London. 162, 576–576.

https://doi.org/10.1144/0016-7649Er161-4

Turgeon, S., Brumsack, H.-J., 2006. Anoxic vs dysoxic events reflected in sediment geochemistry during the Cenomanian–Turonian Boundary Event (Cretaceous) in the Umbria–Marche Basin of central Italy. Chem. Geol. 234, 321–339.

van Bentum, E.C., Hetzel, A., Brumsack, H.-J., Forster, A., Reichart, G.-J., Sinninghe Damsté, J.S., 2009. Reconstruction of water column anoxia in the equatorial Atlantic during the Cenomanian–Turonian oceanic anoxic event using biomarker and trace metal proxies. Palaeogeogr. Palaeoclimatol. Palaeoecol. 280, 489–498. https://doi.org/10.1016/j.palaeo.2009.07.003

Voigt, S., Gale, A.S., Flögel, S., 2004. Midlatitude shelf seas in the Cenomanian-Turonian greenhouse world: Temperature evolution and North Atlantic circulation. Paleoceanography 19, 1–17. https://doi.org/10.1029/2004PA001015

Wagreich, M., 2012. "OAE 3" - Regional Atlantic organic carbon burial during the Coniacian-Santonian. Clim. Past 8, 1447–1455. https://doi.org/10.5194/cp-8-1447-2012

Webb, G.E., Kamber, B.S., 2000. Rare earth elements in Holocene reefal microbialites: A new shallow seawater proxy. Geochim. Cosmochim. Acta 64, 1557–1565. https://doi.org/10.1016/S0016-7037(99)00400-7

Wright, J., Schrader, H., Holser, W.T., 1987. Paleoredox variations in ancient oceans recorded by rare earth elements in fossil apatite. Geochim. Cosmochim. Acta 51, 631–644. https://doi.org/10.1016/0016-7037(87)90075-5

Zheng, X.-Y., Jenkyns, H.C., Gale, A.S., Ward, D.J., Henderson, G.M., 2013. Changing ocean circulation and hydrothermal inputs during Ocean Anoxic Event 2 (Cenomanian–Turonian): Evidence from Nd-isotopes in the European shelf sea. Earth Planet. Sci. Lett. 375, 338–348.

Zhong, S., Mucci, A., 1995. Partitioning of rare earth elements (REEs) between calcite and seawater solutions at 25°C and 1 atm, and high dissolved REE concentrations. Geochim. Cosmochim. Acta 59, 443–453. https://doi.org/10.1016/0016-7037(94)00381-U

Zhou, X., Jenkyns, H.C., Owens, J.D., Junium, C.K., Zheng, X.Y., Sageman, B.B., Hardisty, D.S., Lyons, T.W., Ridgwell, A., Lu, Z., 2015. Upper ocean oxygenation dynamics from I/Ca ratios during the Cenomanian-Turonian OAE 2. Paleoceanography 30, 510–526. https://doi.org/10.1002/2014PA002741

CHAPTER 4 - LI ISOTOPE EVIDENCE FOR A COLLAPSE OF REVERSE WEATHERING IN THE LATE PERMIAN

Introduction

Chemical weathering transfers elements from the continents into the oceans and exerts a series of feedbacks on global biogeochemical cycles. In particular, silicate weathering regulates long-term climate by consuming atmospheric carbon dioxide (CO_2) and controlling the rate of marine carbonate precipitation (Walker et al., 1981). The Permian and the Early Triassic is one of the most interesting periods in the Phanerozoic era to study the long-term chemical weathering because dramatic variations in tectonic and climate occur concomitantly during this period. Pangea supercontinent formation ended in the Early Permian with major continent-to-continent collisions, including the Hercynian and Uralian Orogeneses (Fluteau et al., 2001; Newell et al., 1999; Veevers, 2013). Later in the Permian period, the Tethys sea started to open initiating Pangea break-up (Stampfli and Borel, 2002). In terms of climate, the mid-Sakmarian deglaciation event marked the end of the Karoo glaciation (Montañez and Poulsen, 2013). The climate warmed progressively throughout the Permian, with hot and dry conditions dominating the continental interiors (Parrish, 1993). The end Permian is marked by massive flood basalt volcanism (i.e., Siberian Traps) accompanied by the most severe mass extinction (Bond and Wignall, 2014; Stanley, 2016). Global warming began at the end-Permian and persisted into the Early Triassic (Joachimski et al., 2012; Sun et al., 2012).

These tectonic and climate changes are associated with large Sr isotopes perturbation in seawater ($(^{87}Sr/^{86}Sr)_{sw}$) recorded in marine carbonate and conodont apatite (Korte et al., 2006, 2005; Martin and Macdougall, 1995; Song et al., 2015). In particular, the Permian is marked by

the most significant decline in the $(^{87}Sr/^{86}Sr)_{sw}$ value during the Phanerozoic era (Korte et al., 2006). $(^{87}Sr/^{86}Sr)_{sw}$ reaches the minimum values shortly before the Permian-Triassic Boundary (257-258 Ma). Then $(^{87}Sr/^{86}Sr)_{sw}$ rises sharply from the Late Permian to the Early Triassic (Spathian) (Bekker et al., 2004; Dudás et al., 2017; Korte et al., 2006, 2005, 2003; Martin and Macdougall, 1995; Sedlacek et al., 2014; Song et al., 2015; Tierney and Saltzman, 2010). However, the magnitude of the chemical weathering rate variations, as well as factors controlling these variations remain unconstrained (Kump et al., 2000). Additionally, Sr is abundant in carbonates, so the contribution of carbonate vs. silicate weathering on $(^{87}Sr/^{86}Sr)_{sw}$ variations are difficult to differentiate (Bataille et al., 2017; Coogan and Dosso, 2015; Veizer, 1989).

Recently, lithium (Li) isotopes in marine carbonate rocks have been used to study chemical weathering in the past (Lechler et al., 2015; Pogge Von Strandmann et al., 2013; Sun et al., 2018). Compared to Sr isotopes, Li isotope fractionations are not related to carbonate weathering due to its low abundance in carbonates. Rather, Li isotope compositions in seawater reflect changes in silicate weathering, weathering regime, hydrothermal activity and reverse weathering (Penniston-Dorland et al., 2017). Li has a residence time of ~1.5 million years (Myr) in the ocean (Huh et al., 1998), which is much longer than the ocean mixing time (~1 kyr for the modern ocean), resulting in homogenous Li isotope composition in the ocean at 1 Myr time interval. Major sources of Li in the ocean are riverine inputs (F_{riv}) and hydrothermal fluids F_{MOR}), and each flux accounts for 50% of the total flux. In the modern setting, δ^7Li of the riverine input (δ^7Li_{riv}) is 23‰ (Huh et al., 2001, 1998) and 8‰ in the hydrothermal input (δ^7Li_{MOR}) (Hathorne and James, 2006; Misra and Froelich, 2012), respectively. The main sink of oceanic Li is through reverse weathering with $\Delta_{Seawater - Sediment}$ = 16‰ required at a steady state with the modern seawater δ^7Li ($(\delta^7Li)_{sw}$) of 31‰ (James et al., 1999; Tomascak et al., 1999;

Vigier et al., 2008; Misra and Froelich, 2012). Li isotope fractionation mechanisms are well studied in modern chemical weathering enviroments. For example, an early study demonstrated that primary mineral dissolution increases the Li concentration ([Li]) in the continental runoff without significant isotope fractionation (Pistiner and Henderson, 2003). By contrast, large Li isotope fractionation occurs during secondary mineral formation by preferential incorporation of ^{6}Li into clay minerals (Chan et al., 1992; Kisakurek et al., 2005; Liu et al., 2013; Rudnick et al., 2004; Teng et al., 2004; Wimpenny et al., 2015, 2010). This leaves the fluid phases such as river water with high $\delta^{7}Li$ and low [Li] (Chan et al., 1992; Kisakurek et al., 2005; Pistiner and Henderson, 2003; Rudnick et al., 2004; Wimpenny et al., 2015, 2010). Therefore, $\delta^{7}Li_{riv}$ has been proposed to reflect weathering congruency, defined as the ratio of primary mineral dissolution to the secondary mineral formation (Dellinger et al., 2017; Pogge von Strandmann and Henderson, 2015). The lack of isotope fractionation dependence on temperature or salinity in marine carbonates, including corals (Rollion-Bard et al., 2009), brachiopods (Dellinger et al., 2018), and foraminifers (Misra and Froelich, 2012), suggests that marine carbonates may record robust seawater $\delta^{7}Li$ (Rollion-Bard et al., 2009; Misra and Froelich, 2012; Pogge von Strandmann et al., 2019). However, major limitations exist before applying Li isotopes in ancient marine carbonates as a weathering proxy. Firstly, uncertainties remain in both the flux and isotope fractionation during reverse weathering, including oceanic basalt alteration and authigenic clay formation. Secondly, vital effects and diagenesis of marine carbonates may cause additional Li isotope fractionation (Dellinger et al., 2020).

In this study, a collection of marine carbonate rocks that were not diagenetically affected and brachiopod fossils were carefully selected to cover the Permian to the Early Triassic periods. Among marine carbonate materials, brachiopods are reliable archives for tracing past $(\delta^{7}Li)_{sw}$

because they have homogeneous δ^7Li with little influence from vital effects, and inter-species variations (Dellinger et al., 2020). More importantly, shells of the brachiopods are more resistant to postdepositional resetting of original signal low-Mg calcite than aragonite (Korte et al., 2006; Veizer et al., 1999). Thus, brachiopods would be used to check for the robustness of the $(\delta^7Li)_{sw}$ record. We analyze Li isotopes in these samples and interpret these data combining Li box model with our knowledge of climate and tectonic activities. Reconstructed seawater δ^7Li values, $(\delta^7Li)_{sw}$ are decoupled from the $(^{87}Sr/^{86}Sr)_{sw}$ record and show large fluctuations. These fluctuations show correspondence with global climate and oceanic activities during the Permian and the Early Triassic. We demonstrate that $(\delta^7Li)_{sw}$ does not only reflect changes in chemical weathering rate and congruency but is also greatly influenced by changes in hydrothermal activity and reverse weathering.

Geologic setting

To cover the study period (Permian and early Triassic), we collected samples of early Permian age from the western United States and the Yangtze platform, South China. The selected sections have well-constrained biostratigraphic age models (Burgess et al., 2014; Galfetti et al., 2007; Lehrmann et al., 2006; Ovtcharova et al., 2006; Shen et al., 2011, 2007; Stevens, 2008; Sun et al., 2017). Those sections are among the thickest and most continuous marine carbonate succession in the world during the selected time interval.

Thick sections of Pennsylvanian to early Permian marine carbonates are present throughout Northeastern Nevada in the Pequop Mountains. Those sediments deposited on the western margin of Laurentia in a shallow shelf sedimentation environment (Sweet 2003). They encompass the latest Pennsylvanian Gzhelian Stage through the lowest Kungurian Stage (Permian) with continuous faunal successions and little evidence for major sedimentation hiatuses (Stevens, 2008; Sweet, 2003).

The Yangtze Platform formed the central part of South China Craton and accumulated shallow marine carbonate sediments (Feng et al., 1997). A ramp existed on its western paleomargin, and the Shangsi section was located on the lower slope of the ramp (Li et al., 1989). The current location of Shangsi section is near Guangyuan City, Sichuan Province (Xiang et al., 2006). This section displays continuous carbonate-dominated marine sedimentation from the Wuchiapingian (Upper Permian) to Lower Triassic (Jiang et al., 2001; Wignall et al., 1995; Lai et al., 2008). The Eastern paleomargin of the Yangtze Platform was embayed by the Nanpanjiang basin. In the Early Triassic, Shanggang section was located south of the Yangtze carbonate platform isolated in the Nanpanjiang Basin (Galfetti et al., 2007, 2008). They are currently located in Guangxi Province (Hautmann et al., 2015). The lower Triassic mixed carbonate-siliciclastic series of the Luolou Formation overlies Late Permian skeletal reef limestone of the Wujiaping Formation.

5 km southeast of Laibin, Guangxi Province, China, the Tieqiao section presents a continuous and thick succession of slope to basinal carbonates that cover the Middle to the Late Permian (Qiu et al., 2014; Shen et al., 2007). Paleo location of this section was at the eastern margin of the Pangea supercontinent in the Jiangnan Basin on the South China block, between the Cathaysian and Yangtze cratons (Wang et al., 2004). This section also had open communication with the ocean, and since it was continuously subsiding, accumulated a thick sediment wedge (Shen et al., 2007). Structurally, these sections are on the slopes of the Laibin Syncline. Permian rocks are extensively exposed along the banks of the Hongshui River, and have not suffered any substantial structural disturbance or metamorphism.

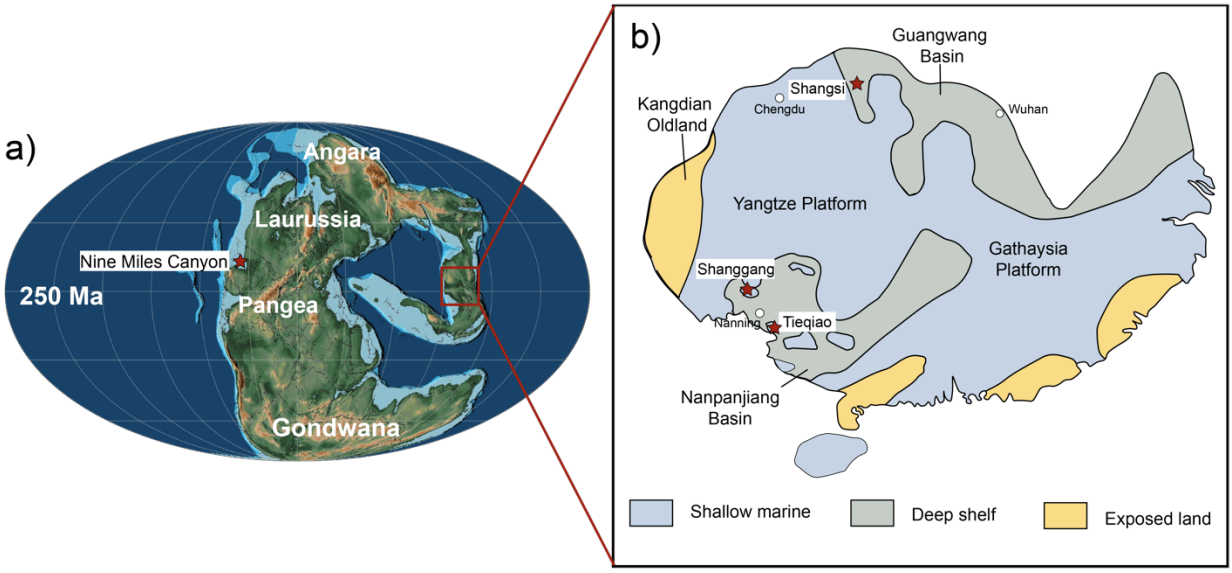

Figure 4.1 Paleogeographic maps of study areas.

a) Paleomap reconfiguration of the Late Permian indicating the position of Nine Miles Canyon and South China. The base map is from Scotese and Wright. (2018). b) Enlarged map of South China showing the study sites, including Shanggang section, Shangsi section, and Tieqiao section. The base map is modified from Wei et al. (2015).

Materials and Methods

The selected samples are from sections with well-constrained biostratigraphic age models (Burgess et al., 2014; Galfetti et al., 2007; Lehrmann et al., 2006; Ovtcharova et al., 2006; Shen et al., 2011, 2007; Stevens, 2008; Sun et al., 2017). Sample preparation and elemental concentration analysis were performed in the Plasma Mass Spectrometry Lab at the University of North Carolina at Chapel Hill. Rock samples were cut using a water-based diamond-bladed saw to produce thin-section billets, then cleaned using ultrapure water (deionized, 18 MΩ) in an ultrasonic bath to remove excess sediment. Fine-grained micritic components were preferentially micro drilled for analysis. Before chemical preparation, samples were analyzed by a Rigaku

Miniflex II X-Ray diffractometer to determine semi-quantitative mineralogy and only samples with >75% calcite were selected for chemical analysis. For each selected sample, about 200mg of powder was leached in a 15ml centrifuge tube following the leaching procedure described in chapter 3. In brief, samples were leached following 10ml of 1M ammonium acetate, 10ml of 1M ammonium carbonate (twice) and 5ml 0.3M acetic acid (twice). Only leachates from acetic acid were collected and evaporated to dryness. After dissolving in 2% nitric acid, a split of the leachates was diluted for 5 times for elemental concentration analysis. Measurements were made using an Agilent™ 7900 quadrupole ICP-MS under UHMI (High Matrix Mode). Precision and accuracy were assessed by repeat analysis of a limestone standard (NIST SRM-1d), which gave a long-term accuracy of <10% for most REY and major elements, with a slightly larger standard deviation for the transitional metals and less concentrated REY (Cao et al., 2020). Four brachiopod samples were micro-drilled, the powders were directly dissolved using 0.4% v/v acetic acid, then analyzed for Li isotopes.

Based on the Li concentration in the leachate, a percentage of leachate calculated to ensure isotope analysis was dried down on hotplate and then treated with a two-step cation exchange chromatography procedure following methods in Liu and Li. (2019). To assess the complete recovery rate of Li, splits of the solution were collected before and after the collected bracket for Li, and were analyzed for Li concentration. Pre and post cuts of the bracket contain <0.1% of Li compared to the Li added into the column. A blank was prepared throughout the leaching, and the column process the same way as preparing the samples. The final measurement of Li content in the blank is lower than 10 ppt. As listed in Table 4.1, part of Li isotope ratios were measured by a Thermo Scientific ™ Neptune Plus MC-ICP-MS in the Department of Earth and Planetary Sciences at Rutgers University. Most analyses were conducted using an Agilent™

7900 Q-ICP-MS at UNC-Chapel Hill using the methods described in Liu and Li. (2019). For a few selected samples, we used both MC-ICP-MS and Q-ICP-MS instruments. We also repeat all chemical prep and analysis for a few samples to confirm the isotope values can be reproduced. The final δ^7Li values were calculated by averaging all measurements for the same sample. Routine runs of the IRMM-016 give reproducibility ≤ 0.6‰ for the MC-ICP-MS measurement (Li et al., 2019) and long-term precision 2SD = ± 1.1‰ for the Q-ICP-MS method (Liu and Li, 2019). Two rock standards JG-2 and NIST-SRM 1d were run along with the sample as the internal standard following (Liu and Li 2019). Li isotope measurements in this study yield δ^7Li of 0.2 ± 0.3‰ (n=4) and 5.1 ± 1.0‰ (n=14) for JG-2 (granite) and NIST-SRM-1d (limestone), respectively, consistent with the published data (Liu and Li, 2019).

A part of leachate solution was separated for Sr analysis and chromatography procedure were carried out in clean laboratory environment. For the Shanggang section, Sr isotopic compositions were measured using a Triton TIMS (Thermal Ionization Mass Spectrometry) at the State Key Laboratory of Isotope Geochemistry, Guanghzou Institute of Geochemistry. $^{87}Sr/^{86}Sr$ was corrected for instrumental mass fractionation by normalizing to $^{88}Sr/^{86}Sr$ = 8.375209. $^{87}Sr/^{86}Sr$ of the Sr reference material NBS-987 and BCR-2 were 0.710235 and 0.704986, respectively. The Sr isotope in the rest of samples were determined using dynamic multicollection with a VG Sector 54 TIMS at the University of North Carolina at Chepel Hill. The laboratory value for the SRM 987 standard is ($^{87}Sr/^{86}Sr$) = 0.710242 ± 0.000010 (one-sigma external reproducibility). For the $^{87}Sr/^{86}Sr$ values the associated uncertainties given are for two-sigma mean internal reproducibility, typically based upon 100 measured ratios. The $^{87}Sr/^{86}Sr$ reported ratios are normalized for instrumental fractionation using a normal Sr ratio of $^{87}Sr/^{88}Sr$ =0.119400.

Results

All δ^7Li values in carbonate rocks from four studied sections and brachiopods are plotted in Fig. 4.2a, and running averages are statistically identified using a locally weighted scatterplot smoothing function (LOWESS). For the Permian to the Early Triassic interval, δ^7Li varies from 16.8‰ to -3.9‰. The highest δ^7Li value occurs in the earliest Permian. This record is marked by three major fluctuations. First, δ^7Li values fall from 12‰ to 6.5‰ in the late Cisuralian between 283 Ma and 265 Ma, followed by a rise to 14‰ from the end of Cisuralian to the middle Guadalupian (~ 265 Ma).Between 265 and 253 Ma, δ^7Li decreases sharply in the late Lopingian and reaches the lowest value at around 253 Ma. The lowest δ^7Li value (-3.9‰) of the whole record occurs in Shangsi section at 253 Ma. Samples from the Shanggang section provide a high-resolution record of the Permian-Triassic boundary, and the lowest value in this section is 0.2‰ near 252 Ma. From 252 Ma to 248 Ma, δ^7Li increases and stays persistently low with an average of 4.5‰.

The $^{87}Sr/^{86}Sr$ values for all samples are illustrated in Fig. 4.2b together with global $^{87}Sr/^{86}Sr$ compiled from fossil records (Korte et al., 2006, 2003; Needham et al., 2006; Song et al., 2015). The $^{87}Sr/^{86}Sr$ curve starts at 0.708335 in the Early Permian, followed by a gradual decrease from the early Sakmarian (~ 295 Ma) and reaches the lowest value of 0.707015 in the end Capitanian (~ 260 Ma). The $^{87}Sr/^{86}Sr$ values show slight variations in the Lopingian (~ 260 - 252 Ma), and rise sharply in the Latest Permian and the Early Triassic, reaching 0.709596 at the end Induan (~ 248 Ma). The $^{87}Sr/^{86}Sr$ values of selected bulk carbonate samples are consistent with the fossil $^{87}Sr/^{86}Sr$ recordx. In the following section, we use a simple box modeling approach to interpret the three major changes in $(\delta^7Li)_{sw,}$ and we propose corresponding conceptual models (Fig. 4.5).

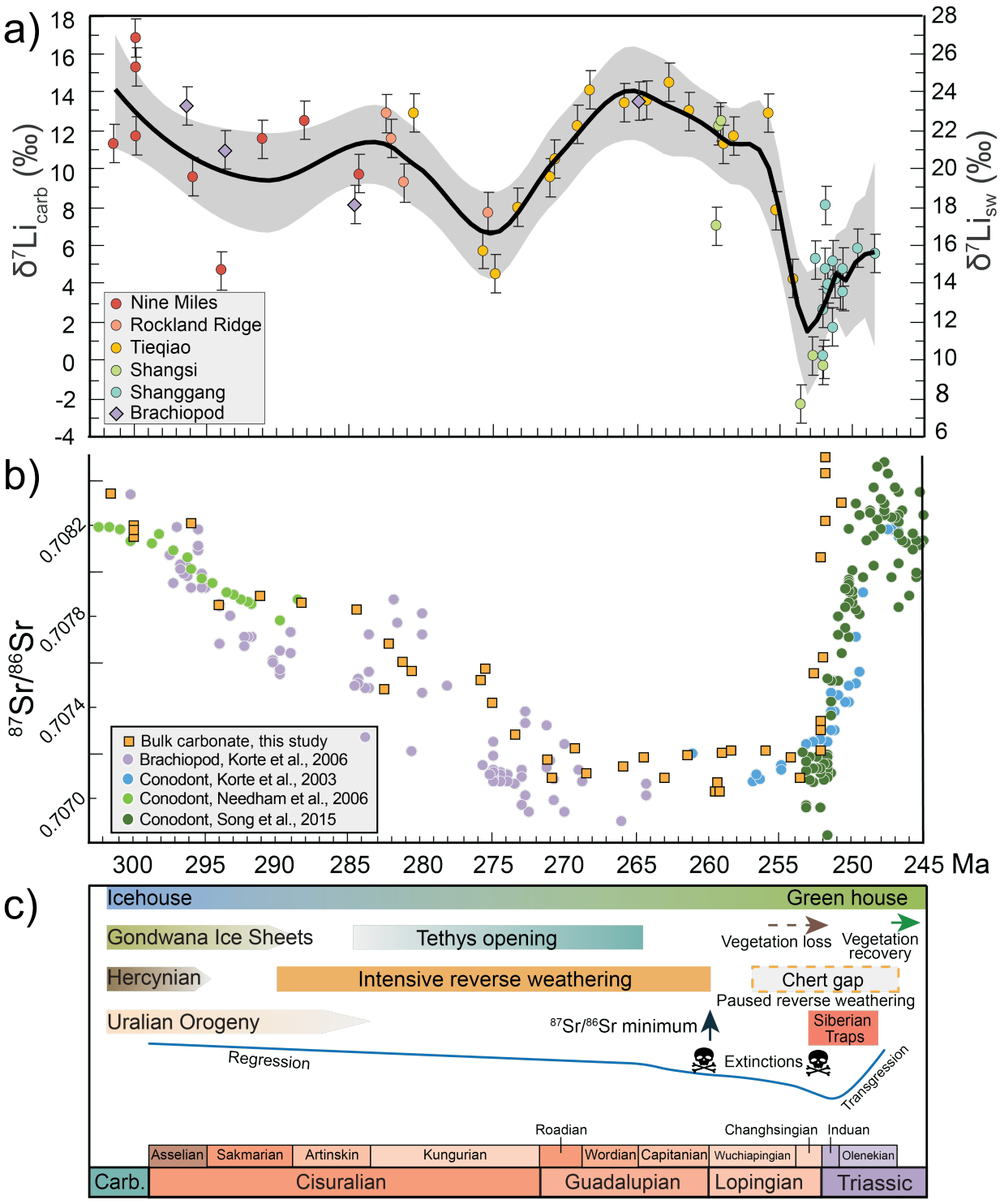
a)
δ7Licarb (‰)
δ7Lisw (‰)
Nine Miles
Rockland Ridge
Tieqiao
Shangsi
Shanggang
Brachiopod
b)
87Sr/86Sr
Bulk carbonate, this study
Brachiopod, Korte et al., 2006
Conodont, Korte et al., 2003
Conodont, Needham et al., 2006
Conodont, Song et al., 2015
300 295 290 285 280 275 270 265 260 255 250 245 Ma
c)
Icehouse
Green house
Gondwana Ice Sheets
Tethys opening
Vegetation loss
Vegetation recovery
Hercynian
Intensive reverse weathering
Chert gap
Paused reverse weathering
Uralian Orogeny
87Sr/86Sr minimum
Siberian Traps
Regression
Extinctions
Transgression
Roadian
Changhsingian
Induan
Asselian
Sakmarian
Artinskin
Kungurian
Wordian
Capitanian
Wuchiapingian
Olenekian
Carb.
Cisuralian
Guadalupian
Lopingian
Triassic

Figure 4.2 Li isotopes, Sr isotopes of bulk carbonates and brachiopods, and compiled geologic events timeline.

a). δ^7Li in bulk carbonate and its corresponding seawater δ^7Li values through time. The shaded area represents 95% confidence bar of the LOWESS smoothing. Vertical bars represent error bars for δ^7Li. b). Compiled $^{87}Sr/^{86}Sr$ in fossil records through time. c). Major events during the Permian and the Early Triassic. The continental ice sheets vanished at the end of the Sakmarian (Hallam, 1985; Korte et al., 2006; Montañez and Poulsen, 2013). Two major mass extinctions, the first at the Guadalupian-Lopingian boundary and the second at the Permian-Triassic boundary (Stanley and Yang, 1994). A few others are added including chert records (Beauchamp and Baud, 2002), vegetation loss and recovery (Looy et al., 1999; Retallack et al., 1996), Tethys opening (Baud et al., 1989; Korte et al., 2005) and transition from icehouse climate to greenhouse climate (Berner, 1991; Brady and Carroll, 1994).

Table 4.1 Li and Sr isotope ratios and other elemental ratios of bulk marine carbonates in this chapter

Sample name	Section	Country	Age Ma	$^{87}Sr/^{86}Sr$ corrected	δ_7Li MC-ICP-MS		δ_7Li Q-ICP-MS		δ_7Li Final	Li ppm	Li/Ca ug/g	Mg/Ca mg/g	Al/Ca mg/g	Fe/Ca mg/g	Mn/Ca mg/g	Sr/Ca mg/g	Rb/Sr mg/g	Mn/Sr mg/g
5466056	Nine Miles	USA	301.38	0.708335	11.2				11.2	0.52	2.30	10	0.02	0.05	0.19	0.95	2.02	0.20
5466135	Nine Miles	USA	299.90	0.708193			16.6	14	15.3	0.51	2.04	9	0.02	0.01	0.10	0.96	0.71	0.11
5466136	Nine Miles	USA	299.87	0.708146	10.7	12.73	11.33		11.6	0.35	1.62	11	0.02	0.46	0.09	1.22	0.42	0.08
5466137	Nine Miles	USA	299.85	0.708177			16.8		16.8	0.14	0.67	11	0.04	0.49	0.12	0.77	0.26	0.17
5153234	Nine Miles	USA	295.88	0.708208	9.5				9.5	0.15	0.71	6	0.05	0.10	0.10	0.67	0.62	0.16
5153277	Nine Miles	USA	293.86	0.707846	4.8		4.5		4.7	0.09	0.39	27	0.04	0.01	0.05	0.54	0.16	0.09
3338	Nine Miles	USA	291.04	0.707885	12.3		10.8		11.5	0.10	0.47	28	0.03	0.00	0.05	0.50	0.71	0.09
5153384	Nine Miles	USA	288.22	0.707853	11.2		13.51		12.4	0.14	0.59	8	0.08	0.01	0.12	0.64	0.39	0.20
5466188	Nine Miles	USA	284.40	0.707820	10.5		8.7		9.6	0.10	0.45	7	0.02	0.02	0.10	0.60	0.47	0.17
3524	Nine Miles	USA	282.35	0.707474			12.9		12.9	0.05	0.30	12	0.08	0.15	0.20	1.38	0.16	0.15
5153534	Rockland Ridge	USA	282.08	0.707673			11.5		11.5	0.04	0.29	15	0.03	0.15	0.21	1.40	0.25	0.15
5466251	Rockland Ridge	USA	281.15	0.707586			9.3		9.3	0.09	0.40	11	0.10	0.01	0.07	5.53	0.06	0.01
5466259	Rockland Ridge	USA	280.54	0.707555	13.7	13.8	14.1	9.7	12.8	0.10	0.70	51	0.02	0.42	0.16	1.75	0.16	0.09
1241670	Tieqiao	China	275.60	0.707511			5.6		5.6	0.12	0.49	9	0.04	0.01	0.59	1.71	0.09	0.36
5466373	Rockland Ridge	USA	275.37	0.707561			7.7		7.7	0.07	0.32	5	0.15	0.01	0.08	0.87	0.33	0.10
1241710	Tieqiao	China	274.88	0.707414			4.4		4.4	0.06	0.25	9	0.03	0.03	0.05	2.79	0.01	0.02
1241790	Tieqiao	China	273.26	0.707274			7.87		7.9	0.09	0.45	42	0.01	0.32	0.08	4.16	0.05	0.02
1241894	Tieqiao	China	271.07	0.707156			9.5		9.5	0.12	0.62	10	0.02	0.26	0.31	1.91	0.41	0.17
1241926	Tieqiao	China	270.67	0.707076			10.42		10.4	0.18	0.87	4	0.03	0.37	0.08	4.93	0.08	0.02
1241960	Tieqiao	China	269.03	0.707205			12.2		12.2	0.06	0.26	4	0.15	0.01	0.18	0.84	0.12	0.22
1242462	Tieqiao	China	265.80	0.707127			11.4	15.6	13.4	0.15	0.58	6	0.04	0.02	0.20	0.76	0.15	0.35
1242478	Tieqiao	China	264.30	0.707166			13.48		13.5	0.04	0.17	3	0.09	0.01	1.19	0.58	0.01	0.28
1242493	Tieqiao	China	262.79	0.707084			14.4		14.4	0.08	0.30	4	0.12	0.01	0.70	0.59	0.04	2.19
1242512	Tieqiao	China	261.24	0.707177			13		13.0	0.14	0.58	4	0.06	0.01	6.34	0.92	0.12	1.22
55005605-5	Shangsi	China	259.38	0.707015			7		7.0	0.04	0.30	6	0.10	0.02	0.13	1.76	0.03	0.35
55006300-5	Shangsi	China	259.19	0.707055			12.2		12.2	0.03	0.21	5	0.19	0.01	0.08	1.22	0.07	0.07
55006900-5	Shangsi	China	259.03	0.707016			12.5		12.5	0.08	0.38	8	0.12	0.01	0.11	2.48	0.06	0.06
2619	Tieqiao	China	258.89	0.707185			11.3		11.3	0.02	0.14	3	0.21	0.01	0.11	0.51	0.08	0.04
2660	Tieqiao	China	258.28	0.707198			11.7		11.7	0.04	0.17	11	0.04	0.07	0.27	0.51	0.19	0.19
2729	Tieqiao	China	255.80	0.707203			12.9		12.9	0.03	0.14	3	0.02	0.07	0.28	0.84	0.09	0.55
2743	Tieqiao	China	255.23				7.8		7.8	0.04	0.30	6	0.12	0.02	0.09	0.85	0.26	0.36
2790	Tieqiao	China	254.03	0.707172			4.2		4.2	0.10	0.33	5	0.07	0.00	0.08	1.39	0.10	0.06
55018585-2	Shangsi	China	253.46	0.707076			-2.98	-1.7	-2.3	0.26	1.32	11	0.04	0.03	0.42	1.97	0.06	0.22
55022169-3	Shangsi	China	252.00	0.707199			0.2		0.2	0.63	2.74	15	0.04	0.48	2.28	1.00	0.70	2.36
55030104-2	Shangsi	China	251.90	0.707335			-0.25		-0.3	0.46	2.62	41	0.02	0.61	2.97	1.96	1.20	1.57
SG-164	Shanggang	China	248.42	0.709224			5.5		5.5	4.39	0.73	7	0.24	1.86	1.23	0.51	0.58	2.43
SG-153a	Shanggang	China	249.58	0.709380			5.8		5.8	18.47	3.45	13	0.48	1.85	0.88	1.13	0.17	0.77
SG-138	Shanggang	China	250.57	0.709403			3.5		3.5	5.64	0.83	9	0.53	7.67	1.57	0.60	0.79	2.64
SG-132	Shanggang	China	250.56	0.708289			4.7		4.7	4.13	0.70	7	0.29	8.84	1.84	0.75	0.26	2.44
SG-111	Shanggang	China	251.10				4.2		4.2	5.98	0.90	9	0.71	2.96	1.43	0.63	0.84	2.26
SG-102	Shanggang	China	251.24	0.709596			1.7		1.7	9.86	8.93	314	0.33	2.37	1.82	0.83	0.32	2.20
SG-92	Shanggang	China	251.31	0.708670			5.1		5.1	5.79	1.13	15	0.06	3.26	1.51	0.89	0.13	1.71
SG-50	Shanggang	China	251.50	0.708688			3.9		3.9	15.29	3.59	81	0.39	13.40	1.79	0.91	0.46	1.96
SG-25	Shanggang	China	251.62	0.708499			3.7		3.7	4.71	1.46	43	1.53	18.76	2.44	1.34	0.81	1.82
SG-16	Shanggang	China	251.68	0.708421			3.9		3.9	7.51	4.03	349	2.05	28.95	3.61	2.07	0.75	1.74

SG-13+0.45	Shanggang	China	251.72	0.708214	4.7	4.7	5.41	2.51	272	0.27	0.96	1.87	0.74	0.38	0.96
SG-12+5.6	Shanggang	China	251.75	0.707611	8	8	2.81	0.35	6	0.02	0.28	0.68	0.71	0.24	1.13
SG-10-0.1	Shanggang	China	251.95	0.708056	0.2	0.2	1.23	0.70	304	0.19	0.17	0.22	0.99	0.07	0.22
SG-10+2.1	Shanggang	China	252.03	0.707294	2.6	2.6	1.09	0.14	5	0.33	0.53	0.38	1.14	0.15	0.34
SG-9+3.4	Shanggang	China	252.53	0.707537	5.2	5.2	0.38	0.09	8	0.29	0.29	0.07	1.32	0.12	0.06

Discussion

5.1 Data evaluation

5.1.1 Evaluation of diagenesis

δ^7Li and Li/Ca, Mg/Ca, Al/Ca, Sr/Ca, Fe/Ca, Mn/Ca, Mn/Sr and Rb/Sr ratios of the carbonates are reported in Tables 4.1. The relationships between δ^7Li and these elemental ratios are examined to ensure the fidelity of these isotope values (Fig. 4.3). All samples except for one have Li/Ca ratios between 0-5 μg/g, and the majority of samples have Sr/Ca ratios lower than 4 mg/g, indicating these carbonates are not completely sediment-buffered (Dellinger et al., 2020). Dolomite usually has higher Li/(Ca+Mg) ratios (15-20 μmol/mol) (Dellinger et al., 2018). No correlation is found between δ^7Li and Li/Ca, indicating no contamination from clay fraction and sediment buffering. Low Mg/Ca ratios support that our selected samples are dominated by calcite with no or little dolomite. Four early Triassic samples have higher Mg/Ca (300-400 mg/g) suggesting these four samples may be high Mg calcite, or they may contain minor amounts of dolomite. Compared to low Mg calcite, high Mg calcite has relatively higher Li/Ca and slightly larger offset of δ^7Li from seawater (Dellinger et al., 2018). Four samples with higher Mg/Ca ratios also have higher Li/Ca (Table 4.1). However, they do not show significantly lower δ^7Li compared to samples with low Mg/Ca. Besides, the lowest δ^7Li values in our record are measured in calcite. However, these high Mg/Ca samples can explain small variations in δ^7Li among early Triassic samples.

5.1.2 Evaluation of potential contamination from non-carbonate phases

Mn/Sr of all the samples is lower than 3, and Rb/Sr lower than 0.001, together are the thresholds for limestone to record primary seawater geochemistry signals like carbon isotopes and Sr isotopes (Kaufman et al., 1993). Al/Ca ratios (<1mg/g) are also low except for two samples, suggesting that no Li is introduced from the silicate fraction (Pogge Von Strandmann et al., 2013).

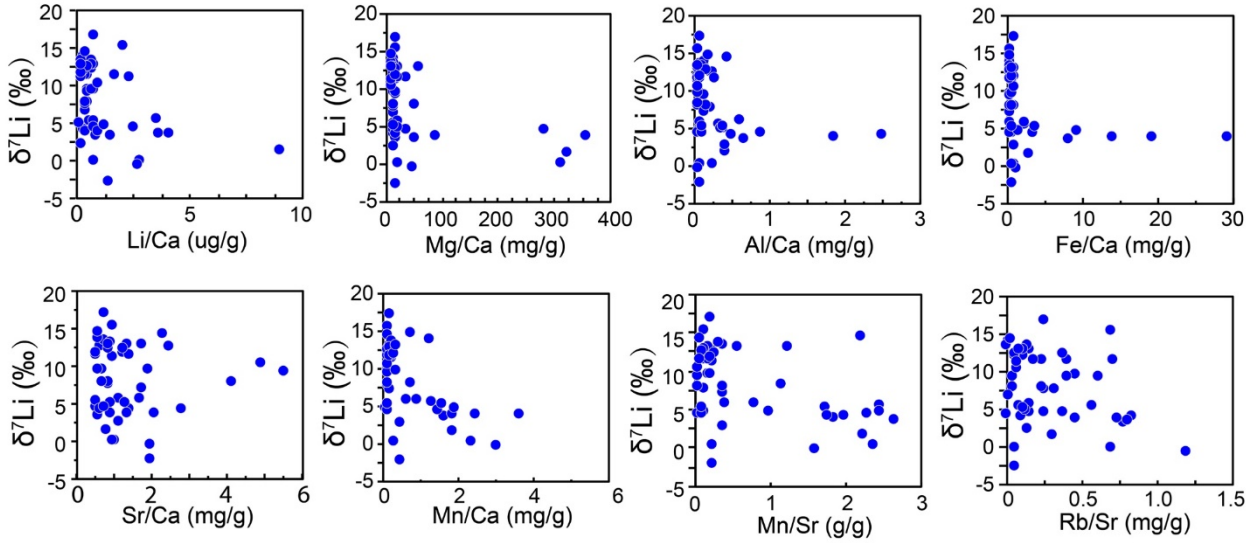

Figure 4.3 A comparison of δ^7Li with major and trace-element alteration proxies for sequentially leached samples.

5.2 Reconstructing seawater δ^7Li values

We determine the fractionation factor of Li isotopes between bulk carbonates and seawater comparing laboratory experiments and natural observations of carbonate materials and modern seawater. Carbonate precipitation experiments have determined that δ^7Li in calcite is 3‰ lower compared to its surrounding fluids (Marriott et al., 2004a). By contrast, modern biogenic calcite carbonates show large variations of δ^7Li in different species, including planktic foraminifera (higher than 26‰) (Hathorne and James, 2006; Misra and Froelich, 2009);

brachiopods (24.7-27.8‰) (Dellinger et al., 2018); and benthic foraminifera (21.1 to 25.0‰) (Marriott et al., 2004b). An examination of bulk core top sediments that only contain calcite has a constant offset from seawater of $\Delta_{sw\text{-}carb} = 6.1 \pm 1.3$‰, and minor amounts of aragonite in bulk carbonates leads to an additional offset of 0.6‰ (Pogge von Strandmann et al., 2019). The average δ^7Li value of meteorically altered low-Mg calcite is 22.0 ± 3.8‰ ($n = 28$, 1σ) which is similar to the original aragonite-rich sediments (22.0 ± 1‰) (Dellinger et al., 2020). Overall, the fractionation between marine calcite carbonates and modern seawater (31‰) be estimated to be 10‰ because the lowest benthic foraminifera δ^7Li is 21.1‰ and the lowest low-Mg calcite δ^7Li is 18.2‰. In this study, the samples are screened by XRD to only select samples with 75% calcite, therefore the samples are assumed to have a consistent offset from the seawater with $\Delta_{sw\text{-}carb} = 10\%$.

The baseline value for $(\delta^7Li)_{sw}$ in the earliest Permian (~301Ma) is about 24‰ assuming the fractionation between seawater and carbonate rock 10‰. To reconstruct a box model for $(\delta^7Li)_{sw}$ at this time, firstly we assume the Li output flux and F_{MOR} are similar to the estimated values in the modern ocean. Secondly, the δ^7Li_{MOR} remains 8‰, and Δ_{alt} (Li isotope fractionation during basalt alteration) remains 13‰ (Li and West, 2014; Misra and Froelich, 2012) (Fig. 4.4a, b). A lower $(\delta^7Li)_{sw}$ in the earliest Permian would result from either deviation in δ^7Li_{riv} or Δ_{sed} (Li isotope fractionation during authigenic clay formation) compared to the modern ocean. Using the Δ_{sed} of 20‰ suggested by Li and West (2014), it would require the δ^7Li_{riv} to be 8‰ (Fig. 4.4a). Assuming that the authigenic clay sediments in the ocean have a δ^7Li of 10‰ (Li and West, 2014), then Δ_{sed} could be lowered to 14‰. If the model adopts 15‰ for Δ_{sed}, it calculates 12‰ for δ^7Li_{riv} (Fig. 4.4b). Both scenarios are possible depending on the continental weathering congruency. On one hand, the Uralian Orogeny would expose fresh silicates at high rates to

maintain congruent silicate weathering. On the other hand, higher δ^7Li_{riv} (12‰) can exist in large alluvial systems where silicate weathering is less congruent. However, it is also possible to contribute the lower $(\delta^7Li)_{sw}$ in the earlierst Permian compared to modern ocean due to changes in the isotope fractionations associated with the Li output. For example, if Δ_{alt} is lowered from 13‰ to 8‰, it would raise the δ^7Li_{riv} to 16‰ (Fig. 4.4c). This scenario would require continental weathering to be less congruent compared to scenario a and b. At this point, it is difficult to rule out all these above possibilities.

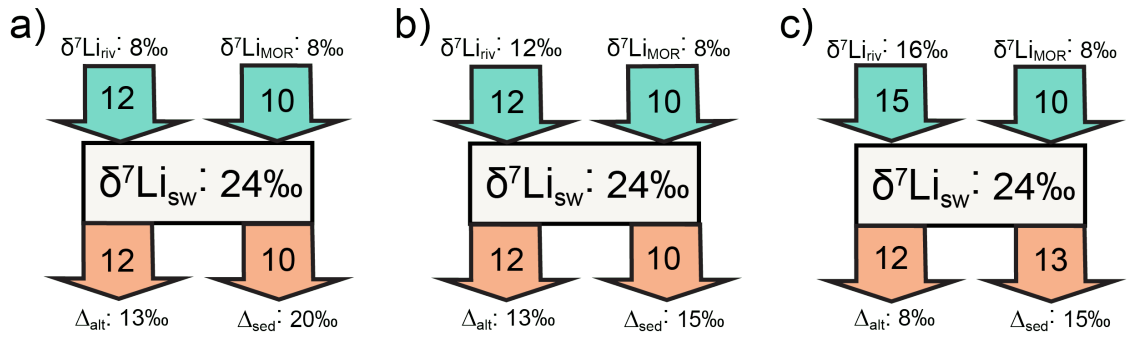

Figure 4.4 Steady state box model of Li cycle when $(\delta^7Li)_{sw}$ = 24‰ in the earliest Permian. Senario a). Lower $(\delta^7Li)_{sw}$ compared to modern ocean (31‰) is mainly caused by a lower δ^7Li_{riv}. F_{MOR}, δ^7Li_{MOR}, Δ_{alt}, and Δ_{sed} remain the same values used in the modern ocean Li box model. Scenario b). A shift in δ^7Li_{riv} and Δ_{sed} drives the changes to the $(\delta^7Li)_{sw}$. Scenario c). Shifts in δ^7Li_{riv}, Δ_{alt}, and Δ_{sed} drive the changes to the $(\delta^7Li)_{sw}$.

5.3. Tethys opening in the mid-Permian

In the early Cisuralian, $(\delta^7Li)_{sw}$ shows small changes before the Tethys opening. Then a negative excursion in $(\delta^7Li)_{sw}$ (284 Ma to 263 Ma) corresponds to the Tethys opening. During this time interval, $(^{87}Sr/^{86}Sr)_{sw}$ shows a continuous decrease and two hypotheses have been proposed. The first hypothesis argues that a decrease in radiogenic Sr flux due to Pangea aridity

and the end of the Hercynian Orogeny is responsible for the observed $(^{87}Sr/^{86}Sr)_{sw}$ (Martin and Macdougall, 1995). Evidence of arid conditions includes the deposition of massive evaporites and red beds in the Middle and Late Permian (Gordon et al., 1975). Overall, the tectonic configuration might have led to a significant decrease in continental runoff and chemical weathering rate (Martin and Macdougall, 1995; Montañez and Poulsen, 2013; Tabor and Montanez, 2002; Veizer et al., 1999). The second hypothesis is that the Tethys opening inputs more unradiogenic Sr into the ocean. The opening of the Tethys Ocean started with the break-up of the Cimmerian microcontinent from Gondwana and progressed westward throughout the Permian (Stampfli and Borel, 2002). This opening might have coincided with higher seafloor spreading rates and faster alteration of mid-oceanic ridge basalts (Korte et al., 2006). However, the responses of $(\delta^7Li)_{sw}$ to these climatic and tectonic events are decoupled from $(^{87}Sr/^{86}Sr)_{sw}$.

We propose that the negative excursion of $(\delta^7Li)_{sw}$ can be best explained by the Tethys opening in the late Ciscuralian and the early Guadalupian other than reduced continental chemical weathering. To test this hypothesis, we constructed a Li box model with $(\delta^7Li)_{sw}$ = 15‰, which occurs near the Ciscuralian-Guadalupian boundary (Fig. 4.4b). Reducing the F_{riv} to 6.5 Gmol/yr and increasing F_{MOR} to 16 Gmol/yr could explain the observed fall in $(\delta^7Li)_{sw}$ at ~275 Ma. Meanwhile, Li output via basalt alteration (F_{alt}) and Li removal via authigenic clay formation (F_{sed}) are similar to values in the modern ocean, and they are 12.5 Gmol/yr and 10 Gmol/yr, respectively. However, Δ_{alt} and Δ_{sed} would have to be as low as 5‰ and 15‰, respectively. Moreover, this model requires the δ^7Li_{riv} to be 3‰, similar to the lowest values observed in modern rivers (Dellinger et al., 2015), suggesting congruent chemical weathering of the supercontinent in the Mid Permian. Although we assume a steady-state for the Li box model, the input and output fluxes to the ocean may not be balanced. In addition, the F_{MOR} is assumed to

be proportional to the spreading rate of the mid-ocean ridges, and so is the F_{alt} (Li and West, 2014). It is reasonable to assume higher F_{alt} when F_{MOR} increases. As for F_{sed}, it could have been higher than the present-day level since the reverse weathering was suggested to be intensive (Beauchamp and Baud, 2002). However, it is difficult to quantify the reverse weathering flux at that time compared to the present-day.

5.4 Paused reverse weathering during Late Permian

Over the Permian, $(^{87}Sr/^{86}Sr)_{sw}$ exhibits the largest decline in the Phanerozoic Eon and reaches the lowest value in the Capitanian (260 Ma), followed by a minor increase in the Lopingian (259 – 252 Ma) (Korte et al., 2006, 2003; Needham et al., 2006). Compared to $(^{87}Sr/^{86}Sr)_{sw}$, the drawdown of $(\delta^7Li)_{sw}$ took place mostly after the $(^{87}Sr/^{86}Sr)_{sw}$ minimum with a sharp decline in $(\delta^7Li)_{sw}$ of 12‰ in the late Guadalupian and the Lopingian (265 Ma to 253 Ma). Besides the Tethys opening, the long term $(^{87}Sr/^{86}Sr)_{sw}$ trend can be explained by reduced Sr flux from chemical weathering of radiogenic continental surfaces due to the Pangea aridity (Korte et al., 2006, 2003; Martin and Macdougall, 1995). The slight increase in $(^{87}Sr/^{86}Sr)_{sw}$ in the Lopingian coincided with the termination of Palaeotethys volcanism and can be explained by reduced radiogenic Sr from the hydrothermal input (Korte et al., 2006). For the $(\delta^7Li)_{sw}$, the box model is reconstructed for the minimum value of the smoothed $(\delta^7Li)_{sw}$, 10‰, the F_{MOR}, δ^7Li_{MOR}, and F_{alt} are assumed to be the same as modern values (Fig. 4.4c). Measured Δ_{alt} ranges from 8 to 23‰ (Chan et al., 2002, 1992; Seyfried et al., 1984), and 13‰ of Δ_{alt} was used in Li and West. (2014), despite the large uncertainties in this estimate. But we assume 5‰ for Δ_{alt} despite that 5‰ for Δ_{alt} is lower than the current observed value, increasing this value will force the δ^7Li_{riv} to be extremely low to satisfy the steady-state in the box model. A sensitivity test of the Li box model identifies three main factors that control the $(\delta^7Li)_{sw}$, including Li output flux

through authigenic clay formation during reverse weathering, Li flux and isotope composition of continental runoff (Appendix 4.1).

We first test if the steep decline in $(\delta^7Li)_{sw}$ was caused by a reduced continental chemical weathering rate due to the Pangea aridity. Unlike $(^{87}Sr/^{86}Sr)_{sw,}$ which decreased since the Early Permian, $(\delta^7Li)_{sw}$ drawdown occurred after the Tethys opening. If the reduced Li flux is the controlling factor for the 12‰ decline in $(\delta^7Li)_{sw}$. For the $(\delta^7Li)_{sw}$ minimum at the stead state, because the output itself would drive the $(\delta^7Li)_{sw}$ up to 10‰, therefore a very negative δ^7Li_{riv} value is required to balance the 8‰ of δ^7Li_{MOR}. However, such low δ^7Li in the continental weathering would require a large source for low δ^7Li, for example, the redissolution of clay minerals.

Sun et al. (2018) has proposed that the extreme light $(\delta^7Li)_{sw}$ in the end Permian was lead by rapid congruent weathering of Siberian basalts, generating an enhanced riverine Li flux with extremely light δ^7Li. However, the earliest age for the onset of the Siberian volcanism was estimated to be at 255.58 ± 0.38 Ma (Burgess and Bowring, 2015) and 253.7 ± 1.2 Ma (Reichow et al., 2002). Based on Ar-Ar age, the bulk of Siberian volcanism took place at ~250 Ma during a period of less than 2 million years (Reichow et al., 2009).This means the decrease in $(\delta^7Li)_{sw}$ values precedes the major eruption of Siberian volcanism by several million years. Consequently, the decrease in $(\delta^7Li)_{sw}$ values cannot be associated with congruent weathering of fresh basalts.The atmospheric CO_2 levels may have been high in the Late Permian (Berner 2006), which could enhance chemical weathering. However, both Li flux and the δ^7Li of the continental runoff should be low because continental aridity persisted into the Late Permian. Also, there was no large fluvial plain to develop high δ^7Li due to the lack of orogenies (Pogge von Strandmann et al., 2017). δ^7Li_{riv} and F_{riv} are calculated to be 2‰ and 4 Gmol/yr, respectively. δ^7Li of the

juvenile continental crust are 3.6‰, and terrigenous sediments, 3‰ (Penniston-Dorland et al., 2017; Tomascak et al., 2016). As a result of weathering, modern δ^7Li_{riv} varies from 3 to 41‰ (Penniston-Dorland et al., 2017; Tomascak et al., 2016). For δ^7Li_{riv} to reach 2‰, other sources of light Li are needed besides primary mineral dissolution. Re-weathering of thick soil or shale may be responsible. For example, minimal values (δ^7Li = 6-10‰) found in the peak of Oceanic Anoxic Event 2 (Cenozoic) were interpreted as the destabilization of continental secondary minerals, also causing addition of isotopically light Li (Pogge Von Strandmann et al., 2013). This is referred to as the "supply limited" weathering regime where the supply of primary mineral is limited by erosion rate (West et al., 2005; West, 2012).

Here we propose that the steep drawdown of $(\delta^7Li)_{sw}$ during the Lopingian is closely linked to a pause in authigenic clay formation during reverse weathering. Starting at the Sakmarina-Artinskin boundary (~290 Ma), intensive reverse weathering deposited massive chert in the Canadian Arctic and Northwest USA. This Permian Chert Event terminated abruptly at the Late Permian, followed by a chert gap in the Early Triassic (Beauchamp and Baud, 2002). The reverse weathering paused for about 8 to 10 million years, and it was not until the Early to Middle Triassic (Anisian) when chert deposition resumed in the distal oceanic areas (Beauchamp and Baud, 2002). After the Tethys opening, the $(\delta^7Li)_{sw}$ slightly lowers down in the Guadalupian, and this time period overlaps with the Permian Chert Event (Fig. 4.1). Then the $(\delta^7Li)_{sw}$ decreases steeply in the Lopingian, consistent with the duration of the chert gap. The availability of biogenic silica or lithogenic (Al, Fe) debris is limiting factors for the formation of aluminosilicate phase (Aller, 2014). Therefore, the authigenic clay formation could have been limited during the chert gap. This could explain the difference we observed in the extent of $(\delta^7Li)_{sw}$ decrease during the Guadalupian and the Lopingian because the Δ_{sed} (15 - 20‰) has

controlling effect on the $(\delta^7Li)_{sw}$. Higher F_{sed} would increase $(\delta^7Li)_{sw}$. By contrast, when F_{sed} is low, $(\delta^7Li)_{sw}$ will decrease. Besides, Phanerozoic sedimentation records suggest that the area of marine sedimentation falls in the Late Permian-Middle Triassic (Husson and Peters, 2018; Ronov et al., 1980). In sum, the collapsed reverse weathering, authigenic clay formation particularly, reduced weathering rate, and high weathering congruency together brought down the $(\delta^7Li)_{sw}$ in the Late Permian.

5.5. Enhanced congruent weathering of the Siberian Traps in the Early Triassic

In the Early Triassic, $(\delta^7Li)_{sw}$ quickly rised up to 14.5‰ in five million years after reaching the extremely low values (6.1‰ to 10.2‰) in the latest Permian. A sharp rise was also recorded in $(^{87}Sr/^{86}Sr)_{sw}$. Two reasons for the $(^{87}Sr/^{86}Sr)_{sw}$ apex include enhanced continental weathering rate and/or increased $^{87}Sr/^{86}Sr$ in the river (Korte et al., 2003; Martin and Macdougall, 1995; Song et al., 2015). The latter one is less possible because there was no large new orogeny at this time except that some studies argue that extreme weathering of the root of Hercycian oregony could be a possible source for ^{87}Sr (Korte et al., 2003; Martin and Macdougall, 1995). A greater leached paleosol record of the earliest Triassic compared to the latest Permian also point to an enhanced chemical weathering (Sheldon, 2006). We propose that the increased $(\delta^7Li)_{sw}$ in the Early Triassic was caused by enhanced chemical weathering rate.

Large areas were exposed in the Late Permian due to a sharp sea-level drop (Yin et al., 2014). In turn, pronounced transgression started in the latest Permian, and many areas of the Tethys and North America were flooded by the Early Triassic (Korte et al., 2003). However, the equatorial inner Pangea was still arid, while only the eastern edge of the supercontinent was influenced by monsoonal rains (Kutzbach and Gallimore, 1989). As discussed earlier, the onset of the Siberian volcanism marks the turning point of $(\delta^7Li)_{sw}$. Combined exposure areas of

basaltic flows, volcaniclastic rocks, and intrusive rocks on the Siberian Platform is about 2.6×10^6 km^2. Volumes of flood basalts are calculated to be on the order of 10^6 km^3 and release ~10^{17} to 10^{19} mol CO_2 (Reichow et al., 2002). The density of basalt varies from 2.8 to 3.0 t/m^3. Assuming a Li concentration of 5 ppm in Siberian basalts, 2×10^{21} mol of total Li is stored in the Siberian Traps. The fresh basalts which can be weathered quickly, lifted CO_2 level in the atmosphere, and acid rains produced by the volcanism provide conditions for a rapid congruent weathering. Another important factor for enhanced chemical weathering rate is the land vegetation loss started in the latest Permian and deteriorated in the Early Triassic, and the vegatation recovery was not until the lower Anisian (Looy et al., 1999; Retallack, 2005). This vegetation loss also caused pronounced erosion and clastic deposits (Algeo and Twitchett, 2010; Newell et al., 1999; Retallack, 2005).

Our box model supports that the rise of $(\delta^7Li)_{sw}$ in the Early Triassic was likely caused by increasing chemical weathering rate (Fig. 4.4d). One representative scenario for Li isotope cycle suggest that F_{riv} increased to 16 Gmol/yr compared to the value in the Late Permian (4 Gmol/yr). If we attribute the increased F_{riv} to the weathering of Siberian Traps, making a Li weathering rate of 12×10^{15} mol/myr, which means less than 0.001% of the basalt was weathered in a million years assuming all Li was delivered into the river.

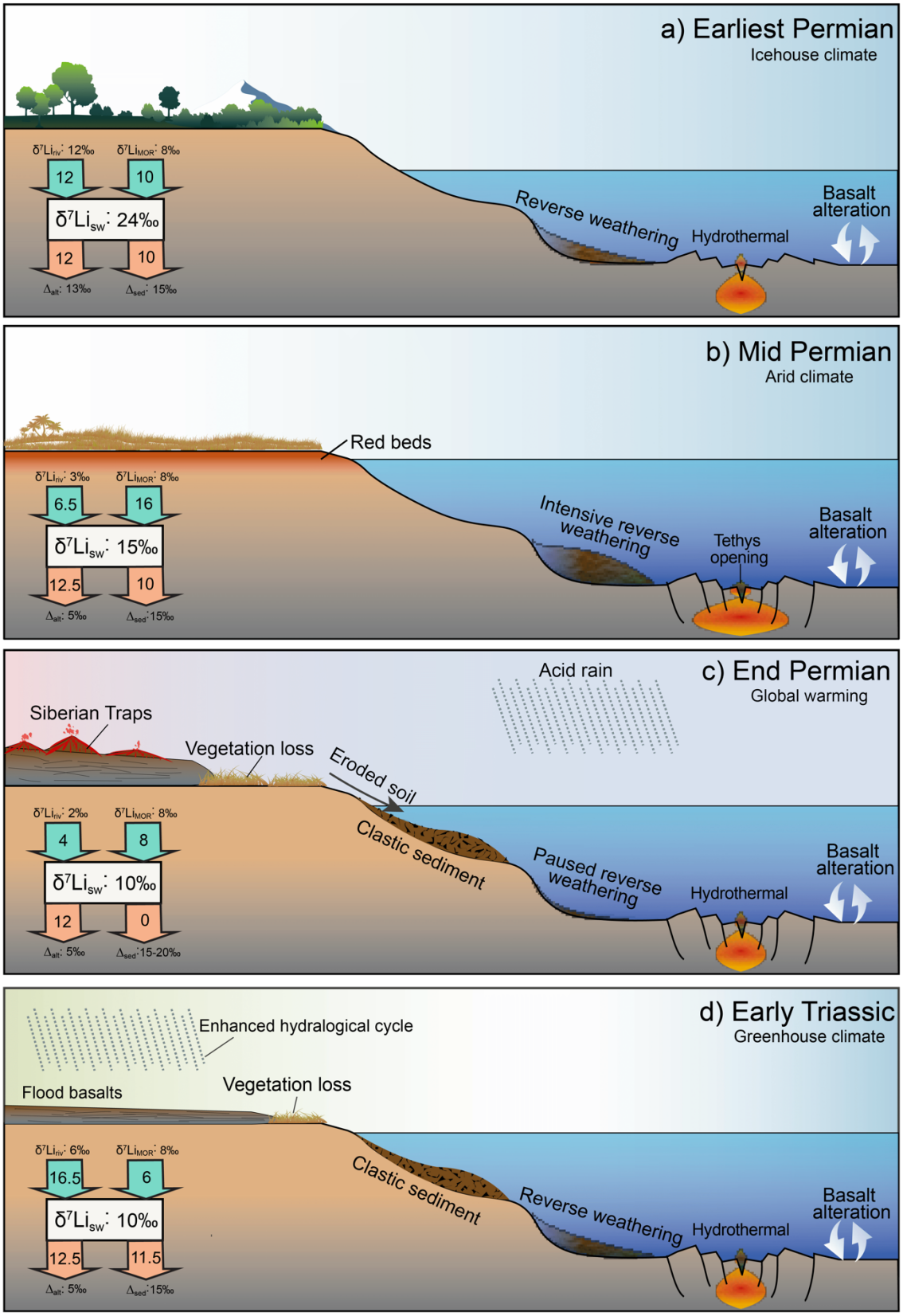
a) Earliest Permian
Icehouse climate
δ7Liriv: 12‰
δ7LiMOR: 8‰
12
10
δ7Lisw: 24‰
12
10
Δalt: 13‰
Δsed: 15‰
Reverse weathering
Hydrothermal
Basalt alteration
b) Mid Permian
Arid climate
Red beds
δ7Liriv: 3‰
δ7LiMOR: 8‰
6.5
16
δ7Lisw: 15‰
12.5
10
Δalt: 5‰
Δsed:15‰
Intensive reverse weathering
Tethys opening
Basalt alteration
c) End Permian
Global warming
Acid rain
Siberian Traps
Vegetation loss
Eroded soil
Clastic sediment
δ7Liriv: 2‰
δ7LiMOR: 8‰
4
8
δ7Lisw: 10‰
12
0
Δalt: 5‰
Δsed:15-20‰
Paused reverse weathering
Hydrothermal
Basalt alteration
d) Early Triassic
Greenhouse climate
Enhanced hydralogical cycle
Flood basalts
Vegetation loss
δ7Liriv: 6‰
δ7LiMOR: 8‰
16.5
6
δ7Lisw: 10‰
12.5
11.5
Δalt: 5‰
Δsed:15‰
Clastic sediment
Reverse weathering
Hydrothermal
Basalt alteration

Figure 4.5 Conceptual reconstruction of terrestrial-marine ecosystem during four critical time periods when large δ^7Li fluctuations occurred.

We also show their representative Li box models. a). Earliest Permian refers to the Carboniferous-Permian boundary, and it is characterized by the late Paleozoic glaciation. b). Mid Permian refers to the late Cisuralian and the early Guadalupian (275 to 273 Ma). Mid Permian is marked by large aridity, the Tethys opening and intensive reverse weathering. c). Latest Permian (253 to 250 Ma) corresponds to the largest δ^7Li drawdown. The early stage of this drop coincides with paused reverse weathering and vegetation loss that are supported by increased clastic sedimentation on the seafloor. d). The end of the δ^7Li drop overlaps with initiations of the Siberian Traps. Vegetation loss continues in the Early Triassic (250 to 247 Ma). Greenhouse climate and enhanced hydrological cycle both favor rapid congruent weathering of flood basalts.

Conclusions

The $(\delta^7Li)_{sw}$ in the Permian to the Early Triassic is marked with large fluctuations over 20‰ and decoupled from $(^{87}Sr/^{86}Sr)_{sw}$. The negative excursion of $(\delta^7Li)_{sw}$ in the late Ciscuralian and the early Guadalupian (283 - 265 Ma) is associated with the Tethys opening. Our box model calculated the Li flux from hydrothermal activities may have doubled during the Tethys opening. The intensive reverse weathering from the Artinskin to the Capitanian (265 – 260 Ma) sustained $(\delta^7Li)_{sw}$ at ~ 24‰. Following the Middle Permian aridity and the paused reverse weathering, $(\delta^7Li)_{sw}$ declined to less than 10‰ near the Permian-Triassic boundary (~ 252Ma). Then it rised to 15‰ in the Early Triassic, likely reflecting enhanced chemical weathering rates caused by the warm climate, the easily-weathered materials from the Siberian Traps and the lack of protection from land plants. The Li flux from the continental weathering in the Early Triassic is estimated to be about four times of its value in the Late Permian. However, the δ^7Li in the continental runoff was probably still low because the equatorial central Pangea was still arid at this time and the fluvial plains that are needed to develop high δ^7Li in the river are missing. Therefore, reconstructing $(\delta^7Li)_{sw}$ in bulk carbonate rocks provides critical information to understand not only secular changes in continental weathering, but also other aspects of the global Li isotope cycle, including changes in hydrothermal activities and reverse weathering.

REFERENCES

Algeo, T.J., Twitchett, R.J., 2010. Anomalous early Triassic sediment fluxes due to elevated weathering rates and their biological consequences. Geology 38, 1023–1026. https://doi.org/10.1130/G31203.1

Aller, R.C., 2014. Sedimentary Diagenesis, Depositional Environments, and Benthic Fluxes, 2nd ed, Treatise on Geochemistry: Second Edition. Elsevier Ltd. https://doi.org/10.1016/B978-0-08-095975-7.00611-2

Alroy, J., Aberhan, M., Bottjer, D., Foote, M., Fursich, F., Harries, P., Hendy, A., Holland, S., Ivany, L., Kiessling, W., Kosnik, M., Marshall, C., McGowan, A., Miller, A., Olszewski, T., Patzkowsky, M., Peters, S., Villier, L., Wagner, P., Bonuso, N., Borkow, P., Brenneis, B., Clapham, M., Fall, L., Ferguson, C., Hanson, V., Krug, A., Layou, K., Leckey, E., Nürnberg, S., Powers, C., Sessa, J., Simpson, C., Tomasovych, A., Visaggi, C., 2008. Phanerozoic trends in the global diversity of marine invertebrates. Science (80-.). 321, 97–100. https://doi.org/10.1126/science.1156963

Bataille, C.P., Willis, A., Yang, X., Liu, X., 2017. Continental igneous rock composition : A major control of past global chemical weathering continental crust to seawater and exerts a direct control on several bio- surfaces have been invoked to explain some more specific features in screened database gath. Sci. Adv. 1–16. https://doi.org/e1602183

Baud, A., Magaritz, M., Holser, W.T., 1989. Permian-Triassic of the Tethys: Carbon isotope studies. Geol. Rundschau 78, 649–677. https://doi.org/10.1007/BF01776196

Beauchamp, B., Baud, A., 2002. Growth and demise of Permian biogenic chert along northwest Pangea: Evidence for end-Permian collapse of thermohaline circulation. Palaeogeogr. Palaeoclimatol. Palaeoecol. 184, 37–63. https://doi.org/10.1016/S0031-0182(02)00245-6

Bekker, A., Holland, H.D., Wang, P.-L., Rumble, I.D., Stein, H.J., Hannah, J.L., Coetzee, L.L., Beukes, N.J., 2004. Dating the rise of atmospheric oxygen. Nature 427, 117–120. https://doi.org/10.1111/gbi.12228

Berner, R.A., 1991. A model for atmospheric CO2 over Phanerozoic time. Am. J. Sci. 291, 339–376. https://doi.org/10.2475/ajs.291.4.339

Brady, P. V., Carroll, S.A., 1994. Direct effects of CO2 and temperature on silicate weathering: Possible implications for climate control. Geochim. Cosmochim. Acta 58, 1853–1856. https://doi.org/10.1016/0016-7037(94)90543-6

Burgess, S.D., Bowring, S., Shen, S., 2014. High-precision timeline for Earth's most severe extinction. Proc. Natl. Acad. Sci. U. S. A. 111, 5060. https://doi.org/10.1073/pnas.1404196111

Burgess, S.D., Bowring, S.A., 2015. High-precision geochronology confirms voluminous

magmatism before, during, and after Earth's most severe extinction. Sci. Adv. 1, 1–14. https://doi.org/10.1126/sciadv.1500470

Chan, L.H., Edmond, J.M., Thompson, G., Gillis, K., 1992. Lithium isotopic composition of submarine basalts: implications for the lithium cycle in the oceans. Earth Planet. Sci. Lett. 108, 151–160. https://doi.org/10.1016/0012-821X(92)90067-6

Coogan, L.A., Dosso, S.E., 2015. Alteration of ocean crust provides a strong temperature dependent feedback on the geological carbon cycle and is a primary driver of the Sr-isotopic composition of seawater. Earth Planet. Sci. Lett. 415, 38–46. https://doi.org/10.1016/j.epsl.2015.01.027

Dellinger, M., Bouchez, J., Gaillardet, J., Faure, L., Moureau, J., 2017. Tracing weathering regimes using the lithium isotope composition of detrital sediments. Geology 45, G38671.1. https://doi.org/10.1130/G38671.1

Dellinger, M., Gaillardet, J., Bouchez, J., Calmels, D., Louvat, P., Dosseto, A., Gorge, C., Alanoca, L., Maurice, L., 2015. Riverine Li isotope fractionation in the Amazon River basin controlled by the weathering regimes. Geochim. Cosmochim. Acta 164, 71–93. https://doi.org/10.1016/j.gca.2015.04.042

Dellinger, M., Hardisty, D.S., Planavsky, N.J., Gill, B.C., Kalderon-asael, B., Asael, D.A.N., Croissant, T., Swart, P.K., West, A.J., 2020. The effects of diagenesis on lithium isotope ratios of shallow marine carbonates. Am. J. Sci. 320, 000–000. https://doi.org/10.2475/10.2475/

Dellinger, M., Joshua West, A., Paris, G., Adkins, J.F., Pogge von Strandmann, P., Ullmann, C. V., Eagle, R.A., Freitas, P., Bagard, M.-L., Ries, J.B., Corsetti, F.A., Perez-Huerta, A., Kampf, A.R., 2018. The Li isotope composition of marine biogenic carbonates: Patterns and Mechanisms. Geochim. Cosmochim. Acta. https://doi.org/10.1016/j.gca.2018.03.014

Dudás, F., Yuan, D.X., Shen, S.Z., Bowring, S.A., 2017. A conodont-based revision of the 87Sr/86Sr seawater curve across the Permian-Triassic boundary. Palaeogeogr. Palaeoclimatol. Palaeoecol. 470, 40–53. https://doi.org/10.1016/j.palaeo.2017.01.007

Fluteau, F., Besse, J., Broutin, J., Ramstein, G., 2001. The late Permian climate. What can be inferred from climate modelling concerning Pangea scenarios and Hercynian range altitude? Palaeogeogr. Palaeoclimatol. Palaeoecol. 167, 39–71. https://doi.org/10.1016/S0031-0182(00)00230-3

Galfetti, T., Bucher, H., Brayard, A., Hochuli, P.A., Weissert, H., Guodun, K., Atudorei, V., Guex, J., 2007. Late Early Triassic climate change: Insights from carbonate carbon isotopes, sedimentary evolution and ammonoid paleobiogeography. Palaeogeogr. Palaeoclimatol. Palaeoecol. 243, 394–411. https://doi.org/10.1016/j.palaeo.2006.08.014

Hallam, A., 1985. A review of Mesozoic climates. J. - Geol. Soc. 142, 433–445.

https://doi.org/10.1144/gsjgs.142.3.0433

Hathorne, E.C., James, R.H., 2006. Temporal record of lithium in seawater: A tracer for silicate weathering? Earth Planet. Sci. Lett. 246, 393–406. https://doi.org/10.1016/j.epsl.2006.04.020

Huh, Y., Chan, L.H., Edmond, J.M., 2001. Lithium isotopes as a probe of weathering processes: Orinoco River. Earth Planet. Sci. Lett. 194, 189–199. https://doi.org/10.1016/S0012-821X(01)00523-4

Huh, Y., Chan, L.H., Zhang, L., Edmond, J.M., 1998. Lithium and its isotopes in major world rivers: implications for weathering and the oceanic budget. Geochim. Cosmochim. Acta 62, 2039–2051. https://doi.org/10.1016/S0016-7037(98)00126-4

Husson, J.M., Peters, S.E., 2018. Nature of the sedimentary rock record and its implications for Earth system evolution. Emerg. Top. Life Sci. 2, 125–136. https://doi.org/10.1042/etls20170152

James, R.H., Rudnick, M.D., Palmer, M.R., 1999. The alkali element and boron geochemistry of the Escanaba Through sediment-hosted hydrothermal system. Earth Planet. Sci. Lett. 171, 157–169. https://doi.org/10.1016/S0012-821X(99)00140-5

Joachimski, M.M., Lai, X., Shen, S., Jiang, H., Luo, G., Chen, B., Chen, J., Sun, Y., 2012. Climate warming in the latest Permian and the Permian-Triassic mass extinction. Geology 40, 195–198. https://doi.org/10.1130/G32707.1

Kaufman, A.J., Jacobsen, S.B., Knoll, A.H., 1993. The Vendian record of Sr and C isotopic variations in seawater: Implications for tectonics and paleoclimate. Earth Planet. Sci. Lett. 120, 409–430. https://doi.org/10.1016/0012-821X(93)90254-7

Kisakurek, B., James, R.H., Harris, N.B.W., 2005. Li and δ7Li in Himalayan rivers: Proxies for silicate weathering? Earth Planet. Sci. Lett. 237, 387–401. https://doi.org/10.1016/j.epsl.2005.07.019

Korte, C., Jasper, T., Kozur, H.W., Veizer, J., 2006. 87Sr/86Sr record of Permian seawater. Palaeogeogr. Palaeoclimatol. Palaeoecol. 240, 89–107. https://doi.org/10.1016/j.palaeo.2006.03.047

Korte, C., Jasper, T., Kozur, H.W., Veizer, J., 2005. δ18O and δ13C of Permian brachiopods: A record of seawater evolution and continental glaciation. Palaeogeogr. Palaeoclimatol. Palaeoecol. 224, 333–351. https://doi.org/10.1016/j.palaeo.2005.03.015

Korte, C., Kozur, H.W., Bruckschen, P., Veizer, J., 2003. Strontium isotope evolution of late permian and triassic seawater. Geochim. Cosmochim. Acta 67, 47–62. https://doi.org/10.1016/S0016-7037(02)01035-9

Kump, L.R., Brantley, S.L., Arthur, M.A., 2000. Chemical Weathering, Atmospheric CO 2 , and Climate. Annu. Rev. Earth Planet. Sci. 28, 611–667. https://doi.org/10.1146/annurev.earth.28.1.611

Kutzbach, J.E., Gallimore, R.G., 1989. Pangaean climates: megamonsoons of the megacontinent. J. Geophys. Res. 94, 3341–3357. https://doi.org/10.1029/JD094iD03p03341

Lechler, M., Pogge von Strandmann, P.A.E., Jenkyns, H.C., Prosser, G., Parente, M., 2015. Lithium-isotope evidence for enhanced silicate weathering during OAE 1a (Early Aptian Selli event). Earth Planet. Sci. Lett. 432, 210–222. https://doi.org/10.1016/j.epsl.2015.09.052

Lehrmann, D.J., Ramezani, J.A., Bowring, S.A., Martin, M.W., Montgomery, P., Enos, P., Payne, J.L., Orchard, M.J., Hongmei, W., Jiayong, W., 2006. Timing of recovery from the end-Permian extinction: Geochronologic and biostratigraphi constraints from south China. Geology 34, 1053–1056. https://doi.org/10.1130/G22827A.1

Li, G., West, A.J., 2014. Evolution of Cenozoic seawater lithium isotopes: Coupling of global denudation regime and shifting seawater sinks. Earth Planet. Sci. Lett. 401, 284–293. https://doi.org/10.1016/j.epsl.2014.06.011

Li, W., Liu, X.M., Godfrey, L. V., 2019. Optimisation of Lithium Chromatography for Isotopic Analysis in Geological Reference Materials by MC-ICP-MS. Geostand. Geoanalytical Res. 43, 261–276. https://doi.org/10.1111/ggr.12254

Liu, X.-M., Li, W., 2019. Optimization of lithium isotope analysis in geological materials by quadrupole ICP-MS. J. Anal. At. Spectrom. 34, 1708–1717. https://doi.org/10.1039/c9ja00175a

Liu, X.M., Rudnick, R.L., McDonough, W.F., Cummings, M.L., 2013. Influence of chemical weathering on the composition of the continental crust: Insights from Li and Nd isotopes in bauxite profiles developed on Columbia River Basalts. Geochim. Cosmochim. Acta 115, 73–91. https://doi.org/10.1016/j.gca.2013.03.043

Looy, C. V., Brugman, W.A., Dilcher, D.L., Visscher, H., 1999. The delayed resurgence of equatorial forests after the Permian-Triassic ecologic crisis. Proc. Natl. Acad. Sci. U. S. A. 96, 13857–13862. https://doi.org/10.1073/pnas.96.24.13857

Marriott, C.S., Henderson, G.M., Belshaw, N.S., Tudhope, A.W., 2004a. Temperature dependence of δ^7Li, δ^{44}Ca and Li/Ca during growth of calcium carbonate. Earth Planet. Sci. Lett. 222, 615–624. https://doi.org/10.1016/j.epsl.2004.02.031

Marriott, C.S., Henderson, G.M., Crompton, R., Staubwasser, M., Shaw, S., 2004b. Effect of mineralogy, salinity, and temperature on Li/Ca and Li isotope composition of calcium carbonate. Chem. Geol. 212, 5–15. https://doi.org/10.1016/j.chemgeo.2004.08.002

Martin, E.E., Macdougall, J.D., 1995. Sr and Nd isotopes at the Permian/Triassic boundary: A record of climate change. Chem. Geol. 125, 73–99. https://doi.org/10.1016/0009-2541(95)00081-V

Misra, S., Froelich, P.N., 2012. Lithium isotope history of cenozoic seawater: Changes in silicate weathering and reverse weathering. Science (80-.). 335, 818–823. https://doi.org/10.1126/science.1214697

Misra, S., Froelich, P.N., 2009. Measurement of lithium isotope ratios by quadrupole-ICP-MS: Application to seawater and natural carbonates. J. Anal. At. Spectrom. 24, 1524–1533. https://doi.org/10.1039/b907122a

Montañez, I.P., Poulsen, C.J., 2013. The Late Paleozoic Ice Age: An Evolving Paradigm. Annu. Rev. Earth Planet. Sci. 41, 629–656. https://doi.org/10.1146/annurev.earth.031208.100118

Newell, A.J., Tverdokhlebov, V.P., Benton, M.J., 1999. Interplay of tectonic and climate on transverse fluvial system, Upper Permian, Souther Uralian Foreland Basin, Russia. Sediment. Geol. 127, 11–29. https://doi.org/10.1016/S0037-0738(99)00009-3

Ovtcharova, M., Bucher, H., Schaltegger, U., Galfetti, T., Brayard, A., Guex, J., 2006. New Early to Middle Triassic U-Pb ages from South China: Calibration with ammonoid biochronozones and implications for the timing of the Triassic biotic recovery. Earth Planet. Sci. Lett. 243, 463–475. https://doi.org/10.1016/j.epsl.2006.01.042

Parrish, J.T., 1993. Climate of the supercontinent Pangea. J. Geol. 101, 215–233. https://doi.org/10.1086/648217

Penniston-Dorland, S., Liu, X.-M., Rudnick, R.L., 2017. Lithium Isotope Geochemistry, in: Reviews in Mineralogy and Geochemistry. pp. 165–217. https://doi.org/10.2138/rmg.2017.82.6

Pistiner, Henderson, G.M., 2003. Lithium-isotope fractionation during continental weathering processes. Earth Planet. Sci. Lett. 214, 327–339. https://doi.org/10.1016/S0012-821X(03)00348-0

Pogge von Strandmann, P.A.E., Frings, P.J., Murphy, M.J., 2017. Lithium isotope behaviour during weathering in the Ganges Alluvial Plain. Geochim. Cosmochim. Acta 198, 17–31. https://doi.org/10.1016/j.gca.2016.11.017

Pogge von Strandmann, P.A.E., Henderson, G.M., 2015. The Li isotope response to mountain uplift. Geology 43, 67–70. https://doi.org/10.1130/G36162.1

Pogge Von Strandmann, P.A.E., Jenkyns, H.C., Woodfine, R.G., 2013. Lithium isotope evidence for enhanced weathering during Oceanic Anoxic Event 2. Nat. Geosci. 6, 668–672. https://doi.org/10.1038/ngeo1875

Pogge von Strandmann, P.A.E., Schmidt, D.N., Planavsky, N.J., Wei, G., Todd, C.L., Baumann, K.H., 2019. Assessing bulk carbonates as archives for seawater Li isotope ratios. Chem. Geol. 530. https://doi.org/10.1016/j.chemgeo.2019.119338

Qiu, Z., Wang, Q., Zou, C., Yan, D., Wei, H., 2014. Transgressive-regressive sequences on the slope of an isolated carbonate platform (Middle-Late Permian, Laibin, South China). Facies 60, 327–345. https://doi.org/10.1007/s10347-012-0359-4

Reichow, M.K., Pringle, M.S., Al'Mukhamedov, A.I., Allen, M.B., Andreichev, V.L., Buslov, M.M., Davies, C.E., Fedoseev, G.S., Fitton, J.G., Inger, S., Medvedev, A.Y., Mitchell, C., Puchkov, V.N., Safonova, I.Y., Scott, R.A., Saunders, A.D., 2009. The timing and extent of the eruption of the Siberian Traps large igneous province: Implications for the end-Permian environmental crisis. Earth Planet. Sci. Lett. 277, 9–20. https://doi.org/10.1016/j.epsl.2008.09.030

Reichow, M.K., Saunders, A.D., White, R. V., Pringle, M.S., Al'Mukhamedov, A.I., Medvedev, A.I., Kirda, N.P., 2002. 40Ar/39Ar dates from the West Siberian Basin: Siberian flood basalt province doubled. Science (80-.). 296, 1846–1849. https://doi.org/10.1126/science.1071671

Retallack, G.J., 2005. Earliest Triassic Claystone Breccias and Soil-Erosion Crisis. J. Sediment. Res. 75, 679–695. https://doi.org/10.2110/jsr.2005.055

Retallack, G.J., Veevers, J.J., Morante, R., 1996. Global coal gap between Permian-Triassic extinction and Middle Triassic recovery of peat-forming plants. Bull. Geol. Soc. Am. 108, 195–207. https://doi.org/10.1130/0016-7606(1996)108<0195:GCGBPT>2.3.CO;2

Rollion-Bard, C., Vigier, N., Meibom, A., Blamart, D., Reynaud, S., Rodolfo-Metalpa, R., Martin, S., Gattuso, J.P., 2009. Effect of environmental conditions and skeletal ultrastructure on the Li isotopic composition of scleractinian corals. Earth Planet. Sci. Lett. 286, 63–70. https://doi.org/10.1016/j.epsl.2009.06.015

Ronov, A.B., Khain, V.E., Balukhovsky, A.N., Seslavinsky, K.B., 1980. Quantitative analysis of Phanerozoic sedimentation. Sediment. Geol. 25, 311–325. https://doi.org/10.1016/0037-0738(80)90067-6

Rudnick, R.L., Tomascak, P.B., Njo, H.B., Gardner, L.R., 2004. Extreme lithium isotopic fractionation during continental weathering revealed in saprolites from South Carolina. Chem. Geol. 212, 45–57. https://doi.org/10.1016/j.chemgeo.2004.08.008

Scotese, C.R., Wright, N., 2018. PALEOMAP Paleodigital Elevation Models (PalwoDEMS) for the Phanerozoic PALEOMAP Project.

Sedlacek, A.R.C., Saltzman, M.R., Algeo, T.J., Horacek, M., Brandner, R., Foland, K., Denniston, R.F., 2014. 87Sr/86Sr stratigraphy from the Early Triassic of Zal, Iran: Linking temperature to weathering rates and the tempo of ecosystem recovery. Geology 42, 779–

782. https://doi.org/10.1130/G35545.1

Seyfried, W.E., Janecky, D.R., Mottl, M.J., 1984. Alteration of the oceanic crust: Implications for geochemical cycles of lithium and boron. Geochim. Cosmochim. Acta 48, 557–569. https://doi.org/10.1016/0016-7037(84)90284-9

Sheldon, N.D., 2006. Abrupt chemical weathering increase across the Permian-Triassic boundary. Palaeogeogr. Palaeoclimatol. Palaeoecol. 231, 315–321. https://doi.org/10.1016/j.palaeo.2005.09.001

Shen, J., Feng, Q., Algeo, T.J., Li, C., Planavsky, N.J., Zhou, L., Zhang, M., 2016. Two pulses of oceanic environmental disturbance during the Permian-Triassic boundary crisis. Earth Planet. Sci. Lett. 443, 139–152. https://doi.org/10.1016/j.epsl.2016.03.030

Shen, S.Z., Crowley, J.L., Wang, Y., Bowring, S.A., Erwin, D.H., Sadler, P.M., Cao, C.Q., Rothman, D.H., Henderson, C.M., Ramezani, J., Zhang, H., Shen, Y., Wang, X.D., Wang, W., Mu, L., Li, W.Z., Tang, Y.G., Liu, X.L., Liu, L.J., Zeng, Y., Jiang, Y.F., Jin, Y.G., 2011. Calibrating the end-Permian mass extinction. Science (80-.). 334, 1367–1372. https://doi.org/10.1126/science.1213454

Shen, S.Z., Wang, Y., Henderson, C.M., Cao, C.Q., Wang, W., 2007. Biostratigraphy and lithofacies of the Permian System in the Laibin-Heshan area of Guangxi, South China. Palaeogeogr. Palaeoclimatol. Palaeoecol. 465, 42–63. https://doi.org/10.1016/j.palwor.2007.05.005

Song, Haijun, Wignall, P.B., Tong, J., Song, Huyue, Chen, J., Chu, D., Tian, L., Luo, M., Zong, K., Chen, Y., Lai, X., Zhang, K., Wang, H., 2015. Integrated Sr isotope variations and global environmental changes through the Late Permian to early Late Triassic, Earth and Planetary Science Letters. https://doi.org/10.1016/j.epsl.2015.05.035

Stampfli, G.M., Borel, G.D., 2002. A plate tectonic model for the Paleozoic and Mesozoic constrained by dynamic plate boundaries and restored synthetic oceanic isochrons. Earth Planet. Sci. Lett. 196, 17–33. https://doi.org/10.1016/S0012-821X(01)00588-X

Stanley, S.M., Yang, X., 1994. A Double Mass Extinction at the End of the Paleozoic Era. Science (80-.). 266, 1340–1344. https://doi.org/10.1126/science.266.5189.1340

Stevens, C.H., 2008. Fasciculate Rugose Corals from Gzhelian and Lower Permian Strata, Pequop Mountains, Northeast Nevada. J. Paleontol. 82, 1190–1200. https://doi.org/10.1666/07-106.1

Sun, H., Xiao, Y., Gao, Y., Zhang, G., Casey, J.F., Shen, Y., 2018. Rapid enhancement of chemical weathering recorded by extremely light seawater lithium isotopes at the Permian–Triassic boundary. Proc. Natl. Acad. Sci. 115, 3782–3787. https://doi.org/10.1073/pnas.1711862115

Sun, Y., Joachimski, M.M., Wignall, P.B., Yan, C., Chen, Y., Jiang, H., Wang, L., Lai, X., 2012. Lethally hot temperatures during the early triassic greenhouse. Science (80-.). 338, 366–370. https://doi.org/10.1126/science.1224126

Sun, Y.D., Liu, X.T., Yan, J.X., Li, B., Chen, B., Bond, D.P.G., Joachimski, M.M., Wignall, P.B., Wang, X., Lai, X.L., 2017. Permian (Artinskian to Wuchapingian) conodont biostratigraphy in the Tieqiao section, Laibin area, South China. Palaeogeogr. Palaeoclimatol. Palaeoecol. 465, 42–63. https://doi.org/10.1016/j.palaeo.2016.10.013

Tabor, N.J., Montanez, I.P., 2002. Shifts in late Paleozoic atmospheric circulation over western equatorial Pangea: Insights from pedogenic mineral δ18O compositions. Geology 30, 1127–1130. https://doi.org/10.1130/0091-7613(2002)030<1127:SILPAC>2.0.CO;2

Teng, F.Z., McDonough, W.F., Rudnick, R.L., Dalpé, C., Tomascak, P.B., Chappell, B.W., Gao, S., 2004. Lithium isotopic composition and concentration of the upper continental crust. Geochim. Cosmochim. Acta 68, 4167–4178. https://doi.org/10.1016/j.gca.2004.03.031

Tierney, K.E., Saltzman, M.R., 2010. Carbon and strontium isotope stratigraphy of the Permian from Nevada and China: Implications from an icehouse to greenhouse transition. Ohio State Univ. Ph.D., 179.

Tomascak, P.B., Carlson, R.W., Shirey, S.B., 1999. Accurate and precise determination of Li isotopic compositions by multi-collector sector ICP-MS. Chem. Geol. 158, 145–154. https://doi.org/10.1016/S0009-2541(99)00022-4

Tomascak, P.B., Magna, T., Dohmen, R., 2016. Advances in Lithium Isotope Geochemistry, Springer. https://doi.org/10.1007/978-3-319-01430-2

Veevers, J.J., 2013. Pangea: Geochronological correlation of successive environmental and strati-tectonic phases in Europe and Australia. Earth-Science Rev. 127, 48–95. https://doi.org/10.1016/j.earscirev.2013.09.001

Veizer, J., 1989. Strontium isotopes in seawater through time. Ann. Rev. Earth Planet. Sci 17, 141–167. https://doi.org/10.1146/annurev.ea.17.050189.001041

Veizer, J., Ala, D., Azmy, K., Bruckschen, P., Buhl, D., Bruhn, F., Garden, G.A.F., Diener, A., Ebneth, S., Godderis, Y., Jasper, T., Korte, C., Pawellek, F., Podlaha, O.G., Strauss, H., 1999. 87 Sr/ 86 Sr, δ 13 C and δ 18 O evolution of Phanerozoic seawater. Chem. Geol. 161, 59–88. https://doi.org/10.1016/S0009-2541(99)00081-9

Vigier, N., Decarreau, A., Millot, R., Carignan, J., Petit, S., France-Lanord, C., 2008. Quantifying Li isotope fractionation during smectite formation and implications for the Li cycle. Geochim. Cosmochim. Acta 72, 780–792. https://doi.org/10.1016/j.gca.2007.11.011

Walker, J.C.G., Hays, P.B., Kasting, J.F., 1981. A negative feedback mechanism for the long-term stabilization of Earth's surface temperature. J. Geophys. Res. 86, 9776–9782.

https://doi.org/10.1029/JC086iC10p09776

Wei, H., Algeo, T.J., Yu, H., Wang, J., Guo, C., Shi, G., 2015. Episodic euxinia in the Changhsingian (late Permian) of South China: Evidence from framboidal pyrite and geochemical data. Sediment. Geol. 319, 78–97. https://doi.org/10.1016/j.sedgeo.2014.11.008

West, A., Galy, A., Bickle, M., 2005. Tectonic and climatic controls on silicate weathering. Earth Planet. Sci. Lett. 235, 211–228. https://doi.org/10.1016/j.epsl.2005.03.020

West, A.J., 2012. Thickness of the chemical weathering zone and implications for erosional and climatic drivers of weathering and for carbon-cycle feedbacks. Geology 40, 811–814. https://doi.org/10.1130/G33041.1

Wimpenny, J., Colla, C.A., Yu, P., Yin, Q.Z., Rustad, J.R., Casey, W.H., 2015. Lithium isotope fractionation during uptake by gibbsite. Geochim. Cosmochim. Acta 168, 133–150. https://doi.org/10.1016/j.gca.2015.07.011

Wimpenny, J., Gíslason, S.R., James, R.H., Gannoun, A., Pogge Von Strandmann, P.A.E., Burton, K.W., 2010. The behaviour of Li and Mg isotopes during primary phase dissolution and secondary mineral formation in basalt. Geochim. Cosmochim. Acta 74, 5259–5279. https://doi.org/10.1016/j.gca.2010.06.028

Yin, H., Jiang, H., Xia, W., Feng, Q., Zhang, N., Shen, J., 2014. The end-Permian regression in South China and its implication on mass extinction. Earth-Science Rev. 137, 19–33. https://doi.org/10.1016/j.earscirev.2013.06.003

CHAPTER 5 - CONCLUSIONS AND OUTLOOK

Marine carbonates and carbonate geochemistry are important archives and tools to investigate the evolution of Earth's surface. Whether or not a robust signal can be extracted from such archive is as essential but often neglected. This dissertation devotes in developing dissolution methods for ancient marine carbonates and uses two case studies to further develop two geochemical proxies. Main conclusions in this dissertation are listed below:

1. A refined sequential leaching protocol for marine carbonate comprises pre-leaching with ammonium acetate and ammonium carbonate, and acid leaching using 0.3M acetic acid. This protocol has been demonstrated to be able to extract authigenic carbonate geochemical signals including rare earth element pattern, Sr isotopes and Li isotopes. Besides, syringe filters for leachates are required to reduce contaminations from non-carbonate phases.
2. Ce anomaly patterns measured in marine carbonates from seven sites of the Late Cretaceous age reveal distinctive redox responses in the global upper ocean across the OAE 2. Additionally, the thermodynamic modeling of Ce oxidation suggests that the upper ocean may have lost up to 50% oxygen in multiple areas in response to this event. Such deoxygenation is a result of global warming and ocean circulation. However, much of the upper ocean remained oxic during most time of the Cretaceous with anoxia in restricted area.

3. The Ce anomaly in marine carbonates is a proxy for local redox condition, but compilation of such records has the potential to imply redox changes over large scales.
4. Large fluctuations over 20‰ in seawater are observed in seawater δ7Li. A negative excursion in $(\delta^7Li)_{sw}$ is likely associated with the variations in hydrothermal input during Tethys opening. A 15‰ decrease in the end Permian and the extremely low $(\delta^7Li)_{sw}$ (around 10‰) suggest a collapse in the authigenic clay formation and a dominating congruent continent weathering regime. An abrupt rise of $(\delta^7Li)_{sw}$ in the Early Triassic can be best explained by enhanced chemical weathering rates as a result of warm climate, available fresh weathering materials, and accelerated hydrological cycle. The Li box model suggests the Li flux of continent weathering in the Early Triassic is about four times of the flux in the Late Permian.
5. Li isotope compositions in ancient marine carbonates provide critical information for seawater Li cycle in deep time. Combined with Sr isotopes, Li box model and geological evidences such as sedimentary records, tectonic activities, as well as climatic reconstructions, Li isotopes can be used as a tracer for not only continental weathering, but also hydrothermal activities and reverse weathering.

The results in this dissertation advanced the application of carbonate geochemistry to study paleoceanography and paleoclimate. The improved sequential leaching protocol has been demonstrated to reduce contaminations from non-carbonate phases. However, this protocol has some limitations. For instance, when the sample contains Mn oxides >2%, moderate contamination will be introduced to authigenic signals, especially for trace elements. Mn oxides are common in natural carbonate samples, existing as coatings on foraminifera. Yet their

existence at this level is difficult to detect, and even more difficult to be quantified. Thus, there is a need to test this protocol on natural carbonate samples with large variations in Mn concentrations. This will allow us to investigate if carbonate samples containing high content of Mn oxides could significantly contaminate these carbonate signals and to what extent. The other direction to refine this protocol is to test on dolomitic samples or samples contain both calcite and dolomite. The current protocol focuses on reducing contaminations from non-carbonate phases, but dolomitization and diagenetic alterations need to be evaluated before interpreting their geochemical signals in marine carbonates. Lastly, such protocol needs to be tested on other elemental and isotope proxies in marine carbonates.

More studies have been focusing on using Li isotopes in marine carbonates to trace continental weathering in deep time. However, there are limited data and large uncertainties in isotope budgets of hydrothermal-basalt interaction and sedimentary fluxes (Chan et al., 2002, 1992; Seyfried et al., 1984; Stoffyn-Egli and Mackenzie, 1984; Vance et al., 2009). These estimates are limited by the sample availability and age resolution of the oceanic crust. For example, the Cenozoic climate has experienced long term cooling, drifting from extreme warmth (e.g. PETM (Paleocene-Eocene Thermal Maximum)), to expansion of ice-sheets (e.g. Miocene and Oligocene glaciation). A large 9‰ increase in $(\delta^7Li)_{seawater}$ over the past 65 Ma (Misra and Froelich, 2012), and increase also in $^{87}Sr/^{86}Sr$ as well as $^{187}Os/^{188}Os$ suggest possible increase in weatherability, contributing to either higher weathering flux or higher riverine isotopic values (Pogge von Strandmann and Henderson, 2015; Ravizza and Zachos, 2003; Raymo et al., 1988). However, much debate has focused on whether increased silicate weathering rates played a causative role in Cenozoic cooling (Li and West, 2014; Ravizza and Zachos, 2003; Si and Rosenthal, 2019; Vigier and Goddéris, 2015). Mass balance modeling also emphasizes the

possibility of reverse weathering contributing to the observed rise in Cenozoic seawater δ^7Li, therefore reducing the extent to which either the isotopic values or weathering flux would have changed over time (Li and West, 2014). To further develop Li isotopes as tracers for chemical weathering proxy, more work is needed to investigate the isotope cycle including low temperature basalt alteration and authigenic clay formation. For example, a few newly planned IODP expeditions have proposed to drill oceanic crust of various ages. Samples from these IODP expeditions would be ideal to benefit our knowledge of the Li isotope cycle. Furthermore, advancing such chemical weathering tracer and apply it to geological time scales will shed light on our understanding of the relationship between chemical weathering and climate in deep time.

REFERENCES

Chan, L.H., Alt, J.C., Teagle, D.A.H., 2002. Lithium and lithium isotope profiles through the upper oceanic crust: A study of seawater-basalt exchange at ODP Sites 504B and 896A. Earth Planet. Sci. Lett. 201, 187–201. https://doi.org/10.1016/S0012-821X(02)00707-0

Chan, L.H., Edmond, J.M., Thompson, G., Gillis, K., 1992. Lithium isotopic composition of submarine basalts: implications for the lithium cycle in the oceans. Earth Planet. Sci. Lett. 108, 151–160. https://doi.org/10.1016/0012-821X(92)90067-6

Li, G., West, A.J., 2014. Evolution of Cenozoic seawater lithium isotopes: Coupling of global denudation regime and shifting seawater sinks. Earth Planet. Sci. Lett. 401, 284–293. https://doi.org/10.1016/j.epsl.2014.06.011

Misra, S., Froelich, P.N., 2012. Lithium isotope history of cenozoic seawater: Changes in silicate weathering and reverse weathering. Science (80-.). 335, 818–823. https://doi.org/10.1126/science.1214697

Pogge von Strandmann, P.A.E., Henderson, G.M., 2015. The Li isotope response to mountain uplift. Geology 43, 67–70. https://doi.org/10.1130/G36162.1

Ravizza, G.E., Zachos, J.C., 2003. Records of Cenozoic Ocean Chemistry, in: Treatise on Geochemistry. pp. 551–581. https://doi.org/10.1016/B0-08-043751-6/06121-1

Raymo, M.E., Ruddiman, W.F., Froelich, P.N., 1988. Influence of late Cenozoic mountain building on ocean geochemical cycles. Geology 16, 649–653. https://doi.org/10.1130/0091-7613(1988)016<0649:IOLCMB>2.3.CO;2

Seyfried, W.E., Janecky, D.R., Mottl, M.J., 1984. Alteration of the oceanic crust: Implications for geochemical cycles of lithium and boron. Geochim. Cosmochim. Acta 48, 557–569. https://doi.org/10.1016/0016-7037(84)90284-9

Si, W., Rosenthal, Y., 2019. Reduced continental weathering and marine calcification linked to late Neogene decline in atmospheric CO2. Nat. Geosci. 12, 833–838. https://doi.org/10.1038/s41561-019-0450-3

Stoffyn-Egli, P., Mackenzie, F.T., 1984. Mass balance of dissolved lithium in the oceans. Geochim. Cosmochim. Acta 48, 859–872. https://doi.org/10.1016/0016-7037(84)90107-8

Vance, D., Teagle, D.A.H., Foster, G.L., 2009. Variable Quaternary chemical weathering fluxes and imbalances in marine geochemical budgets. Nature 458, 493–496. https://doi.org/10.1038/nature07828

Vigier, N., Goddéris, Y., 2015. A new approach for modeling Cenozoic oceanic lithium isotope paleo-variations: The key role of climate. Clim. Past 11, 635–645. https://doi.org/10.5194/cp-11-635-2015

APPENDIX 2.1: RAW CA AND REY CONCENTRATIONS OF REFERNCE MATERIALS IN FIG. 2.1

ppm	**Montmorillonite**	**Kaolinite**	**Ilitte**	**NOD**	**SBC**	**KL**	**Seawater**	
							South Pacific surface water	South Pacific deep water
Ca	8212	1591	4473	123113	123113	420667		
La	49.003	23.511	41.679	114.843	52.500	0.122	8.26E-08	7.64E-07
Ce	100.916	49.898	82.602	763.984	108.000	0.130	9.51E-09	2.45E-08
Pr	11.996	6.060	9.505	24.477	12.600	0.028	3.51E-08	1.04E-07
Nd	45.196	24.676	35.091	103.697	49.200	0.132	6.20E-09	2.26E-08
Sm	9.935	5.054	6.196	22.613	9.600	0.035	1.24E-09	5.50E-09
Eu	0.659	1.951	1.239	5.498	1.980	0.008	5.47E-09	2.67E-08
Gd	9.413	5.123	5.473	26.658	8.500	0.043	8.14E-10	3.85E-09
Tb	1.433	0.730	0.814	3.845	1.200	0.007	5.06E-09	2.39E-08
Dy	8.473	4.262	5.062	23.867	7.100	0.048	2.56E-08	1.11E-07
Y	40.039	21.074	25.632	111.276	36.500	0.558	1.03E-09	7.55E-09
Ho	1.573	0.811	1.027	7.550	1.400	0.014	3.07E-09	1.30E-08
Er	3.913	2.088	3.067	12.965	3.800	0.039	4.52E-10	1.91E-09
Tm	0.556	0.268	0.452	1.905	0.560	0.006	2.99E-09	1.22E-08
Yb	3.476	1.531	2.992	12.172	3.640	0.035	4.27E-10	1.85E-09
Lu	0.4615	0.1955	0.427	1.854905	0.54	0.004206	9.51E-10	3.92E-09
Ce/Ce*	0.94	0.99	0.95	3.92	0.99	0.67		
Eu/Eu*	0.31	1.83	0.98	1.09	1.03	1.00		

APPENDIX 2.2: RAW REY CONCENTRATIONS OFAMMONIUM ACETATE LEACHING

Sample				La	Ce	Pr	Nd	Sm	Eu	Gd	Tb	Dy	Y	Ho	Er	Tm	Yb	Lu
Figure (a)	NOD-A-1	No filter	S1	0.0459	0.1110	0.0447	0.0527	0.0687	0.0799	0.0956	0.0775	0.0849	0.0934	0.0847	0.0861	0.0956	0.0910	0.0880
			S2	0.0601	0.1361	0.0587	0.0690	0.0875	0.1043	0.1211	0.0985	0.1063	0.1096	0.1052	0.1115	0.1176	0.1131	0.1182
	NOD-A-1	Filter	S1	0.0170	0.0007	0.0174	0.0257	0.0386	0.0647	0.0679	0.0472	0.0507	0.0768	0.0532	0.0530	0.0462	0.0431	0.0436
			S2	0.0180	0.0009	0.0189	0.0278	0.0417	0.0672	0.0753	0.0527	0.0549	0.0866	0.0573	0.0584	0.0528	0.0459	0.0515
Figure (b)	NOD-A-1		S1	0.0082	0.0031	0.0018	0.0091	0.0029	0.0009	0.0036	0.0005	0.0024	0.0388	0.0007	0.0019	0.0003	0.0018	0.0009
			S2	0.0094	0.0085	0.0017	0.0084	0.0024	0.0009	0.0028	0.0004	0.0020	0.0252	0.0005	0.0016	0.0002	0.0014	0.0005
			S3	0.0061	0.0018	0.0012	0.0062	0.0019	0.0007	0.0024	0.0004	0.0015	0.0172	0.0004	0.0009	0.0002	0.0012	0.0004
	Montmorillonite		S1	0.6501	1.2057	0.1489	0.5706	0.1225	0.0133	0.1261	0.0173	0.0894	0.4072	0.0161	0.0402	0.0047	0.0261	0.0034
			S2	0.5016	0.9555	0.1208	0.4743	0.1072	0.0095	0.1156	0.0165	0.0851	0.4204	0.0169	0.0395	0.0048	0.0236	0.0033
			S3	0.3962	0.7434	0.0961	0.3930	0.0924	0.0088	0.1035	0.0148	0.0742	0.3815	0.0144	0.0350	0.0044	0.0202	0.0032
	SBC-1		S1	0.3768	0.7687	0.1033	0.5703	0.1438	0.0574	0.1606	0.0186	0.0965	0.6128	0.0194	0.0482	0.0058	0.0368	0.0061
			S2	0.3045	0.6507	0.0896	0.4682	0.1339	0.0551	0.1461	0.0177	0.0863	0.5516	0.0171	0.0411	0.0050	0.0280	0.0050
			S3	0.2586	0.6446	0.0901	0.4852	0.1377	0.0387	0.1493	0.0177	0.0868	0.5095	0.0178	0.0398	0.0048	0.0241	0.0047
Figure (c)		Concentration																
	NOD-A-1	0.2M	S1	0.024	0.002	0.007	0.029	0.008	0.007	0.013	0.003	0.008	0.060	0.003	0.007	0.002	0.005	0.002
			S2	0.022	0.001	0.005	0.024	0.006	0.004	0.009	0.001	0.004	0.050	0.001	0.004	0.000	0.002	0.001
			S3	0.028	0.008	0.007	0.033	0.008	0.007	0.014	0.002	0.008	0.062	0.003	0.008	0.002	0.005	0.001
		1M	S1	0.400	0.026	0.091	0.511	0.137	0.050	0.198	0.027	0.147	1.183	0.033	0.091	0.010	0.058	0.011
			S2	0.527	0.041	0.124	0.693	0.182	0.065	0.271	0.033	0.198	1.613	0.044	0.122	0.014	0.084	0.014
			S3	0.558	0.054	0.134	0.751	0.196	0.067	0.301	0.037	0.214	1.819	0.048	0.134	0.016	0.090	0.016
		2M	S1	8.244	5.778	1.963	10.838	2.980	0.887	4.592	0.579	3.401	26.349	0.755	2.260	0.258	1.622	0.272
			S2	4.889	4.656	1.162	6.335	1.684	0.482	2.487	0.317	1.906	13.977	0.427	1.192	0.151	0.904	0.161
			S3	5.286	4.804	1.231	6.754	1.758	0.527	2.544	0.327	1.915	15.173	0.430	1.235	0.152	0.959	0.174
		Reaction time																
	NOD-A-1	0.5h	S1	0.400	0.026	0.091	0.511	0.137	0.050	0.198	0.027	0.147	1.183	0.033	0.091	0.010	0.058	0.011
			S2	0.527	0.041	0.124	0.693	0.182	0.065	0.271	0.033	0.198	1.613	0.044	0.122	0.014	0.084	0.014
			S3	0.558	0.054	0.134	0.751	0.196	0.067	0.301	0.037	0.214	1.819	0.048	0.134	0.016	0.090	0.016
		1h	S1	1.190	4.611	0.269	1.264	0.308	0.089	0.412	0.056	0.321	2.095	0.070	0.207	0.028	0.162	0.027
			S2	0.711	0.174	0.165	0.898	0.251	0.075	0.355	0.041	0.251	2.120	0.056	0.167	0.019	0.111	0.020
			S3	0.722	0.084	0.167	0.953	0.254	0.076	0.349	0.042	0.253	2.188	0.056	0.166	0.020	0.117	0.020
		24h	S1	0.124	0.049	0.029	0.168	0.044	0.021	0.071	0.010	0.056	0.497	0.013	0.032	0.005	0.026	0.004
			S2	0.174	0.013	0.038	0.220	0.058	0.026	0.090	0.011	0.066	0.575	0.014	0.041	0.005	0.028	0.004
			S3	0.147	0.018	0.032	0.178	0.047	0.022	0.067	0.008	0.049	0.457	0.012	0.031	0.004	0.023	0.003
		pH																
	NOD-A-1	7	S1	0.008	0.003	0.002	0.009	0.003	0.001	0.004	0.001	0.002	0.039	0.001	0.002	0.000	0.002	0.001
			S2	0.009	0.008	0.002	0.008	0.002	0.001	0.003	0.000	0.002	0.025	0.001	0.002	0.000	0.001	0.001
			S3	0.006	0.002	0.001	0.006	0.002	0.001	0.002	0.000	0.002	0.017	0.000	0.001	0.000	0.001	0.000
		6	S1	0.215	0.015	0.047	0.260	0.072	0.022	0.100	0.012	0.064	0.646	0.015	0.044	0.004	0.031	0.005
			S2	1.904	0.313	0.548	2.371	0.726	0.310	0.961	0.227	0.673	5.262	0.245	0.471	0.153	0.360	0.158
			S3	2.684	0.297	0.596	3.348	0.902	0.248	1.333	0.156	0.902	8.352	0.204	0.565	0.067	0.400	0.078
		5	S1	3.279	0.324	0.758	4.245	1.136	0.302	1.597	0.184	1.084	10.581	0.233	0.650	0.075	0.448	0.079
			S2	0.551	0.015	0.123	0.710	0.219	0.047	0.250	0.023	0.181	1.658	0.027	0.102	0.005	0.085	0.005
			S3	1.247	0.115	0.275	1.675	0.421	0.122	0.600	0.062	0.365	3.826	0.081	0.242	0.020	0.165	0.026

APPENDIX 2.3: ELEMENTAL CONCENTRATION OF ACID COMPARISON

				Mg	Al	Ca	Mn	Fe	Rb	Sr	La	Ce	Pr	Nd	Sm	Eu	Gd	Tb	Dy	Y	Ho	Er	Tm	Yb	Lu	Sum REY	10^{-6} g	%
	Bulk/ppm			13718	9380	123113	92097	49787	7.7	789	114.843	763.9836	24.4769	103.6974	22.6132	5.4985	26.6577	3.8450	23.8673	111.2761	7.5497	12.9653	1.9054	12.1720	1.8549	1237	61.9	
		pH = 2	S1	59670	6400	496061	1620	680	2.5	5108	69.4635	12.0138	15.4388	75.5692	17.4154	4.5105	21.5758	2.6538	15.3586	94.2065	3.1348	8.6500	1.2268	7.7452	1.2132	350	1.8	2.8
			S2	7072	4190	19603	2094	714	0.9	487	29.6974	15.2367	6.4091	28.2010	5.7797	1.4531	6.6656	0.9003	5.3593	29.5550	1.0570	3.0098	0.4622	2.8311	0.4068	137	0.7	1.1
		pH = 2.5	S1	52911	3254	445192	785	14	2.2	4375	22.9616	2.5212	4.6589	23.6643	5.5093	1.4003	7.0335	0.8232	4.4887	35.8342	0.9704	2.6952	0.3439	2.1716	0.3880	115	0.6	0.9
			S2	6915	2329	48815	1358	46	0.6	859	16.5616	3.7938	3.2620	14.5440	3.0577	0.7540	3.5884	0.4659	2.7321	18.5454	0.5922	1.6419	0.2263	1.4000	0.2184	71	0.4	0.6
	Acetic acid	pH = 3	S1	35546	922	276322	158	<0.000	1.5	2693	1.9603	0.1821	0.3605	1.8973	0.4238	0.1077	0.5459	0.0571	0.3327	3.6888	0.0777	0.2281	0.0306	0.1874	0.0332	10	0.1	0.1
			S2	8869	985	73194	424	<0.000	0.5	950	2.8332	0.3010	0.4681	2.2145	0.4522	0.1179	0.6104	0.0705	0.4464	4.3569	0.0961	0.2809	0.0382	0.2267	0.0434	13	0.1	0.1
		1M sodium acetate	S1	36945	1093	333043	152	47	4.2	3464	23.6521	3.3902	6.4099	33.7892	9.0855	2.4252	11.2946	1.5768	9.4191	66.8411	1.9946	5.5242	0.7135	4.5063	0.8383	181	0.9	1.5
NOD-A-1			S2	12154	1440	156677	313	98	3.1	1534	23.4787	4.3773	5.9582	30.2452	7.9352	2.0612	10.0205	1.3867	8.0974	60.1456	1.7331	4.9916	0.6706	4.3726	0.7447	166	0.8	1.3
		0.05M	S1	43921	7957	319595	3733	1097	2.4	3557	178.9112	120.3332	35.9061	149.7512	31.3364	7.7438	35.9278	5.1618	30.9580	146.8778	6.4590	18.5771	2.5003	15.1322	2.4950	788	3.9	6.4
			S2	12665	5885	93160	3343	2243	1.5	917	98.9088	138.3614	21.3590	89.6855	19.3786	4.7604	21.4158	3.0888	18.7946	88.0272	3.8344	11.2280	1.5280	9.5753	1.5193	531	2.7	4.3
		0.1M	S1	52227	12032	377362	5724	5553	3.1	4266	265.6665	312.5948	56.4697	238.8286	51.4260	12.4268	56.9025	8.2013	49.7044	227.9642	10.2156	29.6084	4.1493	25.1205	4.0095	1353	6.8	10.9
	Nitric acid		S2	13264	7105	89619	4062	6358	1.7	884	91.2909	216.2792	19.7029	82.2761	18.0880	4.3688	19.7918	2.8897	17.9102	89.9031	3.7157	10.9731	1.5389	9.7242	1.5292	590	2.9	4.8
		0.2M	S1	65327	18204	470658	8652	15880	4.3	5318	353.8604	605.5725	75.6705	316.2943	68.9963	16.9441	76.9551	11.0714	67.6076	322.0886	14.1343	40.5841	6.1991	38.5394	5.5798	2020	10.1	16.3
			S2	8789	7163	27561	4481	12583	2.1	329	69.5580	325.6316	15.2919	63.3080	13.6114	3.4052	15.5271	2.3577	14.5170	69.1793	3.1095	9.4140	1.2959	8.5492	1.4648	616	3.1	5.0
		0.3M	S1	38282	12550	270511	6069	15710	3.3	3141	220.4632	506.4071	47.9507	202.6006	43.6471	10.7674	49.6149	7.2749	44.0171	208.8370	9.1139	26.6768	3.6818	23.2752	3.6698	1408	7.0	11.4
			S2	14801	869	107106	1068	594	18.4	2270	5.8241	11.4618	1.5107	6.6170	1.7373	0.1887	2.1806	0.3909	2.3307	14.2369	0.4694	1.2760	0.1862	1.0345	0.1628	50	0.2	0.4
	Bulk			9182	63738	8212	184	17494	12.7	183	49.0025	100.9155	11.9960	45.1960	9.9345	0.6585	9.4130	1.4330	8.4725	40.0385	1.5730	3.9125	0.5560	3.4760	0.4615	287	14.4	
		pH = 2	S1	1224	148	5892	33	381	2.5	115	0.0354	0.0960	0.0154	0.0711	0.0267	0.0021	0.0247	0.0040	0.0231	0.1221	0.0042	0.0129	0.0018	0.0112	0.0017	0	0.0	0.02
			S2	801	110	3459	27	394	1.7	68	0.0600	0.1472	0.0203	0.0892	0.0261	0.0019	0.0230	0.0033	0.0161	0.0728	0.0030	0.0073	0.0009	0.0059	0.0004	0	0.0	0.02
		pH = 2.5	S1	761	39	3694	22	198	3.5	77	0.2161	0.4577	0.0537	0.1976	0.0466	0.0025	0.0399	0.0057	0.0325	0.1342	0.0054	0.0125	0.0016	0.0087	0.0008	1	0.0	0.04
			S2	503	73	2322	17	183	1.4	47	1.1911	2.5446	0.2935	1.0721	0.2251	0.0130	0.2182	0.0309	0.1686	0.7395	0.0302	0.0751	0.0102	0.0551	0.0066	7	0.0	0.23
	Acetic acid	pH = 3	S1	245	6	1197	6	49	2.6	25	0.0087	0.0188	0.0025	0.0088	0.0018	0.0002	0.0018	0.0003	0.0013	0.0056	0.0005	0.0007	0.0002	0.0006	0.0001	0	0.0	0.002
			S2	216	21	1020	7	68	1.4	21	0.3194	0.6664	0.0772	0.2774	0.0622	0.0033	0.0535	0.0081	0.0438	0.1815	0.0077	0.0190	0.0023	0.0125	0.0013	2	0.0	0.06
Montmorillonite		1M sodium acetate	S1	10067	9723	14506	5781	18166	2.1	261	46.6687	310.7842	11.9740	52.1703	11.2226	2.1294	9.9341	1.6806	11.9448	63.3270	2.5049	6.5699	0.9835	6.3548	1.0717	539	2.7	18.7
			S2	827	249	2239	312	215	3.2	42	1.6204	3.6219	0.4943	2.2430	0.7224	0.0496	0.7684	0.1125	0.6533	3.7862	0.1240	0.3134	0.0348	0.1975	0.0217	15	0.1	0.5
		0.05M	S1	3909	241	22046	124	1582	5.7	523	2.1771	4.9075	0.6068	2.4342	0.6533	0.0374	0.6398	0.0966	0.5602	2.4607	0.0995	0.2672	0.0356	0.2103	0.0258	15	0.1	0.5
			S2	2416	198	11256	177	3148	2.3	251	3.4899	7.7094	0.9309	3.5543	0.8842	0.0487	0.8479	0.1255	0.7206	3.0552	0.1294	0.3321	0.0408	0.2377	0.0315	22	0.1	0.8
	Nitric acid	0.1M	S1	6665	920	34726	244	3235	6.9	761	12.8236	28.5617	3.5267	13.4195	3.5283	0.1851	3.2338	0.4741	2.6614	13.3957	0.4722	1.2292	0.1481	0.9232	0.1287	85	0.4	2.9
			S2	2694	816	10483	283	5900	2.7	216	21.3883	46.7226	5.4943	20.7348	5.0190	0.2636	4.3152	0.6499	3.4944	16.4073	0.6101	1.5183	0.1891	1.1054	0.1502	128	0.6	4.4
		0.2M	S1	7496	2335	44634	356	4931	7.1	869	67.3403	147.4841	17.7580	67.3452	15.7787	0.8624	14.3166	2.1194	11.8037	53.4956	2.0793	5.2944	0.7430	4.2719	0.5094	411	2.1	14.3

		0.3M	S2	1991	1520	7030	323	7785	2.7	112	62.3802	131.8079	15.1180	55.4976	12.2101	0.6529	11.1089	1.6242	8.8725	39.6863	1.5438	3.9278	0.4756	2.7178	0.3404	348	1.7	12.1
			S1	7757	3166	41138	391	6290	8.1	892	119.9467	259.1234	30.3735	113.7434	25.8762	1.4260	23.3421	3.4071	19.2033	84.9819	3.3723	8.8326	1.0798	6.1798	0.8030	702	3.5	24.4
			S2	1691	1508	3577	333	8757	2.7	75	63.6106	132.8525	15.1670	54.5438	11.6032	0.6143	10.4597	1.4628	8.4972	37.0372	1.4417	3.7083	0.4523	2.5876	0.3359	344	1.7	12.0
	Bulk			15600	222353	21071	1162	178	147	178	52.5000	108.0000	12.6000	49.2000	9.6000	1.9800	8.5000	1.2000	7.1000	36.5000	1.4000	3.8000	0.5600	3.6400	0.5400	297	14.9	
		pH = 2	S1	4470	2251	79831	3002	2834	4.8	287	7.9283	33.1672	5.3398	27.9182	8.8766	2.0794	8.6531	1.0859	5.4360	22.5902	0.9022	1.9889	0.2158	1.1847	0.1422	128	0.6	4.3
			S2	647	708	4724	238	2176	1.8	22	0.8025	3.4034	0.5448	2.9300	0.9367	0.2169	0.9021	0.1158	0.5889	2.2541	0.0955	0.2262	0.0250	0.1402	0.0169	13	0.1	0.4
		pH = 2.5	S1	4259	1466	78742	2846	1795	4.3	290	5.9994	24.1655	3.8213	20.4369	6.6150	1.4620	6.1332	0.7939	4.0715	16.5066	0.6601	1.4771	0.1653	0.9234	0.1240	93	0.5	3.1
			S2	572	479	6101	280	1680	2.2	28	0.8776	3.5902	0.5543	2.9700	0.9463	0.2234	0.9320	0.1213	0.6162	2.3923	0.1020	0.2301	0.0270	0.1324	0.0178	14	0.1	0.5
	Acetic acid		S1	3581	719	64588	2099	823	4.3	235	2.3736	8.8149	1.3268	7.0891	2.2872	0.5429	2.2751	0.2816	1.4512	6.4568	0.2450	0.6083	0.0646	0.3882	0.0540	34	0.2	1.1
		pH = 3	S2	671	396	13622	528	785	1.7	56	0.6253	2.5166	0.3900	2.0496	0.6701	0.1567	0.6643	0.0865	0.4434	1.8042	0.0731	0.1706	0.0182	0.0970	0.0115	10	0.0	0.3
		1M sodium acetate	S1	5393	900	104767	3512	1967	14.0	381	7.2978	20.3140	2.6460	11.9785	3.2219	0.7778	3.3247	0.5040	2.7684	15.6837	0.5223	1.4277	0.2031	1.2776	0.1373	72	0.4	2.4
SBC-1			S2	712	421	8898	954	887	7.0	37	1.7920	5.4298	0.7268	3.3314	0.9832	0.2427	0.9624	0.1387	0.8058	4.0961	0.1476	0.3552	0.0474	0.2444	0.0314	19	0.1	0.6
		0.05M	S1	5358	3304	88369	3281	7105	8.3	322	15.9252	60.7079	8.9639	44.9958	13.3698	3.0792	13.9985	1.8307	9.1324	40.5872	1.5650	3.4786	0.3627	1.8302	0.2151	220	1.1	7.4
			S2	1065	1028	5522	287	6906	4.0	24	5.0584	19.5454	2.8595	14.6129	4.3214	0.9762	4.4653	0.5937	3.0799	11.0607	0.5166	1.1952	0.1281	0.6683	0.0823	69	0.3	2.3
		0.1M	S1	7158	5253	89300	3477	22179	14.7	334	25.8470	100.5344	14.9439	74.3470	21.9032	4.9215	22.2926	2.9285	14.7889	63.3697	2.4805	5.7602	0.5980	3.0191	0.3745	358	1.8	12.0
			S2	1557	1405	1954	241	14932	4.8	11	6.0266	23.5127	3.4049	17.2801	4.9058	1.1155	4.9314	0.6503	3.3771	11.7556	0.5689	1.3381	0.1440	0.7433	0.0910	80	0.4	2.7
	Nitric acid		S1	5510	4162	87209	3264	12437	11.5	325	25.6123	99.2792	14.5596	72.6963	21.8806	4.7775	21.6753	2.8559	14.6059	62.2275	2.4418	5.5643	0.5649	2.9290	0.3677	352	1.8	11.8
		0.2M	S2	1951	1527	1859	233	13851	5.6	9	3.1301	11.8940	1.6861	8.2696	2.1684	0.4703	2.1112	0.2873	1.5642	6.0250	0.2799	0.6988	0.0812	0.4672	0.0606	39	0.2	1.3
			S1	6872	5530	96787	3835	20528	15.9	373	33.4521	129.8934	19.4299	96.3039	27.9679	6.3021	27.8837	3.7681	19.6056	77.6520	3.2095	7.3955	0.7403	3.8129	0.4834	458	2.3	15.4
		0.3M	S2	2369	1796	2571	263	18532	7.3	12	2.1865	8.0449	1.1100	5.3960	1.3882	0.3216	1.4531	0.2055	1.1498	4.7058	0.2145	0.5659	0.0734	0.4474	0.0611	27	0.1	0.9

APPENDIX 2.4: ELEMENTAL CONCENTRATIONS OF TWO-COMPONENT MIXING EXPERIMENTS

Sample	Reagent	pH / molarity	Steps	Volume(ml)	Mg	Al	Ca	Mn	Fe	Rb	Sr	CaCO3 %	La	Ce	Pr	Nd	Sm	Eu	Gd	Tb	Dy	Y	Ho	Er	Tm	Yb	Lu	Sum REY	10-6g	1000sum REY/Ca	% of Carbonate	% of mix
NOD-A-1	Acetic acid	pH = 2	S1	1	44920.93	643.04	3700348.18	92.29	48.24	1.43	14280.20	29	26.19	4.36	6.69	33.54	8.31	2.12	10.24	1.43	8.47	47.90	1.74	4.80	0.61	3.57	0.58	161	0.8	0.43	415	1.62
			S2	1	25080.56	971.79	2645394.77	194.51	70.27	0.47	10865.86	21	35.01	6.31	9.15	46.13	11.54	2.99	14.14	2.00	11.75	66.83	2.44	6.83	0.87	5.20	0.82	222	1.1	0.84	574	2.23
		pH = 2.5	S1	4	79359.82	372.00	6436578.56	91.58	4.97	2.88	25021.85	50	9.79	0.61	2.41	13.71	3.60	0.99	5.20	0.64	3.63	26.70	0.77	2.08	0.23	1.41	0.24	72	0.4	0.11	186	0.72
			S2	4	40530.33	934.53	4078195.11	265.33	7.32	0.87	16699.50	32	21.75	2.52	5.41	29.95	7.68	2.04	10.42	1.32	7.58	54.17	1.63	4.50	0.53	3.21	0.55	153	0.8	0.38	396	1.54
		pH = 3	S1	15	14193.85	3.31	1444394.36	7.15	83.70	0.57	4949.99	11	0.05	0.00	0.01	0.04	0.01	0.00	0.01	0.00	0.01	0.13	0.00	0.01	0.00	0.01	0.00	0	0.0	0.00	1	0.00
			S2	15	22628.49	3.60	1435503.38	5.62	82.93	1.43	5503.63	11	0.02	0.00	0.00	0.02	0.00	0.00	0.01	0.00	0.00	0.05	0.00	0.00	0.00	0.00	0.00	0	0.0	0.00	0	0.00
		1M sodium acetate	S1	10	12121.17	610.38	1022672.55	223.06	142.46	1.59	4513.51	8	21.95	5.01	5.34	28.09	6.99	1.82	8.65	1.24	7.60	42.49	1.59	4.50	0.62	3.78	0.61	140	0.7	1.37	363	1.41
			S2	10	33630.13	534.22	3167822.02	132.36	293.04	3.03	12125.80	25	23.57	3.53	5.37	29.66	7.25	1.88	9.04	1.29	7.56	44.82	1.60	4.50	0.59	3.72	0.57	145	0.7	0.46	375	1.46
		0.05M	S1	15	71843.34	144.35	3893213.67	162.36	9.56	4.05	17440.83	30	0.70	0.22	0.10	0.47	0.08	0.03	0.14	0.02	0.14	1.64	0.04	0.10	0.02	0.09	0.02	4	0.0	0.01	10	0.04
			S2	15	36093.45	41.66	3915628.21	64.46	7.01	1.68	14675.65	31	0.31	0.04	0.05	0.24	0.05	0.02	0.07	0.01	0.08	0.95	0.02	0.06	0.01	0.04	0.01	2	0.0	0.00	5	0.02
		0.1M	S1	7	71406.78	61.01	3530836.96	71.31	6.00	3.21	14565.65	28	0.34	0.03	0.05	0.21	0.04	0.01	0.06	0.01	0.06	0.80	0.02	0.05	0.01	0.04	0.01	2	0.0	0.00	4	0.02
			S2	7	22527.50	651.06	3643031.87	136.92	699.58	2.70	12854.61	28	5.12	8.19	1.17	5.18	1.27	0.16	1.65	0.25	1.57	13.65	0.34	1.00	0.13	0.73	0.11	41	0.2	0.11	105	0.41
		0.2M	S1	3.5	9169.30	7.57	461550.47	22.26	7.70	0.62	2556.78	4	0.31	0.03	0.04	0.18	0.03	0.01	0.05	0.01	0.05	0.63	0.01	0.04	0.01	0.03	0.00	1	0.0	0.03	4	0.01
			S2	3.5	21598.80	28.33	2757938.13	28.49	8.44	0.88	10051.39	22	0.31	0.02	0.04	0.19	0.04	0.01	0.06	0.01	0.05	0.68	0.01	0.04	0.01	0.03	0.00	2	0.0	0.01	4	0.02
		0.3M	S1	2.5	63858.44	24.34	2878750.92	29.36	7.47	2.72	12798.46	22	0.35	0.02	0.04	0.19	0.04	0.01	0.06	0.01	0.05	0.61	0.01	0.04	0.01	0.03	0.00	1	0.0	0.01	4	0.01
			S2	2.5	3066.17	13.71	486620.77	9.05	20.97	0.13	2341.30	4	0.60	0.03	0.08	0.35	0.07	0.02	0.11	0.01	0.09	1.09	0.02	0.06	0.01	0.05	0.01	3	0.0	0.05	7	0.03
Montmorillonite	Acetic acid	pH = 2	S1	1	19055.33	286.35	2764725.78	110.30	73.40	3.63	10572.42	22	2.17	2.71	0.52	2.33	0.56	0.14	0.76	0.13	0.89	8.90	0.21	0.64	0.09	0.56	0.08	21	0.1	0.07	54	0.88
			S2	1	16925.86	688.83	3058308.90	114.17	335.75	1.39	11920.87	24	2.68	3.73	0.64	2.79	0.71	0.16	0.96	0.16	1.16	10.92	0.27	0.81	0.11	0.69	0.10	26	0.1	0.08	67	1.11
		pH = 2.5	S1	4	38955.70	241.39	5746450.50	208.45	26.86	10.09	20786.66	45	3.52	4.28	0.83	3.84	0.96	0.22	1.38	0.22	1.49	14.74	0.35	1.10	0.14	0.90	0.13	34	0.2	0.06	88	1.46
			S2	4	31754.05	865.28	5326890.47	225.39	290.57	3.83	20862.22	42	4.57	6.50	1.10	4.66	1.17	0.24	1.56	0.28	1.94	17.36	0.44	1.39	0.20	1.21	0.18	43	0.2	0.08	111	1.83
		pH = 3	S1	15	41440.02	18.26	6212780.63	153.88	7.64	14.07	20326.67	49	0.20	0.16	0.03	0.16	0.05	0.02	0.07	0.01	0.07	1.06	0.02	0.06	0.01	0.05	0.01	2	0.0	0.00	5	0.09
			S2	15	27808.08	67.56	4887548.62	143.47	14.27	3.11	17336.94	38	3.39	4.06	0.77	3.59	0.83	0.20	1.23	0.19	1.27	13.12	0.30	0.91	0.12	0.74	0.12	31	0.2	0.06	80	1.32
		1M sodium acetate	S1	10	48585.25	735.28	7905341.10	756.29	320.04	12.68	29428.78	62	5.38	6.71	1.27	5.70	1.41	0.33	1.92	0.32	2.26	21.66	0.53	1.65	0.23	1.38	0.21	51	0.3	0.06	132	2.18
			S2	10	17622.20	647.08	2991584.81	758.34	444.84	6.28	10541.40	23	2.50	3.68	0.58	2.47	0.67	0.13	0.89	0.16	1.03	9.02	0.24	0.71	0.10	0.60	0.09	23	0.1	0.08	59	0.98
		0.05M	S1	15	26484.44	22.30	3346849.60	134.44	16.90	11.00	12950.78	26	0.14	0.17	0.03	0.11	0.03	0.02	0.04	0.01	0.05	0.63	0.01	0.04	0.01	0.03	0.00	1	0.0	0.00	3	0.06
			S2	15	18108.50	54.47	3010286.92	113.54	126.24	3.37	11037.50	24	1.98	2.51	0.39	1.82	0.42	0.08	0.62	0.09	0.63	6.59	0.15	0.47	0.06	0.37	0.05	16	0.1	0.05	42	0.69
	Nitric acid	0.1M	S1	7	25962.83	68.23	3251342.87	193.61	237.91	12.78	12643.57	25	0.14	0.13	0.02	0.08	0.02	0.02	0.04	0.01	0.04	0.56	0.01	0.03	0.00	0.03	0.00	1	0.0	0.00	3	0.05
			S2	7	62840.38	224.69	7449346.39	233.33	9.48	2.40	26627.48	58	0.65	0.05	0.09	0.40	0.08	0.02	0.14	0.02	0.11	1.54	0.03	0.09	0.01	0.08	0.01	3	0.0	0.00	9	0.14
		0.2M	S1	3.5	6899.87	10.59	839490.12	83.70	6.81	3.05	3202.08	7	0.03	0.03	0.00	0.01	0.01	0.02	0.01	0.00	0.01	0.10	0.00	0.01	0.00	0.00	0.00	0	0.0	0.00	1	0.01
			S2	3.5	4788.01	51.57	837931.64	41.84	10.73	0.69	3212.12	7	1.70	1.66	0.22	1.07	0.23	0.04	0.41	0.05	0.36	4.22	0.09	0.28	0.04	0.19	0.03	11	0.1	0.13	27	0.45
		0.3M	S1	2.5	22320.48	22.20	2793982.29	159.68	158.86	8.61	11247.17	22	0.10	0.07	0.01	0.04	0.01	0.02	0.02	0.00	0.02	0.24	0.00	0.01	0.00	0.01	0.00	1	0.0	0.00	1	0.02

					17155.38	84.59	2832189.68	80.23	229.10	1.68	10255.27	22	2.72	3.02	0.39	1.81	0.35	0.05	0.59	0.08	0.46	4.95	0.11	0.33	0.04	0.22	0.03														
			S2	2.5																								15	0.1	0.05	39	0.65								
					18768.98	1001.96	3517347.46	1243.22	1327.97	1.32	13413.76	27	5.11	10.76	1.67	7.47	1.89	0.47	2.07	0.33	2.09	15.86	0.45	1.33	0.19	1.17	0.16														
			S1	1																								51	0.3	0.15	132	2.11								
		pH = 2			20177.85	542.58	3246027.86	366.77	464.24	2.30	11784.32	25	3.41	5.84	0.95	4.37	1.09	0.28	1.30	0.21	1.34	11.64	0.30	0.90	0.13	0.78	0.11														
			S2	1																								33	0.2	0.10	84	1.35								
					17793.66	363.97	2921808.10	443.89	255.64	4.93	10722.23	23	3.19	6.00	0.93	4.22	1.01	0.26	1.21	0.19	1.23	10.02	0.27	0.81	0.11	0.71	0.11														
			S1	4																								30	0.2	0.10	78	1.25								
		pH = 2.5			19300.69	1217.82	3091935.08	1701.43	1331.03	3.69	12203.32	24	4.49	10.29	1.45	6.61	1.66	0.42	1.87	0.30	1.81	13.19	0.39	1.15	0.16	1.02	0.15														
			S2	4																								45	0.2	0.15	116	1.86								
	Aceti c acid				25669.09	215.33	4634697.88	456.29	54.76	7.69	15672.50	36	2.01	3.08	0.52	2.45	0.56	0.16	0.74	0.11	0.71	7.15	0.11	0.56	0.07	0.43	0.07														
			S1	15																								19	0.1	0.04	48	0.77								
		pH = 3			23966.74	334.22	4560663.93	1093.36	88.95	5.07	16190.42	36	4.79	9.08	1.38	6.46	1.57	0.41	1.83	0.28	1.71	14.66	0.37	1.13	0.15	0.97	0.14														
			S2	15																								45	0.2	0.10	116	1.86								
					38554.10	913.46	7060247.95	1784.10	993.83	17.51	25352.36	55	7.34	13.88	2.19	9.81	2.45	0.62	2.85	0.45	2.85	23.65	0.64	1.88	0.27	1.62	0.24														
		1M sodium acetate	S1	10																								71	0.4	0.10	183	2.92								
					16704.31	811.95	3082589.98	1906.74	1099.91	13.68	11040.30	24	3.93	8.87	1.28	5.70	1.48	0.37	1.60	0.25	1.58	11.45	0.32	0.97	0.13	0.81	0.12														
SBC			S2	10																								39	0.2	0.13	100	1.61								
					23328.66	175.49	3455030.11	1725.96	137.86	8.57	12471.75	27	0.62	1.11	0.16	0.88	0.22	0.09	0.33	0.04	0.24	2.42	0.06	0.16	0.02	0.10	0.02														
		0.05M	S1	15																								6	0.0	0.02	17	0.27								
					54536.29	448.08	9292976.82	2109.22	190.23	11.63	33010.15	73	3.76	7.41	1.06	5.94	1.35	0.38	1.75	0.23	1.30	12.76	0.29	0.76	0.09	0.49	0.04														
			S2	15																								38	0.2	0.04	97	1.55								
					63025.10	412.32	9584735.93	6587.06	527.80	17.33	29391.05	75	0.45	0.80	0.11	0.62	0.16	0.06	0.24	0.03	0.16	1.51	0.04	0.10	0.01	0.06	0.01														
		0.1M	S1	7																								4	0.0	0.00	11	0.18								
					45352.31	469.85	8198353.32	1012.44	170.99	8.24	27804.15	64	4.01	7.65	1.02	5.85	1.34	0.34	1.78	0.20	1.22	11.26	0.25	0.67	0.07	0.35	0.02														
	Nitric acid		S2	7																								36	0.2	0.04	93	1.49								
					18428.78	49.99	2741887.47	739.98	10.51	6.13	9639.46	21	0.06	0.07	0.02	0.04	0.02	0.05	0.03	0.01	0.02	0.21	0.01	0.02	0.01	0.02	0.01														
		0.2M	S1	3.5																								1	0.0	0.00	1	0.02								
					13395.48	253.94	2415990.85	463.24	5.31	4.40	8313.28	19	1.72	2.48	0.35	1.88	0.44	0.12	0.63	0.07	0.42	4.22	0.10	0.28	0.03	0.18	0.03														
			S2	3.5																								13	0.1	0.05	33	0.53								
					20785.66	86.07	3069918.73	2928.54	477.89	6.22	11067.22	24	0.55	0.71	0.09	0.56	0.12	0.05	0.19	0.02	0.10	0.98	0.02	0.06	0.00	0.03	0.00														
		0.3M	S1	2.5																								3	0.0	0.01	9	0.14								
					14676.23	196.78	2529015.38	326.83	104.61	2.57	8931.37	20	4.52	7.92	1.05	5.97	1.19	0.29	1.67	0.17	0.85	7.13	0.17	0.44	0.04	0.20	0.03														
			S2	2.5																								32	0.2	0.13	82	1.31								
		limestone (KL)			1254.59	34.36	210333.64	5.45	30.56	0.08	773.77		0.12	0.13	0.03	0.13	0.04	0.01	0.04	0.01	0.05	0.56	0.01	0.04	0.01	0.03	0.00	1	0.19	0.06	100	1.60								
		80% KL + 20% NOD-A-1			103110.90	1903.40	192889.80	18423.72	9995.49	1.60	776.72		23.07	152.90	4.92	20.84	4.55	1.11	5.37	0.77	4.81	22.70	1.52	2.62	0.39	2.46	0.37	248	49.7												
		80% KL + 20% Montmorillonite			103110.90	1903.40	192889.80	18423.72	9995.49	1.60	776.72		9.90	20.29	2.42	9.14	2.02	0.14	1.92	0.29	1.73	8.45	0.33	0.81	0.12	0.72	0.10	58	11.7												
		80% KL + 20% SBC-1			2840.01	12775.17	169909.37	41.23	3536.78	2.61	655.70		10.60	21.70	2.54	9.95	1.95	0.40	1.73	0.25	1.46	7.75	0.29	0.79	0.12	0.76	0.11	60	12.1												

APPENDIX 2.5: ELEMENTAL RATIOS OF ACID COMPARISON EXPERIMENT

Sample	Reagent	pH / molarity	Steps	1000Mg/Ca	1000Al/Ca	1000Mn/Ca	1000Sr/Ca	1000Fe/Ca	1000Rb/Sr	Mn/Sr	Y/Ho	Ce/Ce*	La/La*	Eu/Eu*	Yb*/Nd*
NOD-A-1	Acetic acid	pH = 2	S1	120.29	12.90	3.26	10.30	2.21	0.48	0.32	30.05	0.01	1.33	1.21	1.46
			S2	360.74	213.76	106.83	24.83	114.41	1.78	4.30	27.96	0.06	1.23	1.16	1.55
		pH = 2.5	S1	118.85	7.31	1.76	9.83	12.47	0.50	0.18	36.93	0.00	1.51	1.19	1.41
			S2	141.66	47.71	27.82	17.60	130.25	0.72	1.58	31.32	0.01	1.36	1.15	1.47
		pH = 3	S1	128.64	3.34	0.57	9.75	57.47	0.56	0.06	47.50	0.00	1.72	1.24	2.37
			S2	121.17	13.46	5.80	12.98	171.91	0.56	0.45	45.33	0.00	1.72	1.21	0.42
	Nitric acid	1M sodium acetate	S1	110.93	3.28	0.46	10.40	47.17	1.22	0.04	33.51	0.00	1.17	1.19	1.85
			S2	77.57	9.19	2.00	9.79	3.79	1.99	0.20	34.70	0.01	1.20	1.16	1.73
		0.05M	S1	137.43	24.90	11.68	11.13	3.32	0.67	1.05	22.74	0.15	1.25	1.12	2.77
			S2	135.95	63.17	35.89	9.85	23.32	1.60	3.64	22.96	0.11	1.17	1.13	2.05
		0.1M	S1	138.40	31.88	15.17	11.25	14.39	0.73	1.35	22.32	0.05	1.20	1.11	2.66
			S2	148.01	79.29	45.33	9.86	68.86	1.90	4.60	24.20	0.13	1.17	1.11	1.94
		0.2M	S1	138.80	38.68	18.38	11.30	32.62	0.81	1.63	22.79	0.10	1.18	1.13	2.55
			S2	318.89	259.91	162.58	11.93	440.90	6.38	13.62	22.25	0.08	1.13	1.12	2.36
		0.3M	S1	141.52	46.39	22.43	11.61	56.41	1.04	1.93	22.91	0.45	1.12	1.10	2.17
			S2	138.19	8.11	9.97	21.19	5.08	8.12	0.47	30.33	0.14	1.16	1.10	1.90
Montmorillonite	Acetic acid	pH = 2	S1	207.80	25.19	5.61	19.55	64.62	21.32	0.29	28.91	0.41	0.64	0.37	3.33
			S2	231.67	31.67	7.83	19.71	114.06	24.69	0.40	24.32	0.58	0.78	0.37	3.40
		pH = 2.5	S1	205.92	10.62	6.07	20.82	53.52	45.74	0.29	24.80	0.95	0.89	0.27	3.22
			S2	216.75	31.42	7.20	20.11	78.67	29.92	0.36	24.50	0.99	0.89	0.28	3.58
		pH = 3	S1	205.07	5.32	4.79	21.07	40.90	104.28	0.23	10.64	0.77	0.73	0.56	4.37
			S2	211.87	20.47	6.47	20.18	66.21	65.85	0.32	23.43	1.00	0.90	0.26	2.83
	Nitric acid	1M sodium acetate	S1	693.95	670.25	398.50	17.97	1252.28	7.92	22.18	25.28	0.62	0.89	0.61	3.35
			S2	369.33	111.16	139.14	18.80	96.11	75.45	7.40	30.54	0.58	0.90	0.41	3.33
		0.05M	S1	177.30	10.95	5.61	23.72	71.75	10.87	0.24	24.74	0.79	0.87	0.27	4.14
			S2	214.63	17.56	15.69	22.26	279.65	8.98	0.70	23.61	0.87	0.86	0.26	2.79
		0.1M	S1	191.94	26.49	7.02	21.92	93.15	9.03	0.32	28.37	0.83	0.83	0.26	4.39
			S2	257.02	77.82	26.99	20.56	562.79	12.32	1.31	26.89	0.93	0.88	0.26	2.73
		0.2M	S1	167.95	52.32	7.97	19.47	110.47	8.18	0.41	25.73	0.88	0.87	0.27	4.53
			S2	283.26	216.23	45.97	15.95	1107.35	23.90	2.88	25.71	1.00	0.91	0.26	2.48
		0.3M	S1	188.55	76.95	9.52	21.69	152.90	9.04	0.44	25.20	0.94	0.89	0.27	3.29
			S2	472.78	421.48	93.10	20.94	2447.99	36.20	4.45	25.69	1.03	0.91	0.26	1.70
SBC-1/ppm	Acetic acid	pH = 2	S1	56.00	28.20	37.61	3.59	56.07	16.84	10.47	25.04	0.36	0.47	1.18	2.15
			S2	136.94	149.99	50.28	4.73	633.02	78.65	10.63	23.60	0.35	0.48	1.16	2.47
		pH = 2.5	S1	54.09	18.62	36.14	3.69	27.63	14.92	9.80	25.01	0.36	0.51	1.12	2.32
			S2	93.77	78.58	45.82	4.54	294.13	79.74	10.10	23.46	0.38	0.51	1.17	2.13
		pH = 3	S1	55.45	11.12	32.49	3.64	12.20	18.47	8.94	26.36	0.40	0.58	1.19	2.43
			S2	49.26	29.06	38.79	4.14	60.38	29.83	9.37	24.68	0.38	0.51	1.15	2.07
	Nitric acid	1M sodium acetate	S1	51.48	8.59	33.52	3.64	7.49	36.65	9.22	30.03	0.63	0.75	1.12	2.28
			S2	79.97	47.36	107.18	4.16	221.05	188.71	25.75	27.75	0.59	0.68	1.18	1.95
		0.05M	S1	60.63	37.39	37.13	3.64	80.40	25.63	10.19	25.93	0.44	0.54	1.11	1.64
			S2	192.81	186.20	51.96	4.39	1250.65	164.35	11.83	21.41	0.44	0.54	1.09	1.14
		0.1M	S1	80.15	58.82	38.94	3.74	248.37	43.97	10.40	25.55	0.44	0.52	1.09	1.28
			S2	796.84	718.89	123.44	5.39	7641.36	457.65	22.90	20.66	0.45	0.54	1.11	0.83
		0.2M	S1	63.18	47.72	37.43	3.72	142.61	35.38	10.06	25.48	0.45	0.53	1.07	5.04
			S2	1049.86	821.47	125.20	4.82	7452.13	630.05	26.00	21.52	0.49	0.55	1.06	1.34
		0.3M	S1	71.00	57.14	39.63	3.86	212.09	42.51	10.28	24.19	0.44	0.51	1.10	0.65
			S2	921.61	698.70	102.29	4.70	7209.02	607.69	21.77	21.94	0.52	0.58	1.09	0.46
limestone （KL)					5.96	0.16	0.03	3.68	0.15	0.11	0.01	40.73	3.91	1.20	1.09	
NOD-A-1/ppm					111.43	76.19	748.07	6.40	404.40	9.70	116.79	14.74	0.91	0.93	0.31	
Montmorillonite/ppm					1118.05	7761.36	22.45	22.33	2130.22	69.47	1.00	25.45	0.91	0.98	1.03	
SBC-1/ppm					740.35	10552.56	55.15	8.45	8.45	825.84	6.53	26.07	0.91	0.98	1.03	
80% KL + 20% NOD-A-1																
80% KL + 20% Montmorillonite																
80% KL + 20% SBC-1																

APPENDIX 2.6: ELEMENTAL RATIOS OF TWO-COMPONENT MIXING EXPERIMENT

Two-endmember mixing experiment																		
Sample	Reagent	pH / molarity	Steps	1000Mg/Ca	1000Al/Ca	1000Mn/Ca	1000Sr/Ca	1000Fe/Ca	1000Rb/Sr	Total REY/10-6g	10000*Total REY/Ca		Mn/Sr	Y/Ho	Yb*/Nd*	Ce/Ce*	La/La*	Eu/Eu*
NOD-A-1	Acetic acid	pH = 2	S1	12.14	0.17	0.02	3.86	0.01	0.10	0.80		0.43	0.01	27.52	1.46	0.00	1.18	1.14
			S2	9.48	0.37	0.07	4.11	0.03	0.04	1.11		0.84	0.02	27.65	1.55	0.00	1.16	1.16
		pH = 2.5	S1	12.33	0.06	0.01	3.89	0.00	0.11	0.36		0.11	0.00	34.79	1.41	0.00	1.39	1.22
			S2	9.94	0.23	0.07	4.09	0.00	0.05	0.77		0.38	0.02	33.33	1.47	0.00	1.34	1.19
		pH = 3	S1	9.83	0.00	0.00	3.43	0.06	0.12	0.00		0.00	0.00	56.44	2.37	0.00	1.47	0.70
			S2	15.76	0.00	0.00	3.83	0.06	0.26	0.00		0.00	0.00	77.93	0.42	0.00	3.71	0.99
		1M sodium acetate	S1	11.85	0.60	0.22	4.41	0.14	0.35	0.70		1.37	0.05	26.72	1.85	0.01	1.30	1.16
			S2	10.62	0.17	0.04	3.83	0.09	0.25	0.72		0.46	0.01	28.04	1.73	0.00	1.46	1.15
	Nitric acid	0.05M	S1	18.45	0.04	0.04	4.48	0.00	0.23	0.02		0.01	0.01	43.23	2.77	0.05	1.92	1.37
			S2	9.22	0.01	0.02	3.75	0.00	0.11	0.01		0.00	0.00	41.12	2.05	0.01	1.72	1.25
		0.1M	S1	20.22	0.02	0.02	4.13	0.00	0.22	0.01		0.00	0.00	50.26	2.66	0.01	2.04	1.30
			S2	6.18	0.18	0.04	3.53	0.19	0.21	0.20		0.11	0.01	39.91	1.94	0.54	1.17	0.53
		0.2M	S1	19.87	0.02	0.05	5.54	0.02	0.24	0.01		0.03	0.01	52.41	2.55	0.01	2.35	1.21
			S2	7.83	0.01	0.01	3.64	0.00	0.09	0.01		0.01	0.00	51.86	2.36	0.00	2.03	1.15
		0.3M	S1	22.18	0.01	0.01	4.45	0.00	0.21	0.01		0.01	0.00	49.34	2.17	0.00	2.44	1.21
			S2	6.30	0.03	0.02	4.81	0.04	0.05	0.01		0.05	0.00	51.74	1.90	0.00	2.21	1.16
Montmorillonite	Acetic acid	pH = 2	S1	6.89	0.10	0.04	3.82	0.03	0.34	0.10		0.07	0.01	42.67	3.33	0.29	1.11	1.00
			S2	5.53	0.23	0.04	3.90	0.11	0.12	0.13		0.08	0.01	40.68	3.40	0.38	1.11	0.89
		pH = 2.5	S1	6.78	0.04	0.04	3.62	0.00	0.49	0.17		0.06	0.01	41.70	3.22	0.28	1.19	0.94
			S2	5.96	0.16	0.04	3.92	0.05	0.18	0.21		0.08	0.01	39.12	3.58	0.40	1.06	0.84
		pH = 3	S1	6.67	0.00	0.02	3.27	0.00	0.69	0.01		0.00	0.01	46.77	4.37	0.22	1.71	1.90
			S2	5.69	0.01	0.03	3.55	0.00	0.18	0.15		0.06	0.01	43.99	2.83	0.29	1.24	0.98
		1M sodium acetate	S1	6.15	0.09	0.10	3.72	0.04	0.43	0.25		0.06	0.03	41.19	3.35	0.30	1.14	0.96
			S2	5.89	0.22	0.25	3.52	0.15	0.60	0.11		0.08	0.07	38.01	3.33	0.46	1.11	0.80
	Nitric acid	0.05M	S1	7.91	0.01	0.04	3.87	0.01	0.85	0.01		0.00	0.01	44.36	4.14	0.53	1.50	2.05
			S2	6.02	0.02	0.04	3.67	0.04	0.30	0.08		0.05	0.01	43.03	2.79	0.43	1.43	0.73
		0.1M	S1	7.99	0.02	0.06	3.89	0.07	1.01	0.01		0.00	0.02	54.05	4.39	0.61	2.58	2.56
			S2	8.44	0.03	0.03	3.57	0.00	0.09	0.02		0.00	0.01	51.04	2.73	0.00	2.05	1.18
		0.2M	S1	8.22	0.01	0.10	3.81	0.01	0.95	0.00		0.00	0.03	41.47	4.53	0.83	1.60	6.49
			S2	5.71	0.06	0.05	3.83	0.01	0.21	0.05		0.13	0.01	46.96	2.48	0.57	2.23	0.57
		0.3M	S1	7.99	0.01	0.06	4.03	0.06	0.77	0.00		0.00	0.01	57.51	3.29	0.73	3.10	4.81
			S2	6.06	0.03	0.03	3.62	0.08	0.16	0.08		0.05	0.01	43.83	1.70	0.62	1.94	0.57
SBC-1/ppm	Acetic acid	pH = 2	S1	5.34	0.28	0.35	3.81	0.38	0.10	0.26		0.15	0.09	35.53	2.15	0.45	0.82	1.11
			S2	6.22	0.17	0.11	3.63	0.14	0.20	0.16		0.10	0.03	38.62	2.47	0.40	0.98	1.10
		pH = 2.5	S1	6.09	0.12	0.15	3.67	0.09	0.46	0.15		0.10	0.04	37.34	2.32	0.44	0.94	1.11
			S2	6.24	0.39	0.55	3.95	0.43	0.30	0.22		0.15	0.14	34.24	2.13	0.54	0.86	1.11
		pH = 3	S1	5.54	0.05	0.10	3.38	0.01	0.49	0.09		0.04	0.03	43.39	2.43	0.36	1.10	1.19
			S2	5.26	0.07	0.24	3.55	0.02	0.31	0.22		0.10	0.07	39.13	2.07	0.45	0.98	1.15
		1M sodium acetate	S1	5.46	0.13	0.25	3.59	0.14	0.69	0.35		0.10	0.07	36.91	2.28	0.43	0.90	1.11
			S2	5.42	0.26	0.62	3.58	0.36	1.24	0.19		0.13	0.17	35.70	1.95	0.52	0.83	1.13
	Nitric acid	0.05M	S1	6.75	0.05	0.50	3.61	0.04	0.69	0.03		0.02	0.14	43.22	1.64	0.42	1.26	1.73
			S2	5.87	0.05	0.23	3.55	0.02	0.35	0.19		0.04	0.06	44.62	1.14	0.42	1.20	1.27
		0.1M	S1	6.58	0.04	0.69	3.07	0.06	0.59	0.02		0.00	0.22	41.76	1.28	0.45	1.39	1.81
			S2	5.53	0.06	0.12	3.39	0.02	0.30	0.18		0.04	0.04	45.19	0.83	0.47	1.35	1.19
		0.2M	S1	6.72	0.02	0.27	3.52	0.00	0.64	0.00		0.00	0.08	17.34	5.04	0.33	0.62	7.36
			S2	5.54	0.11	0.19	3.44	0.00	0.53	0.06		0.05	0.06	42.50	1.34	0.46	1.63	1.29
		0.3M	S1	6.77	0.03	0.95	3.61	0.16	0.56	0.02		0.01	0.26	44.15	0.65	0.48	2.28	2.17
			S2	5.80	0.08	0.13	3.53	0.04	0.29	0.16		0.13	0.04	41.14	0.46	0.48	1.48	1.17
		80% KL + 20% NOD-A-1		534.56	9.87	95.51	4.03	51.82	2.05	49.68			23.72	14.93	1.63	0.22	1.22	1.14
		80% KL + 20% Montmorillonite		23.91	257.99	1.37	3.80	157.85	45.01	11.67			0.36	25.97	1.09	0.90	0.93	0.33
		80% KL + 20% SBC-1		16.71	75.19	0.24	3.86	20.82	3.99	12.08			0.06	26.62	1.05	0.22	1.22	1.14

APPENDIX 2.7: CALCIUM AND REY CONCENTRATIONS OF MULTI-COMPONENT MIXING EXPERIMENT

		Ca	CaCO3 %	La	Ce	Pr	Nd	Sm	Eu	Gd	Tb	Dy	Y	Ho	Er	Tm	Yb	Lu
A1	5%	400291	5	0.0110	0.0068	0.0019	0.0120	0.0036	0.0012	0.0053	0.0004	0.0046	0.0720	0.0009	0.0053	0.0005	0.0047	0.0002
	10%	372483	5	0.0090	0.0080	0.0015	0.0098	0.0033	0.0010	0.0041	0.0004	0.0043	0.0831	0.0011	0.0062	0.0007	0.0053	0.0005
	13%	293230	4	0.1578	0.1718	0.0856	0.1067	0.0973	0.0927	0.1202	0.0981	0.1365	0.4019	0.1208	0.1360	0.1217	0.1343	0.1278
	15%	259218	4	0.0076	0.0063	0.0011	0.0049	0.0016	0.0005	0.0053	0.0006	0.0032	0.0598	0.0011	0.0034	0.0003	0.0033	0.0014
	20%	274047	4	0.0175	0.0257	0.0040	0.0144	0.0062	0.0041	0.0122	0.0034	0.0122	0.1088	0.0052	0.0100	0.0037	0.0106	0.0046
	21%	341290	5	0.0212	0.0284	0.0064	0.0138	0.0035	0.0067	0.0165	0.0046	0.0133	0.1196	0.0063	0.0116	0.0042	0.0107	0.0040
	25%	344329	6	0.0413	0.0303	0.0097	0.0352	0.0127	0.0049	0.0167	0.0062	0.0166	0.1527	0.0086	0.0164	0.0056	0.0103	0.0060
	40%	357095	7	0.0695	0.1043	0.0165	0.0830	0.0348	0.0138	0.0489	0.0070	0.0462	0.4610	0.0129	0.0339	0.0074	0.0304	0.0063
A2	5%	118874	2	0.0218	0.0148	0.0058	0.0181	0.0086	0.0035	0.0098	0.0026	0.0090	0.0988	0.0030	0.0057	0.0028	0.0079	0.0021
	10%	179606	2	0.0170	0.0134	0.0026	0.0155	0.0042	0.0005	0.0065	0.0011	0.0067	0.1077	0.0023	0.0074	0.0006	0.0060	0.0006
	13%	135678	2	0.0452	0.0263	0.0095	0.0443	0.0118	0.0039	0.0182	0.0015	0.0188	0.1680	0.0044	0.0141	0.0013	0.0139	0.0021
	15%	207080	3	0.0639	0.0827	0.0128	0.0627	0.0220	0.0054	0.0308	0.0070	0.0320	0.3653	0.0094	0.0301	0.0078	0.0228	0.0064
	20%	182901	3	0.0518	0.0719	0.0114	0.0652	0.0193	0.0055	0.0295	0.0049	0.0289	0.2832	0.0094	0.0216	0.0044	0.0210	0.0027
	21%	280621	4	0.1306	0.1850	0.0283	0.1412	0.0519	0.0105	0.0543	0.0103	0.0667	0.5611	0.0166	0.0436	0.0059	0.0302	0.0071
	25%	200668	3	0.0554	0.0443	0.0134	0.0431	0.0201	0.0090	0.0278	0.0095	0.0243	0.2049	0.0128	0.0190	0.0078	0.0144	0.0075
	40%	164172	3	0.1318	0.2122	0.0417	0.1555	0.0397	0.0157	0.0629	0.0125	0.0589	0.5248	0.0163	0.0416	0.0103	0.0362	0.0091
S1	5%	4648684	31	3.497	1.724	0.777	3.915	0.969	0.267	1.365	0.197	1.461	13.437	0.349	1.014	0.131	0.751	0.132
	10%	4651612	32	3.468	4.092	0.801	3.751	0.940	0.255	1.296	0.200	1.578	14.949	0.374	1.127	0.158	0.947	0.153
	13%	4341987	31	4.365	1.251	1.030	5.325	1.354	0.360	1.834	0.243	1.711	14.254	0.388	1.082	0.139	0.838	0.146
	15%	2913681	21	2.094	2.704	0.508	2.392	0.548	0.146	0.760	0.123	0.972	8.990	0.224	0.705	0.099	0.591	0.088
	20%	3327605	26	2.806	4.326	0.747	3.567	0.872	0.232	1.125	0.171	1.345	11.167	0.287	0.889	0.121	0.724	0.113
	21%	4458501	35	5.217	5.156	1.361	6.552	1.640	0.448	2.082	0.309	2.108	17.008	0.466	1.379	0.182	1.131	0.181
	25%	4239017	35	5.311	1.356	1.326	7.329	1.929	0.501	2.518	0.321	2.055	16.258	0.453	1.271	0.159	0.924	0.154
	40%	3891933	41	6.136	12.394	1.863	8.610	2.248	0.569	2.515	0.396	2.726	19.754	0.575	1.672	0.243	1.511	0.228
S2	5%	3871558	25	5.984	3.247	1.445	6.810	1.648	0.413	2.005	0.302	2.249	16.978	0.484	1.436	0.195	1.176	0.191
	10%	3187647	22	2.715	3.832	0.698	3.075	0.764	0.200	0.970	0.162	1.255	10.820	0.286	0.869	0.122	0.764	0.113
	13%	3042367	22	8.774	3.727	2.106	10.228	2.559	0.653	3.142	0.429	2.969	20.685	0.632	1.824	0.245	1.514	0.248
	15%	1198338	9	1.137	1.609	0.289	1.346	0.351	0.090	0.419	0.075	0.539	4.933	0.124	0.377	0.056	0.304	0.047
	20%	1791026	14	2.343	4.493	0.694	3.151	0.782	0.192	0.899	0.147	1.050	8.170	0.239	0.687	0.096	0.618	0.085
	21%	1338468	11	4.303	5.044	1.121	5.020	1.249	0.295	1.462	0.209	1.388	9.686	0.294	0.856	0.116	0.698	0.105
	25%	2085024	17	11.455	4.365	2.775	13.926	3.410	0.879	4.333	0.567	3.519	24.605	0.752	2.135	0.280	1.723	0.290
	40%	1038793	11	3.809	10.320	1.493	7.415	2.139	0.503	2.163	0.326	1.939	10.986	0.362	1.030	0.134	0.823	0.109
S3	5%	896410	6	3.470	2.222	0.783	3.635	0.882	0.211	1.054	0.147	0.972	7.113	0.210	0.627	0.081	0.527	0.083
	10%	599910	4	0.925	2.014	0.323	1.554	0.455	0.098	0.524	0.072	0.476	3.368	0.092	0.270	0.035	0.215	0.030
	13%	714411	5	5.692	2.719	1.340	6.449	1.578	0.390	1.804	0.239	1.505	10.175	0.315	0.885	0.119	0.730	0.118
	15%	498876	4	0.970	2.423	0.383	2.025	0.642	0.127	0.652	0.085	0.539	3.492	0.104	0.294	0.037	0.207	0.029
	20%	723572	6	2.333	7.006	1.072	5.515	1.697	0.351	1.644	0.226	1.313	7.348	0.240	0.618	0.080	0.431	0.058
	21%	404381	3	2.851	5.742	0.948	4.847	1.265	0.309	1.341	0.187	1.071	6.161	0.211	0.552	0.074	0.408	0.068
	25%	476880	4	6.606	3.092	1.588	8.128	1.979	0.494	2.368	0.292	1.690	11.969	0.359	0.991	0.131	0.804	0.133
	40%	193779	2	1.704	6.902	1.175	6.640	2.236	0.470	2.053	0.270	1.231	5.328	0.198	0.464	0.050	0.291	0.035

APPENDIX 2.8: ELEMENTAL CONCENTRATIONS IN ROUTINE ANALYSIS OF NIST-SRM-1D

	Mg	Al	K	Ca	Mn	Fe	Zn	Sr	Y	La	Ce	Pr	Nd	Sm	Eu	Gd	Tb	Dy	Ho	Er	Tm	Yb	Lu
Certificate number (ppm)	2040	2780	1127	377500	209	2229	18	258															
Georem Reference value																							
Georem Information value									5	4	4	0.6	3	0.5	0.1	0.5	0.09	0.6	0.1	0.4		0.3	
LA ICP-MS[1]					199	1806	9.73	273	4.18	3.57	4.03	0.54	2.62	0.51	0.1	0.43	0.08	0.52	0.09	0.34	0.04	0.31	0.04
Date																							
9/9/16	1743.5			391308.8	214.6			256.6	3.68	2.62	3.56	0.52	2.09	0.40	0.09	0.44	0.07	0.42	0.09	0.27	0.04	0.22	0.03
9/9/16	1909.8			428707.2	235.9			280.8	3.95	2.82	3.80	0.57	2.28	0.43	0.10	0.47	0.07	0.44	0.10	0.28	0.04	0.23	0.04
9/9/16	1853.9			432553.2	224.7			265.9	3.55	2.52	3.43	0.50	2.09	0.36	0.08	0.42	0.06	0.39	0.09	0.26	0.03	0.20	0.03
12/23/16	1890.2	2780.7	1227.9	382807.7	218.8	2304.4	19.2	253.4	3.91	2.69	3.63	0.54	2.16	0.41	0.09	0.47	0.07	0.43	0.09	0.27	0.04	0.25	0.03
12/23/16	1942.5	2759.0	1264.9	396465.3	227.4	2371.8		253.9	4.00	2.73	3.70	0.55	0.57	0.41	0.10	0.47	0.07	0.43	0.09	0.29	0.04	0.24	0.03
12/23/16	1761.9	2279.8	1099.2	405666.7	195.0	2406.8		245.1	3.91	2.64	3.37	0.49	1.97	0.38	0.09	0.42	0.06	0.40	0.08	0.27	0.04	0.21	0.03
12/23/16	1720.4	2646.6	1139.0	384207.7	209.4	2126.1		267.6	4.20	2.82	3.75	0.56	2.26	0.45	0.10	0.49	0.07	0.44	0.10	0.27	0.04	0.22	0.03
1/10/17	1648.4	2428.6	985.1	391478.2	196.4	2265.1	20.5	253.1	4.04	2.65	3.57	0.53	2.14	0.40	0.09	0.45	0.07	0.42	0.10	0.27	0.03	0.22	0.03
1/10/17	1425.2	3107.3	912.3	375531.7	203.9	2061.4	17.1	254.7	3.95	2.71	3.59	0.53	2.14	0.41	0.09	0.47	0.07	0.42	0.09	0.27	0.04	0.52	0.03
1/13/17	1700.2	2793.9	1071.2	370086.7	204.5	2131.8	18.5	234.1	3.71	2.60	3.53	0.52	2.00	0.40	0.09	0.42	0.06	0.40	0.09	0.29	0.03	0.24	0.03
1/13/17	1630.1	2668.1	1024.5	353411.3	197.5	2051.7	17.9	230.5	3.72	2.60	3.51	0.51	2.07	0.38	0.08	0.43	0.07	0.41	0.08	0.26	0.03	0.22	0.03
2/6/17	2010.8	2989.2	1296.2	442115.9	246.7	2456.0	22.1	265.5	4.23	2.90	3.90	0.59	2.26	0.45	0.09	0.49	0.07	0.45	0.10	0.29	0.04	0.24	0.04
2/6/17	1639.3	2389.5	1072.2	356046.5	200.5	2001.3	17.7	247.3	3.87	2.64	3.61	0.52	2.07	0.41	0.09	0.45	0.07	0.44	0.09	0.25	0.03	0.22	0.03
2/6/17	1727.3	2484.3	1135.1	373890.4	209.9	2108.0	19.0	248.9	3.96	2.69	3.58	0.52	2.11	0.40	0.09	0.45	0.07	0.43	0.09	0.26	0.03	0.23	0.03
2/6/17	1883.9	2776.3	1197.8	409677.3	229.3	2305.3	21.0	247.9	3.94	2.77	3.55	0.52	2.09	0.40	0.09	0.45	0.07	0.41	0.09	0.27	0.04	0.23	0.03
2/16/17	1611.3	2485.6	1066.3	363643.9	202.9	2063.3	18.6	233.2	3.67	2.51	3.35	0.50	1.95	0.36	0.08	0.40	0.06	0.39	0.08	0.26	0.03	0.21	0.03
2/16/17	1656.1	2549.6	1113.7	379156.8	212.0	2149.2	20.3	240.9	3.84	2.56	3.42	0.51	2.00	0.38	0.09	0.42	0.06	0.40	0.09	0.27	0.04	0.22	0.03
2/16/17	1557.5	2568.8	1096.4	363233.4	201.2	1994.3	17.9	226.5	3.53	2.42	3.23	0.48	1.85	0.35	0.08	0.37	0.06	0.36	0.08	0.25	0.04	0.22	0.03
2/24/17	1566.6	2519.7	1026.6	366816.7	201.4	2143.4	18.3	235.1	3.81	2.55	3.46	0.51	2.04	0.40	0.08	0.44	0.06	0.42	0.08	0.26	0.04	0.23	0.03
2/24/17	1554.1	2526.2	1011.4	353989.7	194.5	2063.9	17.7	234.2	3.78	2.51	3.43	0.50	1.98	0.40	0.08	0.43	0.06	0.41	0.08	0.26	0.04	0.23	0.03
3/6/17	1704.1	2514.7	1065.4	364683.3	207.4	2154.3	17.8	238.7	3.73	2.64	3.52	0.52	2.01	0.37	0.09	0.42	0.06	0.41	0.09	0.25	0.03	0.21	0.03
3/6/17	1685.2	2494.3	1057.9	358319.5	203.5	2075.4	17.8	233.3	3.66	2.57	3.47	0.51	1.94	0.36	0.08	0.42	0.06	0.38	0.08	0.25	0.03	0.22	0.03
3/6/17	1730.0	2618.5	1081.5	369235.2	207.1	2111.7	20.0	239.0	3.76	2.64	3.53	0.52	2.02	0.37	0.08	0.44	0.06	0.39	0.09	0.25	0.03	0.23	0.03
3/6/17	1754.3	2767.3	1126.1	375902.1	209.2	2174.4	18.1	240.5	3.68	2.60	3.52	0.51	2.02	0.39	0.09	0.44	0.06	0.43	0.09	0.27	0.04	0.22	0.03
3/6/17	1743.5	2768.5	1101.9	366369.4	207.2	2112.0	20.1	238.3	3.70	2.57	3.50	0.50	2.03	0.40	0.09	0.42	0.06	0.42	0.09	0.26	0.04	0.22	0.03
4/16/17	1784.3	2790.7	1119.1	385634.5	217.2	2214.7	18.0	250.6	3.73	2.62	4.26	0.52	2.00	0.41	0.08	0.45	0.07	0.39	0.09	0.26	0.04	0.22	0.03
4/20/17	1870.5	2952.8	1299.9	408431.2	224.2	2355.5	22.7	259.1	4.19	2.87	3.93	0.58	2.23	0.43	0.09	0.49	0.07	0.48	0.10	0.29	0.04	0.23	0.04
4/20/17	2100.0	3260.0	1451.5	447158.7	243.2	2556.9	24.8	281.8	4.42	3.07	4.12	0.58	2.35	0.50	0.10	0.50	0.08	0.47	0.10	0.30	0.04	0.26	0.04
4/20/17	1839.6	2936.7	1360.6	414610.9	232.7	2398.4	22.7	272.4	4.31	3.10	4.29	0.58	2.31	0.49	0.10	0.48	0.07	0.47	0.10	0.31	0.04	0.25	0.04
4/20/17	1887.8	2952.9	1325.1	409029.9	230.4	2458.4	23.1	264.9	4.07	2.86	3.94	0.57	2.35	0.44	0.10	0.45	0.07	0.44	0.10	0.28	0.04	0.24	0.03
9/11/17	1905.4	3051.7	1336.3	415201.3	235.5	2472.2	22.7	270.4	4.17	2.92	4.18	0.57	2.22	0.41	0.09	0.46	0.06	0.45	0.09	0.28	0.04	0.24	0.03
9/11/17	1955.5	2970.1	1305.4	411707.1	239.8	2502.4	23.7	279.7	4.15	2.98	3.90	0.58	2.33	0.45	0.10	0.49	0.07	0.47	0.10	0.30	0.04	0.26	0.04
10/17/17	1898.1	2704.9	1278.0	404856.2	234.0	2478.8	23.2	270.0	4.11	2.88	4.05	0.56	2.26	0.43	0.10	0.49	0.07	0.45	0.10	0.30	0.04	0.25	0.04
12/5/17	2078.6	3108.2	1391.6	428214.0	238.3	2478.1	23.3	262.5	4.31	3.00	4.08	0.57	2.27	0.48	0.10	0.49	0.07	0.43	0.10	0.29	0.04	0.23	0.03
12/8/17	2078.6	3108.2	1391.6	428214.0	238.3	2478.1	23.3	262.5	4.31	3.00	4.08	0.57	2.27	0.48	0.10	0.49	0.07	0.43	0.10	0.29	0.04	0.23	0.03
12/8/17	2057.4	3442.8	1410.2	471275.6	258.9	2574.2	24.8	328.2	5.02	3.04	4.11	0.64	2.41	0.45	0.10	0.48	0.07	0.47	0.10	0.30	0.04	0.26	0.04
12/8/17	1941.2	3314.5	1392.0	466927.6	252.0	2548.1	25.1	310.0	4.81	2.89	3.88	0.57	2.29	0.43	0.09	0.44	0.07	0.44	0.10	0.30	0.04	0.24	0.04
1/12/18	1960.9	3018.4	1345.6	409477.3	255.5	2641.4	25.5	293.3	4.84	3.17	3.53	0.63	2.56	0.50	0.11	0.51	0.08	0.52	0.12	0.34	0.04	0.26	0.03
1/12/18	1902.9	2830.4	1290.1	408113.4	239.6	2502.4	23.7	284.9	4.67	3.30	3.55	0.63	2.49	0.49	0.10	0.51	0.08	0.52	0.11	0.31	0.05	0.28	0.04
1/12/18	2061.0	3128.8	1325.9	431976.8	253.1	2628.5	25.0	288.4	4.64	3.16	4.23	0.62	2.45	0.47	0.11	0.53	0.08	0.48	0.11	0.31	0.04	0.26	0.04
1/12/18	2142.9	3335.6	1452.8	463011.8	262.1	2627.9	24.0	291.3	4.59	3.08	3.84	0.58	2.40	0.44	0.09	0.49	0.07	0.44	0.10	0.28	0.04	0.24	0.03
1/12/18	2087.8	3268.0	1396.4	454762.3	259.6	2594.3	25.0	300.7	4.74	3.18	4.38	0.61	2.44	0.48	0.10	0.52	0.08	0.47	0.10	0.31	0.04	0.25	0.04
1/12/18	1965.7	2996.6	1286.9	428441.6	253.5	2606.7	25.0	299.6	4.80	3.23	4.30	0.64	2.50	0.49	0.10	0.55	0.08	0.50	0.11	0.33	0.05	0.27	0.04
1/25/18	2138.8	3253.2	1375.7	451418.2	257.4	2721.4	26.2	299.4	4.78	3.21	4.17	0.63	2.52	0.48	0.10	0.53	0.08	0.49	0.11	0.31	0.04	0.28	0.04
1/25/18	1842.1	2955.5	1253.9	403305.9	233.9	2463.2	23.2	318.3	5.04	3.56	4.77	0.71	2.81	0.58	0.13	0.63	0.09	0.60	0.12	0.40	0.06	0.32	0.05
1/25/18	1830.6	2974.2	1272.3	405880.4	237.5	2526.9	23.0	329.0	5.30	3.67	4.90	0.72	2.89	0.57	0.13	0.65	0.10	0.67	0.14	0.44	0.06	0.37	0.05
3/9/18	2216.1	3369.0	1411.1	465852.6	267.7	2770.9	26.6	309.8	4.63	3.22	4.66	0.65	2.53	0.49	0.10	0.54	0.08	0.51	0.11	0.33	0.04	0.28	0.03
3/9/18	2189.3	3366.1	1430.9	468584.8	269.8	2780.7	26.6	317.6	4.71	3.28	4.63	0.64	2.57	0.50	0.11	0.53	0.08	0.52	0.11	0.33	0.04	0.28	0.03
3/9/18	2210.2	3429.1	1461.2	481411.5	275.9	2813.7	27.1	330.2	4.77	3.39	4.71	0.67	2.63	0.51	0.11	0.56	0.08	0.52	0.11	0.34	0.04	0.28	0.03
3/16/18	1767.8	2745.7	1141.8	382970.5	218.1	2270.2	18.9	259.2	3.86	2.73	3.65	0.55	2.14	0.41	0.09	0.46	0.07	0.45	0.09	0.27	0.04	0.24	0.04
3/16/18	1806.3	2789.7	1215.8	398154.0	220.6	2280.5	18.6	255.3	4.08	2.79	3.75	0.55	2.13	0.41	0.09	0.45	0.07	0.43	0.09	0.27	0.04	0.23	0.03
3/16/18	1772.9	2782.5	1248.3	408738.6	225.9	2327.0	18.9	274.7	4.41	3.02	3.62	0.59	2.30	0.45	0.10	0.48	0.07	0.45	0.10	0.29	0.04	0.24	0.04
3/23/18	1619.6	2553.7	1154.2	377976.1	209.9	2192.7	17.9	249.4	3.93	2.71	3.65	0.52	2.08	0.40	0.09	0.44	0.06	0.41	0.09	0.26	0.04	0.22	0.03
3/23/18	1783.7	2730.1	1176.2	384917.2	210.8	2243.5	17.9	242.2	4.00	2.77	3.80	0.54	2.13	0.41	0.09	0.45	0.07	0.43	0.09	0.27	0.04	0.23	0.03
3/23/18	1821.0	2788.1	1235.5	393999.6	214.5	2275.5	18.0	244.7	4.00	2.79	3.75	0.53	2.13	0.41	0.09	0.46	0.07	0.42	0.09	0.27	0.04	0.23	0.03
3/23/18	1779.7	2772.4	1213.5	393246.3	210.9	2226.2	17.9	246.9	3.93	2.74	3.70	0.53	2.08	0.39	0.09	0.44	0.06	0.42	0.09	0.27	0.04	0.22	0.03
5/8/18	1654.3	2629.3	1109.1	371217.0	206.1	2196.8	17.9	244.0	3.82	2.78	3.73	0.53	2.24	0.43	0.09	0.47	0.07	0.42	0.09	0.26	0.04	0.24	0.03
5/8/18	1526.3	2288.8	937.6	327085.6	185.4	2040.5	17.1	216.5	3.98	2.75	3.72	0.53	2.15	0.38	0.09	0.47	0.07	0.38	0.08	0.24	0.04	0.20	0.03
5/8/18	1569.6	2333.1	940.5	322329.6	181.2	2058.0	16.4	210.3	3.77	2.75	3.74	0.52	2.11	0.42	0.10	0.46	0.07	0.37	0.08	0.23	0.03	0.20	0.03
5/8/18	1566.4	2493.0	1048.8	352064.4	195.5	2072.3	17.2	229.4	3.68	2.59	3.57	0.51	1.99	0.38	0.08	0.42	0.06	0.42	0.09	0.25	0.04	0.22	0.03
5/14/18	1600.4	2475.9	1024.6	345958.1	194.7	2025.5	16.9	225.0	3.66	2.54	3.46	0.51	2.05	0.38	0.09	0.41	0.06	0.41	0.09	0.26	0.04	0.22	0.03
5/14/18	1727.9	2648.7	1176.6	374950.6	207.9	2152.1	17.5	241.6	4.13	2.78	3.72	0.54	2.11	0.41	0.09	0.44	0.06	0.45	0.09	0.27	0.04	0.23	0.03
5/14/18	1766.9	2817.1	1229.9	381902.5	205.1	2094.6	16.8	247.2	3.82	2.84	3.75	0.54	2.15	0.41	0.09	0.46	0.07	0.43	0.09	0.26	0.04	0.23	0.03

5/15/18	1574.3	2490.7	1041.9	350847.0	194.4	2045.7	16.6	226.1	3.65	2.56	3.48	0.52	1.94	0.35	0.08	0.40	0.07	0.38	0.08	0.26	0.03	0.22	0.03
5/15/18	1513.2	2407.9	1017.6	340449.1	184.8	1932.0	16.3	223.9	3.65	2.61	3.43	0.49	1.94	0.40	0.09	0.45	0.06	0.40	0.08	0.26	0.04	0.20	0.03
ave	1813.0	2836.6	1212.7	401346.4	222.1	2310.6	20.8	261.2	4.1	2.8	3.8	0.6	2.2	0.4	0.1	0.5	0.1	0.4	0.1	0.3	0.0	0.2	0.0
std	156.4	306.2	147.9	37374.5	23.3	230.5	3.3	29.4	0.4	0.3	0.4	0.1	0.3	0.0	0.0	0.0	0.0	0.1	0.0	0.0	0.0	0.0	0.0
Relative std	9	11	12	9	11	10	16	11	11	10	10	10	14	12	10	10	11	12	11	12	12	19	11
% recovery	-11.1	2.0	7.6	6.3	6.3	3.7	15.7	1.2	-1.6	-20.5	-5.5	3.0	-16.7	-16.4	-6.4	8.8	-14.0	-15.2	5.3	-16.7	-2.8	-21.6	-14.6

1: Barca, D., Belfiore, C.M., Crisci, G.M., La Russa, M.F., Pezzino, A., Ruffolo, S.A., 2011. A new methodological approach for the chemical characterization of black crusts on building stones: a case study from the Catania city centre (Sicily, Italy). J. Anal. At. Spectrom. 26, 1000. https://doi.org/10.1039/c0ja00226g

APPENDIX 3.1: CERIUM OXIDATION THERMODYNAMIC MODEL AND CALIBRATION

The behavior of REYs in the modern ocean has been well characterized. Trivalent Ce can be oxidized to the very insoluble Ce (IV) state on the surface of ferromanganese oxyhydroxides in the presence of oxygen, and this process is rapid in shallow water through bacterial mediation and abiotic oxidation (Moffett, 1994a, 1994b, 1990). The preferential adsorption of Ce(IV) onto Fe-Mn oxyhydroxides leaves residual seawater depleted in Ce relative to other trivalent REY (German and Elderfield, 1990). Hence a negative Ce anomaly is ubiquitous in the well-oxidized open ocean, whereas the REY distribution in modern anoxic water, (e.g. Cariaco Trench, Black Sea) clearly illustrates the paucity of dissolved Ce (German et al., 1991; German and Elderfield, 1990). On the other hand, the extent of a negative Ce anomaly in the ocean also varies with water depth. For example, the Ce anomaly profile of the North Pacific Ocean shows a sharp decrease at the surface ocean, and stabilizes at intermediate levels and in the deep ocean. This observation also supports the contention the oxidation of Ce primarily takes place in shallow water (Fig. A3.2.1). The use of the Ce anomaly as a paleo-redox proxy is not well calibrated, especially in distinguishing between suboxic and oxic redox conditions. In this study, we endeavor to understand the relationship between the Ce anomaly and dissolved oxygen in the ocean using thermodynamic calculations.

The thermodynamics of chemical equilibria is strictly valid only for a closed system. To apply the thermodynamic predictions to either the open ocean or a local basin, we utilize thermodynamic principles to the maximum possible degree. First, we summarize the dissolved Ce speciation in the seawater under a normal range of pe-pH conditions (Table A3.2). In thermodynamic calculations, we use C_{Ce} to represent total dissolved trivalent Ce, which can be estimated using the relative coefficient of each complexed species (Table A3.1). Next, with

reference to the dominant dissolved Ce species, we considered the major complexation reactions of trivalent Ce with phosphate (PO_4^{3-}), carbonate (CO_3^{2-}) and hydroxide (OH^-) (Table A3.2). The carbonate complexations ($Ce(CO_3)^+$ or $Ce(CO_3)_2^-$) become predominant at near-neutral to basic pH (Cantrell and Byrne, 1987; Nakada et al., 2017). Free Ce^{4+} would not exist within the stability field of water, but it is known to hydrolyze very strongly. $Ce(OH)_4$ can exist in the real ocean but it is predicted to be metastable relative to CeO_2. Subsequently, we use Ce^{3+} and oceanic dissolved oxygen as a redox pair for the Ce oxidation in shallow-water environments. We can then calculate stability constants for a series of reactions based on different Ce complexations and oxidized Ce species. The final reactions are listed in Table A3.2, reaction (19) – (24). We also build up eleven Ce oxidation thermodynamic models based on these equations, as expressed in Model #1-#11. Finally, we further calibrate our model using a reconstructed oceanographic profile containing dissolved rare-earth elements, phosphorite, pH, alkalinity, dissolved oxygen, and temperature. Below are detailed derivations for model #1-#11, All reactions used in the derivations can be found in Table A3.2.

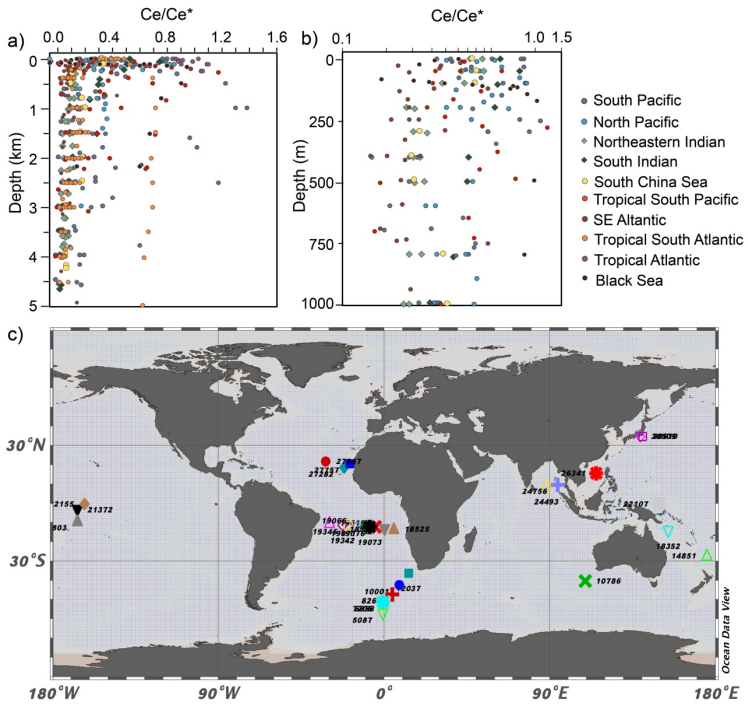

Figure A3.1.1 Compilation of Ce anomaly data in the modern ocean.

a). Compilations of modern ocean depth profiles of the Ce anomaly: South Pacific Ocean (Alibo and Nozaki, 1999; Molina-Kescher et al., 2014; Zhang and Nozaki, 1996); North Pacific Ocean (Zhang and Nozaki, 1998); northeastern Indian Ocean (Nozaki and Alibo, 2003a); South Indian Ocean (Nozaki and Alibo, 2003b); South China Sea (Alibo and Nozaki, 2000); Tropical South Pacific Ocean (Molina-Kescher et al., 2018); southeast Atlantic Ocean (Garcia-Solsona et al., 2014); tropical South Atlantic Ocean (Zheng et al., 2016); tropical Atlantic Ocean (Tachikawa et al., 1999) Black Sea (German et al., 1991). b). Enlarged compilation of modern ocean depth profile of the Ce anomaly, with only 0–1km displayed. *x*-axis is in log scale. c). World map of station numbers and locations used to extract annual dissolved oxygen in World Ocean Atlas 13. Ce anomalies are recalculated in this study using (eq. 1) using compiled REE concentrations. For the Black Sea, we use Ce/Ce* = Ce^2/(La*Pr) to calculate the Ce anomaly because Pr was not measured in the original study.

Complexation with phosphorus ion

This idea is based on the equation developed in Liu et al. (1988) with some modification. In this model, Ce^{3+} is complexed extensively by PO_4^{3-} as described in reaction (5). Ce^{3+} is oxidized to Ce^{4+} (reaction (8)) and quickly forms $Ce(OH)_4$ (reaction (10)). The assumption here is that dissolved oxygen is the electron acceptor (reaction (16)). With these four equations plus equation (18), we have the following:

$$CePO_4^0 + 3OH^- + \frac{1}{4}O_2 + \frac{1}{2}H_2O = PO_4^{3-} + Ce(OH)_4, logK = 17.2$$

$$\log\{CePO_4^0\} = 24.8 + \log\{PO_4^{3-}\} + \log\{Ce(OH)_4\} - 3pH - 0.25\,log(pO_2)$$

Liu et al. (1988) calculated that $a_{Ce(OH)_4} \sim 1.6 \times 10^{-4}$,

Therefore,

$$\log\{0.1 * C_{Ce}\} \sim log\{CePO_4^0\} = 21 + \log\{PO_4^{3-}\} - 3pH - 0.25\,log(pO_2) \quad \text{(Model \#1)}$$

Because it is difficult to obtain reliably the coefficient for $Ce(OH)_4$, we also consider that $Ce(OH)_4$ quickly forms CeO_2 as indicated in reaction (14). Thus, we have the following:

$$CePO_4^0 + 3OH^- + \frac{1}{4}O_2 = CeO_2 + \frac{3}{2}H_2O, logK = 30.58$$

$$\log\{0.1 * C_{Ce}\} \sim \{CePO_4^0\} = 11.42 + \log\{PO_4^{3-}\} - 3pH - 0.25\,log(pO_2) \quad \text{(Model \#2)}$$

Model #2 differs substantially from model #1, and also does not apply to modern ocean. If we calculate this through reactions (5), (9), (18), we have the following reaction,

$$CePO_4^0 + \frac{1}{4}O_2 + \frac{3}{2}H_2O = PO_4^{3-} + 3H^+ + CeO_2, \qquad logk = -17.9$$

$$\log\{0.1 * C_{Ce}\} \sim \{CePO_4^0\} = 17.9 + \log\{PO_4^{3-}\} - 3pH - 0.25\,log(pO_2) \text{ (Model \#3)}$$

We also calibrated this model at 10°C to see assess the influence of temperature.

For $H_2O = \frac{1}{2}O_2 + 2H^+ + 2e^-$ $\qquad E^0 = 0.84$ ($For\ seawater\ at\ 10℃, O_2 = 0.2, pH = 8.1$

$$Eh = E^0 + \frac{0.056}{4} log(pO_2) + 0.056\log\{H^+\}$$

When $pO_2 = 0.2, pH = 8.1, T =$ 10℃, $Eh = 0.38V$.

$Eh = 0.84 + 0.014\, logpO_2 + 0.056\log\{H^+\}$ (eq. 4)

For reaction (6), K = $\frac{\{CePO_4^0\}\cdot\{OH^-\}^4}{\{Ce(OH)_4\}\cdot\{PO_4^{-3}\}\cdot\{e^-\}}$, Thus, $\{e^-\} = \frac{\{CePO_4^0\}\cdot\{OH^-\}^4}{\{Ce(OH)_4\}\cdot\{PO_4^{-3}\}\cdot K}$

$-log\{e^-\} = pe = logK + log\frac{\{Ce(OH)_4\}\cdot\{PO_4^{-3}\}}{\{CePO_4^0\}\cdot\{OH^-\}^4}$

$Eh = \frac{2.3RT}{F} = 0.056\, pe\ (T = 10℃) = -0.62 + 0.056log\frac{\{Ce(OH)_4\}\cdot\{PO_4^{-3}\}}{\{CePO_4^0\}\cdot\{OH^-\}^4}$ (eq.5)

For $K(CePO_4^0) = 10^{-16}$ (Rao et al., 1970), measured $\{Ce(OH)_4\} = \sim 1.6 \times 10^{-4}$

Substituting (eq. 4) into (eq. 5),

$$log\{CePO_4^0\} = 24.9 + log\{PO_4^{-3}\} - 0.25\log(pO_2) - 3pH$$

For $K(CePO_4^0) = 10^{-18.52}$ (Smith and Martell, 1976), $\{Ce(OH)_4\} = \sim 10^{-6}$

$\log\{0.1 * C_{Ce}\} \sim log\{CePO_4^0\} = 24.9 + \log\{PO_4^{3-}\} - 3pH - 0.25\, log(pO_2)$ (Model #4)

for $\{Ce(OH)_4\} = \sim 1.6$ x 10^{-4},

$\log\{0.1 * C_{Ce}\} \sim log\{CePO_4^0\} = 22.6 + log\{PO_4^{-3}\} - 0.25\log(pO_2) - 3pH$ (Model #5)

In Liu et al., (1988), an average of $(PO_4^{3-}) = 10^{-9.4}$ in seawater was used as a substitute for $\{PO_4^{-3}\}$ in (P5),

$\log\{0.1 * C_{Ce}\} \sim log\{CePO_4^0\} = 13.2 - 0.25\ log\ (pO_2) - 3pH$ (Model #6)

Complexation with carbonate ion

REY complexation is generally dominated by the formation of carbonate complexes MCO_3^+, and then $M(CO_3)_2^-$ (Byrne and Sholkovitz, 1996; Cantrell and Byrne, 1987; Luo and

Byrne, 2004; Ohta and Kawabe, 2000; Tang and Johannesson, 2003).These phenomena are described in reactions (2) and (4). For oxidation of trivalent Ce, this model approach uses reaction (8) or (9).

$$\log\{0.157 * C_{Ce}\} \sim \log\{Ce(CO_3)_2^-\} = 18.13 + 2\log\{CO_3^{2-}\} - 3pH - 0.25log(pO_2)$$

(Model #11)

We summarized the Ce oxidation model in the following equation:

$$\log(\gamma_i\ C_{Ce}) = K - \frac{1}{4}log(pO_2) + \partial_i \log\{\mathcal{X}_i\} - \beta_i pH \quad \text{(eq. 4)}$$

C_{Ce}: total dissoved trivalent Ce

$\gamma_i = \frac{(\{CePO_4^0\},\{CeCO_3^+\},\{Ce(CO_3)_2^-\})}{C_{Ce}}$: relative activity coefficient

$(\partial_i, \mathcal{X}_i)$ are expressed as $(1, PO_4^{3-})$, $(1, HCO_3^-)$, $(2, CO_3^{2-})$

$\beta_i \in (1,2,3)$

Therefore,

$$C_{Ce} \sim \frac{1}{\{pO_2\}^{\frac{1}{4}}}$$

$$C_{Ce} \sim \mathcal{X}_i^{\partial_i}$$

$$\log(C_{Ce}) \sim -\beta_i pH$$

If we assume the Nd and Pr concentration in the water column does not change significantly over the OAE 2 period, then the Ce anomaly mainly reflects changes in C_{Ce} and we can use the following relationship to quantify changes in pO_2, pH and complexation ligands like PO^{3-}.

$$\frac{Ce}{Ce^*} \sim C_{Ce} \sim \frac{1}{\{pO_2\}^{\frac{1}{4}}} \quad \text{(eq.5)}$$

$$\frac{Ce}{Ce^*} \sim C_{Ce} \sim \mathcal{X}_i^{\partial_i} \quad \text{(eq.6)}$$

$\frac{Ce}{Ce^*} \sim C_{Ce} \sim \{H^+\}^{\beta_i}$ (eq.7)

3.3 Carbonic acid equilibrium

From reaction (25),

$$\mathrm{K}_H = \frac{\{H_2CO_3(aq)\}}{p_{CO_2}\{H_2O\ (l)\}} = \frac{\{H_2CO_3(aq)\}}{p_{CO_2}\gamma_{H_2O}\chi_{H_2O}} = \frac{\{H_2CO_3(aq)\}}{p_{CO_2}\cdot 0.981}$$

$$\{H_2CO_3(aq)\} = 0.981 \cdot \mathrm{K}_H \cdot p_{CO_2}$$

From reaction (26),

$$\mathrm{K1} = \frac{\{HCO_3^-\}\{H^+\}}{\{H_2CO_3(aq)\}} = \frac{\{HCO_3^-\}\{H^+\}}{0.981 \cdot \mathrm{K}_H \cdot p_{CO_2}}$$

$$\{HCO_3^-\} = \frac{0.981 \cdot \mathrm{K}_1 \cdot \mathrm{K}_H \cdot p_{CO_2}}{\{H^+\}}$$

From reaction (27),

$$\mathrm{K}_2 = \frac{\{CO_3^{2-}\}\{H^+\}}{\{HCO_3^-(aq)\}} = \frac{\{CO_3^{2-}\}\{H^+\}^2}{0.981\cdot \mathrm{K}_1\cdot \mathrm{K}_H\cdot p_{CO_2}}$$

$$\{CO_3^{2-}\} = \frac{0.981 \cdot \mathrm{K}_1 \cdot \mathrm{K}_2 \cdot \mathrm{K}_H \cdot p_{CO_2}}{\{H^+\}^2}$$

$$\mathrm{CA}\ (\{HCO_3^-\} + 2\{CO_3^{2-}\}) \approx 0.958\ \mathrm{TA}\ (\{HCO_3^-\} + \{CO_3^{2-}\} + \{\mathrm{B}(OH)_4^-(aq)\})$$

$$\partial 1 = \frac{\{HCO_3^-\}}{TA} = \left[\frac{\{H^+\}}{\mathrm{K}_1} + \frac{\mathrm{K}_2}{\{H^+\}} + 1\right]^{-1}$$

$$\partial 2 = \frac{\{CO_3^{2-}\}}{TA} = \left[\frac{\{H^+\}^2}{\mathrm{K}_1\mathrm{K}_2} + \frac{\{H^+\}}{\mathrm{K}_2} + 1\right]^{-1}$$

CA means carbonate alkalinity and TA means total alkalinity.

Table A3.1 The speciation of Ce in seawater (Salinity = 35, T = 25°C, pH = 8.2).

Dissolved species	% of total Ce	Activity coefficient	Relative activity	Reference
Ce^{3+}	3.53	0.049	0.173	
$CeHCO_3^{2+}$	0.178	0.289	0.052	
$CeCO_3^{+}$	56.5	0.794	44.9	
$Ce(CO_3)_2^{-}$	24.2	0.648	15.7	
$Ce(OH)_2^{+}$	5.91	0.289	1.71	De Baar et al., (1988)
$Ce(OH)_2^{+}$	5.33	0.794	4.23	
$Ce(OH)_3^{0}$	0.166	1.0	0.166	
$CeSO_4^{+}$	1.88	0.794	1.49	
$Ce(SO_4)_2^{-}$	0.245	0.648	0.159	
$CePO_4^{0}$	Less than 0.1	-	-	Liu et al., (1988)
$Ce(OH)_4$	0.126	-	-	Calculated based on Nozaki (2001b)

Table A3.2 Selected stability constants (K^0) of reactions at 25°C, standard pressure, and reaction constant calculated or compiled from literature (β, k).

No.	Reaction	logβ / log k	Log K^0	Reference
(1)	$Ce^{3+} + 2CO_3^{2-} = Ce(CO_3)_2^{-}$	9.26 (I = 0.68)	17.53	Cantrell and Byrne, (1987)
		5.41 (I = 0.68)	7.61	Cantrell and Byrne, (1987)
(2)	$Ce^{3+} + CO_3^{2-} = CeCO_3^{+}$	6.95		Millero, (1992)
			7.31	Liu and Byrne, (1995)
			7.40	Lee and Byrne, (1993)
			7.43	
(3)	$Ce^{3+} + 2HCO_3^{-} = Ce(CO_3)_2^{-} + 2H^{+}$	7.78 (I = 0.68)	8.9	[1]Calculated based on Luo and Byrne, (2004)
(4)	$Ce^{3+} + HCO_3^{-} = CeCO_3^{+} + H^{+}$	2.34 (I = 0.68)	3.27	[1]Calculated based on Luo and Byrne, (2004)
(5)	$Ce^{3+} + PO_4^{3-} = CePO_4^{0}$		18.5	Ehrlich, (1968)
			16	Byrne and Bingler, (1989)
(6)	$Ce^{3+} + 4OH^{-} = Ce(OH)_4 + e^{-}$	29.0		Liu et al, (1988)
(7)	$Ce(OH)_4 + PO_4^{3-} + e^{-} = CePO_4^{0} + 4OH^{-}$	10.5		Liu et al, (1988)
(8)	$Ce^{3+} = Ce^{4+} + e^{-}$	-21.6		Ehrlich, (1968)
(9)	$Ce^{3+} + 2H_2O = CeO_2 + 4H^{+} + e^{-}$	-21.3		De Baar et al, (1988)
(10)	$Ce^{4+} + 4OH^{-} = Ce(OH)_4$	50.6		Sillen and Martell, (1964)
(11)	$Ce^{4+} + 4H_2O = Ce(OH)_4 + 4H^{+}$		-5.6	Sillen and Martell, (1971)
(12)	$Ce^{4+} + 2H_2O = CeO_2 + 4H^{+}$		8.14	De Baar et al. (1988)
(14)	$Ce(OH)_4 = CeO_2 + 2H_2O$		13.56	De Baar et al. (1988)
(15)	$CO_2 + H_2O = H_2CO_3$	-1.53		
(16)	$\frac{1}{2}H_2O = \frac{1}{4}O_2 + H^{+} + e^{-}$		-20.7	Sillen and Martell, (1971)
(17)	$H_2O_2 = O_2 + 2H^{+} + 2e^{-}$		-23.0	Sillen and Martell, (1964)
(18)	$H^{+} + OH^{-} = H_2O$		14.0	
(19)	$CePO_4^{0} + 3OH^{-} + \frac{1}{4}O_2 + \frac{1}{2}H_2O = PO_4^{3-} + Ce(OH)_4$		17.2	Calculated in this study

(20)	$CePO_4^0 + \frac{1}{4}O_2 + \frac{3}{2}H_2O = PO_4^{3-} + 3H^+ + CeO_2$		-17.9	Calculated in this study
(21)	$CeCO_3^+ + \frac{3}{2}H_2O + \frac{1}{4}O_2 = HCO_3^- + 2H^+ + CeO_2$		-2.94	Calculated in this study
(22)	$CeCO_3^+ + \frac{3}{2}H_2O + \frac{1}{4}O_2 = CO_3^{2-} + 3H^+ + CeO_2$		-7.91	Calculated in this study
(23)	$Ce(CO_3)_2^- + \frac{3}{2}H_2O + \frac{1}{4}O_2 = 2HCO_3^- + H^+ + CeO_2$		-8.38	Calculated in this study
(24)	$Ce(CO_3)_2^- + \frac{3}{2}H_2O + \frac{1}{4}O_2 = 2CO_3^{2-} + 3H^+ + CeO_2$	-9.86 (I=0.68)	-18.13	Calculated in this study
(25)	$CO_2 + H_2O = H_2CO_3$		-1.53	
(26)	$H_2CO_3 = HCO_3^- + H^+$	-6.1 (T=10°C)	-6.0	Riley and Skirrow, (1975)
(27)	$HCO_3^- = CO_3^{2-} + H^+$		-9.11	

Notes: [1]Calculated using the data of Cantrell and Byrne (1987) at I = 0.68m.

$log^H_{CO_3}\beta_1 = log^H_{CO_3}\beta_1^0 - 4.088\frac{I^{0.5}}{1+3.033I^{0.5}} + 0.042I$ (Luo and Byrne, 2004)
In Seawater, $I = 0.68$, $log^H_{CO_3}\beta_1^0\ (Ce) = 3.27$, $log^H_{CO_3}\beta_2^0\ (Ce) = 8.90$
For reaction (3), $log^H_{CO_3}\beta_2 = \frac{\{Ce(CO_3)_2^-\}\{H^+\}^2}{\{Ce^{3+}\}\{HCO_3^-\}^2} = 7.78$
For reaction (4), $log^H_{CO_3}\beta_1 = \frac{\{CeCO_3^+\}\{H^+\}}{\{Ce^{3+}\}\{HCO_3^-\}} = 2.34$

Model calibration

To determine whether our model agrees with real-world observation, we compile a dataset of REY profiles in the modern ocean. Part of dissolved oxygen is compiled from literature and the rest is estimated using World Ocean Atlas 13 (WOA 13). We navigate WOA 13 using Ocean Data View to locate nearest station to each site where REY profiles were measured, and extract annual average oxygen at each depth. Ce anomalies are recalculated following eq.3 to be consistent in this study. As shown in Fig A3.1.2a, the majority of Ce anomalies are lower than 0.4 in oxic regions. Higher values only occur in suboxic to anoxic water masses, including the tropical South Atlantic Ocean and the Black Sea. This observation indicates that the Ce anomaly has distinctive behavior in oxic and anoxic environments. Dissolved free oxygen is assumed to oxidize dissolved Ce, so that all calculated models #1- #11

give the same relationship for the Ce anomaly and dissolved oxygen, as illustrated in eq. 4. Hence, we also plot the Ce anomaly *v.s.* one over the square root of the oxygen partial pressure in Fig. A3.1.2. Data showing high oxygen content ($pO_2 > 0.05$) mostly have a Ce anomaly lower than 0.4, with few outliers. Because part of oxygen data comes from estimation based on WOA 13, those high Ce anomalies in oxic waters may result from the offset between the actual onsite dissolved oxygen and estimation. As pO_2 decreases below 0.01, the Ce anomaly progressively increases to 1.0. However, the absolute value of the Ce anomaly does not necessarily correlate with dissolved oxygen in oxic environments. By contrast, under suboxic to anoxic environment, the value of the Ce anomaly is sensitive to minor changes in dissolved oxygen. This phenomenon is well illustrated in the depth profiles for the Ce anomaly and dissolved oxygen in the Black Sea (Fig. A3.1.3). From the sea surface to about 75m depth, the Ce anomaly decreases from 0.5 to 0.1. Below 75 m, with progressive loss of dissolved oxygen in the water column, the Ce anomaly increases from 0.1 to ~1.0, stabilizing between 0.8-1.0 below the sulfidic interface.

We further examine two profiles to calibrate Model #1–#11, including the South China Sea (Tables A3.3), representing the open ocean, and the Black Sea (Tables A3.4) representing an anoxic to euxinic basin. Dissolved rare-earth element concentrations are from Alibo and Nozaki. (2000) and German et al. (1991), respectively. Temperature, dissolved oxygen (annual average), and phosphate concentrations for the depth profiles are compiled in from the references and estimated in WOA 13 using Ocean Data View navigation. Alkalinity and pH are obtained from National Oceanic and Atmospheric Administration (NOAA) (Yaitskaya, 2011). We use dissolved oxygen, phosphorite concentration, pH and alkalinity to estimate total dissolved Ce using Model #1- #11 and compare them to the measured dissolved Ce (Fig. A3.1.4). Model #3 gives the best fit to dissolved Ce in the upper ocean(100–500m) compared to measured

concentrations in both profiles. For the South China Sea profile, the error given in Model #3 for the Ce concentration is smaller than 100% at 0–100m level, and increases to 5000% due to the large variations in phosphate concentration. However, models based on carbonate complexations have more consistent errors at different depth because of minor variations in alkalinity. Errors in the best-fit model, namely Model #11, are all within -80% to -100% independent of depth. For the Black Sea, errors in Model #3 vary from -48% to -95%. However, Model #11 does not work so well here because alkalinity is about 0.1% of that in the open ocean. At 150 and 200m, where there is almost no oxygen, Model #9 has an error of 130% and 213%, respectively. Larger offsets seen in other models may be due to influences from temperature, thermodynamic data quality, or other processes controlling the Ce concentration including dust input and adsorption.

Decrease in temperature may influence the major-element complexations. For example, under 15°C hydrolysis through the formation of $Ce(OH)_2^+$ is enhanced and formation of $Ce(CO_3)_2^-$ is reduced. However, Cantrell and Byrne. (1987) reported only modest temperature effect: the overall Ce speciation at 15°C is found to be very similar to that at 25°C. Decrease in temperature may also influence the stability constants for reactions. As we can see in (eq. 4), even though the constant K would change with temperature, the relationship between dissolved Ce concentration and other variables will not change along with temperature. Thus, we can use the relative Ce anomaly change during OAE 2 to estimate the extent that the ocean lost dissolved oxygen, and potentially estimate changes in pH, phosphate and alkalinity. Fig A3.1.5 is an example of model output when increasing the Ce anomaly tenfold.

Table A3.3 Dissolved rare earth elements and hydrographic properties in the South China Sea

Depth	Temperature	[1]Dissolved O_2	PO_4^{3-}	Alkalinity	Ce	pH	H^+	∂1	HCO_3^-	∂2	CO_3^{2-}	Ce	log{C_{Ce}}	pO_2	log (PO_2)	#1	#2	#3	#4	#5	#6	#7	#8	#9	#10	#11
m	℃	ml/l	uM	μeq/L	pmol/kg		mol/L		mol/L		mol/L	(mol/L)				Model calculated log{C_{Ce}}										
0	26.8	4.5368	0.15	2204	8.09	8.253	5.6E-09	0.87	2.0E-03	0.12	2.8E-04	8.1E-12	-11.09	0.3406	-0.47	-9.5	-19.0	-12.6	-5.6	-7.9	-10.4	-15.8	-19.9	-4.3	-21.1	-12.9
50	26.21	4.579	0.1	2282	9.31	8.273	5.3E-09	0.87	2.1E-03	0.13	3.0E-04	9.3E-12	-11.03	0.3478	-0.46	-9.7	-19.3	-12.8	-5.8	-8.1	-10.5	-15.8	-20.0	-4.3	-21.1	-12.9
100	18.61	3.463	0.87	2290	6.61	8.122	7.6E-09	0.90	2.2E-03	0.09	2.2E-04	6.6E-12	-11.18	0.2754	-0.56	-8.3	-17.9	-11.4	-4.4	-6.7	-10.0	-15.5	-19.6	-4.1	-20.9	-12.7
297	11.82	2.6915	1.58	2326	3.2	7.922	1.2E-08	0.93	2.3E-03	0.06	1.5E-04	3.2E-12	-11.49	0.1884	-0.72	-7.4	-17.0	-10.5	-3.5	-5.8	-9.4	-15.0	-19.2	-3.9	-20.6	-12.5
398	10.12	2.361	1.83	2312	3.01	7.85	1.4E-08	0.94	2.3E-03	0.05	1.2E-04	3.0E-12	-11.52	0.1775	-0.75	-7.1	-16.7	-10.2	-3.2	-5.5	-9.2	-14.9	-19.0	-3.8	-20.5	-12.4
495	8.75	2.1429	2.08	2362	3.31	7.865	1.4E-08	0.93	2.3E-03	0.05	1.3E-04	3.3E-12	-11.48	0.1630	-0.79	-7.1	-16.7	-10.2	-3.2	-5.5	-9.2	-14.9	-19.0	-3.8	-20.5	-12.4
795	5.75	1.9388	2.46	2428	5.51	7.668	2.1E-08	0.95	2.4E-03	0.03	8.7E-05	5.5E-12	-11.26	0.1449	-0.84	-6.4	-16.0	-9.5	-2.5	-4.8	-8.6	-14.5	-18.6	-3.5	-20.3	-12.2
997	4.53	2.0173	2.62	2406	8.03	7.673	2.1E-08	0.95	2.4E-03	0.03	8.7E-05	8.0E-12	-11.10	0.1413	-0.85	-6.4	-16.0	-9.5	-2.5	-4.8	-8.6	-14.5	-18.6	-3.5	-20.3	-12.2
1488	2.93	2.2297	2.7	2417	8.96	7.657	2.2E-08	0.95	2.4E-03	0.03	8.4E-05	9.0E-12	-11.05	0.1630	-0.79	-6.3	-15.9	-9.4	-2.4	-4.7	-8.6	-14.5	-18.6	-3.5	-20.3	-12.2
1981	2.52	2.3085	2.66	2457	11.95	7.665	2.2E-08	0.95	2.4E-03	0.03	8.7E-05	1.2E-11	-10.92	0.1739	-0.76	-6.4	-16.0	-9.5	-2.5	-4.8	-8.6	-14.5	-18.6	-3.5	-20.3	-12.2
2473	2.39	2.5016	2.65	2455	12.85	7.669	2.1E-08	0.95	2.4E-03	0.03	8.8E-05	1.3E-11	-10.89	0.1812	-0.74	-6.4	-16.0	-9.5	-2.5	-4.8	-8.6	-14.5	-18.6	-3.5	-20.3	-12.2
2963	2.37	2.5402	2.6	2458	5.99	7.676	2.1E-08	0.95	2.4E-03	0.03	8.9E-05	6.0E-12	-11.22	0.1942	-0.71	-6.4	-16.0	-9.5	-2.5	-4.8	-8.7	-14.5	-18.6	-3.5	-20.3	-12.2
3941	2.43	2.6435	2.61	2455	5.58	7.677	2.1E-08	0.95	2.4E-03	0.03	8.9E-05	5.6E-12	-11.25	0.1957	-0.71	-6.4	-16.0	-9.5	-2.5	-4.8	-8.7	-14.5	-18.6	-3.5	-20.3	-12.2
4182	2.46	2.6495	2.63	2456	6.25	7.68	2.1E-08	0.95	2.4E-03	0.04	9.0E-05	6.3E-12	-11.20	0.1957	-0.71	-6.4	-16.0	-9.5	-2.5	-4.8	-8.7	-14.5	-18.7	-3.6	-20.3	-12.2
4231	2.46	2.5004	2.65	2436	6.02	7.691	2.0E-08	0.94	2.4E-03	0.04	9.2E-05	6.0E-12	-11.22	0.1957	-0.71	-6.5	-16.1	-9.6	-2.6	-4.9	-8.7	-14.5	-18.7	-3.6	-20.3	-12.2

[1]Dissolved oxygen is estimated using WOA 13

Table A3.4 Dissolved rare earth elements and hydrographic properties in the Black Sea

Depth	Temperature	[1]Dissolved O_2	[1]PO_4^{3-}	[1]Alkalinity	Ce	[1]pH	H^+	∂1	HCO_3^-	∂2	CO_3^{2-}	Ce	log{C_{Ce}}	pO_2	log(PO_2)	#1	#2	#3	#4	#5	#6	#7	#8	#9	#10	P11
m	℃	ml/l	uM	µeq/L			mol/L		mol/L		mol/L	(mol/L)				Model calculated log{C_{Ce}}										
6	14.28	6.565	0.1807		22.2							2.2E-11	-10.65	0.2125	-0.67											
15	12.61	6.743	0.183	2.99	18.4							1.8E-11	-10.74	0.2182	-0.66											
31	9.42	6.765	0.2084		16.8	8.44	3.6E-09	0.82		0.18		1.7E-11	-10.77	0.2189	-0.66	-9.8	-19.4	-12.9	-5.9	-8.2	-11.0					
50	7.71	5.499	0.3676	3.05	5.8	8.39	4.1E-09	0.84	2.7E-06	0.16	5.1E-07	5.8E-12	-11.24	0.1780	-0.75	-9.4	-19.0	-12.5	-5.5	-7.8	-10.8	-18.9	-23.0	###	-26.9	-18.8
65	7.71	3.780	0.6011		2.6							2.6E-12	-11.59	0.1223	-0.91											
70	7.76	3.249	0.6772		2.8							2.8E-12	-11.55	0.1051	-0.98											
76	7.81	2.820	0.736	3.07	1.6	8.37	4.3E-09	0.84	2.7E-06	0.15	4.9E-07	1.6E-12	-11.80	0.0913	-1.04	-9.0	-18.6	-12.1	-5.1	-7.4	-10.7	-18.8	-22.9	###	-26.8	-18.8
81	7.86	2.477	0.7877		2.1							2.1E-12	-11.68	0.0801	-1.10											
86	7.93	2.161	0.8524		3.1							3.1E-12	-11.51	0.0699	-1.16											
91	7.99	1.879	0.9294		9.7							9.7E-12	-11.01	0.0608	-1.22											
96	8.05	1.606	1.1151		13.7							1.4E-11	-10.86	0.0520	-1.28											
100	8.11	1.398	1.3949		16.5							1.7E-11	-10.78	0.0452	-1.34											
105					18.8							1.9E-11	-10.73													
110					27.5							2.8E-11	-10.56													
115					31.1							3.1E-11	-10.51													
120					55.1							5.5E-11	-10.26													
125	8.3178	0.6525	2.7881		63.1							6.3E-11	-10.20	0.0211	-1.68											
130					57.4							5.7E-11	-10.24													
150	8.4903	0.3395	3.616	3.07	106	8.08	8.3E-09	0.91	2.9E-06	0.08	2.7E-07	1.1E-10	-9.97	0.0110	-1.96	-7.2	-16.8	-10.3	-3.3	-5.6	-9.6	-17.9	-22.1	-9.5	-26.2	-18.4
180	8.5883	0.2592	4.306	3.13	144.6	8.12	7.6E-09	0.90	2.9E-06	0.09	3.0E-07	1.4E-10	-9.84	0.0084	-2.08	-7.2	-16.8	-10.3	-3.3	-5.6	-9.6	-18.0	-22.1	-9.5	-26.2	-18.5
500	8.882	0.1845	6.1443	3.69	180.9							1.8E-10	-9.74	0.0060	-2.22											
800	8.9179	0.0319	6.7069	3.8	141.8							1.4E-10	-9.85	0.0010	-2.99											
1500	9.0267	0	6.9324		104.9							1.0E-10	-9.98													
2153	9.0936	0	8.4894		96.3							9.6E-11	-10.02													
2174					89.6							9.0E-11	-10.05													
2185	9.1012	0	8.4876		52.9							5.3E-11	-10.28													

[1]Data estimated from WOA 13

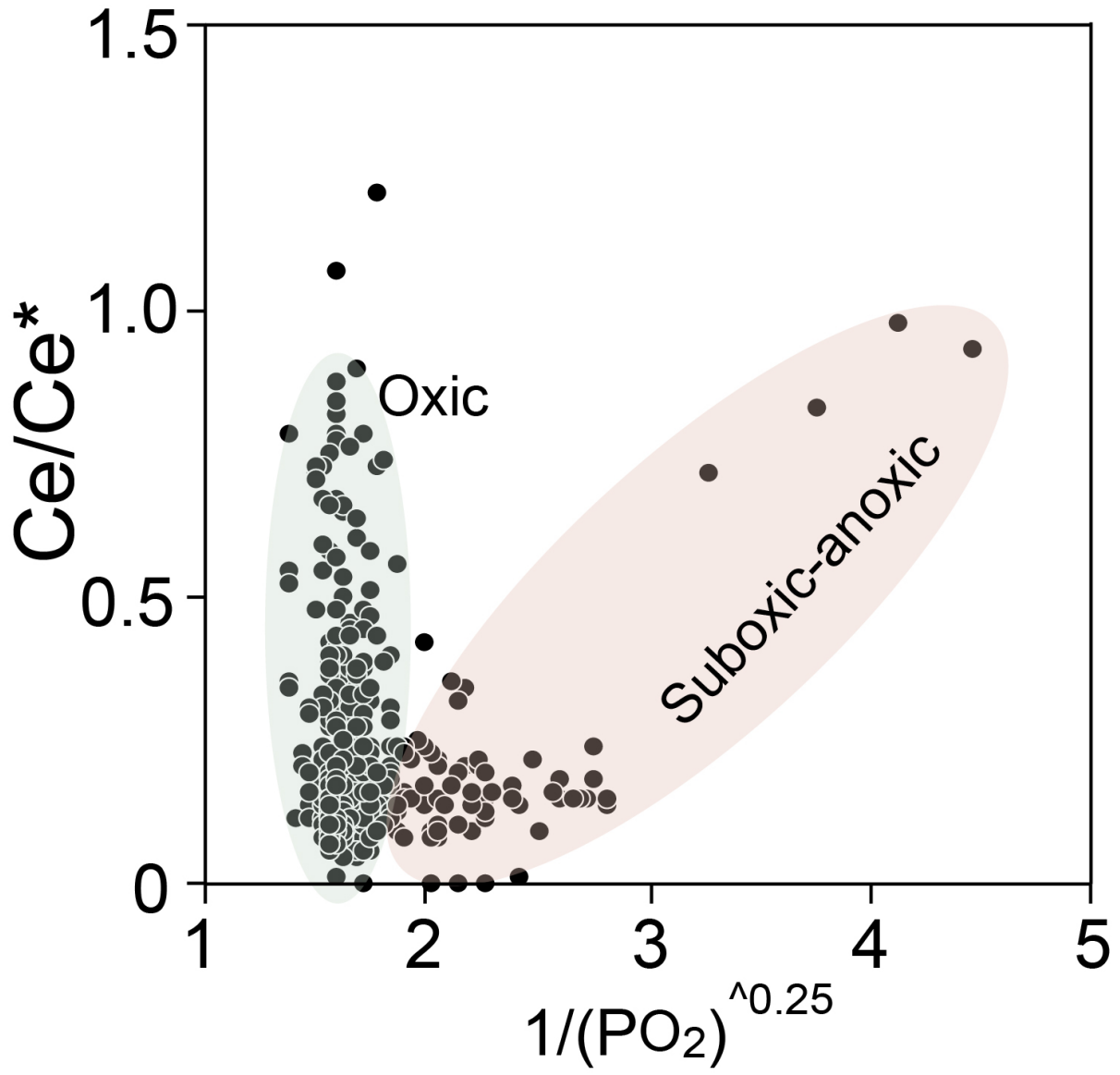

Figure A3.1.2 A cross-plot of compiled Ce anomalies and one over the square root of the partial pressure of dissolved oxygen following eq.4.

Dissolved oxygen is compiled from references listed in caption of Fig A3.1 as well as estimated using WOA 13 by extracting annual average dissolved oxygen at each station.

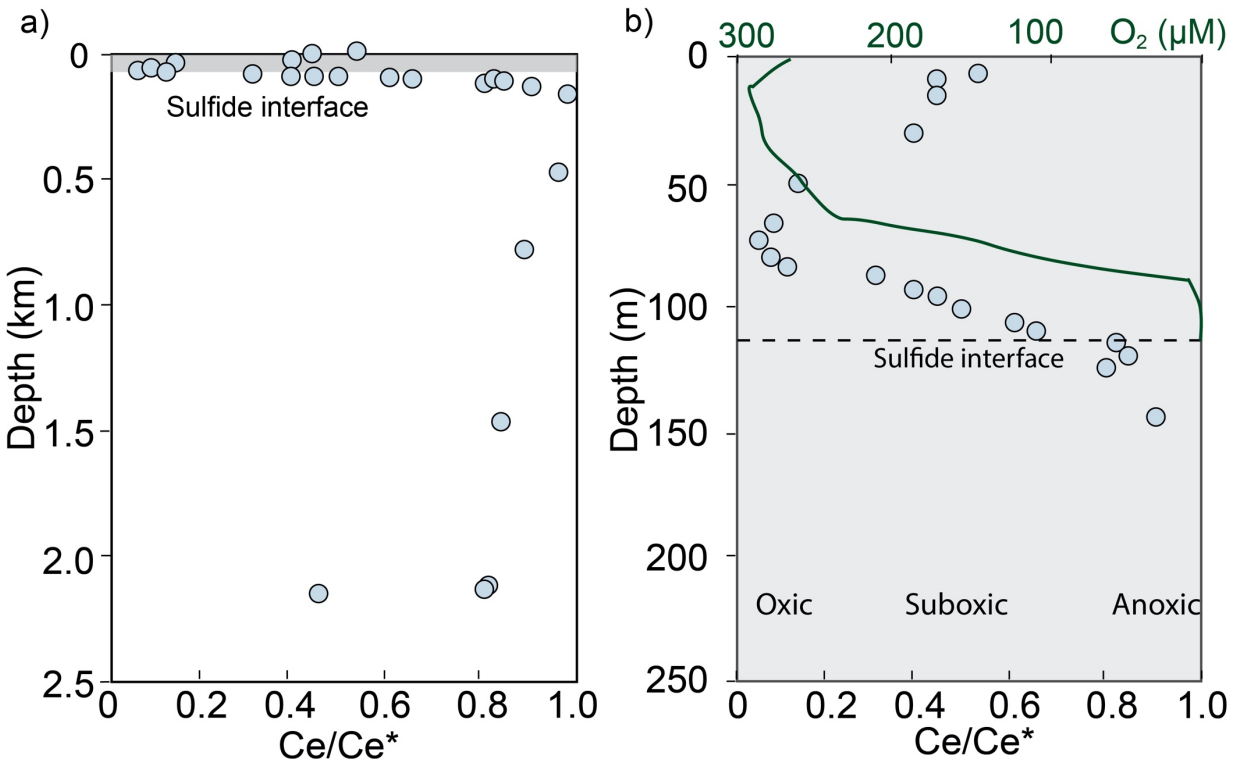

Figure A3.1.3 Depth profile of dissolved Ce anomaly in the Black Sea.

a). Modified depth profiles of dissolved Ce anomaly in the Black Sea after German et al. (1991).

b). Expanded profiles of dissolved Ce anomaly and dissolved oxygen. Dissolved oxygen is in reverse order. The Ce anomaly is calculated using $Ce/Ce^* = 3(Ce_n/(2La_n+Nd_n)$ from German et al. (1991); n refers to shale-normalized concentrations.

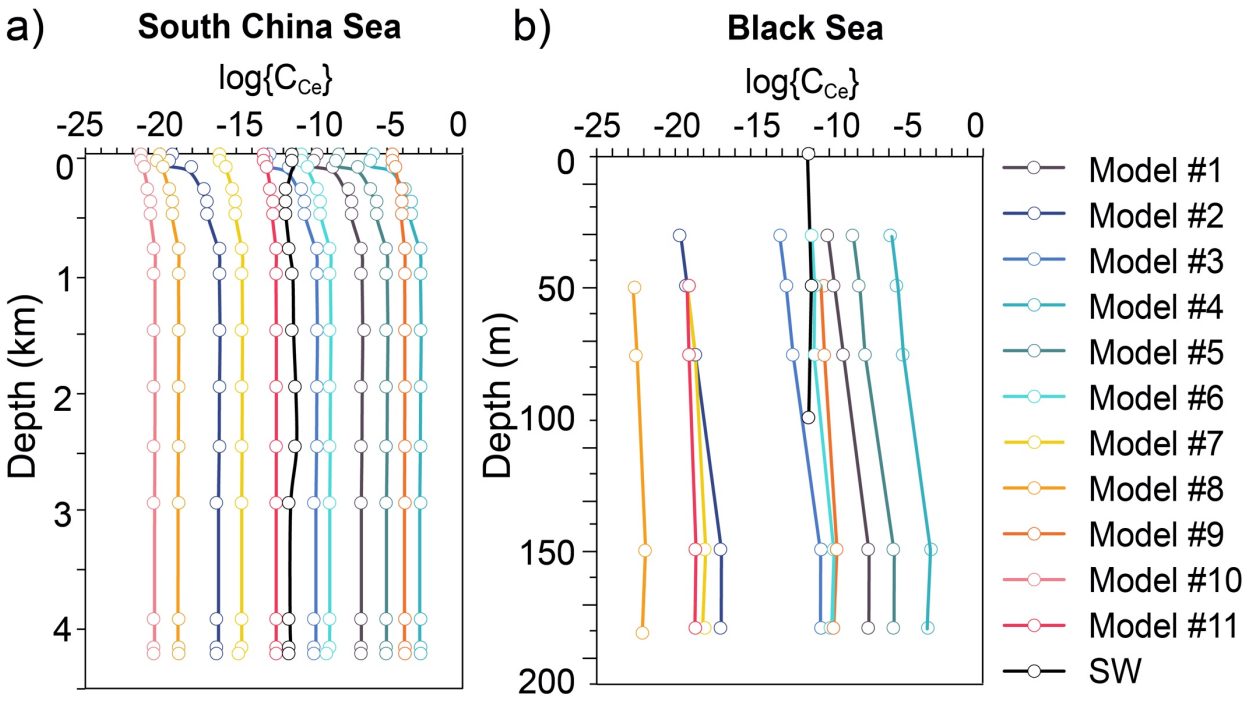

Figure A3.1.4 A comparison of REY with major- and trace-element alteration proxies for sequentially leached samples.

log{C_{Ce}} are calculated from models #1–#11 and seawater measurements in a) South China Sea, and b) Black Sea.

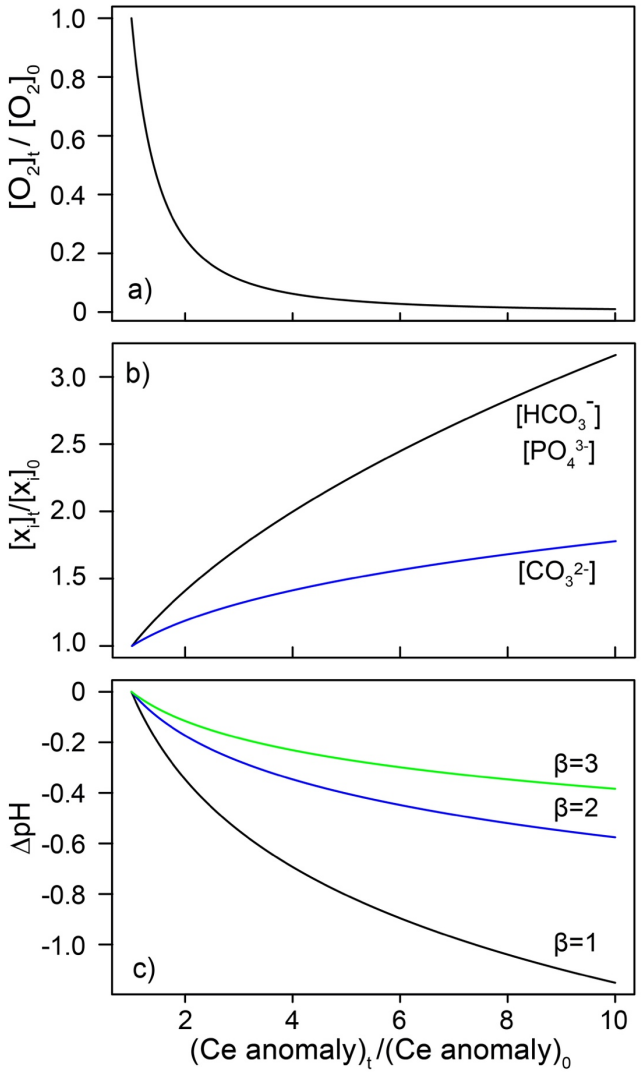

Figure A3.1.5 Modeled outputs of changes in dissolved oxygen, dissolved HCO_3^-, PO_4^{3-}, CO_3^{2-} and pH in relation to changes in the Ce anomaly.

Only results showing increases in the Ce anomaly are displayed.

REFERENCES

Algeo, T.J., Twitchett, R.J., 2010. Anomalous early Triassic sediment fluxes due to elevated weathering rates and their biological consequences. Geology 38, 1023–1026. https://doi.org/10.1130/G31203.1

Alibo, D.S., Nozaki, Y., 2000. Dissolved rare earth elements in the South China Sea: Geochemical characterization of the water masses. J. Geophys. Res. Ocean. 105, 28771–28783. https://doi.org/10.1029/1999JC000283

Alibo, D.S., Nozaki, Y., 1999. Rare earth elements in seawater: Particle association, shale-normalization, and Ce oxidation. Geochim. Cosmochim. Acta 63, 363–372. https://doi.org/10.1016/S0016-7037(98)00279-8

Beauchamp, B., Baud, A., 2002. Growth and demise of Permian biogenic chert along northwest Pangea: Evidence for end-Permian collapse of thermohaline circulation. Palaeogeogr. Palaeoclimatol. Palaeoecol. 184, 37–63. https://doi.org/10.1016/S0031-0182(02)00245-6

Burgess, S.D., Bowring, S.A., 2015. High-precision geochronology confirms voluminous magmatism before, during, and after Earth's most severe extinction. Sci. Adv. 1, 1–14. https://doi.org/10.1126/sciadv.1500470

Byrne, R.H., Bingler, L.S., 1989. Comment on "Cerium: A chemical tracer for paleo-oceanic redox conditions" by Y.-G. Liu, M. R. U. Miah and R. A. Schmitt. Geochim. Cosmochim. Acta. https://doi.org/10.1016/0016-7037(89)90081-1

Byrne, R.H., Sholkovitz, E.R., 1996. Marine Chemistry and Geochemistry of the lanthanides, in: Gschneidner Jr., K.A., Eyring, L. (Eds.), Handbook on the Physics and Chemistry of Rare Earths. Elsevier Sci., Amsterdam, pp. 497–592.

Cantrell, K.J., Byrne, R.H., 1987. Rare earth element complexation by carbonate and oxalate ions. Geochim. Cosmochim. Acta 51, 597–605. https://doi.org/10.1016/0016-7037(87)90072-X

Chan, L.H., Alt, J.C., Teagle, D.A.H., 2002. Lithium and lithium isotope profiles through the upper oceanic crust: A study of seawater-basalt exchange at ODP Sites 504B and 896A. Earth Planet. Sci. Lett. 201, 187–201. https://doi.org/10.1016/S0012-821X(02)00707-0

Chen, X.Y., Teng, F.Z., Huang, K.J., Algeo, T.J., 2020. Intensified chemical weathering during Early Triassic revealed by magnesium isotopes. Geochim. Cosmochim. Acta. https://doi.org/10.1016/j.gca.2020.02.035

De Baar, H.J.W., German, C.R., Elderfield, H., van Gaans, P., 1988. Rare earth element distributions in anoxic waters of the Cariaco Trench. Geochim. Cosmochim. Acta 52, 1203–1219. https://doi.org/10.1016/0016-7037(88)90275-X

Dellinger, M., Gaillardet, J., Bouchez, J., Calmels, D., Louvat, P., Dosseto, A., Gorge, C., Alanoca, L., Maurice, L., 2015. Riverine Li isotope fractionation in the Amazon River basin controlled by the weathering regimes. Geochim. Cosmochim. Acta 164, 71–93. https://doi.org/10.1016/j.gca.2015.04.042

Dellinger, M., Gaillardet, J.Ô., Bouchez, J., Calmels, D., Galy, V., Hilton, R.G., Louvat, P., France-Lanord, C., 2014. Lithium isotopes in large rivers reveal the cannibalistic nature of modern continental weathering and erosion. Earth Planet. Sci. Lett. 401, 359–372. https://doi.org/10.1016/j.epsl.2014.05.061

Ehrlich, A., 1968. Rare earth abundances in manganese nodules. Massachusetts Inst of Tech cambridge.

Garcia-Solsona, E., Jeandel, C., Labatut, M., Lacan, F., Vance, D., Chavagnac, V., Pradoux, C., 2014. Rare earth elements and Nd isotopes tracing water mass mixing and particle-seawater interactions in the SE Atlantic. Geochim. Cosmochim. Acta 125, 351–372. https://doi.org/10.1016/j.gca.2013.10.009

German, C., Holliday, B.P., Elderfield, H., 1991. Redox cycling of rare earth elements in the suboxic zone of the Black Sea. Geochim. Cosmochim. Acta 55, 3553–3558. https://doi.org/10.1016/0016-7037(91)90055-A

German, C.R., Elderfield, H., 1990. Application of the Ce anomaly as a paleoredox indicator: The ground rules. Paleoceanography 5, 823–833. https://doi.org/10.1029/PA005i005p00823

Huh, Y., Chan, L.H., Chadwick, O.A., 2004. Behavior of lithium and its isotopes during weathering of Hawaiian basalt. Geochemistry, Geophys. Geosystems 5. https://doi.org/10.1029/2004GC000729

Huh, Y., Chan, L.H., Edmond, J.M., 2001. Lithium isotopes as a probe of weathering processes: Orinoco River. Earth Planet. Sci. Lett. 194, 189–199. https://doi.org/10.1016/S0012-821X(01)00523-4

Huh, Y., Chan, L.H., Zhang, L., Edmond, J.M., 1998. Lithium and its isotopes in major world rivers: implications for weathering and the oceanic budget. Geochim. Cosmochim. Acta 62, 2039–2051. https://doi.org/10.1016/S0016-7037(98)00126-4

James, R.H., Rudnick, M.D., Palmer, M.R., 1999. The alkali element and boron geochemistry of the Escanaba Through sediment-hosted hydrothermal system. Earth Planet. Sci. Lett. 171, 157–169. https://doi.org/10.1016/S0012-821X(99)00140-5

Kisakurek, B., James, R.H., Harris, N.B.W., 2005. Li and δ7Li in Himalayan rivers: Proxies for silicate weathering? Earth Planet. Sci. Lett. 237, 387–401. https://doi.org/10.1016/j.epsl.2005.07.019

Korte, C., Jasper, T., Kozur, H.W., Veizer, J., 2006. 87Sr/86Sr record of Permian seawater.

Palaeogeogr. Palaeoclimatol. Palaeoecol. 240, 89–107. https://doi.org/10.1016/j.palaeo.2006.03.047

Korte, C., Kozur, H.W., Bruckschen, P., Veizer, J., 2003. Strontium isotope evolution of late permian and triassic seawater. Geochim. Cosmochim. Acta 67, 47–62. https://doi.org/10.1016/S0016-7037(02)01035-9

Lee, C.T.A., Cheng, X., Horodyskyj, U., 2006. The development and refinement of continental arcs by primary basaltic magmatism, garnet pyroxenite accumulation, basaltic recharge and delamination: Insights from the Sierra Nevada, California. Contrib. to Mineral. Petrol. 151, 222–242. https://doi.org/10.1007/s00410-005-0056-1

Lee, J.H., Byrne, R.H., 1993. Complexation of trivalent rare earth elements (Ce, Eu, Gd, Tb, Yb) by carbonate ions. Geochim. Cosmochim. Acta 57, 295–302. https://doi.org/10.1016/0016-7037(93)90432-V

Lemarchand, E., Chabaux, F., Vigier, N., Millot, R., Pierret, M.C., 2010. Lithium isotope systematics in a forested granitic catchment (Strengbach, Vosges Mountains, France). Geochim. Cosmochim. Acta 74, 4612–4628. https://doi.org/10.1016/j.gca.2010.04.057

Li, G., West, A.J., 2014. Evolution of Cenozoic seawater lithium isotopes: Coupling of global denudation regime and shifting seawater sinks. Earth Planet. Sci. Lett. 401, 284–293. https://doi.org/10.1016/j.epsl.2014.06.011

Liu, X.-M., Rudnick, R.L., 2011. Constraints on continental crustal mass loss via chemical weathering using lithium and its isotopes. Proc. Natl. Acad. Sci. U. S. A. 108, 20873–20880. https://doi.org/10.1073/pnas.1115671108

Liu, X., Byrne, R.H., 1995. Comparative carbonate complexation of yttrium and gadolinium at 25 °C and 0.7 mol dm-3 ionic strength. Mar. Chem. 51, 213–221. https://doi.org/10.1016/0304-4203(95)00067-4

Liu, X.M., Rudnick, R.L., McDonough, W.F., Cummings, M.L., 2013. Influence of chemical weathering on the composition of the continental crust: Insights from Li and Nd isotopes in bauxite profiles developed on Columbia River Basalts. Geochim. Cosmochim. Acta 115, 73–91. https://doi.org/10.1016/j.gca.2013.03.043

Liu, Y., Miah, M.R.U., Schmitt, R.A., 1988. Cerium : A chemical tracer for paleo-oceanic redox conditions. Geochim. Cosmochim. Acta 52, 1361–1371.

Luo, Y.R., Byrne, R.H., 2004. Carbonate complexation of yttrium and the rare earth elements in natural waters. Geochim. Cosmochim. Acta 68, 691–699. https://doi.org/10.1016/S0016-7037(03)00495-2

Martin, E.E., Macdougall, J.D., 1995. Sr and Nd isotopes at the Permian/Triassic boundary: A record of climate change. Chem. Geol. 125, 73–99. https://doi.org/10.1016/0009-

2541(95)00081-V

Millero, F.J., 1992. Stability constants for the formation of rare earth-inorganic complexes as a function of ionic strength. Geochim. Cosmochim. Acta 56, 3123–3132. https://doi.org/10.1016/0016-7037(92)90293-R

Misra, S., Froelich, P.N., 2012. Lithium isotope history of cenozoic seawater: Changes in silicate weathering and reverse weathering. Science (80-.). 335, 818–823. https://doi.org/10.1126/science.1214697

Moffett, J.W., 1994a. A radiotracer study of cerium and manganese uptake onto suspended particles in Chesapeake Bay. Geochim. Cosmochim. Acta 58, 695–703. https://doi.org/10.1016/0016-7037(94)90499-5

Moffett, J.W., 1994b. The relationship between cerium and manganese oxidation in the marine environment. Limnol. Oceanogr. 39, 1309–1318. https://doi.org/10.4319/lo.1994.39.6.1309

Moffett, J.W., 1990. Microbially mediated cerium oxidation in sea water. Nature 345, 421–423. https://doi.org/10.1038/345421a0

Molina-Kescher, M., Frank, M., Hathorne, E., 2014. South Pacific dissolved Nd isotope compositions and rare earth element distributions: Water mass mixing versus biogeochemical cycling. Geochim. Cosmochim. Acta 127, 171–189. https://doi.org/10.1016/j.gca.2013.11.038

Molina-Kescher, M., Hathorne, E.C., Osborne, A.H., Behrens, M.K., Kölling, M., Pahnke, K., Frank, M., 2018. The influence of basaltic islands on the oceanic REE distribution: A case study from the Tropical South Pacific. Front. Mar. Sci. 5. https://doi.org/10.3389/fmars.2018.00050

Müller, R.D., Sdrolias, M., Gaina, C., Steinberger, B., Heine, C., 2008. Long-term sea-level fluctuations driven by ocean basin dynamics. Science (80-.). 319, 1357–1362. https://doi.org/10.1126/science.1151540

Nozaki, Y., 2001. Rare Earth Elements and Their Isotopes in the Ocean. Encycl. Ocean Sci. 2354–2366. https://doi.org/10.1029/2002EO000342

Nozaki, Y., Alibo, D.S., 2003a. Dissolved rare earth elements in the Southern Ocean, southwest of Australia: Unique patterns compared to the South Atlantic data. Geochem. J. 37, 47–62. https://doi.org/10.2343/geochemj.37.47

Nozaki, Y., Alibo, D.S., 2003b. Importance of vertical geochemical processes in controlling the oceanic profiles of dissolved rare earth elements in the northeastern Indian Ocean. Earth Planet. Sci. Lett. 205, 155–172. https://doi.org/10.1016/S0012-821X(02)01027-0

Ohta, A., Kawabe, I., 2000. Theoretical study of tetrad effects observed in REE distribution

coefficients between marine Fe-Mn deposit and deep seawater, and in REE(III)-carbonate complexation constants. Geochem. J. 34, 455–473. https://doi.org/10.2343/geochemj.34.455

Penniston-Dorland, S., Liu, X.-M., Rudnick, R.L., 2017. Lithium Isotope Geochemistry, in: Reviews in Mineralogy and Geochemistry. pp. 165–217. https://doi.org/10.2138/rmg.2017.82.6

Pistiner, Henderson, G.M., 2003. Lithium-isotope fractionation during continental weathering processes. Earth Planet. Sci. Lett. 214, 327–339. https://doi.org/10.1016/S0012-821X(03)00348-0

Pogge von Strandmann, P.A.E., Burton, K.W., James, R.H., van Calsteren, P., Gíslason, S.R., Mokadem, F., 2006. Riverine behaviour of uranium and lithium isotopes in an actively glaciated basaltic terrain. Earth Planet. Sci. Lett. 251, 134–147. https://doi.org/10.1016/j.epsl.2006.09.001

Pogge Von Strandmann, P.A.E., Jenkyns, H.C., Woodfine, R.G., 2013. Lithium isotope evidence for enhanced weathering during Oceanic Anoxic Event 2. Nat. Geosci. 6, 668–672. https://doi.org/10.1038/ngeo1875

Rao, V.K., Shanhani, C.J., Rao, C.L., 1970. Standard Thermodynamic Values. Radiochim. Acta 14, 31–34. https://doi.org/https://doi.org/10.1524/ract.1970.14.1.31

Reichow, M.K., Saunders, A.D., White, R. V., Pringle, M.S., Al'Mukhamedov, A.I., Medvedev, A.I., Kirda, N.P., 2002. 40Ar/39Ar dates from the West Siberian Basin: Siberian flood basalt province doubled. Science (80-.). 296, 1846–1849. https://doi.org/10.1126/science.1071671

Retallack, G.J., 2005. Earliest Triassic Claystone Breccias and Soil-Erosion Crisis. J. Sediment. Res. 75, 679–695. https://doi.org/10.2110/jsr.2005.055

Retallack, G.J., Metzger, C.A., Greaver, T., Jahren, A.H., Smith, R.M.H., Sheldon, N.D., 2006. Middle-Late Permian mass extinction on land. Bull. Geol. Soc. Am. 118, 1398–1411. https://doi.org/10.1130/B26011.1

Rowley, D.B., 2002. Rate of plate creation and destruction: 180 Ma to present. Bull. Geol. Soc. Am. 114, 927–933. https://doi.org/10.1130/0016-7606(2002)114<0927:ROPCAD>2.0.CO;2

Seyfried, W.E., Janecky, D.R., Mottl, M.J., 1984. Alteration of the oceanic crust: Implications for geochemical cycles of lithium and boron. Geochim. Cosmochim. Acta 48, 557–569. https://doi.org/10.1016/0016-7037(84)90284-9

Sillen, L.G., Martell, A.G., 1971. Supplement No. 1, in: Stability Constants of Metal Ion Complexes. Chem. Soc. Spec. Publ., London, p. 865P.

Smith, R.M., Martell, A.G., 1976. Inorganic complexes, in: Critical Stability Constants. Vol.4. Plenum Press.

Song, Haijun, Wignall, P.B., Tong, J., Song, Huyue, Chen, J., Chu, D., Tian, L., Luo, M., Zong, K., Chen, Y., Lai, X., Zhang, K., Wang, H., 2015. Integrated Sr isotope variations and global environmental changes through the Late Permian to early Late Triassic, Earth and Planetary Science Letters. https://doi.org/10.1016/j.epsl.2015.05.035

Tachikawa, K., Jeandel, C., Vangriesheim, A., Dupré, B., 1999. Distribution of rare earth elements and neodymium isotopes in suspended particles of the tropical Atlantic Ocean (EUMELI site). Deep Sea Res. Part I Oceanogr. Res. Pap. 46, 733–755. https://doi.org/10.1016/S0967-0637(98)00089-2

Tang, J., Johannesson, K.H., 2003. Speciation of rare earth elements in natural terrestrial waters: Assessing the role of dissolved organic matter from the modeling approach. Geochim. Cosmochim. Acta 67, 2321–2339. https://doi.org/10.1016/S0016-7037(02)01413-8

Teng, F.Z., McDonough, W.F., Rudnick, R.L., Dalpé, C., Tomascak, P.B., Chappell, B.W., Gao, S., 2004. Lithium isotopic composition and concentration of the upper continental crust. Geochim. Cosmochim. Acta 68, 4167–4178. https://doi.org/10.1016/j.gca.2004.03.031

Tomascak, P.B., Tera, F., Helz, R.T., Walker, R.J., 1999. The absence of lithium isotope fractionation during basalt differentiation: New measurements by multicollector sector ICP-MS. Geochim. Cosmochim. Acta 63, 907–910. https://doi.org/10.1016/S0016-7037(98)00318-4

Vigier, N., Decarreau, A., Millot, R., Carignan, J., Petit, S., France-Lanord, C., 2008. Quantifying Li isotope fractionation during smectite formation and implications for the Li cycle. Geochim. Cosmochim. Acta 72, 780–792. https://doi.org/10.1016/j.gca.2007.11.011

Wanner, C., Sonnenthal, E.L., Liu, X.M., 2014. Seawater δ7Li: A direct proxy for global CO2 consumption by continental silicate weathering? Chem. Geol. 381, 154–167. https://doi.org/10.1016/j.chemgeo.2014.05.005

West, A.J., 2012. Thickness of the chemical weathering zone and implications for erosional and climatic drivers of weathering and for carbon-cycle feedbacks. Geology 40, 811–814. https://doi.org/10.1130/G33041.1

Wimpenny, J., Gíslason, S.R., James, R.H., Gannoun, A., Pogge Von Strandmann, P.A.E., Burton, K.W., 2010. The behaviour of Li and Mg isotopes during primary phase dissolution and secondary mineral formation in basalt. Geochim. Cosmochim. Acta 74, 5259–5279. https://doi.org/10.1016/j.gca.2010.06.028

Witherow, R.A., Lyons, W.B., Henderson, G.M., 2010. Lithium isotopic composition of the McMurdo Dry Valleys aquatic systems. Chem. Geol. 275, 139–147. https://doi.org/10.1016/j.chemgeo.2010.04.017

Yaitskaya, N., 2011. Temperature, Salinity, Oxygen, Phosphate, Silicate, Nitrite, pH and Alkalinity data collected in the Black Sea, Tyrrhenian Sea and Western Basin from R/Vs GORIZONT and OKEANOGRAF, 1960 - 1969 (NCEI Accession 0074609).Alkalinity and pH used. NOAA National. Russ. Acad. Sci.

Zhang, J., Nozaki, Y., 1998. Behavior of rare earth elements in seawater at the ocean margin: a study along the slopes of the Sagami and Nankai troughs near Japan. Geochim. Cosmochim. Acta 62, 1307–1317. https://doi.org/10.1016/S0016-7037(98)00073-8

Zhang, J., Nozaki, Y., 1996. Rare earth elements and yttrium in seawater: ICP-MS determinations in the East Caroline, Coral Sea, and South Fiji basins of the western South Pacific Ocean. Geochim. Cosmochim. Acta 60, 4631–4644. https://doi.org/10.1016/S0016-7037(96)00276-1

Zheng, X.Y., Plancherel, Y., Saito, M.A., Scott, P.M., Henderson, G.M., 2016. Rare earth elements (REEs) in the tropical South Atlantic and quantitative deconvolution of their non-conservative behavior. Geochim. Cosmochim. Acta 177, 217–237. https://doi.org/10.1016/j.gca.2016.01.018

APPENDIX 3.2: OAE 2 SECTIONS USED FOR CE ANOMALY MEASUREMENT AND MULTI-PROXY COMPARISONS

Section name/Location	Estimated paleo-latitude	Deposition Environment/ Paleo water depth	Lithology	Existing proxies for comparison
Eastbourne, UK	35°N	Pelagic shelf sea	Chalk	$\delta^{13}C$, $\delta^{18}O$, I/Ca, $\delta^{238}U$, $\delta^{34}S_{CAS}$, $\delta^{7}Li$, $\delta^{44/42}Ca$, εNd(t)
Clot Chevalier, France	30°N	Deep subtropical Basin	Marlstone and limestone	$\delta^{13}C$ & $\delta^{18}O$, TOC
Raia del Pedale, Italy	20°N	Shallow-water carbonate platform	Limestone	$\delta^{13}C$, $\delta^{18}O$, I/Ca, $\delta^{238}U$, $\delta^{34}S_{CAS}$, $\delta^{7}Li$, $\delta^{87/88}Sr$, εNd(t)
ODP Hole 763B	45°S	1000m	Claystone	εNd(t), $\delta^{18}O$
ODP Hole 765C	40°S	Plain / 4000m	Zeolitic claystone and nannofossil chalk	εNd(t)
ODP Hole 766A	45°S	Plateau / 3000m	Zeolitic claystone and nannofossil chalk	εNd(t)
ODP Hole 1138A	55°S	Plateau / 500m	Chalk and nannofossil	εNd(t)

APPENDIX 3.3: AGE AND CHEMOSTRATIGRAPHY PROFILE OF OAE 2 SECTIONS

	No.	Sample ID	Depth (mbsf)	Age (Ma)	Ce/Ce*	εNd(t)	1000Mg/Ca	1000Al/Ca	1000Mn/Ca	1000Sr/Ca	1000Fe/Ca	1000Rb/Sr	Mn/Sr	Y/Ho	Total REE	Total REE/Ca	La/La*	Eu/Eu*	Yb/Nd	Nd/Nd*
763B	1	13-5, 52-54			0.49		1.37	0.03	0.30	1.92	0.01	0.12	0.16	37.45	156.97	0.05	2.45	1.39	2.58	1.20
	2	14-1, 131-133	305.32	80.80	0.40	-8.20	1.48	0.03	0.45	1.95	0.01	0.11	0.23	39.39	204.28	0.06	2.49	1.45	2.59	1.16
	3	14-5, 82-84			0.42		1.36	0.03	0.78	1.94	0.06	0.12	0.40	37.80	154.93	0.05	2.60	1.77	2.71	1.17
	4	15-1, 116-118	314.66	82.28	0.49	-7.80	1.50	0.02	0.33	1.81	0.00	0.25	0.18	38.22	121.14	0.03	2.76	1.70	2.76	1.21
	5	15-5, 50-52			0.41		1.64	0.02	0.19	1.72	0.01	0.09	0.11	38.50	122.99	0.04	2.69	2.66	3.00	1.11
	6	16-1, 91-93	323.92	83.75	0.50	-7.70	1.51	0.01	0.17	1.77	0.00	0.20	0.10	49.13	41.55	0.01	4.20	10.97	2.93	1.29
	7	17-1, 117-119	333.67	85.30	0.52	-7.70	1.34	0.01	0.32	1.69	0.00	0.36	0.19	39.01	121.86	0.03	2.79	1.69	2.91	1.20
	8	17-4, 75-77			0.37		1.27	0.02	0.34	1.43	0.01	0.30	0.24	36.06	180.15	0.05	2.21	1.50	2.46	1.17
	9	18-1, 42-44	342.43	86.63	0.45	-7.80	1.27	0.06	0.42	1.36	0.01	0.43	0.31	32.04	315.48	0.11	1.60	1.87	2.14	1.01
	10	18-3, 53-55			0.51		1.38	0.02	0.60	1.38	0.01	0.30	0.43	38.29	169.85	0.05	2.33	2.83	3.26	1.09
	11	19-1, 87-89	352.37	88.13		-8.40	28.95	12.15	0.54	7.06	2.60	9.02	0.08	36.84	231.83	108.67	1.95	2.42	2.19	1.06
	12	19-5, 45-47			0.46		1.47	0.04	0.71	1.09	0.02	0.59	0.65	32.55	282.36	0.09	1.70	2.04	2.48	1.04
	13	20-1, 26-28			0.45		1.27	0.07	0.75	1.19	0.02	0.38	0.63	30.52	279.89	0.10	1.63	1.92	2.68	1.03
	14	21-CC, 16-18					19.96	4.67	0.28	19.14	2.77	6.47	0.01	21.73	0.25	0.08	1.16	160.67	3.21	0.93
	15	22-1, 17-19			0.60		1.51	0.27	1.12	2.05	0.07	0.22	0.55	33.03	223.76	0.13	1.50	1.98	1.59	1.01
	16	22-CC, 25-27			0.75		1.77	0.36	2.60	1.43	0.16	0.24	1.82	32.96	302.87	0.16	1.50	1.64	2.34	0.97
	17	23-1, 134-136			0.90		1.48	0.35	2.81	2.64	0.19	0.16	1.06	32.53	158.11	0.13	1.39	1.98	1.77	0.91
	18	23-3, 16-18	392.66	94.11	0.89	-10.50	1.79	0.47	2.63	3.10	0.25	0.25	0.85	32.37	178.45	0.16	1.22	1.80	1.33	0.98
	19	23-5, 45-47			0.84		1.57	0.21	4.36	2.51	0.12	0.10	1.74	32.48	221.60	0.11	1.36	2.15	1.88	0.95
	20	24-1, 115-117	400.16	95.13	0.88	-11.10	1.48	0.23	5.34	2.74	0.05	0.15	1.95	33.97	236.11	0.12	1.46	2.21	2.14	0.95
	21	24-3, 81-83	405.37	95.83	0.93	-10.70	1.21	0.43	3.14	3.06	0.19	0.17	1.03	32.83	202.44	0.13	1.40	2.10	1.87	0.97
	22	24-5, 37-39			0.90		1.07	0.59	1.82	3.32	0.27	0.17	0.55	31.05	198.94	0.15	1.25	2.00	1.32	0.95
	23	19–3, 61–62	355.10	89.28	0.52		1.27	0.02	0.98	1.38	0.01	0.29	0.71	38.18	226.86	0.05	2.36	2.83	2.51	1.14
	24	19–6, 61–63	359.62	89.99	0.52	-8.00	1.45	0.02	0.98	1.17	0.01	0.40	0.84	36.06	266.81	0.08	1.94	2.26	2.20	1.04
	25	20–1, 33.5–34.5	361.34	90.26	0.40	-7.50	1.11	0.04	0.76	1.32	0.02	0.42	0.58	32.00	387.35	0.11	1.59	2.01	1.79	1.05
	26	20–2, 95–96	363.46	90.59	0.38	-7.50	1.59	0.02	0.90	1.33	0.01	0.28	0.68	37.31	248.05	0.07	2.04	2.23	1.79	1.13
	27	21–1, 8–9	370.59	91.70	0.79	-9.40	1.12	0.02	1.20	1.29	0.01	0.21	0.93	36.34	234.44	0.06	2.06	3.07	2.33	1.06
	28	21–1, 118.5–119.5	371.69	91.88	0.42	-8.70	2.19	0.09	2.03	1.40	2.80	0.13	1.46	34.60	133.24	0.07	1.75	1.78	2.63	1.04
	29	21–2, 69–70	372.70	92.03	0.81	-9.50	1.32	0.03	1.41	1.15	0.01	0.22	1.23	38.09	323.35	0.07	1.95	2.63	2.49	1.04
	30	22–1, 85.5–86.5	380.86	93.31	0.68	-10.90	1.38	0.04	2.31	1.81	0.01	0.22	1.28	33.34	460.37	0.14	1.61	2.13	1.85	1.01
	31	22–2, 18–19	381.69	93.44	0.74	-10.70	1.42	0.06	2.46	1.63	0.03	0.17	1.50	34.49	530.02	0.13	1.68	2.15	2.11	1.03
	32	23–1, 43–44	389.94	94.54	0.86	-10.50	1.58	0.05	5.64	2.10	0.02	0.16	2.69	36.12	424.59	0.09	1.53	2.62	2.16	0.94
	33	23–2, 33–34	391.34	94.72	0.94	-10.40	1.51	0.22	3.75	2.82	0.11	0.24	1.33	34.11	358.01	0.15	1.39	2.03	1.53	1.00
	34	23–4, 55–56	394.56	95.13	0.78	-10.80	1.46	0.17	4.18	2.97	0.09	0.15	1.41	34.33	292.01	0.12	1.33	2.07	1.44	0.94
	35	23–5, 41.5–42.5	395.92	95.31	0.87	-10.40	1.62	0.26	4.36	2.88	0.18	0.17	1.51	34.42	236.13	0.14	1.27	2.16	1.42	0.98
	36	24–7, 30.5–31.5	408.31	96.90	0.98	-10.30	1.22	0.38	3.48	3.55	0.26	0.23	0.98	35.28	244.86	0.18	1.28	2.00	1.27	0.97
	37	25–1, 45–46	408.96	96.98	1.27	-10.10	1.80	0.40	5.89	3.50	0.09	0.32	1.68	36.60	306.72	0.35	1.53	1.81	0.96	1.13
	38	25–3, 50.5–51.5	412.01	97.37	1.17	-10.10	1.58	0.98	1.61	3.84	0.29	0.28	0.42	33.78	233.06	0.26	1.02	1.80	0.94	0.97
	39	26–3, 81–82	421.81	98.63	1.08	-9.70	8.68	1.27	6.00	3.21	0.19	0.42	1.87	32.92	384.30	0.44	1.01	1.56	1.00	0.98
	40	27–4, 85–86	432.85	100.04		-9.30	4.15	0.58	11.68	2.40	0.69	0.24	4.87	35.29	233.13	0.17	1.37	1.90	1.79	1.03
	41	28–4, 82–84	442.35	101.26		-9.70	2.86	0.50	11.56	2.45	0.69	0.25	4.72	36.10	289.42	0.19	1.41	1.83	1.91	0.93
	42				0.72		1.25	0.02	1.39	1.57	0.00	0.13	0.88	37.77	202.17	0.07	2.05	2.71	2.03	1.13
765C	1	23-2, 35-37	561.55	75.02		-10.4	23.52	16.83	2.72	1.52	1.85	10.82	1.79	25.30	8.64	0.30	0.58	0.95	1.43	0.72
	2	23-4, 22-24	564.43	76.61	1.17	-8.4	1.41	0.35	3.10	2.32	0.03	0.12	1.34	32.09	541.86	0.12	1.55	1.75	2.54	0.97
	3	24-4, 6-8		84	0.38		1.10	0.13	2.09	1.60	0.01	0.14	1.31	28.31	1020.13	0.17	1.54	1.38	2.83	0.99
	4	25-1, 37-39			0.37		1.27	0.18	1.59	1.24	0.02	0.33	1.28	29.54	827.00	0.17	1.46	1.41	2.22	0.99
	5	25-1, 99.0-101.0			0.35		1.27	0.06	1.51	1.25	0.19	0.21	1.21	29.86	713.73	0.14	1.52	1.49	2.76	0.98
	6	25-3, 4-6			0.60		1.12	0.30	1.71	1.53	0.01	0.19	1.12	29.09	524.08	0.15	1.59	1.91	2.99	0.95
	7	25-4, 53-55	584.03	90.62	0.62	-7.7	1.32	0.29	1.98	1.40	0.02	0.19	1.41	30.98	625.96	0.17	1.62	1.70	2.75	1.00
	8	25-5, 33-35	585.37	91.51	0.60	-7.3	1.50	0.28	2.03	1.37	0.02	0.24	1.49	29.76	730.52	0.21	1.48	1.64	2.30	1.00
	9	26-2, 94-96	590.7	96.29	0.75	-8.4	1.52	0.50	2.52	1.56	0.01	0.21	1.62	30.96	511.65	0.15	1.73	1.97	3.54	0.94
	10	26-3, 79-81	592.02	98.17		-8.2	37.45	45.65	20.75	3.35	1.27	6.84	6.20	23.09	70.48	2.74	0.66	1.28	0.89	0.82
	11	26-5, 41-43	594.17	101.24	0.84	-8.2	6.99	10.16	3.81	1.76	0.40	2.23	2.17	23.25	1159.79	4.05	0.66	1.17	0.86	0.88
	12	25–3, 61–62	582.6	90.01		-6.7	6.82	5.88	2.65	1.80	1.20	1.37	1.47	25.20	456.62	1.35	0.77	1.33	0.89	0.89
	13	25–5,49.5–50.5	585.53	91.96	0.74	-7.2	2.16	0.15	3.74	1.11	0.00	0.42	3.35	30.76	529.31	0.18	1.62	1.73	2.14	1.02
	14	26–1, 4–5	588.34	93.83	0.71	-7.1	2.25	2.00	1.65	1.40	0.01	0.92	1.18	28.50	1047.19	1.00	0.99	1.36	1.05	0.96
	15	26–1, 34–35	588.64	94.03	0.45	-6.7	1.83	0.99	2.16	1.54		0.49	1.40	28.04	747.21	0.42	1.25	1.54	1.62	0.93
	16	26–1, 57–58	588.87	94.19		-6.3	47.09	85.24	39.96	10.48	1.37	4.22	3.81	24.41	186.14	12.09	0.83	1.31	1.02	0.89
	17	26–1, 84–85	589.13	94.73	0.68	-7.4	1.73	0.89	2.44	1.51	0.02	0.44	1.62	28.66	833.40	0.42	1.22	1.57	1.53	0.94
	18	26–2, 24–25	589.98	95.95	0.63	-7.7	1.27	0.40	2.41	1.59	0.01	0.24	1.52	28.58	547.51	0.17	1.72	1.66	3.26	0.93
	19	26–2, 55.5–56.5	590.3	96.4	0.85	-7.7	1.31	0.49	2.40	1.54	0.02	0.27	1.56	29.51	554.65	0.18	1.65	1.85	3.07	0.92
	20	26–2, 64–65	590.4	96.55	0.83	-7.7	1.42	0.40	2.53	1.55	0.02	0.23	1.63	30.93	540.74	0.18	1.62	1.77	3.04	0.92

	21						46.51	156.87	21.18	7.41	3.69	8.92	2.86	23.63	88.02	10.29	0.62	1.73	0.67	0.87
	22	26–4, 28–29	592.93	100.16		-8.4	42.42	95.85	4.57	6.67	2.40	6.96	0.68	22.53	172.22	13.49	0.63	1.25	0.70	0.84
	23	26–2, 7.5–8.5	589.83	95.73		-6.7	41.94	135.11	39.08	9.59	2.28	3.41	4.07	23.60	204.41	18.18	0.66	1.58	0.68	0.88
	24	26–1, 136–137	589.65	95.48	0.55	-6.6	1.28	0.36	2.27	1.67	0.01	0.29	1.35	27.80	499.93	0.20	1.62	1.77	2.68	0.98
	1	11-1, 107-109			0.44		1.06	0.04	0.08	2.19	0.00	0.14	0.04	29.02	224.18	0.07	1.62	1.16	1.61	1.03
	2	11-2, 117-119	97.38	72.4	0.39	-9.85	1.03	0.02	0.06	2.55	0.00	0.11	0.02	33.69	81.91	0.02	2.35	1.41	1.47	1.15
	3	11-3, 60-62	98.31	72.78	0.61	-9.73	1.22	0.03	0.09	2.47	0.00	0.12	0.04	34.83	141.73	0.04	2.44	1.73	2.05	1.09
	4	11-4, 79-81	100	73.46	0.39	-10.13	1.09	0.03	0.06	2.60	0.00	0.12	0.02	31.70	174.47	0.05	1.84	1.32	1.40	1.08
	5	11-5, 33-35	101.04	73.88	0.45	-9.89	1.12	0.02	0.07	2.45	0.00	0.10	0.03	34.16	115.06	0.03	2.25	1.46	1.68	1.06
	6	12-1, 119-121	105.5	75.67	0.43	-9.89	1.05	0.03	0.06	2.43	0.00	0.14	0.02	33.13	113.40	0.03	2.31	1.33	1.72	1.08
	7	12-2, 10-12	105.91	75.84	0.37	-9.89	1.10	0.02	0.05	2.32	0.00	0.11	0.02	32.57	143.55	0.04	2.10	1.28	1.40	1.08
	8	13-1, 87-89	114.78	82.68	0.30	-7.29	0.79	0.16	0.11	2.02	0.02	0.33	0.06	27.51	245.31	0.09	1.74	2.11	1.81	1.01
	9	13-2, 98-100		83	0.28		0.78	0.08	0.16	1.83	0.00	0.26	0.09	26.23	244.67	0.08	1.59	1.94	1.50	1.00
	10	13-3, 97-99	117.88	85.16	0.30	-5.99	0.93	0.08	0.14	1.33	0.01	0.52	0.11	29.25	160.13	0.06	1.69	2.52	1.16	1.10
	11	14-4, 35-37	128.46	90.14	0.33	-6.71	1.04	0.06	0.13	0.87	0.01	0.60	0.15	30.12	166.67	0.07	1.74	2.62	1.53	1.02
	12	14-2, 87-89	125.98	88.59	0.27	-5.47	1.30	0.21	0.14	0.83	0.01	0.99	0.17	28.62	292.84	0.16	1.43	2.01	1.47	1.00
	13	14-3, 56-58	127.17	89.42	0.13	-5.63	0.86	0.08	0.08	1.24	0.01	0.39	0.06	23.81	468.51	0.15	1.33	1.59	1.77	0.93
	14	14-4, 66-68	128.77	90.31	0.34	-5.87	1.04	0.08	0.09	1.11	0.00	0.53	0.09	28.62	195.06	0.08	1.74	2.49	2.56	0.97
	15	14-5, 45-47	130.06	91.02	0.28	-7.28	1.01	0.07	0.07	1.26	0.01	0.21	0.06	28.81	469.49	0.15	1.48	1.55	1.89	0.99
	16	15-1, 38-40			0.34		1.24	0.17	0.18	1.39	0.01	0.40	0.13	26.94	398.32	0.19	1.39	1.68	1.96	0.90
	17	15-2, 17-19	134.88	93.81	0.26	-6.21	1.16	0.08	0.11	1.61	0.01	0.26	0.07	26.52	379.57	0.15	1.43	1.44	2.11	0.90
	18	15-4, 104-106	138.75	96.8	0.87	-8.48	1.17	0.14	0.64	1.35	0.01	0.30	0.47	29.01	337.48	0.15	1.58	1.38	2.09	0.95
	19	15-5, 34-36	139.55	97.41	0.93	-8.28	0.94	0.10	0.86	1.60	0.01	0.26	0.54	27.94	411.54	0.14	1.67	1.57	2.42	0.93
	20	15-6, 25-27	140.96	97.93	0.67	-8.43	1.36	0.22	0.72	1.51	0.02	0.42	0.48	26.19	461.19	0.26	1.36	1.42	1.50	0.92
766A	21	16-1, 47-49	143.38	98.61	0.81	-8.24	1.47	0.18	0.70	1.24	0.01	0.58	0.57	28.39	302.92	0.15	1.42	1.58	1.67	0.93
	22	16-2, 97-99	145.38	99.17	0.56	-8.72	1.24	0.06	0.19	1.58	0.01	0.26	0.12	28.69	242.28	0.07	1.87	1.66	1.78	1.01
	23	16-3, 113-115	147.04	99.64	0.78	-7.83	1.12	0.04	0.24	1.79	0.01	0.22	0.13	30.14	197.60	0.06	2.07	1.59	2.29	1.04
	24	16-4, 29-31	147.7	99.82	0.78	-8.09	1.44	0.06	0.28	1.72	0.00	0.29	0.16	29.16	250.48	0.08	1.83	1.63	1.98	1.02
	25	16-5, 86-88	149.77	101.74	0.58	-8.8	1.28	0.08	0.19	1.58	0.00	0.36	0.12	26.27	273.48	0.09	1.48	1.46	1.92	0.90
	26	16-6, 22-24	150.63	100.65	0.53	-8.17	1.42	0.04	0.17	1.42	0.01	0.45	0.12	28.18	237.05	0.08	1.59	1.64	1.53	0.97
	27	11-6, 40-42	102.61	74.51	0.35	-9.81	1.13	0.01	0.06	2.45	0.00	0.11	0.02	35.17	123.30	0.04	2.04	1.25	1.37	1.04
	28	11-7, 21-23	103.92	75.04	0.39	-9.87	1.27	0.02	0.06	2.15	0.00	0.18	0.03	33.60	116.62	0.03	2.18	1.29	1.31	1.09
	29	14–4, 146.5–147.5	129.56	91.42	0.30	-7.3	1.00	0.03	0.10	1.36	0.01	0.26	0.07	32.21	191.36	0.06	2.08	2.42	2.05	1.05
	30	14–5, 70.5–71.5	130.3	91.76	0.39	-6.8	1.42	0.03	0.07	1.15	0.00	0.46	0.06	30.60	219.88	0.07	1.81	2.39	2.17	1.03
	31	15–1, 8–9	133.26	93.11	0.30	-5.3	1.19	0.04	0.09	1.04	0.01	0.39	0.09	28.98	317.79	0.09	1.64	1.73	2.14	0.96
	32	15–1, 115–116	134.35	93.55	0.31	-6.6	1.85	0.18	0.12	1.38	0.02	0.52	0.09	27.81	383.19	0.19	1.27	1.60	1.39	0.97
	33	15–2, 55–56	135.26	94.63	0.35	-6.4	72.51	132.36	15.28	8.51	1.41	5.45	1.80	22.89	110.83	8.20	0.65	1.50	0.76	0.78
	34	15–2, 94–95	135.64	95.09		-7.9	102.39	135.23	36.55	6.62	4.82	15.14	5.52	22.27	15.63	4.30	0.71	2.53	0.64	0.84
	35	15–3, 12–13	136.32	95.89	0.95	-8.5	0.99	0.04	1.15	1.36	0.01	0.31	0.85	29.77	352.08	0.10	2.02	1.74	2.02	1.04
	36	15–3 29–30	136.49	96.1		-6.5	3.95	1.75	0.22	1.54	0.05	1.71	0.14	27.17	916.40	1.54	0.91	1.32	0.69	0.99
	37	15–3, 38.5–39.5	136.58	96.2	1.00	-7.5	1.02	0.03	1.25	1.37	0.00	0.26	0.92	30.08	282.47	0.08	2.04	1.87	2.19	1.00
	38	15–3, 46.5–47.5	136.68	96.32	0.75	-7.6	0.98	0.03	0.41	1.53	0.01	0.23	0.27	27.64	365.78	0.12	1.86	1.81	1.82	0.97
	39	15–3, 99–100	137.2	96.94	1.02	-8.1	1.17	0.08	1.33	1.25	0.01	0.39	1.06	28.08	505.06	0.17	1.62	1.58	1.77	0.95
	40	15–4, 69–70	138.38	98.35	0.70	-8.3	1.13	0.04	0.49	1.57	0.01	0.20	0.31	31.15	298.71	0.09	1.93	1.47	1.96	1.04
	41	15–5, 100–101	140.2	100.12	0.76	-8.5	1.12	0.08	0.71	1.67	0.01	0.25	0.42	28.19	383.49	0.12	1.80	1.61	2.26	0.97
	1	67–2, 5–6	632.17	86.4	0.62	-6.7	1.41	0.06	0.79	2.13	1.10	0.26	0.37	29.00	273.95	0.08	1.43	1.86	1.62	1.00
	2	67–2, 75–76	632.87	92.99	0.63	-5.4	1.83	0.10	1.40	1.77	3.24	0.19	0.79	30.12	208.47	0.08	1.59	1.62	2.77	0.92
	3	68–1, 6–7	640.47	93.31	0.58	-6.8	1.46	0.02	1.69	2.43	1.70	0.16	0.70	32.34	252.67	0.07	1.59	1.62	2.13	0.97
	4	68–1, 42.5–43.5	640.83	93.33	0.56	-6.6	1.77	0.11	1.76	1.94	2.44	0.14	0.90	33.63	172.18	0.07	1.57	1.52	1.92	0.98
	5	68–2, 36–37	643.62	93.44	0.67	-7.2	1.43	0.09	1.51	1.77	2.02	0.24	0.86	29.82	222.18	0.09	1.32	1.84	1.63	0.97
	6	68–3, 21–22	644.88	93.5	0.68	-1.8	2.53	0.05	1.92	1.99	1.54	0.24	0.97	29.83	203.70	0.09	1.31	1.67	1.38	0.91
	7	68–4, 25.5–26.5	645.82	93.53	0.58	-7.5	1.74	0.11	1.32	1.83	1.26	0.20	0.72	29.09	172.54	0.08	1.27	1.94	1.51	0.98
	8	69–2, 52.5–53.5	651.95	93.71	0.62	-8	1.77	0.11	2.05	2.29	1.62	0.17	0.89	31.57	226.74	0.12	1.37	1.60	1.67	0.97
	9	69–5, 60–61	656.18	93.83	0.62	-8.4	4.27	2.38	0.45	16.85	8.99	0.63	0.03	33.68	338.37	1.13	0.97	1.26	0.78	1.01
	10	69–6, 52–53	657.6	93.87	1.09	-5.1	5.32	0.49	0.43	3.89	0.76	0.91	0.11	24.81	54.08	0.10	1.00	1.40	0.80	0.88
	11	70–1, 17.5–18.5	659.78	93.94		-2.6	4.80	0.19	3.44	0.67	2.73	0.35	5.15	21.08	186.10	0.14	0.93	1.31	0.78	0.91
1138A	12	70–1, 130–131	660.95	93.97		-2.6	6.24	0.17	2.52	0.74	1.42	0.52	3.39	20.66	302.57	0.20	0.89	1.31	0.96	0.88
	13	70–2, 56–57	661.67	93.99		-2.3	6.45	0.08	2.43	0.67	1.30	0.48	3.65	20.68	350.11	0.19	0.90	1.34	0.96	0.90
	14	71–2, 60–62	671.1	94.27	0.99	-1.3	10.54	0.70	1.17	3.10	0.65	0.95	0.38	19.69	156.23	0.22	0.80	1.38	1.10	0.83
	15	72–2, 20–21	680.6	94.54	1.23	0.9	97.38	2.90	15.44	5.57	5.49	0.53	2.77	27.06	1.50	0.04	1.05	1.50	1.03	1.15
	16	18-2, 22-24	168.84		0.64	-8.1	1.22	0.17	2.12	1.58	3.32	0.20	1.34	33.03	195.06	0.08	1.52	1.48	1.95	0.95
	17	54-2, 20-22	507.31	68.61	0.46		1.28	0.02	0.70	2.34	0.51	0.08	0.30	35.49	197.46	0.05	1.89	2.07	2.49	1.05
	18	56-2, 52-54			0.27		1.56	0.01	0.28	2.49	0.62	0.08	0.11	46.51	96.40	0.03	3.08	4.11	2.14	1.21
	19	57-1, 61-63	525.43	73.34	0.36	-8.7	1.25	0.01	0.62	2.17	0.61	0.07	0.29	41.73	66.47	0.02	3.06	6.12	3.08	1.14
	20	59-1, 50-52	554.11	76.39	0.27	-8.4	1.33	0.01	0.24	1.99	0.64	0.08	0.12	44.74	115.49	0.03	3.00	3.51	2.53	1.17
	21	60-2, 22-24	565.04	77.55	0.25	-8.2	1.43	0.01	0.26	1.77	0.76	0.05	0.15	45.56	115.50	0.03	3.17	3.53	2.48	1.23
	22	61-1, 48-50	573.39	78.44	0.25	-8	1.67	0.02	0.24	1.82	1.00	0.06	0.13	41.99	181.01	0.06	2.02	2.67	1.11	
	23	62-1, 30-32	582.81	79.44	0.25	0	1.43	0.01	0.19	2.02	0.70	0.10	0.10	44.13	133.57	0.04	2.95	3.00	2.52	1.19

	24	63-1, 40-42	592.61	80.48	0.27	-8	1.39	0.01	0.21	1.54	0.71	0.12	0.14	41.94	167.83	0.04	2.60	2.68	2.11	1.20
	25	64-1, 72-74	602.53	81.54	0.29	-7.9	1.43	0.01	0.29	1.57	0.99	0.07	0.19	42.84	13.48	0.04	2.70	2.90	2.75	1.18
	26	65-1, 58-60	612.09	82.56	0.29	-8.2	1.47	0.02	0.39	1.34	1.20	0.10	0.29	42.24	158.90	0.04	2.46	2.26	2.36	1.12
	27	66-1, 49-51	621.6	84.15	0.41	-7.8	1.52	0.02	0.47	1.86	1.87	0.08	0.25	39.58	175.09	0.05	2.17	2.13	2.87	1.05
	28	67-1, 95-97	631.66	85.85	0.40	-7	2.05	0.09	1.97	1.36	2.65	0.27	1.45	36.47	170.25	0.08	1.69	1.71	2.27	0.97
	29	69-1, 57-59	650.58	93.48	0.62	-4.4	1.19	0.28	1.72	2.66	1.42	0.14	0.65	31.01	283.65	0.15	1.31	1.59	1.40	0.98
	30	69–3, 23.5–24.5	652.83	93.73	0.64	-7.5	1.08	0.49	1.15	1.80	1.09	0.49	0.64	32.84	201.20	0.18	1.12	1.63	0.73	0.98
	31	73–2, 46–47	689.75	94.81		0.6	110.52	8.22	151.59	7.63	28.61	2.12	19.86	22.91	1.21	0.14	0.64	1.65	0.81	0.79
			cm																	
CDC			30		0.84		3.18	0.17	0.43	4.25	3.07	0.27	0.10	33.52	980.28	0.29	1.20	1.10	1.25	0.90
			293		1.13		3.31	0.03	0.03	0.39	0.11	0.08	0.09	34.89	47.71	0.01	1.23	1.23	1.11	0.87
			300		0.89		2.42	0.17	0.60	3.47	2.59	0.30	0.17	34.91	2094.60	0.49	1.38	1.29	1.16	0.95
			600		0.72		4.48	0.48	0.75	3.90	3.58	0.26	0.19	35.42	1421.63	0.72	1.28	1.21	1.16	0.91
			930		0.79		4.36	0.30	0.52	3.76	3.70	0.29	0.14	35.87	2969.94	0.96	1.21	1.17	0.97	0.96
			1290		0.75		4.09	0.17	0.49	3.35	3.39	0.34	0.15	38.29	2335.32	0.66	1.32	1.15	1.04	0.97
			1440		0.66		2.86	0.23	0.43	3.15	3.85	0.34	0.14	36.70	2497.50	0.81	1.23	1.13	1.17	0.95
			1770		0.76		3.39	0.16	0.36	3.38	3.91	0.41	0.11	38.84	3872.74	1.02	1.32	1.14	1.19	0.96
			1950		0.61		3.97	0.17	0.44	3.96	7.08	0.13	0.11	41.86	1148.05	0.45	1.49	1.09	1.21	0.94
			2520		0.68		3.63	0.12	0.36	3.16	2.21	0.28	0.11	38.28	2044.28	0.58	1.36	1.19	1.25	0.97
			2730		0.64		3.86	0.14	0.44	2.95	2.52	0.38	0.15	36.77	2018.06	0.58	1.30	1.19	1.18	0.97
			3390		0.56		3.55	0.11	0.45	3.38	2.84	0.11	0.13	40.84	992.94	0.30	1.63	1.22	1.39	1.04
			m																	
RDP			3		1.06		6.88	0.02	0.03	0.40	0.13	0.05	0.08	31.99	65.88	0.018	1.15	1.14	0.75	0.90
			20		1.46		8.90	0.03	0.02	0.53	0.05	0.04	0.03	37.70	30.30	0.008	1.42	1.48	1.01	1.33
			34		1.28		7.45	0.02	0.02	0.40	0.06	0.06	0.05	35.45	51.84	0.013	1.59	1.07	1.71	0.96
			47		1.41		10.08	0.03	0.01	0.67	0.03	0.05	0.02	41.07	19.61	0.005	1.48	1.35	2.99	0.86
			77		1.17		6.04	0.01	0.04	0.39	0.03	0.08	0.09	34.80	19.98	0.005	1.70	1.55	0.78	0.81
			82.25		1.11		6.03	0.03	0.03	0.38	0.10	0.06	0.08	37.42	94.16	0.025	1.08	1.19	1.15	0.93
			137		1.74		7.82	0.02	0.01	0.59	0.02	0.07	0.02	40.69	12.76	0.003	2.32	2.41	0.84	1.91
			149		1.09		7.42	0.04	0.01	0.67	0.05	0.11	0.01	44.24	57.51	0.02	0.93	1.20	1.17	0.88
			177		0.98		7.89	0.03	0.01	0.72	0.06	0.11	0.01	47.04	14.86	0.005	1.91	2.04	1.14	1.12
			190		1.41		7.77	0.01	0.01	0.68	0.03	0.04	0.01	60.33	2.32	0.001	1.83	13.55	2.08	3.84
			217		1.09		10.59	0.06	0.01	0.85	0.05	0.10	0.01	38.22	31.33	0.02	0.89	1.24	0.90	0.97
			242		1.38		4.56	0.01	0.01	0.40	0.08	0.03	0.03	45.93	7.99	0.002	1.69	2.71	2.48	0.82
			260		1.11		3.38	0.01	0.06	0.33	0.05	0.00	0.19	48.58	15.52	0.004	1.64	1.98	2.54	0.87
			280		0.80		4.65	0.05	0.05	0.26	0.22	0.34	0.19	40.32	83.43	0.02	1.63	1.18	1.93	1.17
			293		0.59		3.91	0.18	0.43	3.86	7.05	0.11	0.11	42.01	1056.33	0.44	1.47	1.13	1.22	0.94
			316		1.06		5.70	0.10	0.02	0.41	0.34	0.16	0.05	32.01	53.85	0.02	0.99	1.10	0.88	0.88
			cm																	
Eastbourne		WC++600	1840		0.55		4.73	0.08	0.87	1.16	1.01	0.16	0.75	39.69	756.76	0.23	1.52	1.13	1.25	
		WC++350	1590		0.59		5.11	0.13	1.29	1.42	1.29	0.43	0.91	36.81	1723.74	0.45	1.43	1.12	1.16	
		WC++250	1490		0.56		6.16	0.12	1.33	1.11	1.67	0.37	1.19	37.83	1004.34	0.35	1.49	1.12	1.18	0.99
		WC++200	1440		0.53		6.54	0.15	1.15	1.07	1.64	0.32	1.08	38.14	1148.14	0.38	1.50	1.06	1.24	1.01
		PM++100	1340		0.57		5.65	0.08	1.30	1.34	2.09	0.30	0.97	34.96	1162.62	0.38	1.61	1.15	1.67	1.03
		PM++60	1330		0.55		6.75	0.21	1.91	1.26	2.07	0.26	1.51	36.12	1103.39	0.44	1.47	1.22	1.27	0.98
		PM++20	1260		0.59		5.16	0.29	1.58	1.54	2.59	0.28	1.03	36.03	1358.10	0.55	1.42	1.14	1.21	0.96
		PM+600	1200		0.67		4.83	0.25	1.28	1.82	2.16	0.23	0.70	33.71	1576.81	0.65	1.37	1.10	1.30	0.97
		PM+540	1140		0.65		4.09	0.25	1.26	2.11	1.28	0.30	0.60	35.12	1820.30	0.59	1.42	1.09	1.07	1.01
		PM+480	1080		0.60		4.47	0.21	1.42	1.71	1.87	0.29	0.83	35.17	1159.38	0.44	1.39	1.04	1.26	0.97
		PM+400	1000		0.66		4.33	0.23	1.19	1.92	1.52	0.34	0.62	34.27	1557.66	0.51	1.34	1.08	1.12	0.97
		PM+200	800		0.79		3.81	0.11	1.89	2.00	1.08	0.36	0.95	34.56	933.41	0.28	1.59	1.15	1.09	1.04
		PM+140	740		0.76		2.74	0.13	1.24	2.02	1.04	0.34	0.62	32.65	972.00	0.29	1.51	1.15	1.18	0.95
		PM+130	730		0.70		4.20	0.28	1.53	1.91	1.53	0.28	0.80	30.94	1160.93	0.54	1.19	1.10	1.02	0.94
		PM+20	620		0.73		4.10	0.24	1.19	1.90	1.24	0.31	0.63	31.45	1114.90	0.43	1.17	1.09	1.14	0.93
		GC-40	560		0.77		3.64	0.08	0.94	2.17	0.96	0.14	0.44	35.60	593.32	0.17	1.65	1.16	1.55	1.03
		GC-120	480		0.74		3.84	0.12	0.74	2.05	1.01	0.21	0.36	37.74	526.27	0.15	1.58	1.22	1.45	1.04
		GC-180	420		0.68		4.15	0.06	0.77	2.03	1.11	0.16	0.38	35.81	571.40	0.17	1.44	1.15	1.56	0.98
		GC-240	360		0.79		3.97	0.07	0.76	2.15	0.91	0.14	0.35	37.34	408.67	0.12	1.78	1.17	1.37	1.04
		GC-340	260		0.72		4.94	0.06	0.94	1.81	1.22	0.17	0.52	35.65	594.51	0.17	1.52	1.19	1.46	1.02
		GC-400	200		0.72		5.37	0.18	0.92	1.76	1.31	0.30	0.52	35.72	721.37	0.22	1.44	1.14	1.33	0.99
		GC-460	140		0.69		5.20	0.08	1.16	1.71	1.10	0.22	0.68	35.32	693.94	0.19	1.43	1.09	1.43	0.94
		GC-520	80		0.68		4.89	0.18	0.85	1.98	0.96	0.22	0.43	34.02	903.07	0.29	1.35	1.12	1.24	0.94
		GC-600	0		0.67		5.41	0.11	1.05	1.66	1.29	0.19	0.63	34.91	713.86	0.22	1.42	1.12	1.32	0.95

APPENDIX 4: LI BOX MODEL

The oceanic Li isotope budget

In this section, we use box model to simulate Li isotope cycle when large δ^7Li variations are observed. Table A4.1 lists all the variables used in the box model and their modern values. Significant sources of Li in the modern ocean are continental weathering (F_{riv}), 10 Gmol/yr, and hydrothermal inputs (F_{MOR}), 13 Gmol/yr (Misra and Froelich, 2012). Li isotope compositions of these two inputs are δ^7Li_{riv}, 23‰ (Huh et al., 1998) and δ^7Li_{MOR}, 8‰ (Misra and Froelich, 2012), respectively. The main sink of the oceanic Li is fluxes during hydrothermal-oceanic crust interaction, also known as reverse weathering, including basalt alteration (F_{alt} = 12 Gmol/yr) and authigenic clay formation (F_{sed} = 11 Gmol/yr). They yield Li isotope fractionations from seawater of Δ_{alt} =13‰ and Δ_{sed} = 20‰, respectively (Li and West, 2014). All the inputs and outputs drive the modern seawater δ^7Li of 31‰ (James et al., 1999; Tomascak et al., 1999; Vigier et al., 2008; Wanner et al., 2014). Assuming a steady-state for Li isotopes in the ocean, we can write the following equations:

$$F_{riv} + F_{MOR} = F_{sed} + F_{alt} \quad (1)$$

$$\delta^7Li_{riv} F_{riv} + \delta^7Li_{MOR} F_{MOR} = (\delta^7Li_{sw} + \Delta_{sed})F_{sed} + (\delta^7Li_{sw} + \Delta_{alt})F_{alt} \quad (2)$$

In (2), if given δ^7Li_{sw}, one or more of these eight variables could have changed to alter the δ^7Li_{sw} to a different value compared to the modern ocean. To further explore what changes in these variables may cause our measured δ^7Li record, we assume uncertainties for each variable and use the steady-state box model to narrow down these uncertainties (detailed model presets are listed in Table A4.2). During the weathering process, primary mineral dissolution releases Li

into the river with an isotopic composition similar to the source rock. However, 70% ± 15% of solubilized Li incorporate into secondary minerals (Wimpenny et al., 2010). With ^{6}Li being preferentially taken from the river, this process results in a higher δ^7Li in the river water. The Li isotopic composition of the present-day river dissolved loads spread widely from 1.3‰ to 43.7‰, but mostly higher than 3‰ (Dellinger et al., 2014; Huh et al., 2001, 1998; Kisakurek et al., 2005; Lemarchand et al., 2010; Liu and Rudnick, 2011; Penniston-Dorland et al., 2017; Pistiner and Henderson, 2003; Pogge von Strandmann et al., 2006; Wimpenny et al., 2010; Witherow et al., 2010). Only low δ^7Li values (1~2‰) only occur in a few particular conditions. These conditions usually exist in cation-poor, organic-rich rivers, where congruent weathering effectively removes cation, such as the Rio Negro in the Amazon flood plain (Dellinger et al., 2014; Huh et al., 2001). Most studies suggest that δ^7Li do not directly reflect the catchment lithology, instead, they are controlled by fractionation during the weathering process (Huh et al., 2004, 2001, 1998; Pistiner and Henderson, 2003; Pogge von Strandmann et al., 2006). Therefore, δ^7Li_{riv} is set to vary from 0 to 23‰ in the model preset considering the possibility of redissolution of Li from the soil into the river during this period due to vegetation loss. In contrast, we assume a constant δ^7Li_{MOR} of 8‰, based on the measurement of Li isotope composition during current hydrothermal activities (Misra and Froelich, 2012). Studies of altered oceanic basalts reveal an offset of 8‰ to 16‰ for Δ_{alt} (Chan et al., 2002; Li and West, 2014; Misra and Froelich, 2012). We allow Δ_{alt} to vary from 5 to 13‰ (Seyfried et al., 1984). Li and West (2014) suggested 20‰ for Δ_{sed}, but lower values (15-20‰) are used in this model to satisfy a steady state. If (1) and (2) are both satisfied (given $(\delta^7Li)_{sw}$ a buffer range of ± 1.0‰), then we count as one solution.

Table A4.1 Description of parameters in the Li box model.

Symbol	Description	Value	Reference
δ^7Li_{sw}	Li isotope composition of seawater	31‰	Misra and Froelich 2012
F_{riv}	Li flux of continental weathering	10 x 10^9 mol/yr	Misra and Froelich 2012
δ^7Li_{riv}	Li isotope of continental runoff	23‰	Huh et al., 1998
F_{MOR}	Hydrothermal Li flux	13 x 10^9 mol/yr	Misra and Froelich 2012
δ^7Li_{MOR}	Li isotope ratio of hydrothermal flux	8.3‰	Misra and Froelich 2012
F_{alt}	Li flux associated with alteration of oceanic crust	12 x 10^9 mol/yr	Chan et al., 2002
Δ_{alt}	Isotopic fractionation associated with AOC	13‰	Li and West 2014
F_{sed}	Li flux associated with secondary mineral formation during reverse weathering	11 x 10^9 mol/yr	Li and West 2014
Δ_{sed}	Isotopic fractionation associated with removal of Li into secondary mineral during reveres weathering	20‰	Li and West 2014

Table A4.2 Model parameter presets and results.

δ^7Lisw		Continental runoff		Hydrothermal		Basalt alteration		Authigenic clay formation	
		F_{riv} (Gmol/yr)	δ^7Li_{riv} (‰)	F_{MOR} (Gmol/yr)	δ^7Li_{MOR} (‰)	F_{alt} (Gmol/yr)	Δ_{alt} (‰)	F_{sed} (Gmol/yr)	Δ_{sed} (‰)
10	model preset	0-30	0-23	8-12	8	0-25	5-13	0-25	15-20
	model result	0-30	0-5	8-12	8	12-24	5-8	0-15	15-20
15	model preset	0-30	3-23	0-20	8	0-25	5-13	0-25	15-20
	model result	6.5-20	3-6	4-16	8	10-12	5-9	10-19	15-20

Model results part 1: $(\delta^7Li)_{sw}$ = 10‰

The most noteworthy feature in the δ^7Li record is the rapid drawdown of δ^7Li in late Permian and the extremely low values before the Permian-Triassic Boundary. Based on the measured δ^7Li adding up an offset of 10‰, we model $(\delta^7Li)_{sw}$ = 10‰ corresponding to the late Permian scenario (253Ma).

The simulation runs every 0.05 Gmol/yr or ‰, and 7232 solutions were found in the $(\delta^7Li)_{sw}$ = 10‰ case. First, we present the model results for the $(\delta^7Li)_{sw}$ = 10‰ case by plotting F_{riv},δ^7Li_{riv}, F_{MOR}, F_{alt}, Δ_{alt}, F_{sed}, Δ_{sed} solution distribution in histograms (Fig. A4.1). $(\delta^7Li)_{sw}$ is recalculated and within our buffered range (10 ± 1.0‰) (Fig. A4.1d). Compared to the uncertainties we input into the model before calculation, the possible ranges for δ^7Li_{riv}, Δ_{alt} and F_{sed} are largely narrowed down (Fig. A4.1b, f, g). For example, the maximum δ^7Li_{riv} is 5‰, and the maximum Δ_{alt} is 8‰. Our model calculated δ^7Li_{riv} and Δ_{alt} are within the range of these modern measurements, but they are on the lower side (Fig. A4.1b, f). Profound differences are also seen in F_{sed}, which has a maximum of 15 Gmol/yr but most solutions require extremely low F_{sed} (Fig. A4.1g).

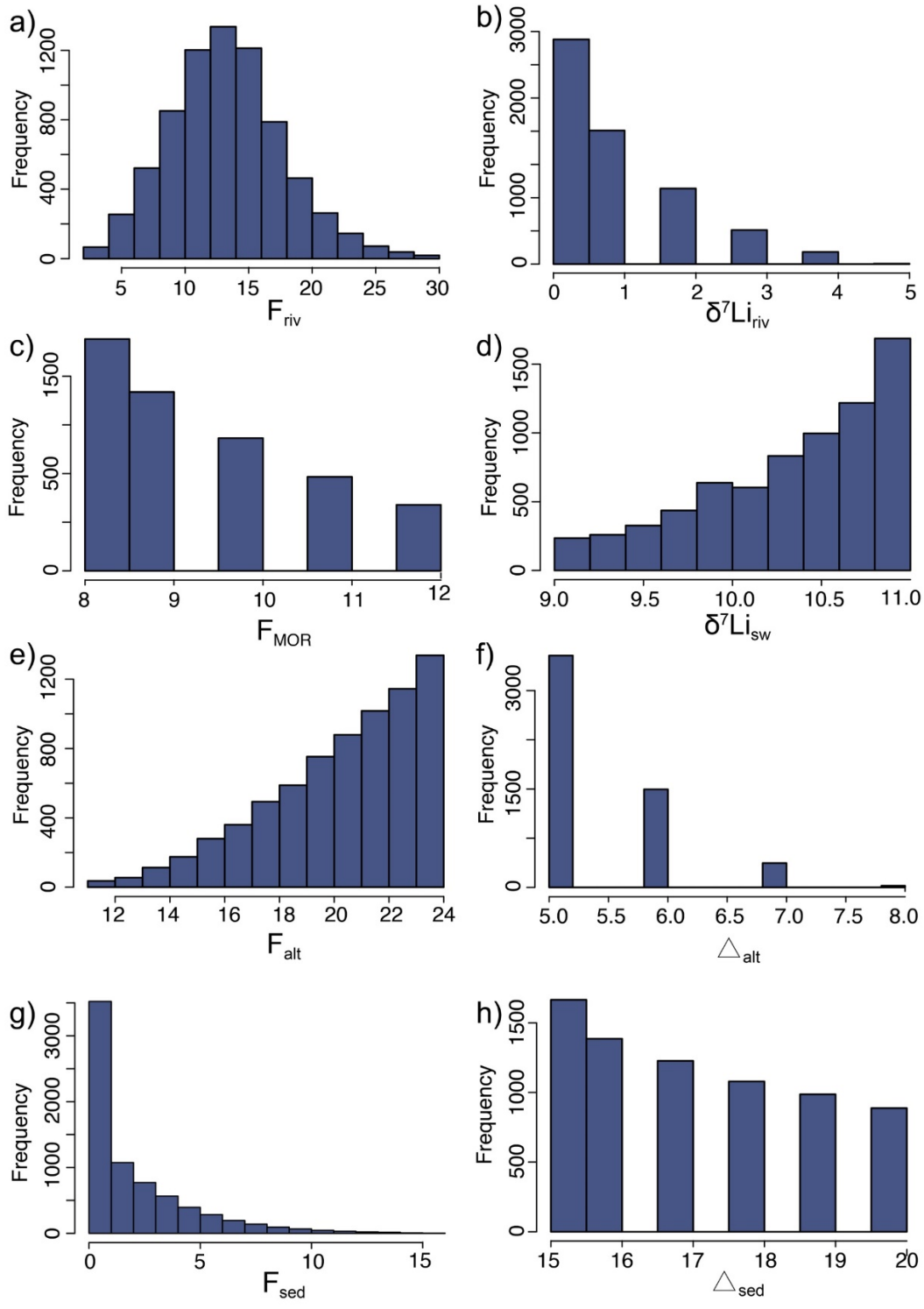

Figure A4.1 Histogram of calculated solutions for $(\delta^7Li)_{sw}$ = 10‰.

Next, we selectively show a few cross plots of these parameters to demonstrate how one parameter is constrained by another under steady-state (Fig. A4.2). When δ^7Li_{riv} increases, F_{riv} varies more, and the maximum δ^7Li_{riv} (5‰) yields F_{riv} of 16 Gmol/yr (Fig. A4.2a). Similar relationship is also observed between δ^7Li_{riv} and F_{sed} (Fig. A4.2c). Higher δ^7Li_{riv} requires lower F_{sed}, and the maximum δ^7Li_{riv} requires F_{sed} reaching 0 Gmol/yr. Next, we discuss the results in five scenarios to examine what changes in these variables are consistent with other geochemical records.

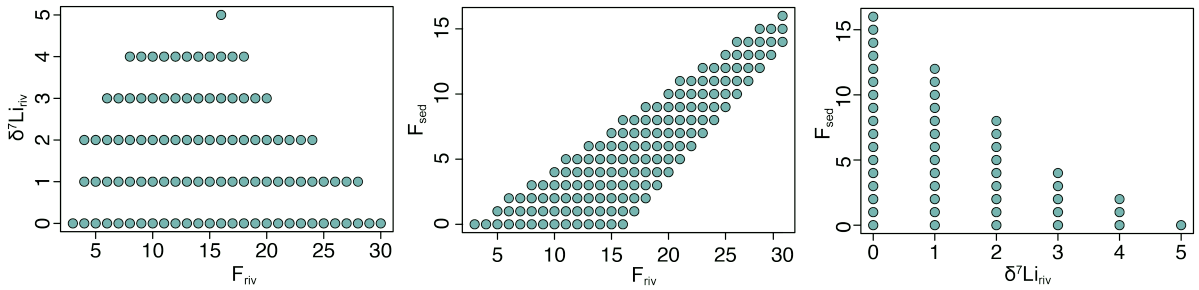

Figure A4.2 Cross plots of selected model parameters (F_{riv}, δ^7Li_{riv}, F_{sed}) for the $(\delta^7Li)_{sw}$ = 10‰ case.

The green dots present solutions obtained from the dynamic modeling. For each parameter, the simulation runs a calculation with a resolution of 0.05, meaning 0.05 Gmol/yr for the flux and 0.05‰ for the isotope composition.

Scenario 1: extreme continental congruent weathering

This scenario discusses variations in F_{riv} and associated δ^7Li_{riv} in the Li box model solutions. As shown in Fig. A4.1, δ^7Li_{riv} is restricted in a range of 0‰ to 4‰. Such low δ^7Li_{riv} values are hardly seen in natural rivers except for a few places that are organic-rich and alkaline (Dellinger et al., 2015). Instead, secondary mineral formation drives the δ^7Li_{riv} higher than the parent-rock δ^7Li and modern δ^7Li_{riv} is usually exceeds 3‰. In this scenario, we make δ^7Li_{riv} = 3‰, then F_{riv} needs to be 20 Gmol/yr, which is twice of the current F_{riv} (Fig. A4.2). A combination of high F_{riv} and low δ^7Li_{riv} requires intensive and congruent continental weathering. However, this is unlikely the situation for continental weathering in the Late Permian. The decrease in the δ^7Li record initiates at ~263 Ma, but the supercontinent was overall arid at this time (Retallack et al., 2006). Besides, the supply for weathering was limited due to the lack of tectonic activities and orogeneses. Additionally, the lowest δ^7Li locates between 253.5 Ma and 251.2 Ma (Table 4.1). Age of bulk Siberian Traps was dated at 249.4± 0.5 Ma, and the earliest onset age was at 255.58 ± 0.38 Ma (Burgess and Bowring, 2015) and 253.7 ± 1.2 Ma (Reichow et al., 2002). The lowest δ^7Li in bulk marine carbonates (δ^7Li_{carb}) overlaps with the onset of Siberian traps. However, the δ^7Li_{riv} starts to decrease 10 million years ago before the eruption of Siberian traps. Thus, the drawdown of $(\delta^7Li)_{sw}$ in the Late Permian is not a result of intensive congruent weathering.

Scenario 2: Weathering of shale or soil erosion

In this scenario, we shift the δ^7Li_{riv} to the lower end and investigate if extremely low δ^7Li_{riv} values are responsible for the drawdown of $(\delta^7Li)_{sw}$ in the Late Permian. Re-weathering of thick soil could lead to low δ^7Li values (<3‰) by releasing low δ^7Li into the river. This is so-called “supply limited” weathering regime (West, 2012). Minimal values (δ^7Li_{carb} = 6-10‰)

found in OAE 2 peak were interpreted as the destabilization of continental secondary minerals, also causing the addition of isotopically light Li (Pogge Von Strandmann et al., 2013). The lightest modern continental clays are unlikely to be lighter than -5‰ (Dellinger et al., 2014; Liu et al., 2013). Claystone breccias in the End Permian suggest they are products of soil erosion following the terminal Permian vegetation loss (Algeo and Twitchett, 2010; Retallack, 2005). This scenario takes 0‰ for δ^7Li_{riv}, making F_{riv} 18 Gmol/yr. This high F_{riv} value is unlikely at the Late Permian when climate should be dry in the inland of the supercontinent.

Scenario 3: Hydrothermal flux input

The hydrothermal flux of Li in the past is assumed to be proportional to the average rate of oceanic crust production and thus the spreading rate of mid-ocean ridges. In this scenario, we assume hydrothermal flux is about the same as present-day F_{MOR} (12 Gmol/yr). To satisfy the steady-state, Li output flux through authigenic clay formation is terminated, and Li removal from the ocean is mainly through basalt alteration. This solves the δ^7Li_{riv} to be 4‰ and F_{riv} to be 12 Gmol/yr, the same as the modern F_{riv} value. In this case, F_{alt} is driven to be as high as 24 Gmol/yr, and this becomes unrealistic when F_{MOR} is not changing.

Scenario 4: Basalt alteration

Li removal via basalt alteration probably does not change much because it is related to seafloor spreading rate, which is conjecturally stable over geologic time (Müller et al., 2008; Rowley, 2002). Therefore, if the changes of δ^7Li is caused or partially caused by changes in Li output via basalt alteration, it should have been due to changes in isotopic fractionation associated with this process (Δ_{alt}). The question is to what extent this change might have been to lower $(\delta^7Li)_{sw}$ by over 10‰ in 10 Million years. The interaction between oceanic basalt and seawater strongly depends on temperature. Above 150°C, hydrothermal fluids extract Li from the

basalt, while below 150°C, Li removes from seawater and enter the altered basalt (Seyfried et al., 1984). In this scenario, Falt equals to 12 Gmol/yr, although basalt alteration could have occurred at slower spreading rates in the Late Permian because of the supercontinent. Therefore, F_{MOR} is set at 8 Gmol/yr here. Modern Δalt varies from 8 to 23‰ (Seyfried et al., 1984). However, Δ_{alt} ranges from 5‰ to 8‰ in the model results. Lower values for Δ_{alt} are used to keep the δ^7Li_{riv} higher than 0‰. Currently, we cannot rule out the possibility of a lower Δalt in Permian due to the large uncertainty and limited research regarding this flux. Based on the discussion of the previous three scenarios, Friv is reduced to 4 Gmol/yr and δ^7Li_{riv} is set at 2‰. To balance the oceanic Li input and output, the Li flux of authigenic clay formation in the ocean is down to zero. The next scenario provides sedimentary evidence for a presumably paused authigenic clay formation that closely linked to the δ^7Li_{carb} drawdown.

Scenario 5: Collapsed authigenic clay formation

For δ^7Li_{sw} to achieve 10‰ at a steady-state, F_{sed} has to be reduced compared to the present-day flux because the Li isotope fractionation associated with authigenic clay formation is 15-20‰. In Scenario 1 and 2, either a extremely low δ^7Li_{riv} and high F_{riv} are needed to balance F_{sed}. And such situation does not align well with climate records of the Late Permian. According to Beauchamp and Baud. (2002), there is massive chert deposition in the Sverdrup basin (Canadian Arctic) as well as at the Northwestern USA starting at the Sakmarian-Artinskian boundary (~290 Ma). The so-called Permian Chert Event, terminated abruptly at the Late Permian. This chert gap follows in the Early Triassic and lasted for about 8 to 10 million years. It was not until the early to middle Triassic (Anisian) when chert deposition resumed in the distal oceanic areas. In the box model, the chert gap is referred to a collapse in the authigenic clay formation ($F_{sed} = 0$). If the total output flux of Li were about the same level of present-day value

in the Late Permian, F_{alt} would have doubled (Scenario 3 and 5). However, the possibility of having enhanced Li flux either from the continental weathering or from the hydrothermal activities has been ruled out.

In sum, we considered the above five scenarios for low $(\delta^7Li)_{sw}$ of 10‰ and concluded that Li box model in Scenario 4 is the mostly likely case. A collapsed authigenic clay formation in the ocean is the forcing factor for the $(\delta^7Li)_{sw}$ drawdown in the Late Permian. This time period is also characterized by reduced continental weathering rate and soil erosion.

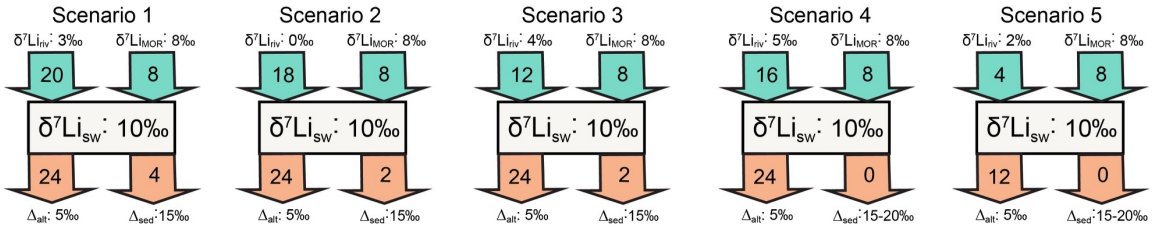

Figure A4.3 Box model of Li isotope cycle at different scenarios when $(\delta^7Li)_{sw}$ = 10‰.

Model results part 2: $(\delta^7Li)_{sw}$ = 15‰

A negative excursion of δ^7Li corresponds to the Tethys opening with the lowest $(\delta^7Li)_{sw}$ of around 15‰. This is also the value for $(\delta^7Li)_{sw}$ in the late Early Triassic. Therefore, we consider $(\delta^7Li)_{sw}$ = 15‰ in the model and discuss the results for each time period. For $(\delta^7Li)_{sw}$ = 15‰, the simulation runs at resolution of 0.5 Gmol/yr or ‰, and 19931 solutions were found in the $(\delta^7Li)_{sw}$ = 15‰ case. Histograms of each variables are shown in Fig. A4.6 including the $(\delta^7Li)_{sw}$ that are calculated using our model solutions, and all values are within the buffer range (Fig. A4.6d).

First, we discuss the possible environmental changes that are responsible for the negative excursion of δ^7Li in late Cisuralian and early Guadalupian (~275 Ma) using the model results. We propose that this fluctuation correlates with the changes in F_{MOR} caused by Tethys opening.

F_{MOR} varies from 4 Gmol/yr to 16 Gmol/yr in our model solutions (Fig. A4.6c). Additionally, two cross plots are show in Fig. A4.7 to demonstrate how F_{MOR} contain F_{riv} and F_{sed}. In Fig. A4.8, we plot two examples of Li isotope cycle for the $(\delta^7Li)_{sw}$ =15‰ case. In the first example, we adopt the maximum value for F_{MOR} (16 Gmol/yr). Then F_{sed} equals to10 Gmol/yr, which is similar to the modern F_{sed} (11 Gmol/yr) (Fig. A4.7). F_{riv} is 6.5 Gmol/yr, a reduced continental weathering flux compared to present-day value. F_{alt} is set at the modern value (12.5 Gmol/yr), and Δ_{alt} is calculated to be 5‰ which is lower than our estimate for the modern Δ_{alt} (13‰). To satisfy the steady state, δ^7Li_{riv} needs to be 3‰. This means no or little secondary minerals were formed on the continent, and δ^7Li_{riv} results from dissolution of primary minerals (congruent weathering). In Fig. A4.8b, we assume a F_{MOR} of 13 Gmol/yr, which is the same as the modern F_{MOR}. However, loss of ridge segments may have occurred due to the formation of supercontinent in the Early Permian, it is reasonable to assume that F_{MOR} before Tethys opening is less than the modern value (Korte et al., 2006). Therefore, 13 Gmol/yr for F_{MOR} in late Cisuralian (~275 Ma) represents an increased F_{MOR} during Tethys opening compared to the rest of the Permian. Under this setting, F_{riv} varies from 8 to 20 Gmol/yr, and F_{sed} varies from 10 to 18 Gmol/yr (Fig. A4.7). Without changing Δ_{alt}, F_{alt}, F_{sed} and Δ_{sed}, δ^7Li_{riv} is adjusted to 4.5‰ and F_{riv} increases to 9.5 Gmol/yr. Two examples demonstrate that changes in F_{MOR} can explain the decrease in $(\delta^7Li)_{sw}$ near Cisuralian-Guadalupian boundary.

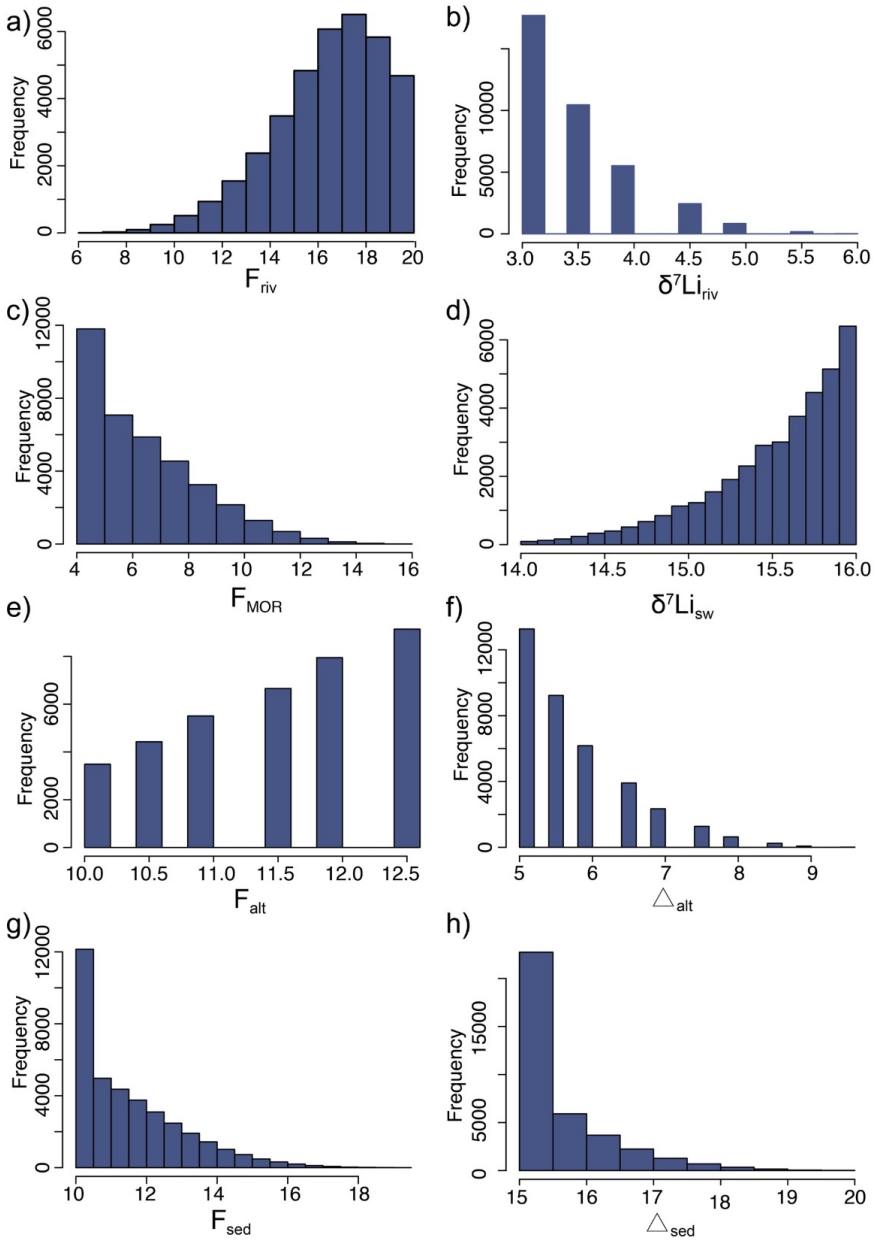

Figure A4.4 Histogram of calculated solutions for the $(\delta^7Li)_{sw}$ = 15‰ case.

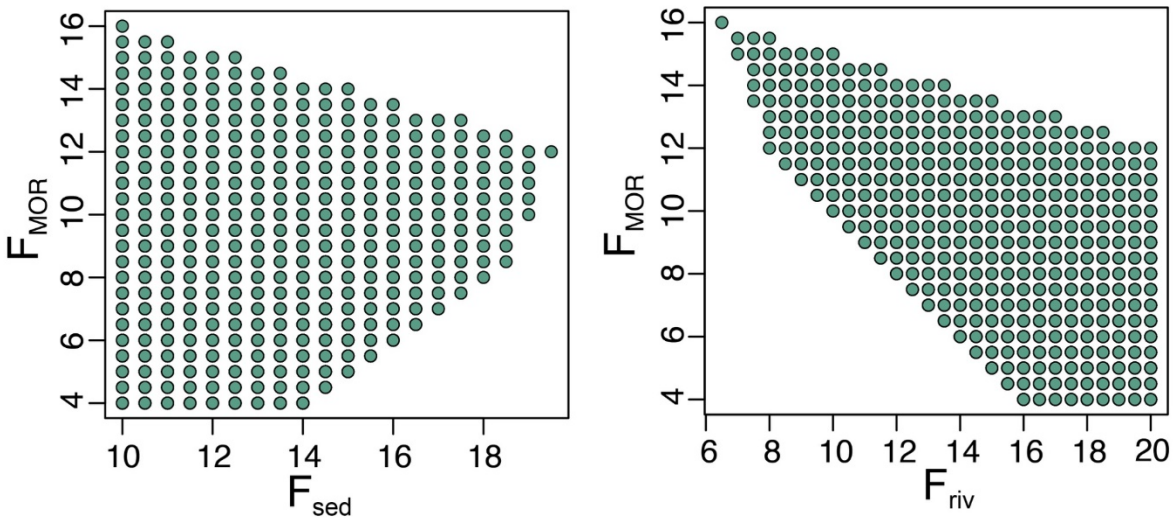

Figure A4.5 Cross plots of F_{MOR} v.s. Fsed and F_{riv} when $(\delta^7Li)_{sw}$ = 15‰.

The green dots present solutions obtained from the dynamic modeling.

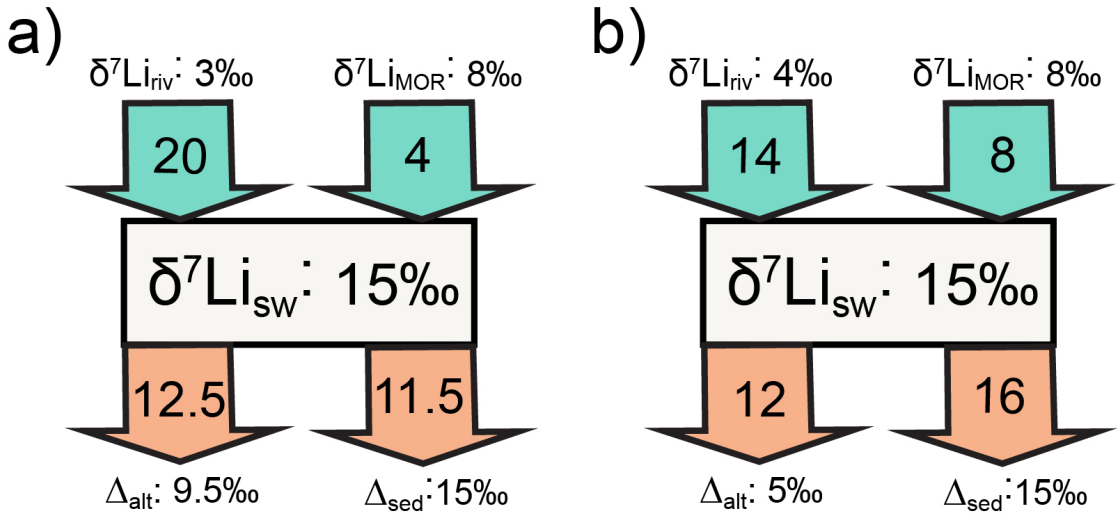

Figure A4.6 Box model of Li isotope cycle in the ocean when $(\delta^7Li)_{sw}$ = 15‰.

This scenario considers major changes in hydrothermal input (F_{MOR}).

Next, we discuss potential environmental changes that are responsible for the average $(\delta^7Li)_{sw}$ =15‰ in the Early Triassic (253 Ma – 247 Ma). Intensified chemical weathering rate has been inferred from the Sr isotopes in marine carbonate materials (Korte et al., 2003; Martin and Macdougall, 1995; Song et al., 2015) and magnesium isotopes in the silicates (Chen et al., 2020). Here we focus on quantifying the enhancement of continental weathering in terms of Li isotope flux from continental weathering. For this time period, the simulation presets the δ^7Li_{riv} to be higher than 3‰ as a result of basalt weathering. The steady-state model calculated δ^7Li_{riv} to vary from 3‰ to 6‰ (Fig. A4.4b). Two models were presented in Fig. A4.8 with one using the maximum δ^7Li_{riv} and the other using the minimum δ^7Li_{riv}. When δ^7Li_{riv} is at its maximum (6‰), F_{riv} is constrained between 16 and 19 Gmol/yr, F_{MOR} is within the range of 4 to 7 Gmol/yr, and F_{sed} is ~10 Gmol/yr (Δ_{sed} = 15‰) (Fig. A4.7). For instance, if assuming F_{MOR} is 6 Gmol/yr, which is about half of present-day value, F_{riv} would have increased by three times compared to the Late Permian (4 Gmol/yr). If increasing F_{MOR} to 8.5 Gmol/yr, F_{riv} is down to 14 Gmol/yr. Both models support the elevated Li flux as a result of intensified continental weathering. After the onset of the Siberian traps, it is likely that fast weathering of fresh basalts in a greenhouse climate increases the continental Li flux. Additionally, it's likely that the continental weathering was congruent in the Early Triassic, because 3‰ for δ^7Li_{riv} would require no or little secondary mineral formation.

Potential changes in Li removal are considered here as well. For example, when Δ_{alt} is set at 9.5 ‰ (Fig. A4.9, Scenario 4), F_{MOR} is reduced from 8 Gmol/yr to 4 Gmol/yr compared to Scenario 5. If F_{sed} increases by 1.5 times, then δ^7Li_{riv} and Δ_{alt} will both decrease. Meanwhile, F_{riv} needs to be doubled to balance the output flux. In sum, a low δ^7Li_{riv} value is necessary in all scenarios. F_{riv} modeled in steady state has a maximum of 20 Gmol/yr in the Early Triassic and

this flux is three times of the mid Permian F_{riv} (6.5 Gmol/yr). To conclude, the box model supports that the rise of $(\delta^7Li)_{sw}$ in the Early Triassic are likely caused by increased congruent chemical weathering (Fig. A4.4).

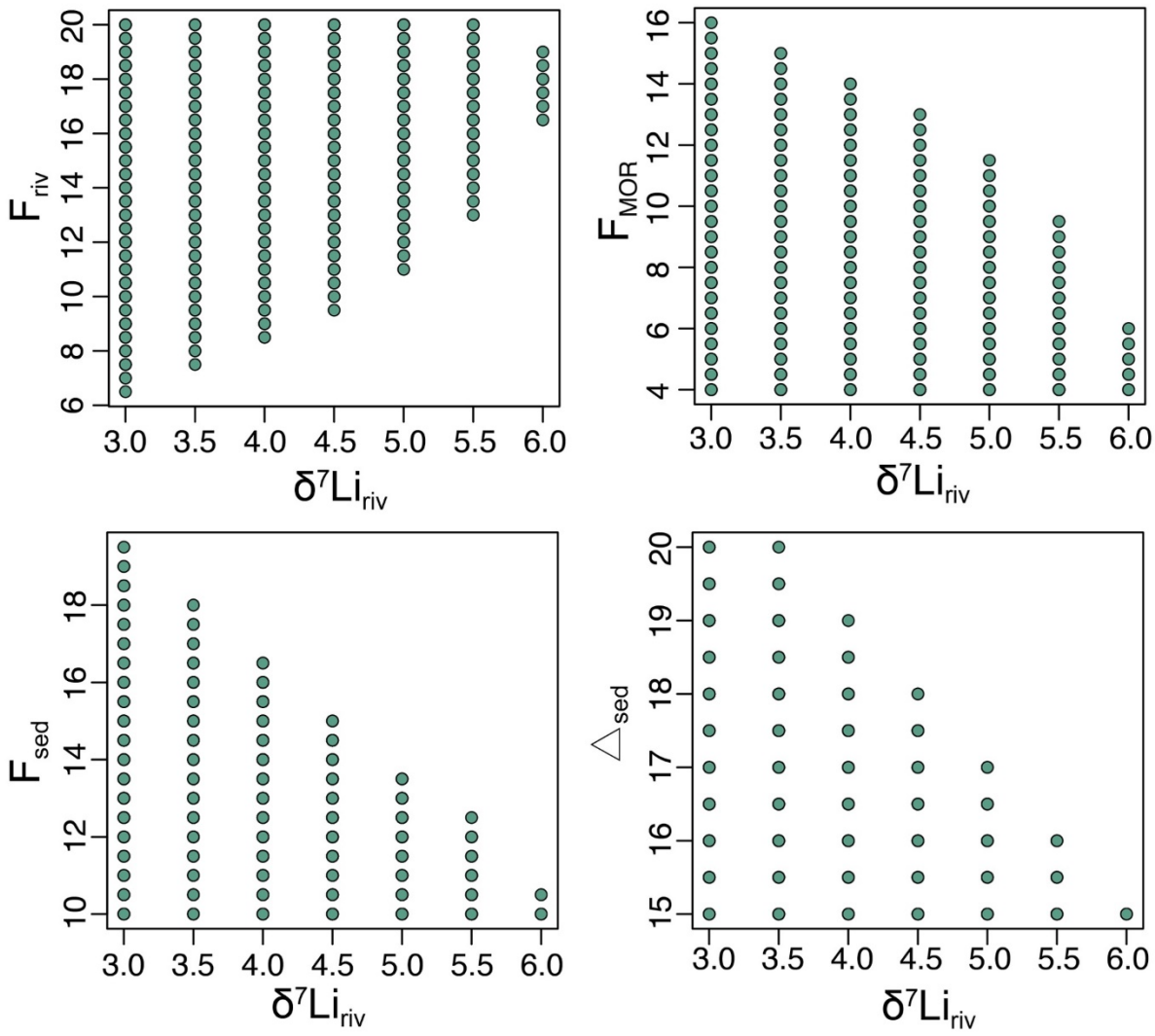

Figure A4.7 Cross plots of δ^7Li_{riv} v.s. F_{riv}, δ^7Li_{riv} v.s. F_{MOR}, δ^7Li_{riv} v.s. F_{sed}, and δ^7Li_{riv} v.s. Δ_{sed}.

The green dots present solutions obtained from the dynamic modeling.

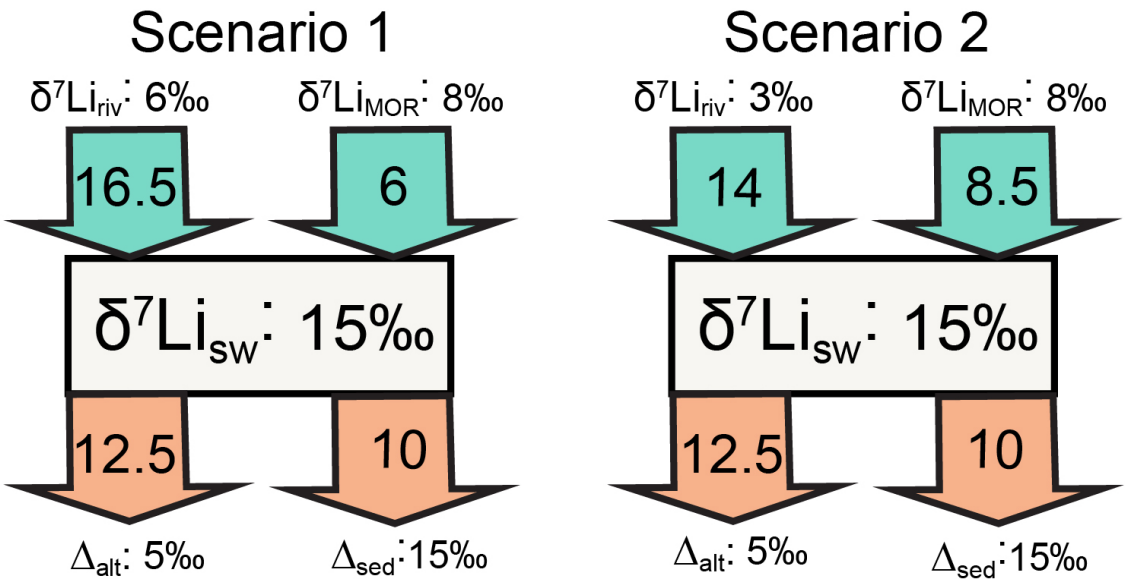

Figure A4.8 Box model of Li isotope cycle when $(\delta^7Li)_{sw}$ = 15‰ in early Triassic.

Scenario 1 represents congruent weathering, and scenario 2 represents extreme low δ^7Li_{riv} related to soil erosion or shale weathering.

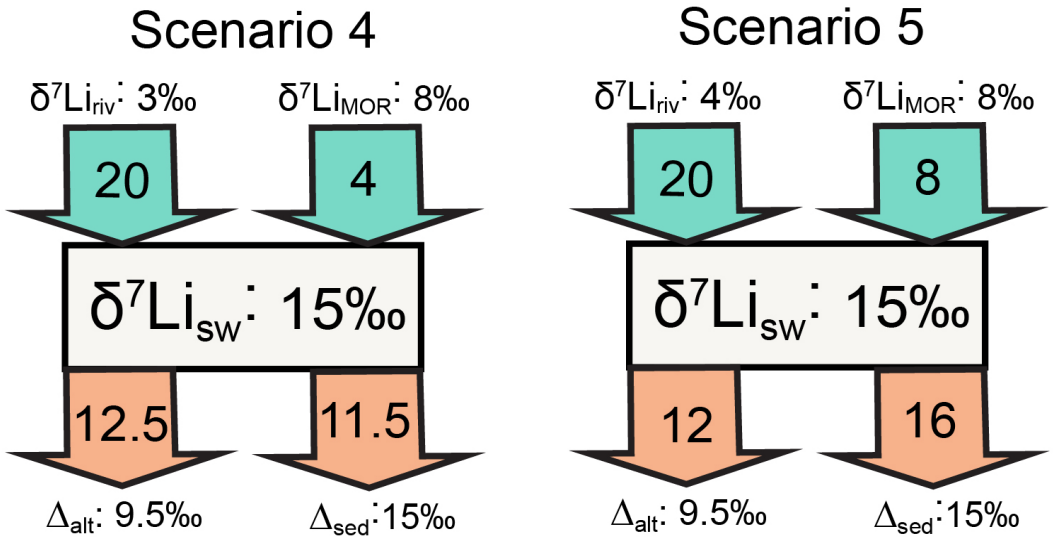

Figure A4.9 Box model of Li isotope cycle when $(\delta^7Li)_{sw}$ = 15‰ in early Triassic with major changes in Li output.

REFERENCES

Algeo, T.J., Twitchett, R.J., 2010. Anomalous early Triassic sediment fluxes due to elevated weathering rates and their biological consequences. Geology 38, 1023–1026. https://doi.org/10.1130/G31203.1

Alibo, D.S., Nozaki, Y., 2000. Dissolved rare earth elements in the South China Sea: Geochemical characterization of the water masses. J. Geophys. Res. Ocean. 105, 28771–28783. https://doi.org/10.1029/1999JC000283

Alibo, D.S., Nozaki, Y., 1999. Rare earth elements in seawater: Particle association, shale-normalization, and Ce oxidation. Geochim. Cosmochim. Acta 63, 363–372. https://doi.org/10.1016/S0016-7037(98)00279-8

Beauchamp, B., Baud, A., 2002. Growth and demise of Permian biogenic chert along northwest Pangea: Evidence for end-Permian collapse of thermohaline circulation. Palaeogeogr. Palaeoclimatol. Palaeoecol. 184, 37–63. https://doi.org/10.1016/S0031-0182(02)00245-6

Burgess, S.D., Bowring, S.A., 2015. High-precision geochronology confirms voluminous magmatism before, during, and after Earth's most severe extinction. Sci. Adv. 1, 1–14. https://doi.org/10.1126/sciadv.1500470

Byrne, R.H., Bingler, L.S., 1989. Comment on "Cerium: A chemical tracer for paleo-oceanic redox conditions" by Y.-G. Liu, M. R. U. Miah and R. A. Schmitt. Geochim. Cosmochim. Acta. https://doi.org/10.1016/0016-7037(89)90081-1

Byrne, R.H., Sholkovitz, E.R., 1996. Marine Chemistry and Geochemistry of the lanthanides, in: Gschneidner Jr., K.A., Eyring, L. (Eds.), Handbook on the Physics and Chemistry of Rare Earths. Elsevier Sci., Amsterdam, pp. 497–592.

Cantrell, K.J., Byrne, R.H., 1987. Rare earth element complexation by carbonate and oxalate ions. Geochim. Cosmochim. Acta 51, 597–605. https://doi.org/10.1016/0016-7037(87)90072-X

Chan, L.H., Alt, J.C., Teagle, D.A.H., 2002. Lithium and lithium isotope profiles through the upper oceanic crust: A study of seawater-basalt exchange at ODP Sites 504B and 896A. Earth Planet. Sci. Lett. 201, 187–201. https://doi.org/10.1016/S0012-821X(02)00707-0

Chen, X.Y., Teng, F.Z., Huang, K.J., Algeo, T.J., 2020. Intensified chemical weathering during Early Triassic revealed by magnesium isotopes. Geochim. Cosmochim. Acta. https://doi.org/10.1016/j.gca.2020.02.035

De Baar, H.J.W., German, C.R., Elderfield, H., van Gaans, P., 1988. Rare earth element distributions in anoxic waters of the Cariaco Trench. Geochim. Cosmochim. Acta 52, 1203–1219. https://doi.org/10.1016/0016-7037(88)90275-X

Dellinger, M., Gaillardet, J., Bouchez, J., Calmels, D., Louvat, P., Dosseto, A., Gorge, C., Alanoca, L., Maurice, L., 2015. Riverine Li isotope fractionation in the Amazon River basin controlled by the weathering regimes. Geochim. Cosmochim. Acta 164, 71–93. https://doi.org/10.1016/j.gca.2015.04.042

Dellinger, M., Gaillardet, J.Ô., Bouchez, J., Calmels, D., Galy, V., Hilton, R.G., Louvat, P., France-Lanord, C., 2014. Lithium isotopes in large rivers reveal the cannibalistic nature of modern continental weathering and erosion. Earth Planet. Sci. Lett. 401, 359–372. https://doi.org/10.1016/j.epsl.2014.05.061

Ehrlich, A., 1968. Rare earth abundances in manganese nodules. Massachusetts Inst of Tech cambridge.

Garcia-Solsona, E., Jeandel, C., Labatut, M., Lacan, F., Vance, D., Chavagnac, V., Pradoux, C., 2014. Rare earth elements and Nd isotopes tracing water mass mixing and particle-seawater interactions in the SE Atlantic. Geochim. Cosmochim. Acta 125, 351–372. https://doi.org/10.1016/j.gca.2013.10.009

German, C., Holliday, B.P., Elderfield, H., 1991. Redox cycling of rare earth elements in the suboxic zone of the Black Sea. Geochim. Cosmochim. Acta 55, 3553–3558. https://doi.org/10.1016/0016-7037(91)90055-A

German, C.R., Elderfield, H., 1990. Application of the Ce anomaly as a paleoredox indicator: The ground rules. Paleoceanography 5, 823–833. https://doi.org/10.1029/PA005i005p00823

Huh, Y., Chan, L.H., Chadwick, O.A., 2004. Behavior of lithium and its isotopes during weathering of Hawaiian basalt. Geochemistry, Geophys. Geosystems 5. https://doi.org/10.1029/2004GC000729

Huh, Y., Chan, L.H., Edmond, J.M., 2001. Lithium isotopes as a probe of weathering processes: Orinoco River. Earth Planet. Sci. Lett. 194, 189–199. https://doi.org/10.1016/S0012-821X(01)00523-4

Huh, Y., Chan, L.H., Zhang, L., Edmond, J.M., 1998. Lithium and its isotopes in major world rivers: implications for weathering and the oceanic budget. Geochim. Cosmochim. Acta 62, 2039–2051. https://doi.org/10.1016/S0016-7037(98)00126-4

James, R.H., Rudnick, M.D., Palmer, M.R., 1999. The alkali element and boron geochemistry of the Escanaba Through sediment-hosted hydrothermal system. Earth Planet. Sci. Lett. 171, 157–169. https://doi.org/10.1016/S0012-821X(99)00140-5

Kisakurek, B., James, R.H., Harris, N.B.W., 2005. Li and δ7Li in Himalayan rivers: Proxies for silicate weathering? Earth Planet. Sci. Lett. 237, 387–401. https://doi.org/10.1016/j.epsl.2005.07.019

Korte, C., Jasper, T., Kozur, H.W., Veizer, J., 2006. 87Sr/86Sr record of Permian seawater.

Palaeogeogr. Palaeoclimatol. Palaeoecol. 240, 89–107. https://doi.org/10.1016/j.palaeo.2006.03.047

Korte, C., Kozur, H.W., Bruckschen, P., Veizer, J., 2003. Strontium isotope evolution of late permian and triassic seawater. Geochim. Cosmochim. Acta 67, 47–62. https://doi.org/10.1016/S0016-7037(02)01035-9

Lee, C.T.A., Cheng, X., Horodyskyj, U., 2006. The development and refinement of continental arcs by primary basaltic magmatism, garnet pyroxenite accumulation, basaltic recharge and delamination: Insights from the Sierra Nevada, California. Contrib. to Mineral. Petrol. 151, 222–242. https://doi.org/10.1007/s00410-005-0056-1

Lee, J.H., Byrne, R.H., 1993. Complexation of trivalent rare earth elements (Ce, Eu, Gd, Tb, Yb) by carbonate ions. Geochim. Cosmochim. Acta 57, 295–302. https://doi.org/10.1016/0016-7037(93)90432-V

Lemarchand, E., Chabaux, F., Vigier, N., Millot, R., Pierret, M.C., 2010. Lithium isotope systematics in a forested granitic catchment (Strengbach, Vosges Mountains, France). Geochim. Cosmochim. Acta 74, 4612–4628. https://doi.org/10.1016/j.gca.2010.04.057

Li, G., West, A.J., 2014. Evolution of Cenozoic seawater lithium isotopes: Coupling of global denudation regime and shifting seawater sinks. Earth Planet. Sci. Lett. 401, 284–293. https://doi.org/10.1016/j.epsl.2014.06.011

Liu, X.-M., Rudnick, R.L., 2011. Constraints on continental crustal mass loss via chemical weathering using lithium and its isotopes. Proc. Natl. Acad. Sci. U. S. A. 108, 20873–20880. https://doi.org/10.1073/pnas.1115671108

Liu, X., Byrne, R.H., 1995. Comparative carbonate complexation of yttrium and gadolinium at 25 °C and 0.7 mol dm-3 ionic strength. Mar. Chem. 51, 213–221. https://doi.org/10.1016/0304-4203(95)00067-4

Liu, X.M., Rudnick, R.L., McDonough, W.F., Cummings, M.L., 2013. Influence of chemical weathering on the composition of the continental crust: Insights from Li and Nd isotopes in bauxite profiles developed on Columbia River Basalts. Geochim. Cosmochim. Acta 115, 73–91. https://doi.org/10.1016/j.gca.2013.03.043

Liu, Y., Miah, M.R.U., Schmitt, R.A., 1988. Cerium : A chemical tracer for paleo-oceanic redox conditions. Geochim. Cosmochim. Acta 52, 1361–1371.

Luo, Y.R., Byrne, R.H., 2004. Carbonate complexation of yttrium and the rare earth elements in natural waters. Geochim. Cosmochim. Acta 68, 691–699. https://doi.org/10.1016/S0016-7037(03)00495-2

Martin, E.E., Macdougall, J.D., 1995. Sr and Nd isotopes at the Permian/Triassic boundary: A record of climate change. Chem. Geol. 125, 73–99. https://doi.org/10.1016/0009-

2541(95)00081-V

Millero, F.J., 1992. Stability constants for the formation of rare earth-inorganic complexes as a function of ionic strength. Geochim. Cosmochim. Acta 56, 3123–3132. https://doi.org/10.1016/0016-7037(92)90293-R

Misra, S., Froelich, P.N., 2012. Lithium isotope history of cenozoic seawater: Changes in silicate weathering and reverse weathering. Science (80-.). 335, 818–823. https://doi.org/10.1126/science.1214697

Moffett, J.W., 1994a. A radiotracer study of cerium and manganese uptake onto suspended particles in Chesapeake Bay. Geochim. Cosmochim. Acta 58, 695–703. https://doi.org/10.1016/0016-7037(94)90499-5

Moffett, J.W., 1994b. The relationship between cerium and manganese oxidation in the marine environment. Limnol. Oceanogr. 39, 1309–1318. https://doi.org/10.4319/lo.1994.39.6.1309

Moffett, J.W., 1990. Microbially mediated cerium oxidation in sea water. Nature 345, 421–423. https://doi.org/10.1038/345421a0

Molina-Kescher, M., Frank, M., Hathorne, E., 2014. South Pacific dissolved Nd isotope compositions and rare earth element distributions: Water mass mixing versus biogeochemical cycling. Geochim. Cosmochim. Acta 127, 171–189. https://doi.org/10.1016/j.gca.2013.11.038

Molina-Kescher, M., Hathorne, E.C., Osborne, A.H., Behrens, M.K., Kölling, M., Pahnke, K., Frank, M., 2018. The influence of basaltic islands on the oceanic REE distribution: A case study from the Tropical South Pacific. Front. Mar. Sci. 5. https://doi.org/10.3389/fmars.2018.00050

Müller, R.D., Sdrolias, M., Gaina, C., Steinberger, B., Heine, C., 2008. Long-term sea-level fluctuations driven by ocean basin dynamics. Science (80-.). 319, 1357–1362. https://doi.org/10.1126/science.1151540

Nozaki, Y., 2001. Rare Earth Elements and Their Isotopes in the Ocean. Encycl. Ocean Sci. 2354–2366. https://doi.org/10.1029/2002EO000342

Nozaki, Y., Alibo, D.S., 2003a. Dissolved rare earth elements in the Southern Ocean, southwest of Australia: Unique patterns compared to the South Atlantic data. Geochem. J. 37, 47–62. https://doi.org/10.2343/geochemj.37.47

Nozaki, Y., Alibo, D.S., 2003b. Importance of vertical geochemical processes in controlling the oceanic profiles of dissolved rare earth elements in the northeastern Indian Ocean. Earth Planet. Sci. Lett. 205, 155–172. https://doi.org/10.1016/S0012-821X(02)01027-0

Ohta, A., Kawabe, I., 2000. Theoretical study of tetrad effects observed in REE distribution

coefficients between marine Fe-Mn deposit and deep seawater, and in REE(III)-carbonate complexation constants. Geochem. J. 34, 455–473. https://doi.org/10.2343/geochemj.34.455

Penniston-Dorland, S., Liu, X.-M., Rudnick, R.L., 2017. Lithium Isotope Geochemistry, in: Reviews in Mineralogy and Geochemistry. pp. 165–217. https://doi.org/10.2138/rmg.2017.82.6

Pistiner, Henderson, G.M., 2003. Lithium-isotope fractionation during continental weathering processes. Earth Planet. Sci. Lett. 214, 327–339. https://doi.org/10.1016/S0012-821X(03)00348-0

Pogge von Strandmann, P.A.E., Burton, K.W., James, R.H., van Calsteren, P., Gíslason, S.R., Mokadem, F., 2006. Riverine behaviour of uranium and lithium isotopes in an actively glaciated basaltic terrain. Earth Planet. Sci. Lett. 251, 134–147. https://doi.org/10.1016/j.epsl.2006.09.001

Pogge Von Strandmann, P.A.E., Jenkyns, H.C., Woodfine, R.G., 2013. Lithium isotope evidence for enhanced weathering during Oceanic Anoxic Event 2. Nat. Geosci. 6, 668–672. https://doi.org/10.1038/ngeo1875

Rao, V.K., Shanhani, C.J., Rao, C.L., 1970. Standard Thermodynamic Values. Radiochim. Acta 14, 31–34. https://doi.org/https://doi.org/10.1524/ract.1970.14.1.31

Reichow, M.K., Saunders, A.D., White, R. V., Pringle, M.S., Al'Mukhamedov, A.I., Medvedev, A.I., Kirda, N.P., 2002. 40Ar/39Ar dates from the West Siberian Basin: Siberian flood basalt province doubled. Science (80-.). 296, 1846–1849. https://doi.org/10.1126/science.1071671

Retallack, G.J., 2005. Earliest Triassic Claystone Breccias and Soil-Erosion Crisis. J. Sediment. Res. 75, 679–695. https://doi.org/10.2110/jsr.2005.055

Retallack, G.J., Metzger, C.A., Greaver, T., Jahren, A.H., Smith, R.M.H., Sheldon, N.D., 2006. Middle-Late Permian mass extinction on land. Bull. Geol. Soc. Am. 118, 1398–1411. https://doi.org/10.1130/B26011.1

Rowley, D.B., 2002. Rate of plate creation and destruction: 180 Ma to present. Bull. Geol. Soc. Am. 114, 927–933. https://doi.org/10.1130/0016-7606(2002)114<0927:ROPCAD>2.0.CO;2

Seyfried, W.E., Janecky, D.R., Mottl, M.J., 1984. Alteration of the oceanic crust: Implications for geochemical cycles of lithium and boron. Geochim. Cosmochim. Acta 48, 557–569. https://doi.org/10.1016/0016-7037(84)90284-9

Sillen, L.G., Martell, A.G., 1971. Supplement No. 1, in: Stability Constants of Metal Ion Complexes. Chem. Soc. Spec. Publ., London, p. 865P.

Smith, R.M., Martell, A.G., 1976. Inorganic complexes, in: Critical Stability Constants. Vol.4. Plenum Press.

Song, Haijun, Wignall, P.B., Tong, J., Song, Huyue, Chen, J., Chu, D., Tian, L., Luo, M., Zong, K., Chen, Y., Lai, X., Zhang, K., Wang, H., 2015. Integrated Sr isotope variations and global environmental changes through the Late Permian to early Late Triassic, Earth and Planetary Science Letters. https://doi.org/10.1016/j.epsl.2015.05.035

Tachikawa, K., Jeandel, C., Vangriesheim, A., Dupré, B., 1999. Distribution of rare earth elements and neodymium isotopes in suspended particles of the tropical Atlantic Ocean (EUMELI site). Deep Sea Res. Part I Oceanogr. Res. Pap. 46, 733–755. https://doi.org/10.1016/S0967-0637(98)00089-2

Tang, J., Johannesson, K.H., 2003. Speciation of rare earth elements in natural terrestrial waters: Assessing the role of dissolved organic matter from the modeling approach. Geochim. Cosmochim. Acta 67, 2321–2339. https://doi.org/10.1016/S0016-7037(02)01413-8

Teng, F.Z., McDonough, W.F., Rudnick, R.L., Dalpé, C., Tomascak, P.B., Chappell, B.W., Gao, S., 2004. Lithium isotopic composition and concentration of the upper continental crust. Geochim. Cosmochim. Acta 68, 4167–4178. https://doi.org/10.1016/j.gca.2004.03.031

Tomascak, P.B., Tera, F., Helz, R.T., Walker, R.J., 1999. The absence of lithium isotope fractionation during basalt differentiation: New measurements by multicollector sector ICP-MS. Geochim. Cosmochim. Acta 63, 907–910. https://doi.org/10.1016/S0016-7037(98)00318-4

Vigier, N., Decarreau, A., Millot, R., Carignan, J., Petit, S., France-Lanord, C., 2008. Quantifying Li isotope fractionation during smectite formation and implications for the Li cycle. Geochim. Cosmochim. Acta 72, 780–792. https://doi.org/10.1016/j.gca.2007.11.011

Wanner, C., Sonnenthal, E.L., Liu, X.M., 2014. Seawater δ7Li: A direct proxy for global CO2 consumption by continental silicate weathering? Chem. Geol. 381, 154–167. https://doi.org/10.1016/j.chemgeo.2014.05.005

West, A.J., 2012. Thickness of the chemical weathering zone and implications for erosional and climatic drivers of weathering and for carbon-cycle feedbacks. Geology 40, 811–814. https://doi.org/10.1130/G33041.1

Wimpenny, J., Gíslason, S.R., James, R.H., Gannoun, A., Pogge Von Strandmann, P.A.E., Burton, K.W., 2010. The behaviour of Li and Mg isotopes during primary phase dissolution and secondary mineral formation in basalt. Geochim. Cosmochim. Acta 74, 5259–5279. https://doi.org/10.1016/j.gca.2010.06.028

Witherow, R.A., Lyons, W.B., Henderson, G.M., 2010. Lithium isotopic composition of the McMurdo Dry Valleys aquatic systems. Chem. Geol. 275, 139–147. https://doi.org/10.1016/j.chemgeo.2010.04.017

Yaitskaya, N., 2011. Temperature, Salinity, Oxygen, Phosphate, Silicate, Nitrite, pH and Alkalinity data collected in the Black Sea, Tyrrhenian Sea and Western Basin from R/Vs GORIZONT and OKEANOGRAF, 1960 - 1969 (NCEI Accession 0074609).Alkalinity and pH used. NOAA National. Russ. Acad. Sci.

Zhang, J., Nozaki, Y., 1998. Behavior of rare earth elements in seawater at the ocean margin: a study along the slopes of the Sagami and Nankai troughs near Japan. Geochim. Cosmochim. Acta 62, 1307–1317. https://doi.org/10.1016/S0016-7037(98)00073-8

Zhang, J., Nozaki, Y., 1996. Rare earth elements and yttrium in seawater: ICP-MS determinations in the East Caroline, Coral Sea, and South Fiji basins of the western South Pacific Ocean. Geochim. Cosmochim. Acta 60, 4631–4644. https://doi.org/10.1016/S0016-7037(96)00276-1

Zheng, X.Y., Plancherel, Y., Saito, M.A., Scott, P.M., Henderson, G.M., 2016. Rare earth elements (REEs) in the tropical South Atlantic and quantitative deconvolution of their non-conservative behavior. Geochim. Cosmochim. Acta 177, 217–237. https://doi.org/10.1016/j.gca.2016.01.018